

NORTHWESTERN UNIVERSITY

Lanthanide Scandate Supported Noble Metal Nanoparticle Catalysts

A DISSERTATION

SUBMITTED TO THE GRADUATE SCHOOL  
IN PARTIAL FULFILLMENT OF THE REQUIREMENTS

for the degree

DOCTOR OF PHILOSOPHY

Field of Materials Science and Engineering

By

Ryan J. Paull

EVANSTON, ILLINOIS

June 2020

ProQuest Number:27834880

All rights reserved

INFORMATION TO ALL USERS

The quality of this reproduction is dependent on the quality of the copy submitted.

In the unlikely event that the author did not send a complete manuscript and there are missing pages, these will be noted. Also, if material had to be removed, a note will indicate the deletion.



ProQuest 27834880

Published by ProQuest LLC (2020). Copyright of the Dissertation is held by the Author.

All Rights Reserved.

This work is protected against unauthorized copying under Title 17, United States Code  
Microform Edition © ProQuest LLC.

ProQuest LLC  
789 East Eisenhower Parkway  
P.O. Box 1346  
Ann Arbor, MI 48106 - 1346

## ABSTRACT

Lanthanide Scandate Supported Noble Metal Nanoparticle Catalysts

Ryan J. Paull

The complex structure of typical heterogeneous catalysts, where nanoparticles of active material are dispersed onto the surface of a thermally stable support with a high surface area, complicates the understanding of how the support can affect the resulting catalyst structure and properties. Using well-faceted and shape-controlled oxides as supports would allow for further control of the catalyst shape and orientation, which would produce model catalytic systems in determining structure-property relationships. In this thesis, lanthanide scandate supports were used with different noble metal nanoparticle catalysts, as they have similar lattice parameters so well-understood concepts related to epitaxy may be used to control the catalyst shape, size, and orientation.

Lanthanide scandate supports were prepared with high surface area and a consistent surface termination using a new water vapor-assisted sol-gel reaction. Reactions that occurred under dry conditions only resulted in an amorphous product, whereas reactions that had a high chemical potential of water led to rare-earth hydroxides as the primary phase. As a consequence, hydrothermal synthesis was unable to produce the desired

perovskite phase, necessitating the need for another synthetic approach. When a balance of water vapor was achieved, the perovskite phase was formed in a high yield. The water vapor assisted in the crystallization process, which we speculate is because the gel was imbibed by the water vapor to preserve the open solid matrix of the gel and allow for greater diffusion at lower temperatures. Further, the supports could be made as beveled cubes, primarily terminated with pseudocubic- $\{100\}$  surfaces by exploiting a two-step heat treatment. The first step was performed at higher temperatures, where the reaction had a strong driving force, which nucleated many small particles of the perovskite particle phase. The second step was then performed at a lower temperature, which lessened the driving force and promoted particle smoothing. This process successfully produced well-faceted particles across the lanthanide scandates explored.

The lanthanide scandate particles were used as supports for gold and platinum catalysts. Gold catalysts deposited using deposition-precipitation were monodisperse in size across any given support. The orientation of the gold nanoparticles was a function of their size and the support used, as both were critical in determining the relative lattice matching and interfacial energy. When the lattice parameter of the gold was well-matched with that of the support, the interfacial energy pushed the system to adopt gold particles where the  $\{110\}$  sat atop the support. When the lattice parameters of the gold and support differed, the gold particles instead oriented with the  $\{111\}$  surface on the support because of the low energy of the close-packed gold  $\{111\}$  surface. During preliminary investigations of these systems for CO oxidation, well lattice-matched catalysts were found to be less active, deactivate quicker, and sinter more significantly.

Utilizing the different lattice parameters of the lanthanide scandates led to varying degrees of tensile strain in platinum nanoparticles. With increasing tensile strain in the platinum, the percentage of CO bound between several metal atoms rather than atop a single platinum atom increased, and a greater percentage of the CO was bound more weakly. The role of basic supports in CO oxidation and the reverse water-gas shift reactions was investigated by using the lanthanide scandates as model supports with platinum catalysts. A greater binding strength of carbon dioxide on the lanthanide scandate support correlated with the bond valence sum of the scandium in the support. The binding strength was a controlling variable in both the rate of CO oxidation and the degree of reverse water-gas shift. A support that bound carbon dioxide more strongly had a stronger driving force for producing carbon dioxide and correspondingly had a greater CO oxidation rate. Similarly, such a system had a smaller driving force for losing carbon dioxide and experienced a lesser degree of reverse water-gas shift.

## Acknowledgements

First I would have to thank my advisors, Laurie and Ken. I can never thank you enough for taking on a student whose research track record suggested an unqualified graduate student; I imagined myself as being something of a risk for you both to take in, but look where we ended up! I would like to thank my thesis committee members, Prof. Justin Notestein and Prof. Michael Bedzyk, as well as my qualifying examination committee members, Prof. Justin Notestein (again) and Prof. Sossina Haile. I would also like to acknowledge my funding through the Institute for Catalysis in Energy Processes (ICEP), which receives its funding from the U.S. Department of Energy Office of Basic Sciences, grant award number DE-FG02-03ER15457.

Much of the scientific work of thesis would not have been possible without a number of collaborators who actually performed a fair amount of this work. I would have to start with my electron microscopist, gym buddy, and beer brewing (and drinking) friend, Zach, who did most (if not all) of the electron microscopy shown in this thesis. Tiffany for our many discussions contemplating nanoparticle growth and with whom I (we) developed the lanthanide scandate synthetic method. Emily for taking over this project because Zach does not know how to grow things and for running many of the catalytic experiments with me. Chris, I appreciate your understanding, one in DFT, one in solid-state science in general, and most importantly one in helping me emotionally and letting me vent about our graduate school struggles. Thank you, Michael, for letting me ask you who knows how

many stupid chemistry questions and for answering them in a way that did not make me feel like an idiot (even though I probably was)! Neil and Selim, thank you for the amazing job you do in running REACT (the facility formally known as CleanCat), and for teaching me not just how to use the equipment but to really appreciate how the equipment works and to think about what I am really measuring in any given experiment. Your “For the general user” series was incredibly helpful for me throughout my Ph.D. I would also like to thank Jerry Carsello for running the Cohen X-Ray Facility and for his hard work in adapting the facility to getting whatever needed to be done done. Lastly, I would not have been able to do all of this work without the support, both emotionally and technically, of my group members, past and current. Particular thanks to those in the Poeppelmeier group who let me listen to my music without headphones, the Marks group still can not imagine letting me do that! I would also like to thank Jake Thornberry and Jesse Robkin for their help running the Poeppelmeier group and managing Ken’s seemingly impossible calendar.

I would have been at a complete loss without all of the friends I met. First, an additional shoutout to all of my former group members, all of whom I have become friends with. All of my friends with whom I have played so many IM’s with, thank you for putting up with my crazy competitiveness and letting me get it out of my system in this somewhat healthier way. GradSWE, thank you for giving me an opportunity to be a part of an organization that is really striving to make worthwhile change. Kazi, you are my best friend and the only other person who is totally willing to drop what they are doing to drink wine. Graduate school really has not been the same after you left. I miss getting to hang out with you and the rest of our gang, including but not limited to

Hannah, Megan, Anthony and Meghan, Nick and Jentry, Sheel, Riley and Jess, Emma, Shay, Adam and Cara, Jack and Allie, Ed and Linda, and Yasmin. Megan, we have not been paid to put up with one another for years now, so I do not know why you continue to put up with how annoying I am but I am very appreciative of it. Hannah, thank you for being witness and all the fun in everything you do, laughing with me at scary movies, picking on Michelle, and completing our very average trivia team. Ian, thanks for the times, even if Ken made me, and take care of Justin for me.

I could not write an acknowledgments section without dedicating a paragraph to my partner, Michelle. I love you so much and I am so excited to continue our lives together in Arizona and wherever the rest of our lives bring us. I have never met another person who understood me as well as you do, and with whom I had an instant connection with and mutual understanding in. One day we will have to convince Northwestern to bring back their TGS holiday party, they do not realize how important it is. I could not have done the last 2+ years without you and all of your support. I also want to thank your parents, Mike and Cindy; you made me feel like I was part of the family from day one, and I am honored to be an (honorary?) member of it.

Last but certainly not least, I would like to thank my family for their constant love and support. I discovered that coming out to Illinois for graduate school was really my first time leaving home, which I found to be incredibly difficult. My lil sis, Amanda, I miss you so much and really wish our lives gave us an opportunity to see each other more than once every two years. I have every intention to visit now that I will have more money, with a cheaper and shorter flight to boot! My parents, I obviously would not even exist without you but the support, financially and emotionally, was more than I could

ever hope to deserve. I will still have to keep working towards earning that (but I will do so while also calling and visiting more)!

## Table of Contents

ABSTRACT	2
Acknowledgements	5
List of Tables	13
List of Figures	14
Chapter 1. Introduction	26
1.1. Heterogeneous Catalysis	26
1.2. Epitaxially Supported Catalysts	28
1.3. Why the Lanthanide Scandates?	28
1.4. Organization	29
Chapter 2. Background and Methods	31
2.1. Powder X-Ray Diffraction	31
2.2. Electron Microscopy	32
2.3. Temperature-Programmed Experiments	34
2.4. Physisorption	35
2.5. Chemisorption	35
2.6. Infrared Spectroscopy	36
2.7. Wulff and Winterbottom Constructions	39

	10
2.8. Atomic Layer Deposition	41
Chapter 3. Thermodynamics and Stability of Lanthanide Hydroxides	43
3.1. Hydrothermal Synthesis	44
3.1.1. Autogenous Pressure	45
3.1.2. Liner and Autoclave Materials	47
3.2. Modeling Lanthanide (Oxide) Hydroxide Phase Space	50
3.3. Experimental Confirmation	54
3.4. Conclusion	63
Chapter 4. Synthesis of Gadolinium Scandate from a Hydroxide Hydrogel	64
4.1. Introduction	64
4.2. Experimental Section	66
4.2.1. Synthesis	66
4.2.2. Characterization	67
4.3. Results	67
4.4. Discussion	68
4.5. Conclusion	81
Chapter 5. Controlled Two-Step Formation of Faceted Perovskite Rare-Earth Scandate Nanoparticles	82
5.1. Introduction	82
5.2. Experimental Section	85
5.3. Results	86
5.4. Discussion	93

	11
5.5. Conclusion	97
Chapter 6. Lanthanide Scandate Formation Energies	99
6.1. Introduction	100
6.2. Density Functional Theory	101
6.3. Results	102
6.4. Conclusion	111
Chapter 7. Syntheses of Lanthanide Gallates	113
7.1. Introduction	113
7.2. Pechini Method	115
7.3. Hydro-Sauna Method	120
7.4. Hydrothermal Synthesis	124
7.5. Conclusion	126
Chapter 8. Effect of Support Interface on the Stability of Au Catalysts	128
8.1. Introduction	128
8.2. Methods	129
8.3. Size and Orientation of Supported Au Nanoparticles	130
8.4. CO Oxidation and Sintering	136
8.5. Conclusion	139
Chapter 9. Strain Engineering for CO Chemisorption on Platinum Nanoparticles	140
9.1. Introduction	140
9.2. Methods	141
9.3. Results	147

	12
9.4. Discussion	151
9.5. Conclusion	154
Chapter 10. CO <sub>2</sub> -Driven Reverse Water-Gas Shift and CO Oxidation over LnScO <sub>3</sub> -Supported Pt Catalysts	156
10.1. Introduction	157
10.2. Methods	158
10.3. Results	159
10.4. Discussion	165
10.4.1. LnScO <sub>3</sub> Basicity	166
10.4.2. Effect of CO <sub>2</sub> Affinity on CO Oxidation and the Reverse Water-Gas Shift	169
10.5. Conclusion	173
Chapter 11. Conclusions and Future Work	174
11.1. Conclusion	174
11.2. Future Work	175
11.2.1. Further Understandings of Hydro-Sauna Syntheses	175
11.2.2. Hydro-Sauna Synthesis of Redox-Active Rare-Earth Perovskites	176
11.2.3. Exsolution of Supported Noble Metal Nanoparticles	177
11.2.4. Interface-Mediated Bimetallic Catalysts	178
References	182

## List of Tables

- 4.1 Rietveld refined cell parameters for  $\text{GdScO}_3$  produced in hydro-sauna conditions at 300 °C compared to that of  $\text{GdScO}_3$  produced via high-temperature solid-state reactions<sup>53</sup> and the Crochralski technique.<sup>66</sup> Note that the single crystal data was originally presented for the *Pnma* space group so the data was transformed to the equivalent *Pbnm* space group here for comparison.

## List of Figures

- 1.1 The pseudo-cubic lattice parameters of  $\text{LnScO}_3$  compared to that of Ag, Au, Pt, and Pd. 29
- 2.1 Schematic outlining the many electron-specimen interactions that can occur in electron microscopy, taken from Williams & Carter.<sup>18</sup> 33
- 2.2 Relationship between the vibrational frequency of CO bound on platinum atoms as a function of the Pt coordination number.<sup>23</sup> 38
- 2.3 Illustration of how methanol binds to basic and Lewis acid sites.<sup>28</sup> 38
- 2.4 (a) An illustration of the Wulff construction of an fcc material where  $\{100\}$  (green) and  $\{111\}$  (yellow) facets dominate.<sup>31</sup> (b) An illustration of how the Winterbottom construction of a Pt nanoparticle changes with a change in the interfacial energy  $\gamma_{\text{Int}}$ .<sup>31</sup>  $\gamma_{\text{Sub}}$  and  $\gamma_{\text{Pt}}$  are the surface energies of the substrate and Pt respectively. 40
- 2.5 The evolution of  $\text{SrTiO}_3$  morphology with increasing  $\text{p}K_{\text{a}}$  of alcohol surfactants.<sup>32</sup> 41
- 3.1 The periodic table illustrating the acid-base properties of representative oxides of specific elements.<sup>37</sup> 45

- 3.2 (a) A graph showing the pressure in an autoclave as a function of temperature and percentage of the sealed vessel filled with water. Adapted from Rabenau.<sup>38</sup>  
(b) A schematic depicting the phase evolution of water in an autoclave as a function of temperature and filling percentage. 46
- 3.3 Calculated vapor pressure of NaOH solutions (a) with different concentration as a function of temperature and (b) with different temperatures as a function of the weight percentage of NaOH. 47
- 3.4 (a) A PXRD pattern and (b) a corresponding EDX spectrum of hydrothermally-prepared  $\text{GdFeO}_3$  . 48
- 3.5 Isocorrosion curves of (a) T316 stainless steel and (b) Nickel 201 in an NaOH solution.<sup>40</sup> 50
- 3.6 Graphs depicting the temperature dependence on the  $\text{Ln}(\text{OH})_3$ - $\text{LnOOH}$  phase stability as a function of lanthanide (a) at a constant pressure of 25000 psi<sup>42</sup> and (b) at a pressure equal to the vapor pressure of water.  $\text{Gd}(\text{OH})_3$ - $\text{GdOOH}$  phase diagram (c) experimentally determined using external pressures<sup>42</sup> and (d) calculated by extrapolating towards lower temperatures and pressures. 53
- 3.7 (a) The  $\text{Er}(\text{OH})_3$ - $\text{ErOOH}$  phase transition as a function of temperature and NaOH concentration.<sup>44</sup> (b) PXRD patterns of  $\text{Er}_2\text{O}_3$  treated in water (red curve) and 10 M NaOH (black curve). The addition of NaOH lowers the pressure of the system such that  $\text{ErOOH}$  is now stable over  $\text{Er}(\text{OH})_3$ . The peak locations for  $\text{Er}(\text{OH})_3$  (ICSD-200097) and  $\text{ErOOH}$  (ICSD-34473) are represented in pink and blue, respectively 54

- 3.8 (a,c,e) The  $\text{Gd}(\text{OH})_3$ - $\text{GdOOH}$  phase diagram with the noted reaction conditions for products that led to the (b,d,f) corresponding PXRD patterns. The peak locations of  $\text{Gd}(\text{OH})_3$  (ICSD-200093) and  $\text{GdFeO}_3$  (ICSD-61346) are represented by the red and blue lines, respectively. 56
- 3.9 PXRD patterns of  $\text{GdFeO}_3$  syntheses with different KOH and KCl concentrations. Increasing solution concentration decreased the pressure in the system, promoted  $\text{GdOOH}$  formation, and subsequent reaction in  $\text{GdFeO}_3$ . 57
- 3.10 PXRD patterns of  $\text{GdScO}_3$  syntheses with different KOH concentrations. Higher KOH concentrations led to increased solubility of scandium species in solution, but none reacted to form  $\text{GdScO}_3$ . 59
- 3.11 (a,c) SE images of the dried precipitate, with (b,d) the corresponding EDX maps for Gd (blue) and Sc (yellow) overlaid onto the SE image. 61
- 3.12 (a,b) PXRD patterns and (c,d) corresponding SE images of  $\text{GdScO}_3$  prepared via hydrothermal synthesis at 350 °C (a,c) without leaking and (b,d) with a leak. 62
- 4.1 Schematic of a gel before and after heating in both a dry and wet environment. The gel is an amorphous solid network with an encapsulated liquid phase. When heated in a dry environment, the encapsulated liquid phase leaves, and capillary forces cause the solid matrix of the gel to collapse. When heated in a wet environment, the water vapor weakens the capillary forces by decreasing the water-steam surface energy,<sup>59</sup> which lessens the collapse of the matrix. 69

- 4.2 Simultaneous TGA (black) and DTA (blue) curves of the decomposition and dehydration of the  $\text{GdSc}(\text{OH})_6 \cdot x\text{H}_2\text{O}$  hydrogel. 70
- 4.3 PXRD patterns of the products obtained after heating the gel in an autoclave at (from top to bottom) 450 °C, 400 °C, 350 °C, 300 °C, and 250 °C. The calculated peak locations and relative peak intensity for  $\text{GdScO}_3$  (pink, PDF 01-074-4353),  $\text{Gd}(\text{OH})_3$  (red, PDF 01-083-2037), and  $\alpha\text{-ScOOH}$  (blue, PDF 01-073-1790) are plotted at the bottom.  $\text{GdScO}_3$  was formed at 300 °C, 350 °C, 400 °C, and 450 °C;  $\text{Gd}(\text{OH})_3$  and  $\alpha\text{-ScOOH}$  were formed at 250 °C, 400 °C, and 450 °C. 73
- 4.4 PXRD pattern of the product obtained after heating the gel in an autoclave at 350 °C with (top) 10 mL of distilled water added to the autoclave or (bottom) no additional water. The calculated peak locations and relative peak intensity for  $\text{GdScO}_3$  (pink, PDF 01-074-4353),  $\text{Gd}(\text{OH})_3$  (red, PDF 01-083-2037),  $\alpha\text{-ScOOH}$  (blue, PDF 01-073-1790), and  $\gamma\text{-ScOOH}$  (green, PDF 01-072-0360) are plotted at the bottom. The increased amount of gel increased the amount of water and formed more  $\text{Gd}(\text{OH})_3$  and  $\text{ScOOH}$  phases as a result, and the addition of water furthered this such that no  $\text{GdScO}_3$  was formed. 74
- 4.5 Rietveld refinement plot of the PXRD data for  $\text{GdScO}_3$  grown in hydro-sauna conditions at 300 °C. Black dots indicate observed data, the red line indicates the calculated pattern, the blue line is the difference between the observed and calculated intensities, and the dark green bars indicate the allowed Bragg reflections for  $\text{GdScO}_3$ . 76

- 4.6 Simultaneous TGA (black) and DTA (blue) curves of  $\text{GdScO}_3$  grown at 300 °C under hydro-sauna conditions. The constant change in heat and small mass loss suggest the release of water adsorbed on the surface and that hydroxide groups in the material are minimal. 78
- 4.7 Raman spectrum of  $\text{GdScO}_3$  grown at 300 °C under hydro-sauna conditions. The 11 peaks are produced due to  $A_g$  modes at 248, 321, 418, 452, and 501  $\text{cm}^{-1}$ ,  $B_{1g}$  modes at 223, 373, and 490  $\text{cm}^{-1}$ ,  $B_{2g}$  modes at 298, 351, 463, and 532  $\text{cm}^{-1}$ , and  $B_{3g}$  modes at 300, 450, and 481  $\text{cm}^{-1}$ . 79
- 4.8 Secondary electron images for the products obtained after heating the gel in an autoclave at (a) 300 °C, (b) 350 °C, (c) 400 °C, and (d) 450 °C. 80
- 5.1 PXRD patterns of the products obtained from the hydro-sauna synthesis attempts of  $\text{GdScO}_3$  at temperatures between 200 °C and 450 °C for 2 days. The calculated pattern for  $\text{GdScO}_3$  is plotted on the bottom.  $\text{Gd}(\text{OH})_3$  (blue \*) was the only crystalline product formed at 200 °C, implying that  $\Delta G_{\text{rxn}}$ , as defined in the text, is positive. Between 250 °C and 300 °C, both  $\text{GdScO}_3$  and  $\text{GdOOH}$  (purple †) are formed, suggesting  $\Delta G_{\text{rxn}}$  is negative but small. Above 300 °C,  $\text{GdScO}_3$  is the primary phase, with only a small amount of  $\text{Gd}_2\text{O}_3$  (red ‡) as a secondary phase, so  $\Delta G_{\text{rxn}}$  is negative and large. 88
- 5.2 SE images of  $\text{GdScO}_3$  synthesized at 350 °C, 400 °C, and 450 °C.  $\text{GdScO}_3$  grown at lower temperatures had a less negative  $\Delta G_{\text{rxn}}$  and consequentially had more faceting and were larger than particles grown at higher temperatures.

Note that SE images do not show the surfaces of  $\text{GdScO}_3$  as clearly as with other oxides, as discussed in the text.

5.3 PXRD patterns of the products obtained from the hydro-sauna syntheses of  $\text{LnScO}_3$  ( $\text{Ln} = \text{La}, \text{Nd}, \text{Sm}, \text{Gd}$ ) using the two-temperature treatment at  $450\text{ }^\circ\text{C}$  for 2 days and then  $300\text{ }^\circ\text{C}$  for 1 day. The calculated patterns for the corresponding  $\text{LnScO}_3$  are plotted below. The perovskite phase was the primary product, with trace  $\text{Ln}(\text{OH})_3$  (blue \*) or  $\text{Ln}_2\text{O}_3$  (red ‡) as secondary products.

5.4 SE images of  $\text{LnScO}_3$  ( $\text{Ln} = \text{La}, \text{Nd}, \text{Sm}, \text{Gd}$ ) synthesized using the two-temperature treatment at  $450\text{ }^\circ\text{C}$  for 2 days and then  $300\text{ }^\circ\text{C}$  for 1 day. Smaller particles were produced because the high temperature step had a more negative  $\Delta G_{\text{rxn}}$  which led to a higher nucleation rate. The particles are better faceted because the low temperature step had a less negative  $\Delta G_{\text{rxn}}$  so terrace growth dominated. Note that SE images do not show the surfaces of  $\text{LnScO}_3$  as clearly as with other oxides, as discussed in the text.

5.5 (a) HREM image of a faceted  $\text{NdScO}_3$  particle synthesized using the two-temperature treatment at  $450\text{ }^\circ\text{C}$  for 2 days and then  $300\text{ }^\circ\text{C}$  for 1 day. (b) HREM image of the lower-right corner of the nanoparticle. (c) Corresponding FFT of the entire particle indexed to show that it is terminated with the pseudo-cubic  $\{100\}$  and  $\{110\}$  surfaces.

- 6.1 Calculated enthalpy of formation of REScO<sub>3</sub> relative to the appropriate binary oxides as a function of the inverse of the six-coordinate Shannon ionic radius for RE<sup>3+</sup>. 104
- 6.2 Crystal structure of CeScO<sub>3</sub>, with CeO<sub>6</sub> trigonal prisms shown. 105
- 6.3 (a,c) The DOS in eV of the occupied eigenstate and (b,d) the corresponding eigenstate orbital shape according to the 3D electron density map. (a,b) The lowest in energy structure corresponded to the state with an out-of-plane orbital shape, whereas (c,d) the highest energy occurred because its lobes pointed closer to an oxygen anion. 107
- 6.4 (a,c) The DOS in eV of the occupied eigenstate and (b,d) the corresponding eigenstate orbital shape according to the 3D electron density map. They are both intermediate in energy. 108
- 6.5 3D electron density maps showing the remaining unoccupied orbital shape. These structures had the highest energy because of the low energy of the in-plane (left) and out-of-plane (right) orbitals. 109
- 6.6 3D electron density maps showing the remaining unoccupied orbital shape for the other five eigenstates. All orbitals look similar and differ only by rotation. 109
- 6.7 Calculated enthalpy of formation of REScO<sub>3</sub> relative to the appropriate binary oxides as a function of lanthanide. 110
- 7.1 The pseudo-cubic lattice parameters of the different LnGaO<sub>3</sub> compared to several noble metals. 115
- 7.2 Schematic of the Pechini method in making a mixed cation gel.<sup>127</sup> 116

- 7.3 The PXRD patterns of the product from Pechini syntheses for  $\text{LnGaO}_3$ . Black bars are  $\text{LnGaO}_3$ , whereas red and blue bars are for  $\text{Ln}_3\text{GaO}_6$  and  $\text{Ln}_3\text{Ga}_5\text{O}_{12}$ , respectively. 118
- 7.4 SE image of (a)  $\text{LaGaO}_3$  and (b)  $\text{NdGaO}_3$  particles. 119
- 7.5 (a) PXRD pattern and (b) EDX of the product from hydro-sauna synthesis on a  $\text{LnGa}(\text{OH})_6 \cdot x\text{H}_2\text{O}$  gel precipitated with ammonium hydroxide. 121
- 7.6 The PXRD patterns of the product from hydro-sauna synthesis on  $\text{LnGa}(\text{OH})_6 \cdot x\text{H}_2\text{O}$  ( $\text{Ln} = \text{La}$  or  $\text{Gd}$ ) gels that underwent a solvent exchange to 10 M NaOH or to water. 124
- 7.7 A PXRD pattern of the product from a hydrothermal synthesis on equimolar amount of  $\text{Yb}_2\text{O}_3$  and  $\text{Ga}_2\text{O}_3$  in 2.5 M NaOH at 225 °C. Identical conditions using  $\text{Mn}_2\text{O}_3$  instead of  $\text{Ga}_2\text{O}_3$  produced  $\text{YbMnO}_3$ . However, in this case  $\text{YbOOH}$  was produced rather than  $\text{YbGaO}_3$ . 125
- 7.8 A PXRD pattern of the product from a hydrothermal treatment on a dried  $\text{GdGa}(\text{OH})_6$  gel.  $\text{Gd}_3\text{Ga}_5\text{O}_{12}$  was thermodynamically preferred (red), but  $\text{GdCrO}_4$  (blue) was also produced because of corrosion of the hydrothermal reactor. 126
- 8.1 The nanoparticle volume of Au on  $\text{NdScO}_3$  as a function of weight loading (a) for the particles as a whole and (b) for the different populations types. The relative populations of {110}, {111}, and multiply-twinned particles (c) as a function of weight loading on  $\text{NdScO}_3$  and (d) as a function of support at a fixed weight loading of 0.4% Au. 131

8.2	Examples of gold as truncated decahedra, icosahedra, and other MTP shapes on $\text{LnScO}_3$ .	132
8.3	Representative image of $\text{LnScO}_3$ -supported Au with the gold oriented with the $\{111\}$ facet on the surface.	133
8.4	Representative image of $\text{LnScO}_3$ -supported Au with the gold oriented with the $\{110\}$ facet on the surface.	133
8.5	The lattice parameters of the different $\text{LnScO}_3$ and the lattice mismatch with the lattice parameter of bulk gold.	135
8.6	The Arrhenius relationship between the CO oxidation rate and the temperature for the various $\text{Au/LnScO}_3$ and $\text{Au/TiO}_2$ .	137
8.7	The change in activity (normalized to the initial activity) as a function of time.	138
9.1	DRIFTS spectra of CO adsorbed on Pt after reduction in $\text{H}_2$ .	143
9.2	Simultaneous TGA-DTA-GC-MS on a bare $\text{LaScO}_3$ support.	145
9.3	DRIFTS spectra collected at 300 °C during typical catalyst pretreatment.	146
9.4	Representative HRTEM images of Pt dispersed on (left) $\text{LaScO}_3$ , (center) $\text{NdScO}_3$ , and (right) $\text{SmScO}_3$ .	148
9.5	DRIFTS spectra of CO chemisorbed on $\text{Pt/LnScO}_3$ .	149
9.6	Temperature-programmed desorption of CO that had been chemisorbed on $\text{Pt/LnScO}_3$ . Black shows the TCD signal, which is representative of all gasses	

- (other than hydrogen or helium), red shows the temperature, blue shows the MS signal from the water, and magenta shows the MS signal from the CO. 150
- 9.7 The pseudo-cubic lattice parameters of the various LnScO<sub>3</sub>, as found in the Inorganic Crystal Structure Database (ICSD),<sup>144</sup> relative to the lattice parameter of bulk platinum. 152
- 9.8 DRIFTS spectra with increasing temperature of CO bound on Pt/LaScO<sub>3</sub>. 154
- 10.1 DRIFTS spectra collected at 65 °C of methanol chemisorbed on LaScO<sub>3</sub> (black), Sc<sub>2</sub>O<sub>3</sub> (red), and La<sub>2</sub>O<sub>3</sub> (blue). 160
- 10.2 (a) TPD showing water and carbon dioxide loss on the various LnScO<sub>3</sub> and (b) the temperature of maximum CO<sub>2</sub> desorption as a function of support. The water is known to desorb in the range of 300-500 °C (see Chapter 3) so the highest temperature desorption peak was attributed to CO<sub>2</sub>, consistent with the GC-MS data in Figure 10.3. 161
- 10.3 Simultaneous TGA-DTA-GC-MS on a bare LaScO<sub>3</sub> support. 162
- 10.4 Representative HRTEM images of Pt dispersed on (left) LaScO<sub>3</sub>, (center) NdScO<sub>3</sub>, and (right) SmScO<sub>3</sub>. 163
- 10.5 CO oxidation reaction rates as a function of temperature for Pt/LnScO<sub>3</sub>. 164
- 10.6 The percentage of CO saturation on each sample of Pt/LnScO<sub>3</sub> as a function of temperature. 165
- 10.7 (a) A HRTEM image of a (110) GdScO<sub>3</sub> surface, with the crystal structure and slice imaging profile overlaid.<sup>149</sup> (b) Crystal structure showing the ScO<sub>6</sub> octahedra of the bulk with the double scandium oxide surface termination

- in blue and red.<sup>149</sup> (c) Angle-resolved X-ray photoelectron spectroscopy of a DyScO<sub>3</sub> single crystal, which shows an increase in the relative intensity of Sc relative to Dy with decreasing signal from the bulk relative to the surface.<sup>149</sup> 167
- 10.8 The temperature of maximum CO<sub>2</sub> desorption against the bond valence sum (BVS) of the scandium in the bulk LnScO<sub>3</sub> perovskite. 169
- 10.9 Example spectrum of Pt/LaScO<sub>3</sub> in CO<sub>2</sub> at 100 °C, showing the presence of peaks arising from adsorption of carbon dioxide in some form. 170
- 10.10 Example spectrum of Pt/LaScO<sub>3</sub> in H<sub>2</sub> at 100 °C, showing the consumption of CO<sub>2</sub>-containing groups in favor of CO bound to the Pt metal. 172
- 10.11 (a) The CO oxidation rate and (b) percentage of CO saturation on each sample of Pt/LnScO<sub>3</sub> as a function of the temperature of maximum CO<sub>2</sub> desorption. 173
- 11.1 (a) Optical pictures (left) and SE images (right) of coarse (top) and fine (bottom) NdScO<sub>3</sub> powders. (b) PXRD of the coarse and the fine powders. The PXRD pattern for coarse powder contains a greater percentage of undesired secondary phases than that of the fine powder. 176
- 11.2 The gold-copper phase diagram showing phase segregation at room temperature of a mixture consisting of 85% gold and 15% copper.<sup>158</sup> 180
- 11.3 The lattice parameters of the various perovskite supports compared to that of gold and gold-copper intermetallic phases. Insets show how phase segregation of the alloy and intermetallic should manifest themselves on some model supports. The intermetallic phase (blue) is well lattice-matched to GdScO<sub>3</sub>

and will segregate to the support-metal interface and the gold-rich solid solution will remain on the particle surface. Similarly, the gold-rich solid solution (gold) is well lattice-matched to  $\text{LaScO}_3$  and will segregate to the support-metal interface so the intermetallic phase will remain on the particle surface.

## CHAPTER 1

**Introduction****1.1. Heterogeneous Catalysis**

Catalysis has been a widely studied topic in chemistry since its concept was first established by Elizabeth Fulhame in her 1794 book, *An Essay on Combustion with a View to a New Art of Dying and Painting, wherein the Phlogistic and Antiphlogistic Hypotheses are Proved Erroneous*,<sup>1</sup> and has been a central component in over 15 Nobel Prizes.<sup>2</sup> Wilhelm Ostwald, who won the 1909 Nobel Prize in chemistry for his work in the field, defined a catalyst to be a material that alters the selectivity or rate of a chemical reaction without being consumed into the final product.<sup>3</sup> These materials are especially important in industrial chemistry, where over 80% of chemical products are produced with the assistance of heterogeneous catalysts.<sup>4</sup> Further, it is estimated that the use of catalysts contributes to over 35% of the world's GDP,<sup>5</sup> with \$15 billion annually being spent on catalysts, primarily for applications in petroleum refinement, chemical and polymer synthesis, and emission control.<sup>6,7</sup>

A catalyst works by providing a different reaction pathway through various transition states that have a lower activation barrier. In a typical heterogeneous catalyst, the transition states occur through the adsorption and the reaction of reactants onto and at specific “active sites” on the catalyst surface. Since these events occur on the surface, it is the interaction between reactants, products, and the catalyst surface structure that

dictates catalytic properties. To improve overall catalyst performance, nanoparticles are often used as catalysts because they have a large surface area, which correlates to a high number of active sites relative to the amount of material used. Since this large surface area comes with a large surface energy, nanoparticle catalysts are prone to sintering. To mitigate this, most nanoparticle catalysts are instead dispersed onto the surface of a catalytic support; this keeps the catalyst particles better separated from one another and minimizes sintering and subsequent loss of surface area and active sites. Catalyst supports need to be thermally stable at the reaction conditions and should also have a high surface area so that a high loading of catalyst may be deposited. Often, the role that the catalytic support plays is much greater than that of just a mechanical framework for keeping nanoparticles separated. The acid-base properties of the support, for example, may affect how the catalyst deposits onto the support<sup>8</sup> or allow for binding of different reactants near the catalyst.

Research in catalysis generally takes one of two approaches: studying single crystal catalyst surfaces in ultrahigh vacuum which have better understood but fewer active sites, or studying real catalysts with a different assortment of active sites under more complex reaction conditions. These two different approaches created what are called a “pressure gap” and a “materials gap”. The “pressure gap” refers to the difference in catalytic behavior between ultrahigh vacuum conditions and more typical atmospheric or high-pressure conditions. The “materials gap” notes that the surface structure of nanoparticles may differ from that of a single crystal, that adsorption and catalytic behavior may differ, and that other surfaces or structural features like edges or corners have differing active sites with potentially differing degrees of activity or selectivity.

## 1.2. Epitaxially Supported Catalysts

In an attempt to bridge the “materials gap”, this thesis investigates catalysts deposited onto epitaxial supports with controlled surface structures. Using supports that have a controlled surface structure of their own allows for better control of the orientation and exposed facets of the catalyst. The epitaxy allows for further tuning on the catalyst structure, as changes in the support lattice parameter affect the catalyst-support interfacial energy which changes the resulting Wigner-Seitz construction.<sup>9</sup> This has been observed through study of Pt nanoparticles deposited on different (Ba,Sr)TiO<sub>3</sub> (100) surfaces.<sup>10</sup> The change in catalyst shape exposed different ratios of active sites that had different selectivities in acrolein hydrogenation. In addition, the epitaxy stabilizes the nanoparticle catalyst, which has been known to improve catalyst stability during reactions.<sup>11</sup>

Since the use of epitaxial supports with controlled surface structure allows for better control of the active sites of the catalyst, they can become a good model system in elucidating the behavior of real catalysts. Systematically varying specific support properties, such as its basicity or lattice parameter, would then allow for a better understanding of how support properties affects catalytic properties.

## 1.3. Why the Lanthanide Scandates?

Lanthanide scandate were selected as the support of interest for several reasons. Scandium and many lanthanides are irreducible so the support will be stable and exhibit minimal activity in reducing or oxidizing reaction conditions. The lattice parameter of the support can be tuned by changing the lanthanide used, with smaller lattice parameters for the heavier lanthanides. In addition, the lattice parameter of many lanthanide scandates

are similar to that of several different noble metals, including gold, silver, platinum, and palladium (Figure 1.1). The acid-base properties may also be tuned by using different lanthanides, as larger lanthanides exhibit greater basic behavior. The ionicity of the support also increases with the increasing basicity. Additionally, changes in the band gap of the support will affect the Schottky barrier and charge transfer at the support-catalyst interface.<sup>12</sup>

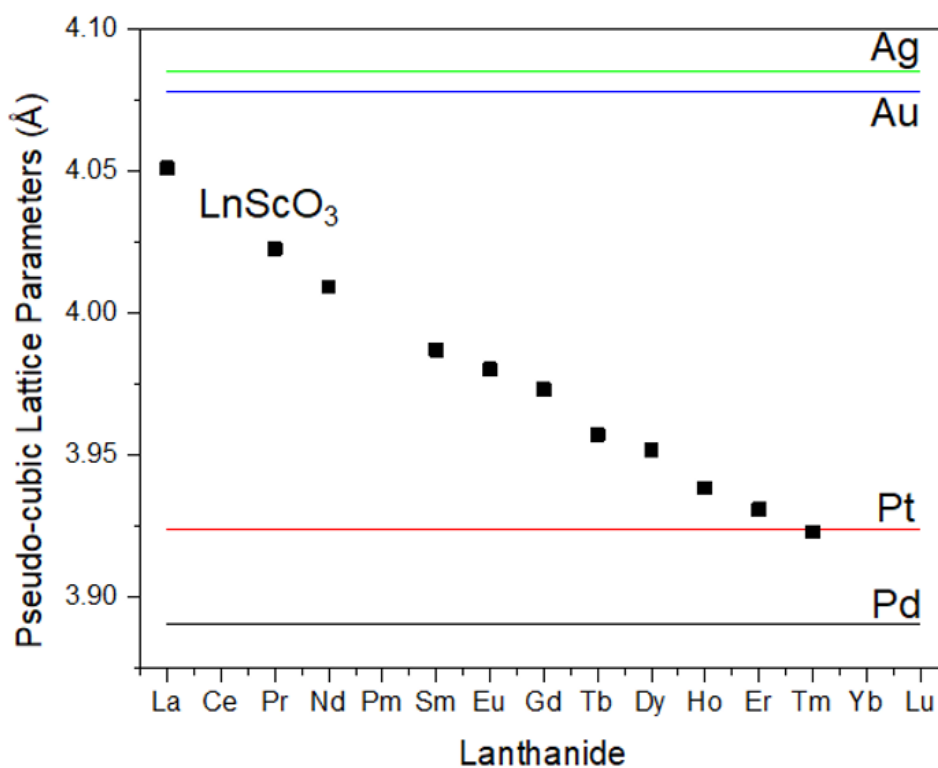


Figure 1.1. The pseudo-cubic lattice parameters of  $\text{LnScO}_3$  compared to that of Ag, Au, Pt, and Pd.

#### 1.4. Organization

This thesis is titled “Lanthanide Scandate Supported Noble Metal Nanoparticle Catalysts” and is organized mostly in a linear fashion from that title. After a background

that will cover the various characterization and synthesis techniques used throughout, there will be several chapters regarding the necessary reaction conditions and synthesis of the lanthanide scandate supports. The energetics for lanthanide scandate formation were determined through density functional theory and will be discussed in the following chapter. Then there will be a chapter investigating several approaches to producing the series of lanthanide gallates. The remaining chapters will investigate catalytic properties of various noble metals supported onto the lanthanide scandates; the first of which will look at the orientation of gold and its stability during CO oxidation, and the latter two will discuss Pt catalysts where the effect of strain on CO adsorption and the role of basic oxide sites on CO oxidation and the reverse water-gas shift, respectively. Lastly, some future work stemming from this project will be proposed.

## CHAPTER 2

**Background and Methods**

This chapter goes into the various experimental characterization techniques used throughout this thesis and into one of the methods used for the synthesis of noble metal nanoparticle catalysts. The syntheses of the lanthanide scandate supports warrant chapters of their own. In addition, some fundamental materials science concepts that are important to understand for this thesis will be discussed. Each section will discuss briefly how each technique works and what information one can obtain from the experiment, with a particular emphasis on why that information is relevant for this work or catalytic characterization in general.

**2.1. Powder X-Ray Diffraction**

Powder X-ray diffraction (PXRD) is a useful tool for determining what crystalline products are present, which will be commonly used to analyze the phase of the synthesized support particles and the relative amount of that phase. In an X-ray diffraction experiment, X-rays are used to probe the crystal structure of a sample. X-rays will scatter off of atomic planes in a periodic structure like a crystal, and these scattered X-rays will interfere. Maximum constructive interference occurs at angles determined by Bragg's Law:

$$n\lambda = 2d_{hkl} \sin(\theta)$$

where  $\lambda$  is the X-ray wavelength,  $\theta$  is the incident and detector angle,  $n$  is an integer (usually taken to be unity), and  $d_{hkl}$  is the lattice spacing between adjacent  $(hkl)$  planes. Different crystalline materials have different lattice parameters and structure factors, so PXRD produces a characteristic diffraction pattern that can act as a material “fingerprint”. Further, the width of a diffraction peak can be related to the strain in the material<sup>13</sup> and the mean crystallite size.<sup>14,15</sup> The Scherrer equation<sup>14</sup> determines the mean crystallite size  $\tau$  up to 100 nm through a relationship with the Bragg angle  $\theta$ , X-ray wavelength  $\lambda$ , the full-width half-maximum of the peak  $\beta$ , and a dimensionless factor  $K$  that accounts for the shape as follows:

$$\tau = \frac{K\lambda}{\beta \cos(\theta)}$$

One can also resolve the relative proportions of crystalline phases and their lattice parameters using Rietveld refinement,<sup>16</sup> which calculates a PXRD pattern using adjusting various structural and instrumental parameters to minimize the least squares difference between the calculated and experimental patterns.

## 2.2. Electron Microscopy

An electron microscope uses electrons and a system of magnetic lenses to create an electron beam to illuminate a sample. Owing to the small wavelength of the high-energy electrons used (typically on the order of picometers), high-resolution images of materials can be obtained, although electron optics have aberrations that ultimately lower the resolution.<sup>17</sup> Conventional transmission electron microscopy (TEM) uses a nearly parallel electron beam and allows for parallel collection of the transmitted electrons. In the case

of a scanning transmission electron microscope (STEM), the electron beam is focused, rastered across the sample, and the electrons that interact with the sample are collected serially. Incoming electrons can interact with a material in a number of different ways, so a wealth of information can be obtained about the sample with the appropriate detectors, as evidenced in Figure 2.1. For example, characteristic X-rays can be collected to perform energy dispersive X-ray spectroscopy (EDX) and yield information about the atomic constituents of the sample. Of particular relevance in this thesis are images collected using secondary electrons (SE), which are low energy electrons that are ejected from the sample by the electron beam. Owing to their low energy, they have a small escape depth, making them very surface sensitive and resulting in images that can provide information about particle morphology. STEM will be used instead of a scanning electron microscopy (SEM) because SE imaging has a higher resolution in STEM than SEM.<sup>18</sup>

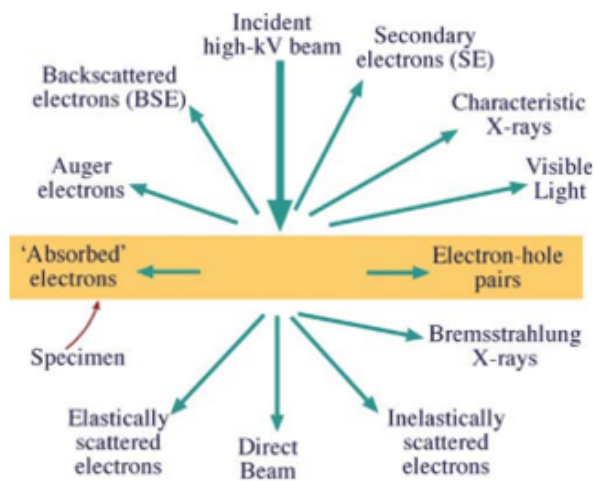


Figure 2.1. Schematic outlining the many electron-specimen interactions that can occur in electron microscopy, taken from Williams & Carter.<sup>18</sup>

### 2.3. Temperature-Programmed Experiments

A wealth of information can be obtained by measuring various responses to a change in temperature and, with the appropriate detectors set up, this information can be collected simultaneously to better determine the ongoing processes. In addition, different environments can be used to see how these materials respond under different conditions. Several different temperature-programmed experiments will be presented throughout this thesis, and will be used to determine what gaseous species desorb and get an idea of how strongly those adsorbates bind to the material. One commonly used example is that of thermogravimetric analysis, (TGA), which measures mass change as a function of temperature. Mass loss can occur through the volatilization of material. Simultaneous differential thermal analysis (DTA) measures the temperature difference between the sample and some inert reference to determine whether endothermic or exothermic reactions are occurring. There are also several ways to also analyze how much gas and what kind of gases are being released. One uses a thermal conductivity detector (TCD) to measure changes in gas composition relative to a reference gas flow through changes in the thermal conductivity. However, it is not gas-specific and can really only be used to differentiate gases from H<sub>2</sub> or He, as most other gases have very similar thermal conductivities. Gas chromatography and mass spectrometry, on the other hand, can be used to determine what gaseous species are being produced and analyze their relative concentrations. Analyzing how the desorption of certain species as a function of temperature is called temperature-programmed desorption, and can be used to probe the desorption energy of the species. The slope from plotting  $\ln(\beta/T_{max}^2)$  against  $1/T_{max}$ , where  $\beta$  is the heating rate and  $T_{max}$  is the

temperature when desorption is at a maximum, is directly proportional to the desorption energy.<sup>19</sup>

## 2.4. Physisorption

Physisorption experiments allow for characterization of some of the physical properties of a powder. For catalytic supports, the properties of interest are the surface area and the pore structure. Typically, supports with high surface areas are desired because this allows for more catalytic nanoparticles to be deposited, which consequently increases the total surface area of catalyst and the number of active sites. During a physisorption experiment, a known amount of inert gas is pulsed at a constant temperature near the condensation point of the gas. At equilibrium, some of the gas pulse adsorbs onto the sample surface, which lowers the pressure of the system. By analyzing this difference in pressure as a function of how much gas has been pulsed in, the surface area and pore structure of the support can be determined. Various models can be used. The Brunauer-Emmett-Teller (BET) model is the most common, as it accurately models the isotherm with multiple layers of physisorbed gas (unlike the Langmuir model).<sup>20</sup> Owing to the physical and unactivated nature of the adsorption process, the technique is unable to differentiate between different types of surfaces or even between surfaces of different materials.

## 2.5. Chemisorption

In order to get an idea of the surface area of specific materials, chemisorption needs to be performed. Unlike physisorption, chemisorption is typically an activated process and occurs in a single monolayer. A specific probe gas that will bind to a specific site of the

system is used as a means to probe the number of those sites. Different probe molecules can then be used to measure a variety of different sites. Carbon monoxide, for example, readily binds to d-band transition metals via  $\sigma$ -bonding while the d-metal donates back  $\pi$ -electrons to the anti-bonding orbitals of the CO to reduce the CO bond strength, but does not bind to most oxide sites. As a result, CO chemisorption specifically yields the surface area of the catalytic metal, and says nothing about the surface area of an oxide support. Certain molecules can probe the acid-base properties of oxides. Carbon dioxide, an acidic molecule, binds strongly to basic sites, whereas pyridine or ammonia, which are basic molecules, adsorb instead onto acidic sites.

Experiments are performed by pulsing of a known amount of probe gas over the material and seeing how much gas is left unadsorbed through changes in the TCD signal. Initial pulses are fully (or nearly fully) adsorbed onto the available adsorption sites and no (or little) probe gas may pass through the detector. After enough pulses, the adsorption sites are fully saturated and the entire probe gas pulse contributes to the TCD signal. Differences in the integrated intensity of the peaks prior to saturation relative to the integrated intensity after saturation measures how much gas uptake occurred. Combined with appropriate knowledge of the gas-catalyst stoichiometry and surface concentration of the catalyst, this measured difference then informs the surface area of the catalyst.

## 2.6. Infrared Spectroscopy

Infrared spectroscopy studies a molecular response to infrared light. Different molecular bonds absorb in different regions of the infrared regime owing to the characteristic vibrational frequencies of the bond, with stronger bonds or bonds between lighter elements having a greater vibrational frequency. In this thesis, we will mainly focus on

diffuse reflectance infrared Fourier transform spectroscopy (DRIFTS), which analyzes the light that reflects in all directions off an irregular material surface. DRIFTS will be used to probe the nature of an adsorbed species on the catalyst. One example will be studying how carbon monoxide adsorbs onto a platinum catalyst. Free CO has a vibrational frequency of  $2143\text{ cm}^{-1}$  but is affected by the d-electron density (dependent on the metal used), the bonding geometry, the coordination number of the site, and the CO coverage. On platinum, CO has a vibrational frequency between  $2000$  to  $2100\text{ cm}^{-1}$  when bound on atop sites (CO is bound linearly on 1 Pt atom), between  $1800$  to  $1970\text{ cm}^{-1}$  when bound on bridged sites (shared between 2 Pt atoms), and between  $1700$  to  $1770\text{ cm}^{-1}$  when on hollow sites (shared between 3 or 4 Pt atoms).<sup>21,22</sup> The vibrational frequency also decreases with decreasing generalized coordination numbers, so the vibrational frequency of CO on facets is higher than that on edges and corners, as illustrated in Figure 2.2.<sup>23,24</sup> The vibrational frequency also increases on cationic species<sup>25,26</sup> or with CO coverage.<sup>27</sup> Another example involves using methanol as a probe molecule to understand oxide acidity or basicity; the methanol dissociates into a methoxy species on basic sites but forms an intact methonal adduct on acidic sites (Figure 2.3).<sup>28</sup> This difference leads to different products being formed during methonal oxidation reactions, where carbon dioxide is formed over basic sites and dimethyl ether is produced on acidic sites.<sup>29</sup>

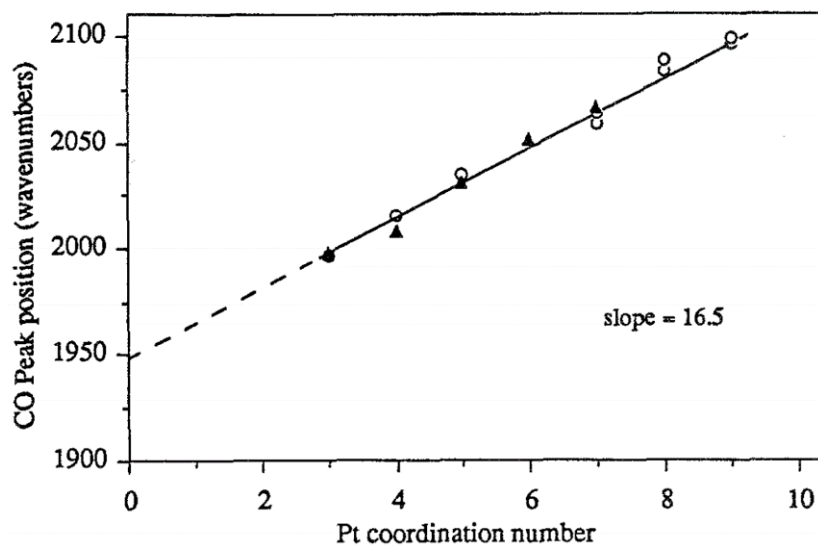


Figure 2.2. Relationship between the vibrational frequency of CO bound on platinum atoms as a function of the Pt coordination number.<sup>23</sup>

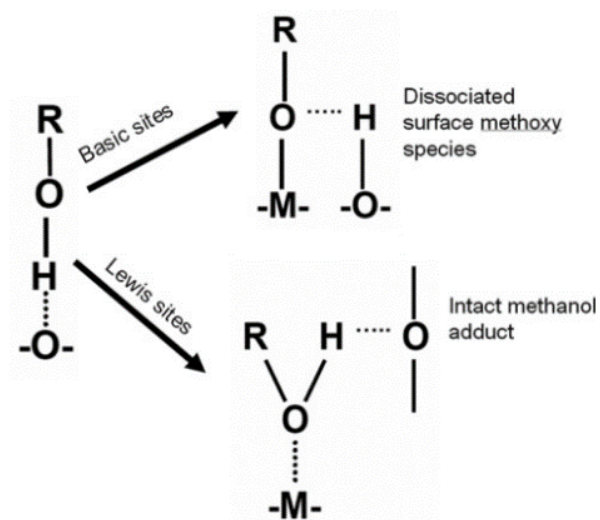


Figure 2.3. Illustration of how methanol binds to basic and Lewis acid sites.<sup>28</sup>

## 2.7. Wulff and Winterbottom Constructions

The shape of a particle is governed by its Wulff construction, which can be thermodynamic or kinetic in origin. The thermodynamic Wulff construction is the shape that minimizes the total surface free energy for a fixed volume of material.<sup>30</sup> Typically, low-index facets have a lower surface energy, and therefore, the resulting crystal is predominantly terminated with low-index facets. For example, Pt, like many face-centered cubic (fcc) metals, forms a tetradecahedron, which is a truncated octahedron composed of six  $\{100\}$  and eight  $\{111\}$  facets (Figure 2.4a). An extension of the thermodynamic Wulff is the Winterbottom construction, which defines the particle shape when an interface with another crystal plane, such as a substrate, is involved.<sup>9</sup> In the case of a crystalline particle on a crystalline substrate, this shape is simply the thermodynamic Wulff shape oriented and truncated in a way that minimizes the total energy, as outlined in Figure 2.4b. The Winterbottom construction determines the shape and orientation of supported catalysts.

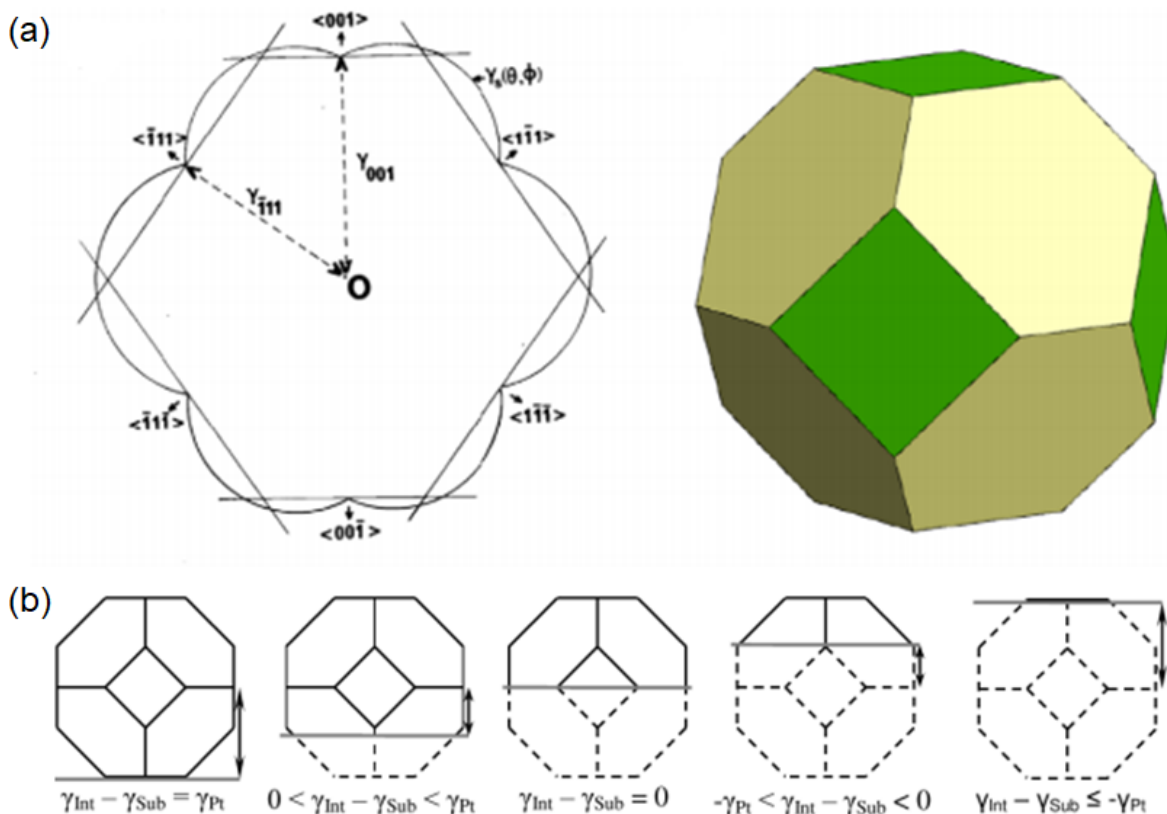


Figure 2.4. (a) An illustration of the Wulff construction of an fcc material where  $\{100\}$  (green) and  $\{111\}$  (yellow) facets dominate.<sup>31</sup> (b) An illustration of how the Winterbottom construction of a Pt nanoparticle changes with a change in the interfacial energy  $\gamma_{Int}$ .<sup>31</sup>  $\gamma_{Sub}$  and  $\gamma_{Pt}$  are the surface energies of the substrate and Pt respectively.

The kinetic Wulff construction is analogous to the thermodynamic Wulff by considering the growth velocities normal to different facets rather than their surface energies. Facets that have a high growth velocity normal to them are quickly consumed, leaving behind only facets with relatively slower growth velocities. This process can be affected by additives that form ions in solution, which alters the morphology by selectively chemisorbing onto certain surfaces, occupying nucleation sites, and hindering growth normal to the surface. Surfactants control the morphology of particles by adhering to and reducing the

surface energy of certain facets. For example,  $\text{SrTiO}_3$  growth showed that the relative ratio of  $\{100\}$ - and  $\{110\}$ -terminated surfaces could be tuned by adjusting the  $\text{p}K_a$  of alcohols in the solution, with high  $\text{p}K_a$  alcohols producing  $\{100\}$ -terminated cuboids and low  $\text{p}K_a$  alcohols producing  $\{110\}$ -terminated rhombic dodecahedra (Figure 2.5).<sup>32,33</sup>

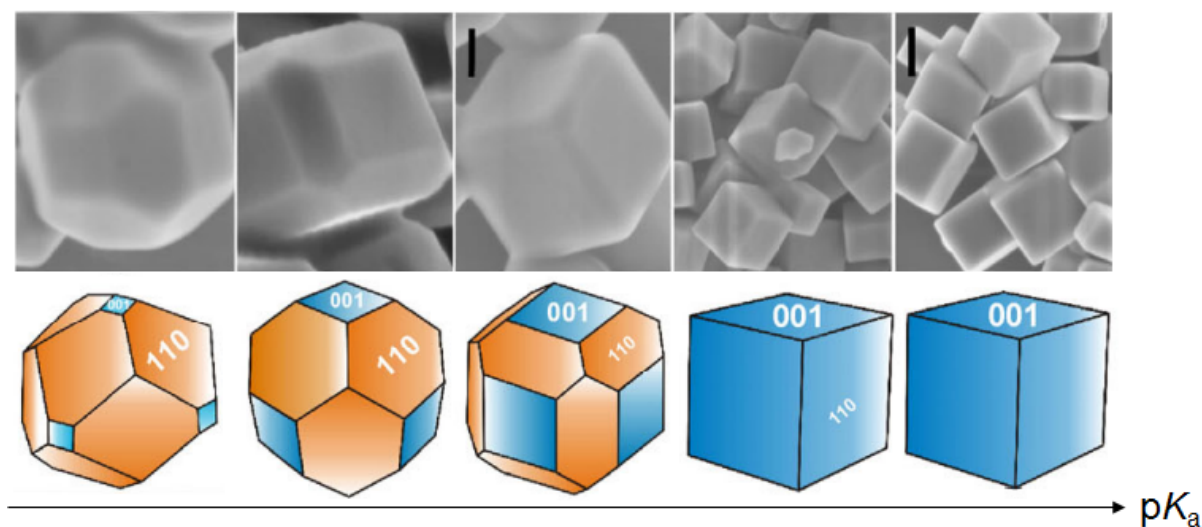


Figure 2.5. The evolution of  $\text{SrTiO}_3$  morphology with increasing  $\text{p}K_a$  of alcohol surfactants.<sup>32</sup>

## 2.8. Atomic Layer Deposition

Atomic layer deposition (ALD) is a vapor-phase synthetic technique that utilizes self-limiting surface reactions to deposit material in a controlled fashion. In this thesis, this technique will be used to deposit platinum nanoparticle catalysts onto the  $\text{LnScO}_3$  supports. Precursors are individually flowed over the support surface to prevent any gas-gas reactions in favor of only gas-surface reactions. Each precursor will react with sites produced by the other precursor but not with sites produced by itself. Therefore, each precursor can only react with the surface in a self-limiting fashion. Surfaces are exposed

to individual precursors in a cyclical fashion to grow material. While this technique is usually used to form conformal thin films, nanoparticles are formed in the low-cycle limit for noble metals. For metals, an organometallic precursor is introduced into the system to react with the support and then another precursor like hydrogen, oxygen, or ozone is added to react with or decompose the organometallic precursors to leave behind only the metal. The metal can then migrate on the surface to form nanoparticles.

## CHAPTER 3

**Thermodynamics and Stability of Lanthanide Hydroxides**

This chapter will explore the phase stability of the lanthanide (hydr)oxides under hydrothermal conditions. This work was started because it was thought that hydrothermal synthesis would be a good route to producing faceted  $\text{LnScO}_3$  and  $\text{LnGaO}_3$ ; this hypothesis was based on the results of  $\text{LaAlO}_3$  and  $\text{GdAlO}_3$  hydrothermally,<sup>34,35</sup> where high temperatures ( $> 300\text{ }^\circ\text{C}$ ) and fairly alkaline conditions were necessary. Those conditions were consistent with previous work producing  $\text{LnMnO}_3$ ,<sup>36</sup> where higher temperatures were necessary to solubilize larger lanthanides. This chapter will show that the formation of the more reactive and soluble lanthanide oxide hydroxide does not only depend on the temperature as originally presumed, but on the pressure as well. Further, we find that the pressure can be tuned with temperature and solution concentration. The combination of these two ideas may illustrate the success of other groups in producing rare-earth perovskites at temperatures lower than that of the initially predicted transition temperature between a lanthanide hydroxide to a lanthanide oxide hydroxide. This necessitated a search for a new liner material for the autoclave capable of withstanding these harsher conditions. However, the thermodynamic calculations and experimental results from this chapter demonstrate that hydrothermal synthesis was not the optimal route to producing  $\text{LnScO}_3$ , as the high chemical potential of water at hydrothermal conditions instead promotes the stability of the lanthanide hydroxides. As a result, we believe that the reports

of hydrothermally-prepared  $\text{LnAlO}_3$  were the result of a leak in their system.<sup>34,35</sup> In fact, having a leak was found to be beneficial to producing a higher phase purity of  $\text{LnScO}_3$ .

### 3.1. Hydrothermal Synthesis

Solvothermal synthesis is a technique in which reactions occur in solution (water in the case of hydrothermal synthesis) inside a sealed vessel at temperatures greater than the boiling point of the solvent and pressures greater than atmospheric pressure. These elevated temperatures and the addition of mineralizers (e.g.  $\text{NaOH}$ ,  $\text{Na}_2\text{CO}_3$ ,  $\text{NaCl}$ ) are used to form soluble complexes. Then, liquid-phase transport of the reactants allow for nucleation and subsequent growth of a crystalline product. This method produces crystals at lower temperatures and on shorter timescales than typical solid-state reactions. A distinct advantage of this method is its ability to produce crystalline particles with consistent morphology through a kinetic Wulff shape achieved by varying different processing parameters, including temperature, pH, different reagents and concentrations thereof, or the addition of surfactants.

Since nucleation of crystallites is often accomplished through liquid-phase transport, it is necessary to dissolve the precursors. In order to predict if a metal oxide or hydroxide will dissolve, it is convenient to look at its acid-base behavior. Basic oxides are soluble in acidic solutions and are typically compounds with a strong ionic character, such as the lanthanide sesquioxides or group 1 and 2 metal oxides. Acidic oxides, on the other hand, dissolve in basic media and are often covalent in character. Amphoteric oxides dissolve in both acids and bases. Transition metals oxides have different acid-base behavior based on their oxidation state, where higher oxidation states lead to more acidic behavior; as an example, chromium (II) oxide and manganese (II) oxide are basic, chromium (III) oxide

and manganese (IV) oxide are amphoteric, and chromium (VI) oxide and manganese (VII) oxide are acidic. These trends in acid-base behavior are evident in Figure 3.1.

	1	2											13	14	15	16	17	18		
1																				
2	Li <sub>2</sub> O	BeO											B <sub>2</sub> O <sub>3</sub>	CO <sub>2</sub>	N <sub>2</sub> O <sub>5</sub>					
3	Na <sub>2</sub> O	MgO											Al <sub>2</sub> O <sub>3</sub>	SiO <sub>2</sub>	P <sub>4</sub> O <sub>10</sub>	SO <sub>3</sub>	Cl <sub>2</sub> O <sub>7</sub>			
4	K <sub>2</sub> O	CaO	Sc <sub>2</sub> O <sub>3</sub>	TiO <sub>2</sub>	V <sub>2</sub> O <sub>5</sub>	CrO <sub>3</sub>	Mn <sub>2</sub> O <sub>7</sub>	Fe <sub>2</sub> O <sub>3</sub>	CoO	NiO	CuO	ZnO	Ga <sub>2</sub> O <sub>3</sub>	GeO <sub>2</sub>	As <sub>2</sub> O <sub>5</sub>	SeO <sub>3</sub>	Br <sub>2</sub> O			
					VO <sub>2</sub>	Cr <sub>2</sub> O <sub>3</sub>	MnO <sub>2</sub>	FeO					GeO	As <sub>2</sub> O <sub>3</sub>	SeO <sub>2</sub>					
						CrO	MnO						In <sub>2</sub> O <sub>3</sub>	SnO <sub>2</sub>	Sb <sub>2</sub> O <sub>5</sub>	TeO <sub>3</sub>				
5	Rb <sub>2</sub> O	SrO	Y <sub>2</sub> O <sub>3</sub>	ZrO <sub>2</sub>	Nb <sub>2</sub> O <sub>5</sub>	MoO <sub>3</sub>	Tc <sub>2</sub> O <sub>7</sub>				Ag <sub>2</sub> O	CdO	In <sub>2</sub> O	SnO	Sb <sub>2</sub> O <sub>3</sub>	TeO <sub>2</sub>	I <sub>2</sub> O <sub>5</sub>	XeO <sub>4</sub>		
6	Cs <sub>2</sub> O	BaO		HfO <sub>2</sub>	Ta <sub>2</sub> O <sub>5</sub>	WO <sub>3</sub>	Re <sub>2</sub> O <sub>7</sub>				Au <sub>2</sub> O <sub>3</sub>	HgO	Tl <sub>2</sub> O <sub>3</sub>	PbO <sub>2</sub>	Bi <sub>2</sub> O <sub>5</sub>	PoO <sub>2</sub>		XeO <sub>3</sub>		
													Tl <sub>2</sub> O	PbO	Bi <sub>2</sub> O <sub>3</sub>					
7	Fr <sub>2</sub> O	RaO																		
			La <sub>2</sub> O <sub>3</sub>	CeO <sub>2</sub>	PrO <sub>2</sub>	Nd <sub>2</sub> O <sub>3</sub>		Sm <sub>2</sub> O <sub>3</sub>	Eu <sub>2</sub> O <sub>3</sub>	Gd <sub>2</sub> O <sub>3</sub>	Tb <sub>2</sub> O <sub>3</sub>	Dy <sub>2</sub> O <sub>3</sub>	Ho <sub>2</sub> O <sub>3</sub>	Er <sub>2</sub> O <sub>3</sub>	Tm <sub>2</sub> O <sub>3</sub>	Yb <sub>2</sub> O <sub>3</sub>	Lu <sub>2</sub> O <sub>3</sub>			
				Ce <sub>2</sub> O <sub>3</sub>	Pr <sub>2</sub> O <sub>3</sub>				EuO											
			Ac <sub>2</sub> O <sub>3</sub>	ThO <sub>2</sub>		UO <sub>3</sub>														
						UO <sub>2</sub>														

Figure 3.1. The periodic table illustrating the acid-base properties of representative oxides of specific elements.<sup>37</sup>

### 3.1.1. Autogenous Pressure

If there is no external pressure applied, the system is said to reach an “autogenous pressure”, which in the absence of a gas-producing reaction is a function of the temperature, the solution, and the degree of filling in the vessel, as shown in Figure 3.2a.<sup>38</sup> As illustrated by the schematic in Figure 3.2b, at high filling percentages, the pressure is largely due to the expansion of liquid solution, but at low filling percentages and temperatures below the critical point, the pressure is primarily determined by the vapor pressure of the solution. It is fairly typical to assume that this solution is solely water in a hydrothermal reaction. However, this assumption is certainly never the case. Raoult’s law

notes that the partial pressure of a component is equal to the vapor pressure of the pure compound weighted by the mole fraction. The vapor pressure of the total solution depends on the vapor pressure of each component and the molar fractions thereof. As shown in Figure 3.3, the vapor pressure of the solution increases with increasing temperature and decreases with increasing NaOH concentration.<sup>39</sup>

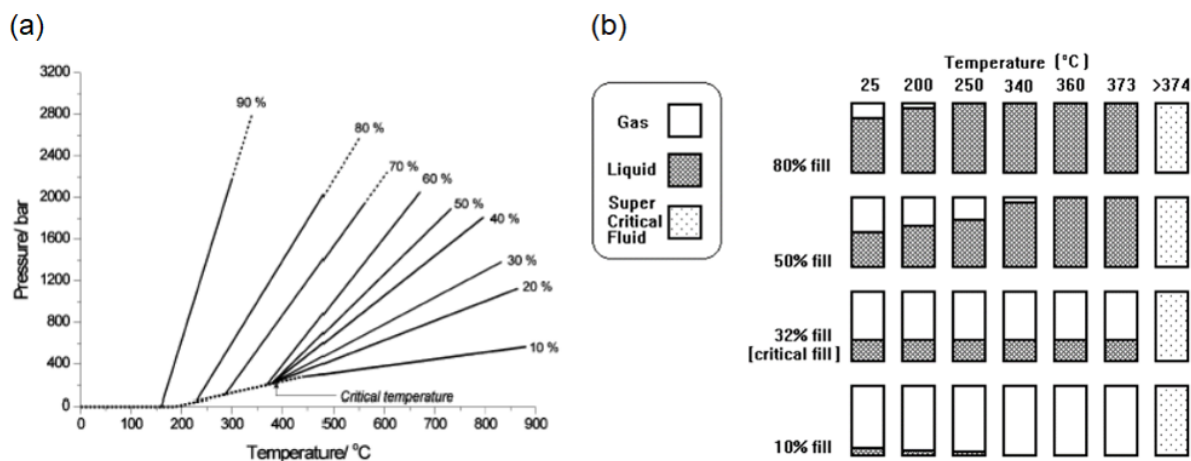


Figure 3.2. (a) A graph showing the pressure in an autoclave as a function of temperature and percentage of the sealed vessel filled with water. Adapted from Rabenau.<sup>38</sup> (b) A schematic depicting the phase evolution of water in an autoclave as a function of temperature and filling percentage.

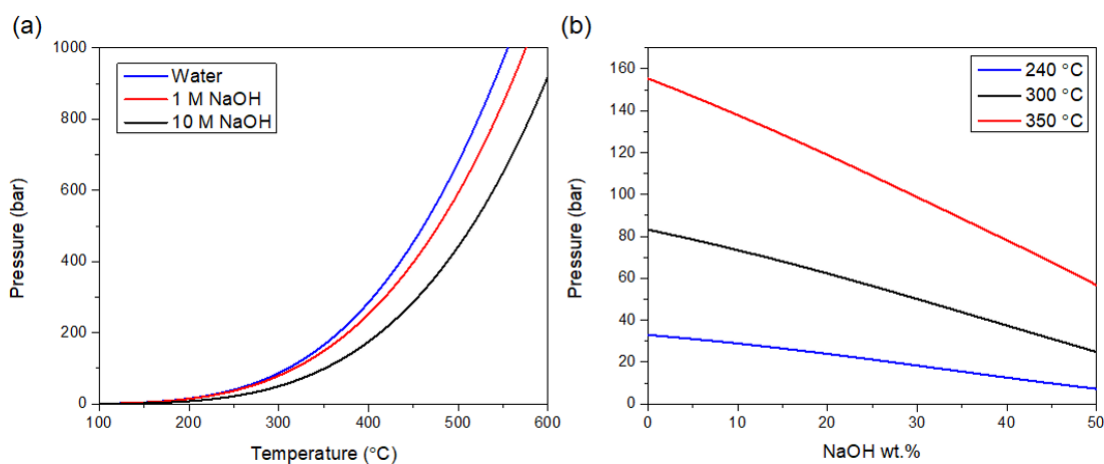


Figure 3.3. Calculated vapor pressure of NaOH solutions (a) with different concentration as a function of temperature and (b) with different temperatures as a function of the weight percentage of NaOH.

### 3.1.2. Liner and Autoclave Materials

Because of the high temperatures and pressures involved in hydrothermal synthesis, the composition of the reaction vessel and liner containing the reaction can play a critical role. For example, the vessel can be corroded by the solution (e.g. solvent, mineralizer, etc.) and act as an unwanted material source. This issue becomes increasingly more problematic in reactions that use higher temperatures or mineralizers like strong acids and bases. Supercritical water ( $T > 374\text{ °C}$ ,  $P > 220\text{ bar}$ ) is also known to be corrosive to many metals. Unfortunately, the corrosion of materials under hydrothermal conditions is not well known and is often discovered through trial and error. Therefore, much work was performed to determine an appropriate liner material to protect the T316 stainless steel reactor vessels we have.

T316 stainless steel is in general stable against caustic conditions. However, at higher temperatures in strongly alkaline conditions, this ceases to be the case. One such example

was found when attempting to reproduce a  $\text{GdAlO}_3$  synthesis from literature,<sup>35</sup> in which a 10 M NaOH solution containing  $\text{Gd}_2\text{O}_3$  and  $\text{Al}(\text{OH})_3$  powders with a molar ratio of 1 Gd : 5 Al was heated to 350 °C. Instead of  $\text{GdAlO}_3$ , the product was determined to be primarily  $\text{GdFeO}_3$ , as evidenced both by the diffraction pattern in Figure 3.4a and by the EDX spectrum in Figure 3.4b. However, since NaOH and KOH are frequently used as mineralizers and surface-affecting agents for oxides, the use of these reagents cannot be avoided, necessitating the use of a liner or an autoclave made from a different material.

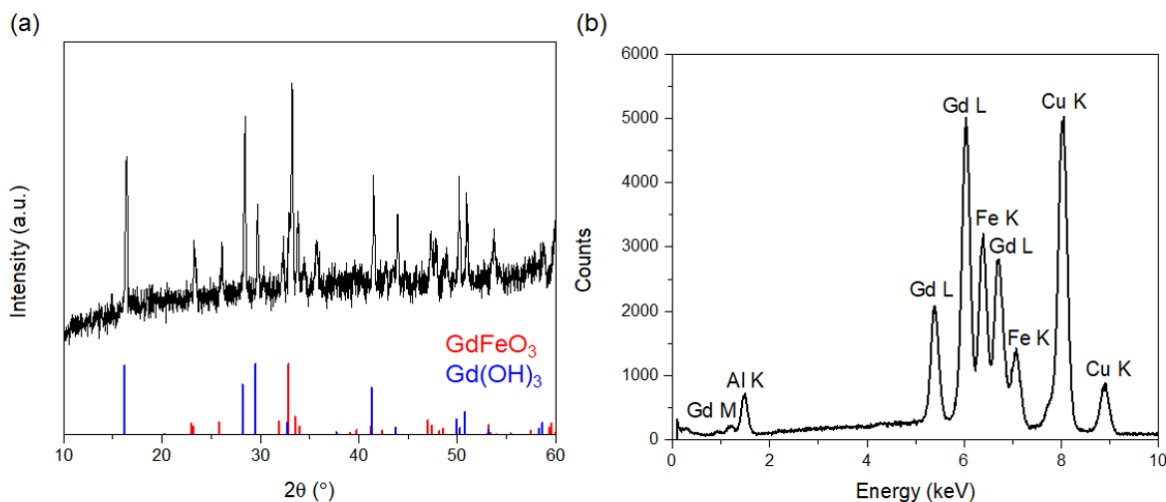


Figure 3.4. (a) A PXR D pattern and (b) a corresponding EDX spectrum of hydrothermally-prepared  $\text{GdFeO}_3$ .

Poly(tetrafluoroethylene) (PTFE) Teflon liners are a popular choice, owing to Teflon's exceptional chemical inertness. However, Teflon melts at 325 °C and undergoes significant deformation due to creep at temperatures as low as 275 °C. With these constraints, a Teflon liner was used only with reaction temperatures less than 250 °C. There is currently no known polymer that is thermally stable at temperatures greater than 250 °C while

simultaneously maintaining chemical inertness against solutions with a  $\text{pH} > 10$ . Another common liner material, borosilicate glass, is readily attacked by NaOH and KOH, especially at higher temperatures. As a result, borosilicate glass was used only for high temperature experiments in water or without solution.

For high temperature applications with hydroxide solutions, several potential metal liners were considered. Ultimately, a custom liner made of Nickel 201 was purchased. Nickel 201 is a low-carbon alloy made of over 99% nickel and is routinely used for applications above 315 °C. In caustic conditions, an oxide film forms on the nickel surface and protects the alloy from further caustic attack.<sup>40</sup> Comparing its isocorrosion curve to that of T316 stainless steel in Figure 3.5, it corrodes significantly less under most NaOH concentrations and temperatures; for example, at 150 °C in a 50 wt.% NaOH solution, T316 stainless steel corrodes at 0.8 mm per year whereas the Nickel 201 liner corrodes at only 0.025 mm per year. These isocorrosion curves also highlight the difficulty in choosing appropriate materials under hydrothermal conditions; there is little to no information on the corrosion resistance at conditions above the boiling point of the solvent, which is precisely where hydrothermal reactions occur.

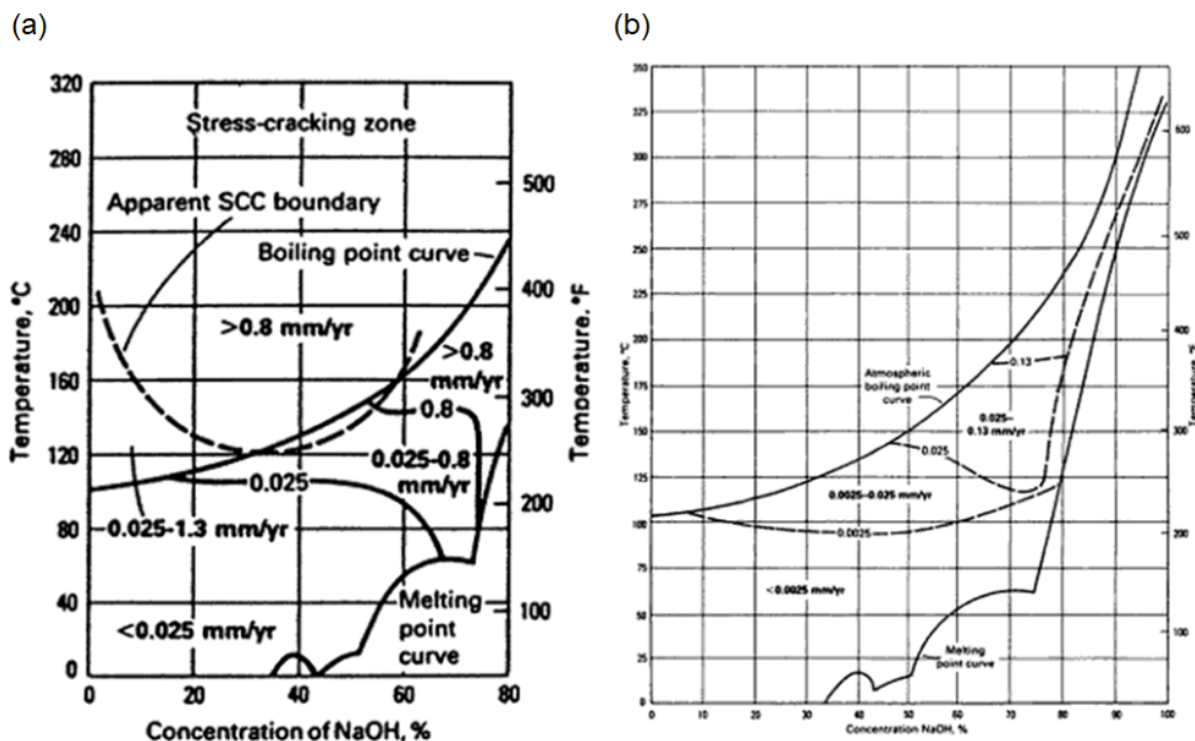
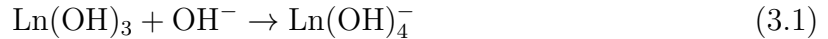


Figure 3.5. Isocorrosion curves of (a) T316 stainless steel and (b) Nickel 201 in an NaOH solution.<sup>40</sup>

### 3.2. Modeling Lanthanide (Oxide) Hydroxide Phase Space

Now that the principles of hydrothermal synthesis have been established, the phase space of rare-earth oxides with water will be investigated. In aqueous or basic solutions, the lanthanide sesquioxides ( $\text{Ln}_2\text{O}_3$ ) readily hydrate into the hydroxide phase ( $\text{Ln}(\text{OH})_3$ ), a stable solid whose solubility in alkaline solutions is negligible. This is to be expected, owing to the strong basicity and ionicity of the lanthanide oxides, as presented in Figure 3.1. As a result, most hydrothermal syntheses involving lanthanides are done under highly caustic conditions, sometimes as high as 20 M KOH. The claim is that a soluble hydroxyl complex ( $\text{Ln}(\text{OH})_4^-$ ) can form under these highly basic conditions, as shown

in reaction 3.1, However, other research suggests that forming a more soluble and reactive precursor is necessary: in the synthesis of  $\text{LnMnO}_3$ , the dehydration of the hydroxide phase into the more soluble and reactive oxide hydroxide ( $\text{LnOOH}$ ), shown in reaction 3.2, was a necessary step.<sup>41</sup>



The latter reaction is expected to occur at a certain transition temperature, and this transition temperature is reported to decrease as the ionic radius of the lanthanide decreases (Figure 3.6a). However, while higher temperatures favor dehydration reactions, the effect of pressure on this transition has not well been explored for autogenous systems. It is to be expected that an increase in pressure would favor the stability of the  $\text{Ln}(\text{OH})_3$  phase, as increasing the pressure pushes reaction 3.2 in the direction that minimizes the volume of the system. While there are studies that begin to show this behavior,<sup>42,43</sup> they were all performed at pressures much greater than the autogenous pressure of the system.

To explore the effect at lower pressures, data from the aforementioned studies was extrapolated towards operating conditions applicable to our hydrothermal system using an exponential fit of the form  $P = Ae^{B/T}$ , where  $A$  and  $B$  were the fitting parameters. The extrapolated plots act as a phase diagram for the appropriate lanthanide species. At a given temperature, this phase diagram defines a maximum pressure for  $\text{Ln}(\text{OH})_3$  dehydration into  $\text{LnOOH}$  to occur. Using the vapor pressure of water as a starting point for the autogenous pressure of the system, we can define a new, and lower, transition temperature, as shown in Figure 3.6b. It should again be noted that the autogenous

pressure in a hydrothermal vessel is not necessarily equal to the vapor pressure of the water but is partly a function thereof.

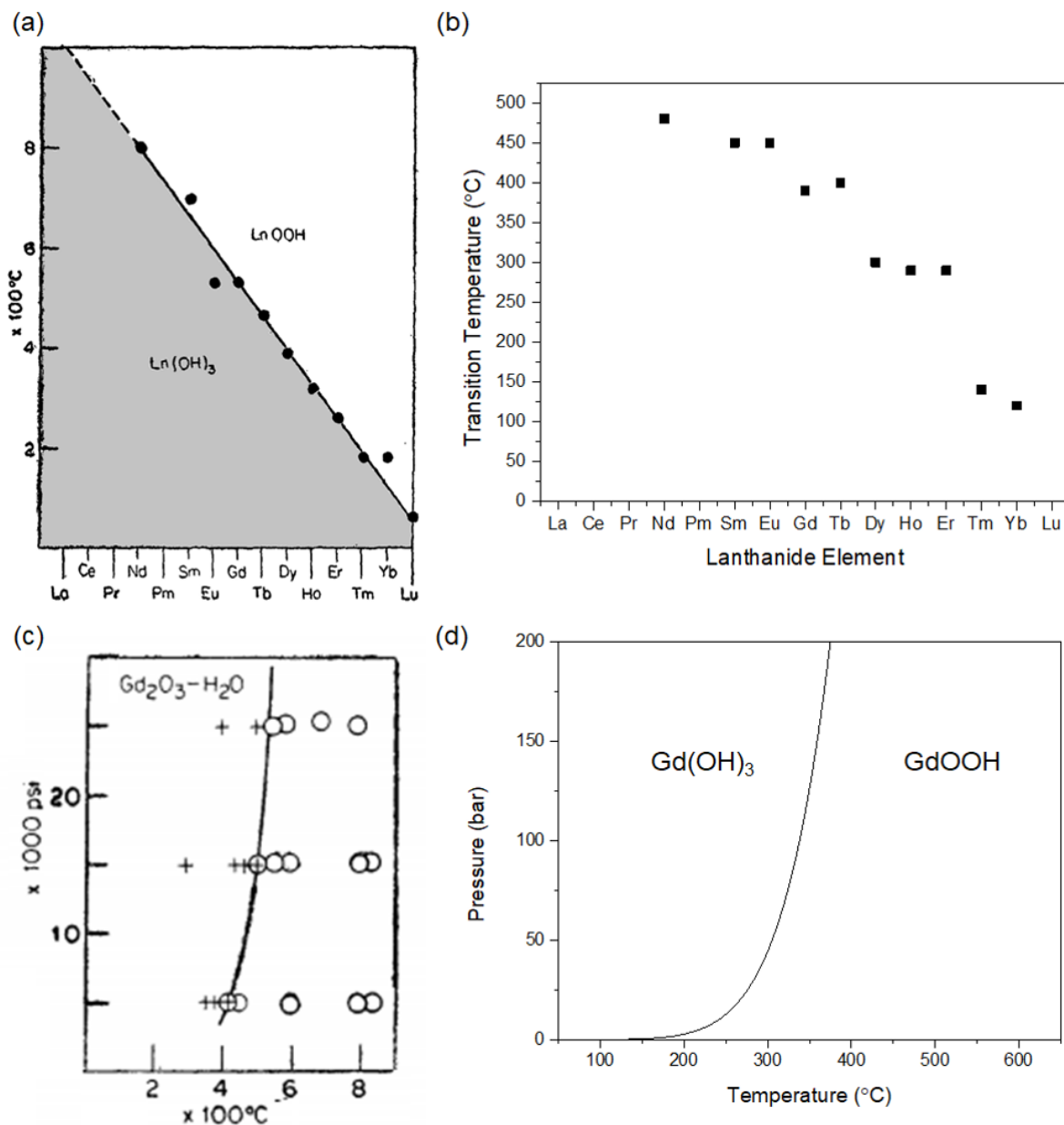


Figure 3.6. Graphs depicting the temperature dependence on the  $\text{Ln}(\text{OH})_3$ - $\text{LnOOH}$  phase stability as a function of lanthanide (a) at a constant pressure of 25000 psi<sup>42</sup> and (b) at a pressure equal to the vapor pressure of water.  $\text{Gd}(\text{OH})_3$ - $\text{GdOOH}$  phase diagram (c) experimentally determined using external pressures<sup>42</sup> and (d) calculated by extrapolating towards lower temperatures and pressures.

### 3.3. Experimental Confirmation

As a proof of concept, hydrothermal treatment of  $\text{Er}_2\text{O}_3$  was investigated. Phase competition between  $\text{Er}(\text{OH})_3$  and  $\text{ErOOH}$  has been studied several times in the literature. The increased solubility of  $\text{ErOOH}$  in  $\text{NaOH}$  has been noted but the addition of  $\text{NaOH}$  never explained the transition from  $\text{Er}(\text{OH})_3$  to  $\text{ErOOH}$  (Figure 3.7a).<sup>44</sup> Research on synthesizing  $\text{ErCrO}_3$  found that increasing the  $\text{KOH}$  concentration yielded  $\text{ErOOH}$  rather than  $\text{Er}(\text{OH})_3$ , but did not propose a reason why.<sup>45</sup> Our investigation was simply to put  $\text{Er}_2\text{O}_3$  into an autoclave with either water or 10 M  $\text{NaOH}$  as a solvent. The addition of  $\text{NaOH}$  lowers the vapor pressure of the solvent (Figure 3.3).<sup>39</sup> At 240 °C, the pressures of the systems were calculated to be 32 bar and 18.4 bar for the water and 10 M  $\text{NaOH}$  solutions, respectively. At the higher pressure,  $\text{Er}(\text{OH})_3$  is the only observed product, whereas the primary product for the lower pressure system is  $\text{ErOOH}$  (Figure 3.7b).

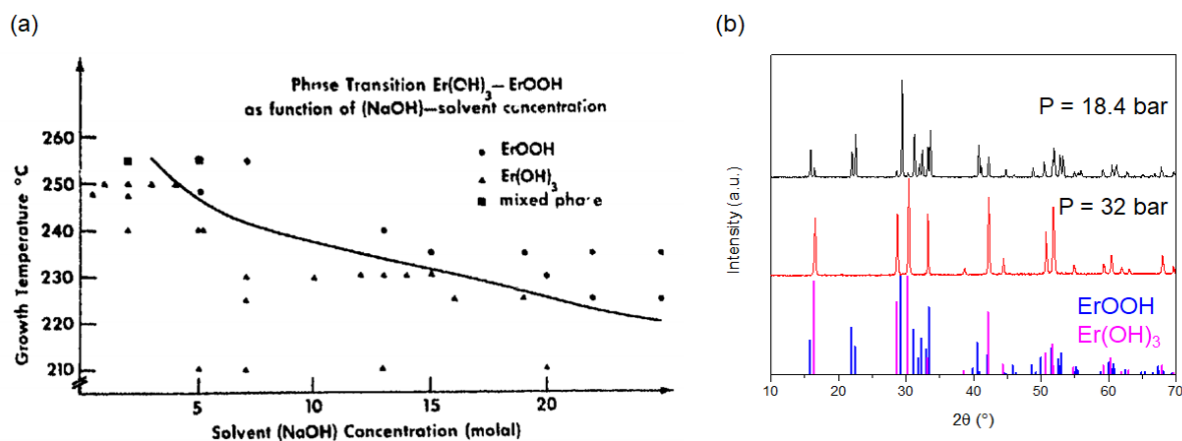


Figure 3.7. (a) The  $\text{Er}(\text{OH})_3$ - $\text{ErOOH}$  phase transition as a function of temperature and  $\text{NaOH}$  concentration.<sup>44</sup> (b) PXRD patterns of  $\text{Er}_2\text{O}_3$  treated in water (red curve) and 10 M  $\text{NaOH}$  (black curve). The addition of  $\text{NaOH}$  lowers the pressure of the system such that  $\text{ErOOH}$  is now stable over  $\text{Er}(\text{OH})_3$ . The peak locations for  $\text{Er}(\text{OH})_3$  (ICSD-200097) and  $\text{ErOOH}$  (ICSD-34473) are represented in pink and blue, respectively

Another confirmation came in the form of investigating the synthesis of Gd-containing perovskites (namely  $\text{GdFeO}_3$ ).  $\text{Gd}_2\text{O}_3$  was put into an unlined T316 stainless steel autoclave, which acted as the iron source. Three different reaction conditions using different temperatures and NaOH concentrations (and therefore different pressures) were attempted, all at different locations on the predicted  $\text{Gd}(\text{OH})_3$ - $\text{GdOOH}$  phase diagram. The first synthesis was done in a region where only  $\text{Gd}(\text{OH})_3$  was predicted (300 °C and 1 M NaOH) and, as expected, it was the only product formed. The next synthesis occurred near the phase transition but on the side of  $\text{Gd}(\text{OH})_3$  (350 °C and 1 M NaOH), and  $\text{Gd}(\text{OH})_3$  was again the primary phase but some  $\text{GdFeO}_3$  formed. The last synthesis was done under conditions in which  $\text{GdOOH}$  should be the preferred phase (350 °C and 10 M NaOH), and indeed only  $\text{GdFeO}_3$  was formed. As mentioned before, the formation of  $\text{GdOOH}$  should be a necessary intermediate for making perovskites.<sup>41</sup> Rehydration of  $\text{GdOOH}$  to  $\text{Gd}(\text{OH})_3$  upon cooling could not be discounted.

To prove that reaction 3.2 is indeed the relevant reaction and that it was not just an increase in reaction 3.1 occurring, various amounts of KOH and KCl were used as mineralizers for  $\text{GdFeO}_3$  synthesis instead. Increasing KCl would not favor reaction 3.1 but Raoult's law suggests that it would still lower the vapor pressure of the system and therefore promote reaction 3.2. Here,  $\text{Gd}_2\text{O}_3$  and  $\text{Fe}(\text{NO}_3)_3 \cdot 9\text{H}_2\text{O}$  were used as precursors into different KOH or KCl solutions at 240 °C in a PTFE Teflon liner. When a 20 M KOH solution and no KCl was added, no  $\text{GdFeO}_3$  was formed. When instead a 20 M KOH and 17 M KCl solution was used instead,  $\text{GdFeO}_3$  was formed. While the pressure with these mineralizers was not known, the study clearly confirmed the relationship between lowering the pressure and the formation of  $\text{GdFeO}_3$ .

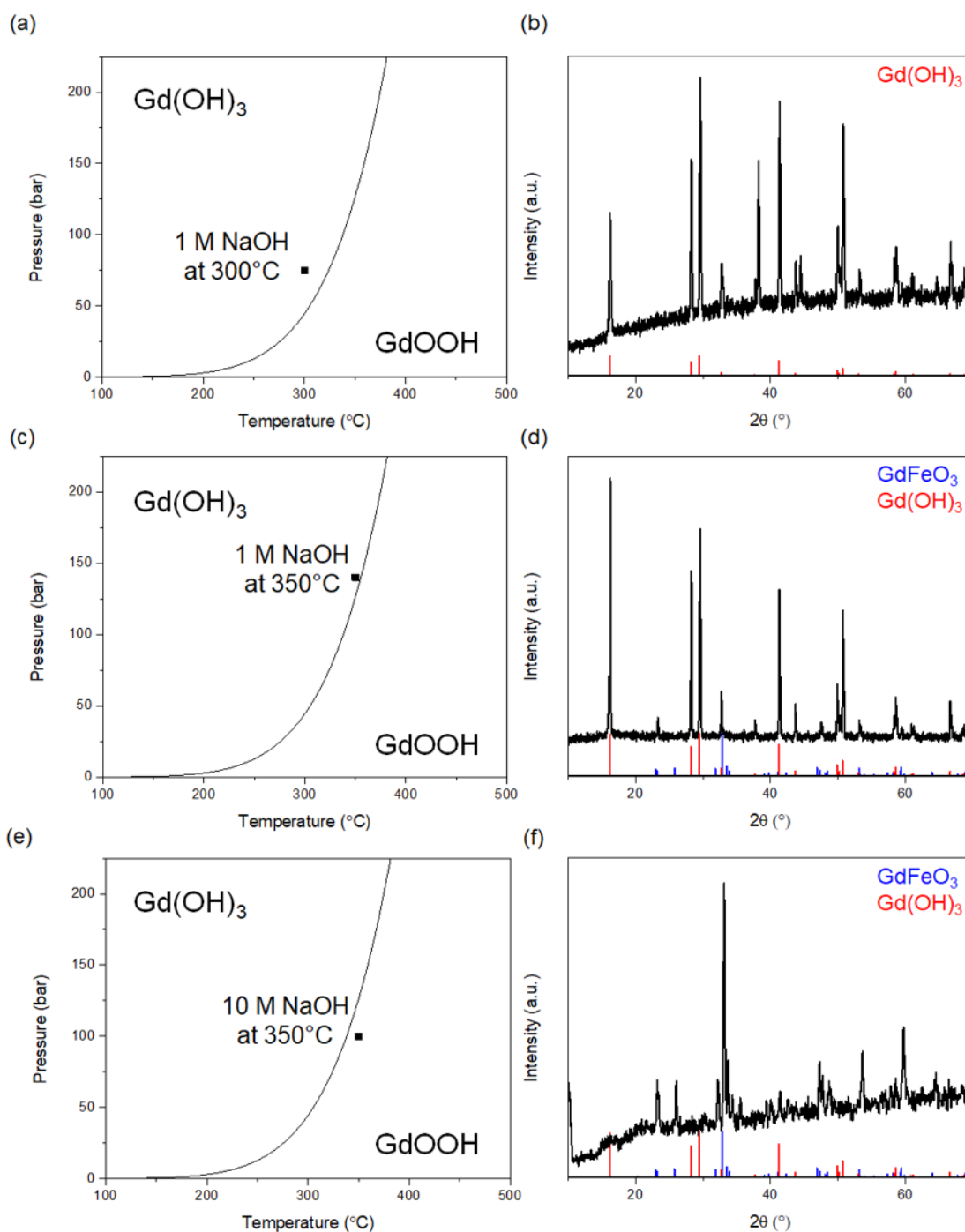


Figure 3.8. (a,c,e) The Gd(OH)<sub>3</sub>-GdOOH phase diagram with the noted reaction conditions for products that led to the (b,d,f) corresponding PXR patterns. The peak locations of Gd(OH)<sub>3</sub> (ICSD-200093) and GdFeO<sub>3</sub> (ICSD-61346) are represented by the red and blue lines, respectively.

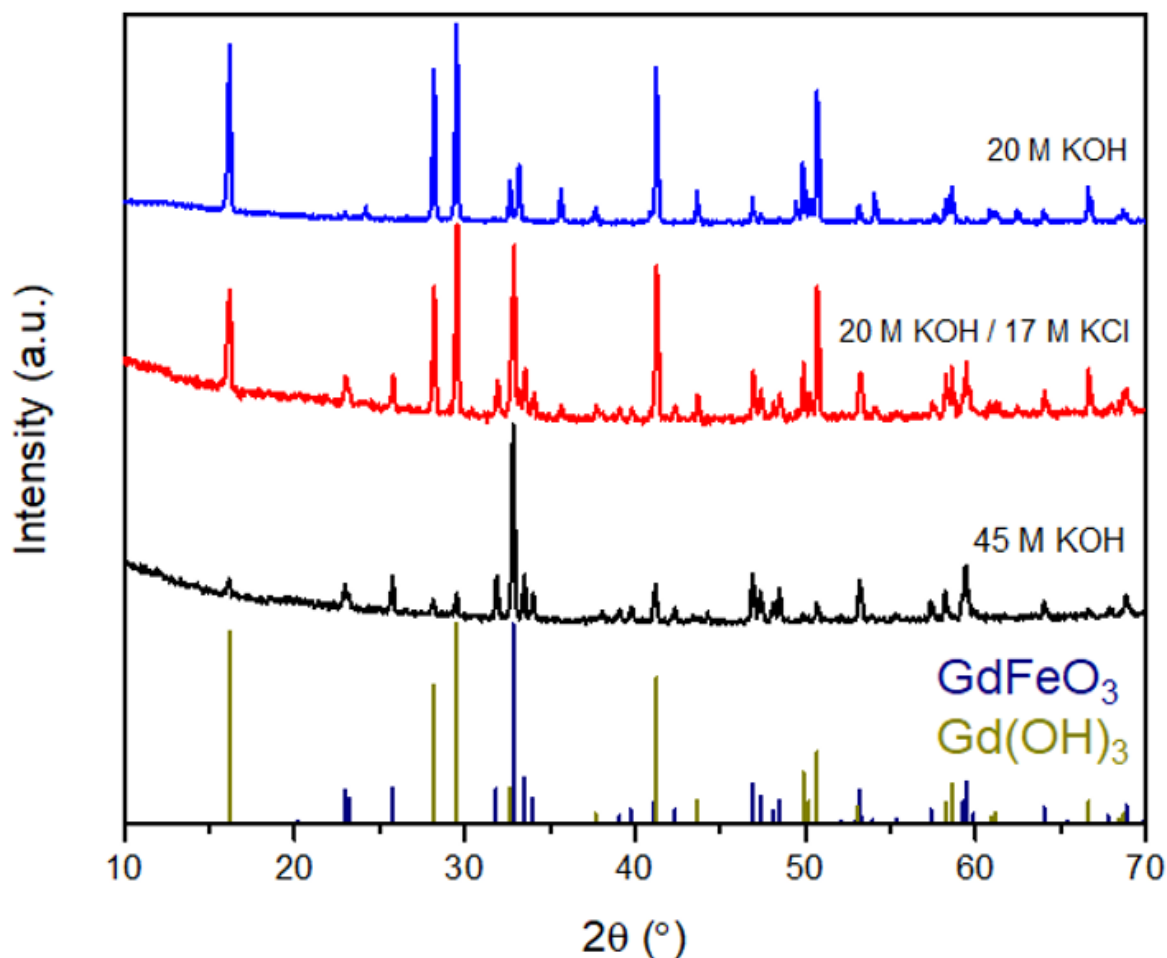


Figure 3.9. PXRD patterns of  $\text{GdFeO}_3$  syntheses with different KOH and KCl concentrations. Increasing solution concentration decreased the pressure in the system, promoted  $\text{GdOOH}$  formation, and subsequent reaction in  $\text{GdFeO}_3$ .

With these confirmations, it was then of interest to form catalytic supports of  $\text{LnScO}_3$  through this route. Synthesis of  $\text{LnMnO}_3$  has been demonstrated to occur under conditions that formed both  $\text{LnOOH}$  and  $\text{Mn(OH)}_4^-$ .<sup>41</sup> Scandium oxide and its hydroxides are basic so they requires very strong base to dissolve as  $\text{Sc(OH)}_4^-$ . The dissolution of  $\text{Sc}_2\text{O}_3$  is kinetically slow,<sup>36</sup> so  $\text{ScCl}_3 \cdot 6\text{H}_2\text{O}$  was used as a precursor instead. In fact,

when  $\text{Sc}_2\text{O}_3$  was put in a 35 M KOH solution at 240 °C, it came out of the autoclave unchanged.  $\text{Gd}(\text{NO}_3)_3 \cdot 6\text{H}_2\text{O}$  and  $\text{ScCl}_3 \cdot 6\text{H}_2\text{O}$  were put into various KOH solutions at 240 °C in a PTFE Teflon liner. These conditions were similar to those which produced  $\text{GeFeO}_3$ , but failed to react and form  $\text{GdScO}_3$ , perhaps owing to the high water content in the hydrothermal reaction. Later chapters will stress that low water vapor pressures are necessary for forming  $\text{LnScO}_3$ .

To circumvent the issue of the reactivity between the  $\text{Gd}(\text{OH})_3$  and  $\text{Sc}_2\text{O}_3$ , a precursor with the appropriate stoichiometry was prepared and then treated under hydrothermal conditions. The precursor was a mixed cation hydroxide xerogel. To make this precursor, first a stoichiometric mixture of the binary oxides was dissolved in 15.8 N nitric acid maintained at 80 °C. The solution was then added slowly to an excess of 10 M NaOH in an ice bath to precipitate a mixed cation hydroxide hydrogel. The gel was dried at 80 °C for several days to create a xerogel that was then ground into a powder to be used as the precursor. As shown in the EDX composition map in Figure 3.11, the cations in the xerogel precursor are fairly well mixed, though some segregation did occur. In the images, rods and platelets were rich in Gd, whereas cubes and hexagonal prisms were rich in Sc. The xerogel was then transferred to an autoclave with distilled water as a solvent and heated to 350 °C. A white powder was obtained, cleaned several times with distilled water, and then dried at 80 °C overnight. The PXRD pattern of the sample in Figure 3.12a shows that, in this way,  $\text{GdScO}_3$  can be formed but suggests that the product was not phase pure and instead also contained  $\text{Gd}(\text{OH})_3$  and  $\text{ScOOH}$ .

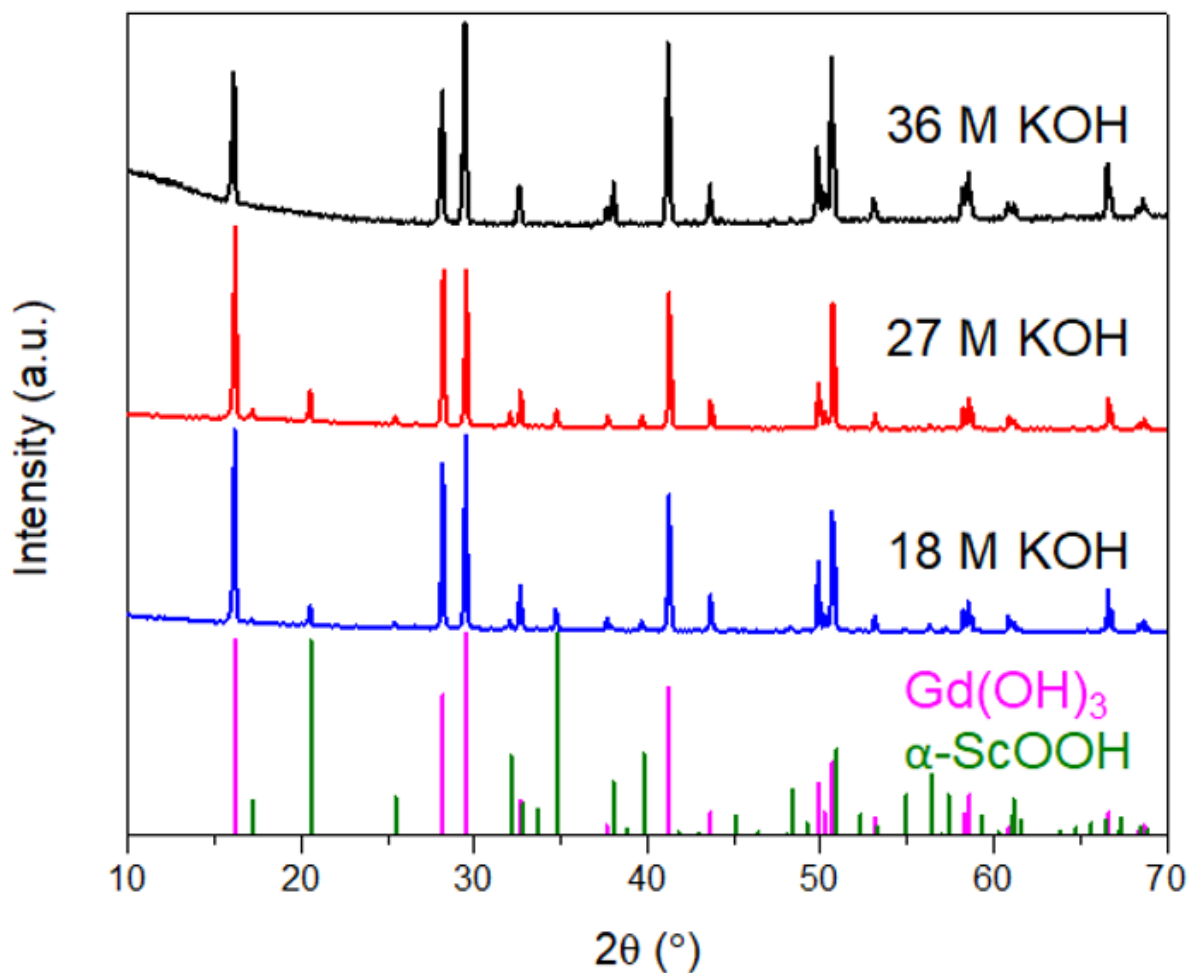


Figure 3.10. PXRD patterns of  $\text{GdScO}_3$  syntheses with different KOH concentrations. Higher KOH concentrations led to increased solubility of scandium species in solution, but none reacted to form  $\text{GdScO}_3$ .

To understand why these other phases would form, the following possible reactions were considered:



The dominant reaction is a function of the pressure and activity of water in the system. An excess of water would favor Reaction 3.3 because it produces less water as a product than Reaction 3.4 does. Therefore, a reduced activity of water is necessary to obtain a higher yield of the perovskite phase. As a result, when the autoclave experienced a leak and excess water was released, the yield of  $\text{GdScO}_3$  *increased* from 66.7 wt.% to 72.8 wt.%, determined by whole profile fitting in Jade, despite the synthesis being terminated 40 hours sooner (Figure 3.12b). Additionally, the decrease in pressure from the leak changed the stable scandium oxide hydroxide phase from  $\alpha$ -ScOOH (23.663 cm<sup>3</sup>/mol) to  $\gamma$ -ScOOH (25.447 cm<sup>3</sup>/mol) because larger molar volumes are preferred at lower pressures. The particles formed through hydrothermal treatment were fairly large, but could be sharper faceted (Figure 3.12c). Unfortunately, the particles were less sharply faceted when the leak occurred (Figure 3.12d), although this may be a result of the decreased reaction time.

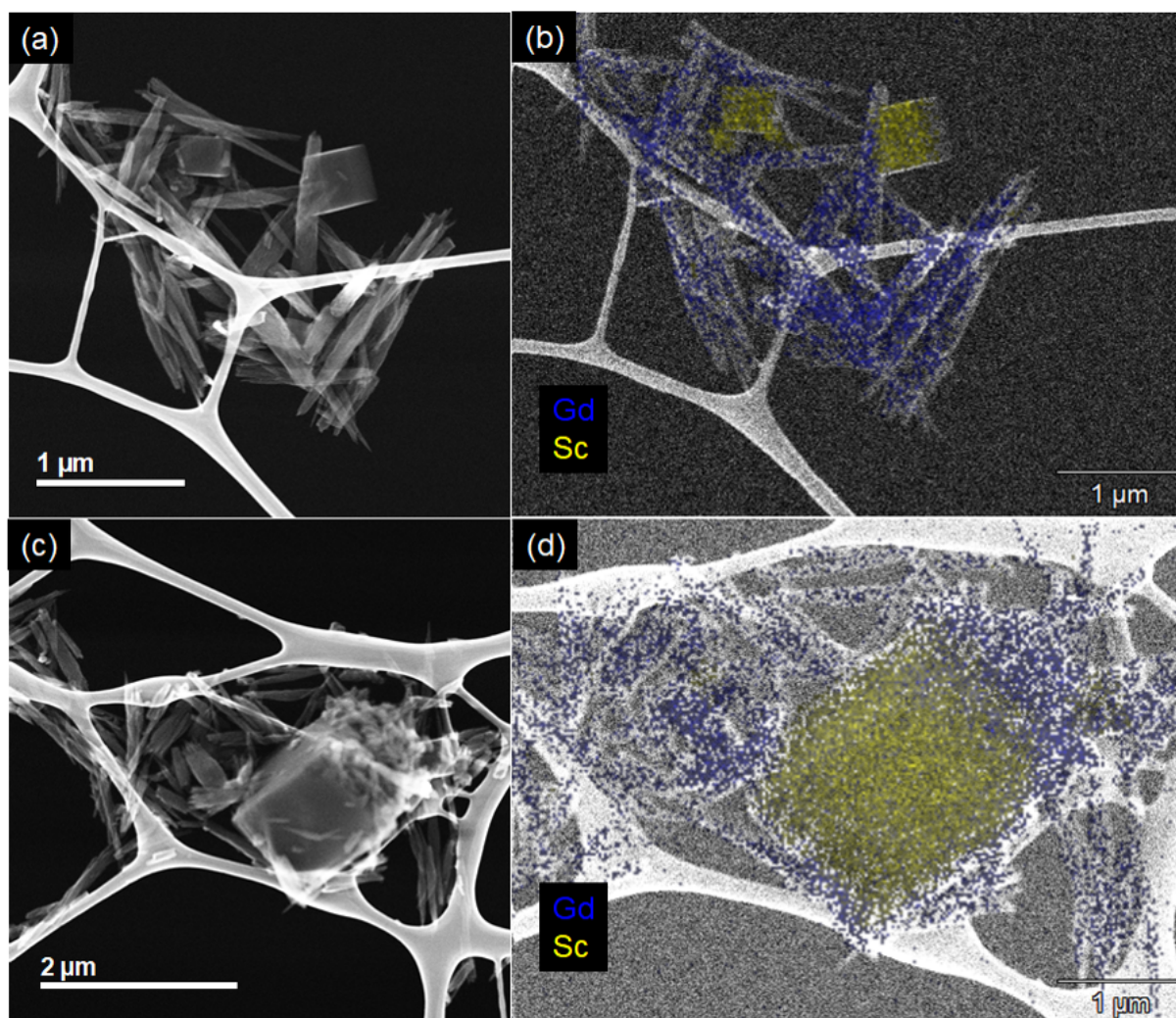


Figure 3.11. (a,c) SE images of the dried precipitate, with (b,d) the corresponding EDX maps for Gd (blue) and Sc (yellow) overlaid onto the SE image.

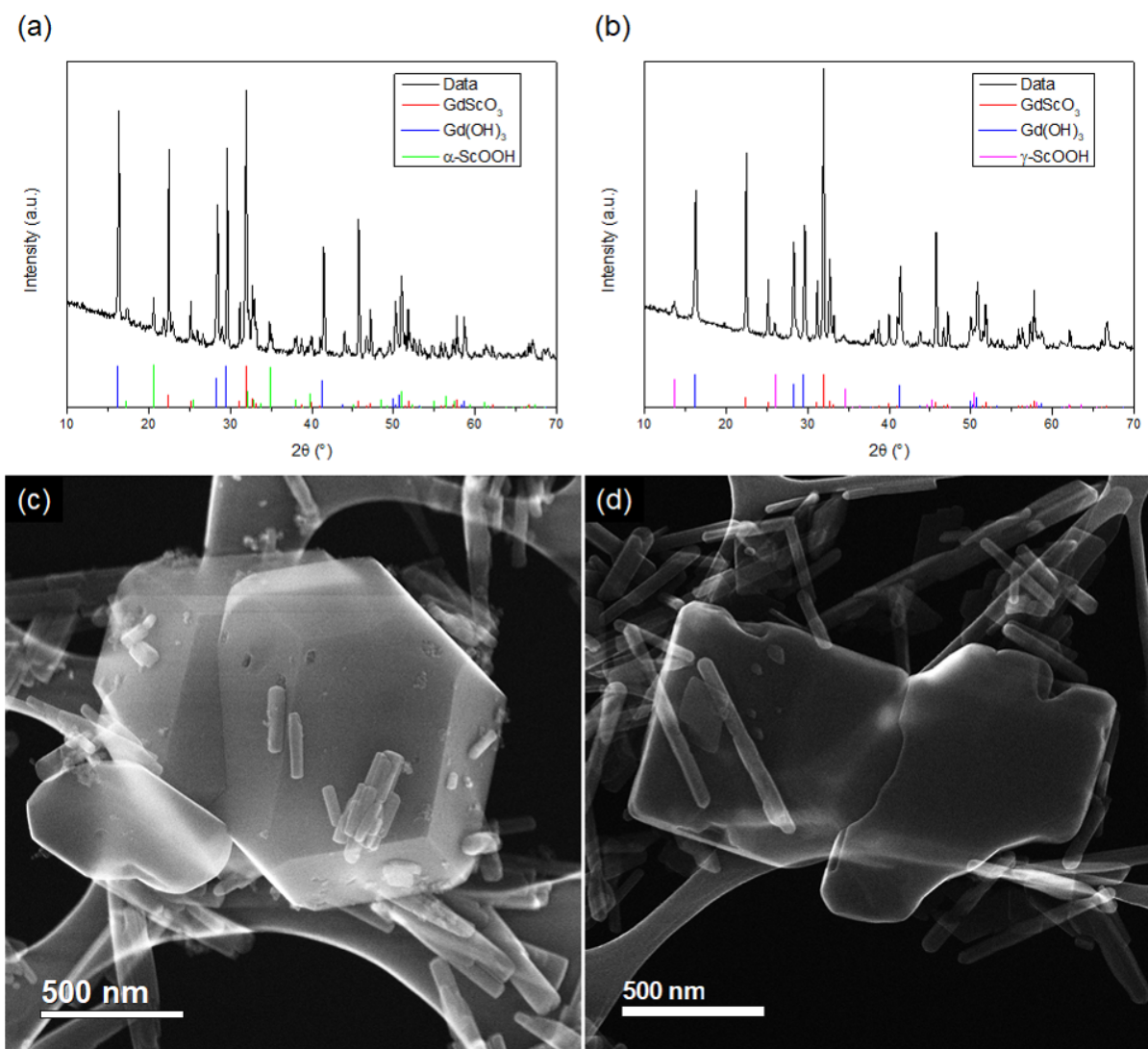


Figure 3.12. (a,b) PXRD patterns and (c,d) corresponding SE images of GdScO<sub>3</sub> prepared via hydrothermal synthesis at 350 °C (a,c) without leaking and (b,d) with a leak.

### 3.4. Conclusion

The phase space between different  $\text{Ln}(\text{OH})_3$  and  $\text{LnOOH}$  treated hydrothermally at autogenous pressures was modeled by extrapolating high-pressure data from literature,<sup>42</sup> where increasing temperatures and decreasing pressures favor  $\text{LnOOH}$  formation. In addition, the autogenous pressure as a function of different temperatures and  $\text{NaOH}$  concentrations was calculated. Owing to these two relationships, syntheses of rare-earth perovskites in literature that claim that high hydroxide concentrations are necessary to form  $\text{Ln}(\text{OH})_4^-$  in solution may in reality just be using the high hydroxide concentrations to lower the pressure and form the more soluble and reactive  $\text{LnOOH}$ . Experimental confirmation of these predictions shows that increasing  $\text{NaOH}$  concentration can lead to  $\text{LnOOH}$  formation and that  $\text{LnOOH}$  formation in turn can lead to the formation of Ln-containing perovskites. However, the formation of  $\text{LnOOH}$  alone did not allow for  $\text{LnScO}_3$  to be formed, likely owing to the barrier of reacting two basic reactants together. If a precursor containing those species already reacted together, the perovskite phase may be formed, but the chemical potential of water must still be low to prevent hydration back into the lanthanide hydroxides.

## CHAPTER 4

**Synthesis of Gadolinium Scandate from a Hydroxide Hydrogel**

This chapter will introduce hydro-sauna synthesis, a water-vapor assisted sol-gel process we developed to synthesize  $\text{LnScO}_3$  particles through the decomposition of a mixed cation hydroxide hydrogel in a humid environment. While the focus here will be on  $\text{GdScO}_3$  in particular, other  $\text{LnScO}_3$  are also possible and will be investigated more in later chapters. For this chapter in particular, the humid environment was created by trapping the water vapor that evaporates out of the hydrogel inside an autoclave. We believe this humidity weakened the capillary forces within the hydrogel to maintain open pore structure, which we hypothesized would allow for greater diffusion of the atomic species and for crystallization to occur at lower temperatures than is typical for sol-gel processes, which are often greater than  $700\text{ }^\circ\text{C}$ .<sup>46</sup> These concepts lay the groundwork for how the faceted  $\text{LnScO}_3$  nanoparticles used throughout my work were synthesized (Chapter 5).

The work in this chapter was done in collaboration with Zachary Mansley and Tiffany Ly, both of which performed the secondary electron imaging shown here. Much of this chapter formed the article "Synthesis of Gadolinium Scandate from a Hydroxide Hydrogel",<sup>47</sup> from which many of these figures are reproduced.

**4.1. Introduction**

As discussed previously (Chapter 1), the lanthanide scandates are of interest to us as catalyst supports because they have lattice parameters similar to that of several different

noble metals and many of their properties may be changed by systematically changing the lanthanide used. Before they can be used as supports, high-surface areas of material must first be synthesized. However, these materials had mainly been studied in applications where high surface areas were not necessary, such as dielectric materials owing to their high- $\kappa$  values and large optical band gaps,<sup>48,49</sup> and as substrates for other novel complex oxides since large single crystals can be grown with high purity using different lanthanides to vary the lattice parameter.<sup>49</sup> Therefore, these materials have mostly been synthesized as thin films by atomic layer deposition<sup>50</sup> or pulsed laser deposition,<sup>51,52</sup> as single crystals using the Czochralski technique,<sup>49</sup> or as powders through solid-state reactions at high temperatures and / or pressures.<sup>53,54</sup> However, these methods are unsuitable for producing the high surface area material necessary to attain high catalytic rates in most cases.

Producing such materials often requires low reaction temperatures to minimize sintering of particles. Solution-based methods, such as solvothermal synthesis (discussed in greater detail in Chapter 3), in which reactions occur in solution in a sealed vessel at temperatures greater than the boiling point of the solution and pressures greater than one atmosphere, are common techniques used to obtain new materials and materials with high surface area at relatively low temperatures. The solvothermal synthesis of oxides occurs in hydroxide solutions; owing to the negligible solubilities of rare-earth species in alkaline media,<sup>55</sup> there are no reports of synthesizing any  $\text{LnScO}_3$  through this method.

Another common route is through the creation of an intermediate phase that acts as a precursor that decomposes into a desired phase, but the lowest reported reaction temperature for crystalline  $\text{GdScO}_3$  using an intermediate phase as a precursor prior to our work was still relatively high at 850 °C.<sup>56</sup> We synthesized crystalline  $\text{GdScO}_3$  at

temperatures as low as 300 °C, the lowest reported temperature for the formation of any crystalline LnScO<sub>3</sub>, through the decomposition of a mixed cation hydroxide precursor in a humid environment, which will be referred to as hydro-sauna conditions. The presence of water vapor allowed for crystallization at lower temperatures than previous sol-gel or precursor-mediated techniques. However, while water is critical for the reaction to proceed, the chemical potential of water must be controlled through the temperature and pressure in order to prevent the formation of additional hydrated or hydroxide phases.

## 4.2. Experimental Section

### 4.2.1. Synthesis

We will describe here the method used to produce GdScO<sub>3</sub>, returning later to explain why these conditions were used. A solution containing equimolar concentrations of gadolinium and scandium species was prepared by dissolving 2 mmol of their sesquioxides in 10 mL of 15.8 N nitric acid maintained at 80 °C and diluting the solution with 10 mL of deionized water. This solution was then added dropwise into 25 mL of 10 M NaOH in an ice bath to precipitate a white mixed cation hydroxide hydrogel, which was then isolated using centrifugation and washed several times with deionized water to remove Na(NO<sub>3</sub>). This amorphous hydrogel, which will be referred to as GdSc(OH)<sub>6</sub> · xH<sub>2</sub>O, was then used as a precursor for GdScO<sub>3</sub> growth. Roughly 700 mg of the hydrogel was sealed in a 300 mL stainless steel autoclave (Parr 4760) and maintained for 48 hours at a reaction temperature between 250 °C and 450 °C. The product was rinsed with distilled water and centrifuged several times, and then put into an oven at 80 °C to dry overnight.

### 4.2.2. Characterization

Simultaneous thermogravimetric and differential thermal analyses (TG-DTA) measurements were performed on a Netzsch Jupiter F3 Simultaneous Thermal Analysis system from room temperature to 550 °C and back at a rate of 10 °C min<sup>-1</sup> under an air flow of 50 mL min<sup>-1</sup>. Powder X-ray diffraction (PXRD) was performed on a Rigaku Ultima diffractometer using a Cu K $\alpha$  source operated at 40 kV and 20 mA. PXRD for Reitveld refinement was performed on the sample grown at 300 °C on a Rigaku Smartlab using a Cu K $\alpha$  source operated at 40 kV and 160 mA with a 0.02° step size and 1 s dwell time. Secondary electron imaging was performed on a Hitachi HD-2300 scanning transmission electron microscope operated at 200 kV.

### 4.3. Results

When the mixed solution of Gd<sup>3+</sup> and Sc<sup>3+</sup> was added to a 10 M NaOH solution, a mixed cation hydroxide hydrogel (GdSc(OH)<sub>6</sub> · xH<sub>2</sub>O) immediately precipitated out. TG-DTA of the hydrogel revealed that, upon heating to 550 °C, an endothermic reaction had occurred at 150-200 °C and an overall mass loss of 86% was observed (Figure 4.2). Heat treatment of GdSc(OH)<sub>6</sub> · xH<sub>2</sub>O in air at 400 °C for 36 hours produced an amorphous product. In order to crystallize the gel, GdSc(OH)<sub>6</sub> · xH<sub>2</sub>O was heated to various temperatures in an autoclave, which kept the hydrogel in a humid environment; PXRD of those products in Figure 4.3 reveal a crystalline product: GdScO<sub>3</sub> was formed at 300 °C, 350 °C, 400 °C, and 450 °C; Gd(OH)<sub>3</sub> and  $\alpha$ -ScOOH were formed at 250 °C and again at 400 °C and 450 °C. When more gel or water was added to the autoclave, the PXRD (Figure 4.4) revealed more Gd(OH)<sub>3</sub> and ScOOH were formed, rather than GdScO<sub>3</sub>. The morphology

of the  $\text{GdScO}_3$  was investigated with SE imaging (Figure 4.8). Particles become larger and more faceted with increasing temperature.

The crystalline  $\text{GdScO}_3$  produced at 300 °C for 48 hours was investigated using several techniques. The unit cell parameters from Rietveld refinement, plotted in Figure 4.5, showed good agreement with literature values of  $\text{GdScO}_3$  prepared by high-temperature solid-state reaction in Table 4.1. TG-DTA revealed little mass loss or energy change upon heating to 550 °C (Figure 4.6). Raman spectroscopy in Figure 4.7 was consistent with that of  $\text{GdScO}_3$  single crystals with the  $A_g$  modes at 248, 321, 418, 452, and 501  $\text{cm}^{-1}$ ,  $B_{1g}$  modes at 223, 373, and 490  $\text{cm}^{-1}$ ,  $B_{2g}$  modes at 298, 351, 463, and 532  $\text{cm}^{-1}$ , and  $B_{3g}$  modes at 300, 450, and 481  $\text{cm}^{-1}$ , observed.<sup>57</sup>

#### 4.4. Discussion

Crystalline materials require diffusion to form in order for the atoms to arrange into a lower energy periodic structure. In the case of most solid-state reactions, this often requires high temperatures for atoms from one precursor to be able to diffuse into and react with atoms in another precursor. One way around this is through the creation of a precursor in which the ions are already intermixed at the atomic level; through this the atoms are, on average, next to their appropriate neighbor, but a temperature greater than 700 °C is often still required for sufficient diffusion of atoms to produce a crystalline phase.<sup>46</sup> This precursor often starts as a gel, an amorphous solid network with an encapsulated liquid phase.<sup>58</sup> When a gel is heated, the encapsulated liquid evaporates and the amorphous solid network collapses due to capillary forces (Figure 4.1),<sup>58</sup> becoming a xerogel, which traps the atoms and prevents crystallization except at high temperatures.

If the open gel matrix is instead preserved upon heating, diffusion through the porous structure for crystallization may be possible.

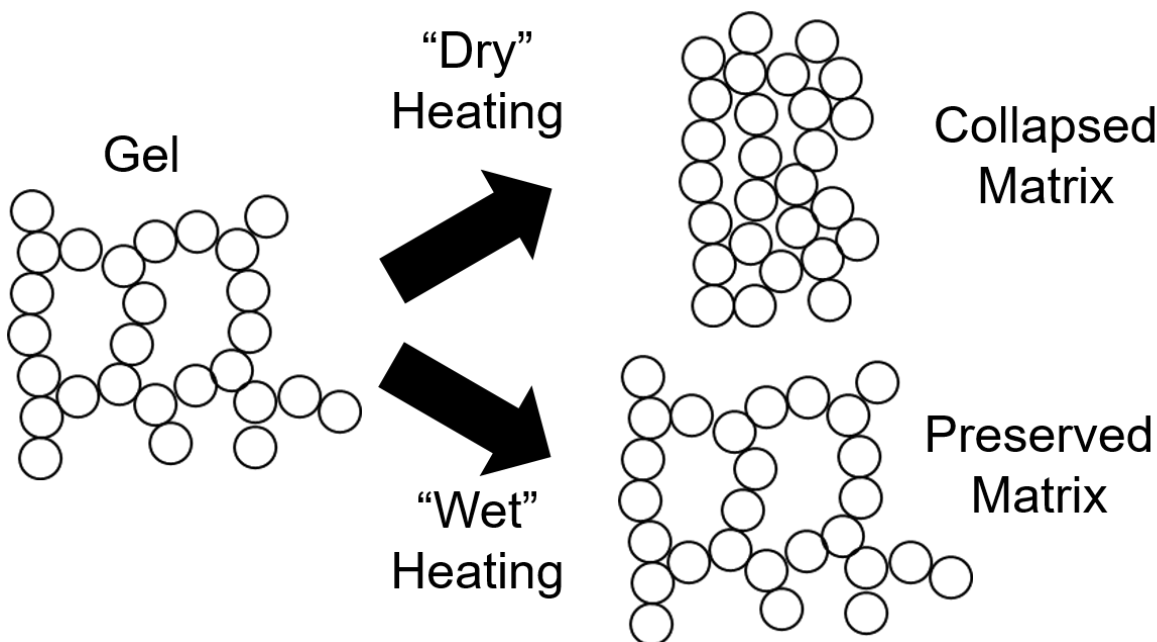


Figure 4.1. Schematic of a gel before and after heating in both a dry and wet environment. The gel is an amorphous solid network with an encapsulated liquid phase. When heated in a dry environment, the encapsulated liquid phase leaves, and capillary forces cause the solid matrix of the gel to collapse. When heated in a wet environment, the water vapor weakens the capillary forces by decreasing the water-steam surface energy,<sup>59</sup> which lessens the collapse of the matrix.

For  $\text{GdScO}_3$ , crystallization was accomplished by decomposing a mixed cation hydroxide hydrogel under hydro-sauna conditions. Rare-earth species have negligible solubilities in basic solutions and readily precipitate out as hydroxides.<sup>55</sup> When the mixed solution of  $\text{Gd}^{3+}$  and  $\text{Sc}^{3+}$  was added to a 10 M NaOH solution, a mixed cation hydroxide hydrogel immediately precipitated out. The solid network of the hydroxide hydrogel likely is a random structure containing  $\text{Gd}(\text{OH})_3$  and  $\text{Sc}(\text{OH})_3$  units, similar to what is observed in the more well-studied aluminum trihydroxide gel system.<sup>60</sup> The  $\text{GdSc}(\text{OH})_6 \cdot x\text{H}_2\text{O}$  hydrogel

was characterized using TG-DTA (Figure 4.2). Upon heating to 550 °C, an endothermic reaction occurred and an overall mass loss of 86% was observed. Most of this mass loss may be attributed to evaporation of water that was encapsulated in the hydrogel, as the dehydration of  $\text{GdSc}(\text{OH})_6$  alone would only correspond to a mass loss of 17%. Heating the hydrogel in air to 400 °C fully evaporated the encapsulated water to form a xerogel, trapped the cations, and yielded an amorphous product.

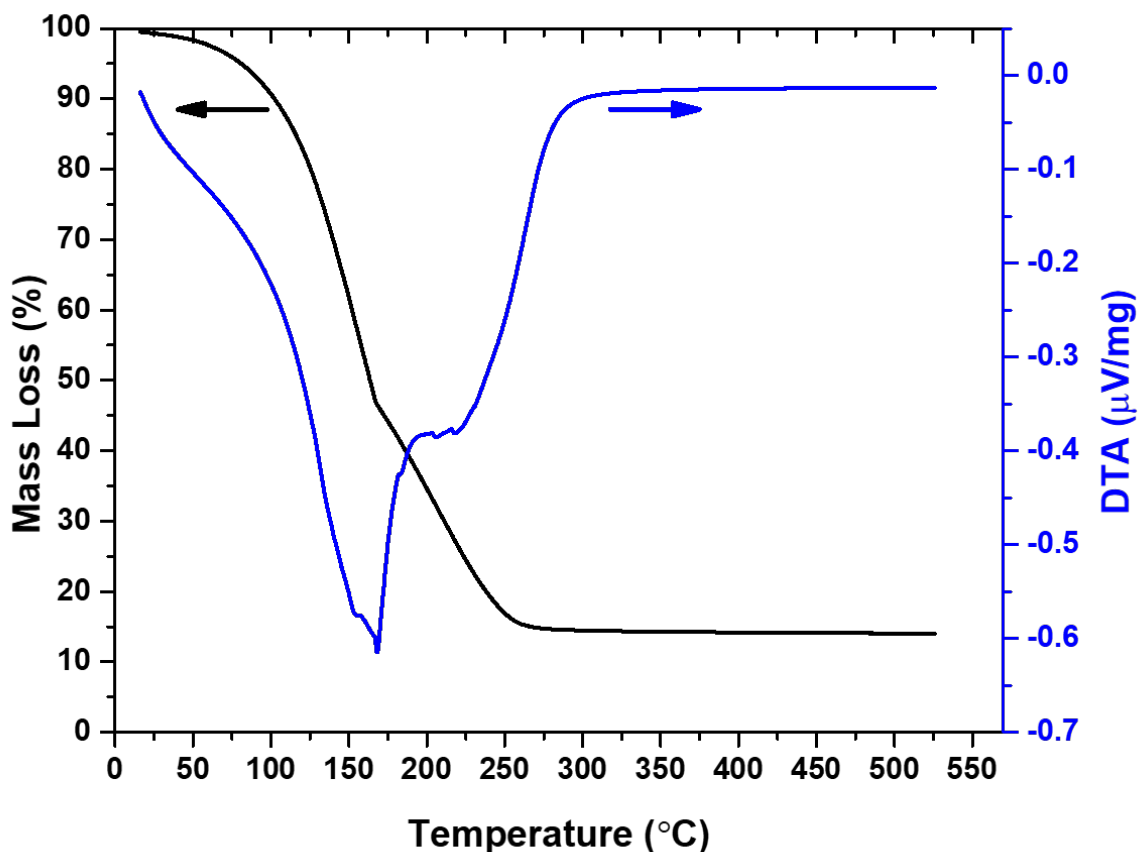


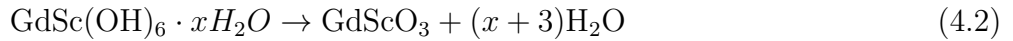
Figure 4.2. Simultaneous TGA (black) and DTA (blue) curves of the decomposition and dehydration of the  $\text{GdSc}(\text{OH})_6 \cdot x\text{H}_2\text{O}$  hydrogel.

To prevent the collapse of the gel matrix, the capillary forces within the gel need to be decreased, as the shrinkage of the matrix depends on the maximum capillary force.<sup>61</sup> The capillary pressure  $P_c$  depends on the surface energy of the liquid-vapor interface  $\gamma_{LV}$ , the contact angle  $\theta$ , and the surface area and volume of the pores ( $S_P$  and  $V_P$ , respectively), according to the following equation:<sup>58,61</sup>

$$P_c = -\gamma_{LV}\cos(\theta)S_P/V_P$$

Since it is unclear how one would controllably change the pore size,  $\gamma_{LV}$  has to be decreased to lessen the magnitude of the capillary pressure. It has been found that increasing the humidity decreases the surface tension of the water-gas interface, with the rationale being that the added steam reduced the net evaporation of the water.<sup>59</sup> Therefore, the hydrogel was heated inside a sealed autoclave; doing so produced water vapor from the evaporation of solvent from the hydrogel, and the presence of this water vapor kept the hydrogel precursor partially imbibed, which allowed for a decreased capillary pressure to maintain the pore structure. Diffusion in the pores is greater than that within a lattice (much like diffusion on surfaces or in grain boundaries) and, as evident from our results, is sufficient for crystallization. Similarly, the crystallization of  $ZrO_2$  from a gel precursor decreased with increasing partial pressures of water, claiming that the nucleation rate is enhanced by the higher mobility of the species.<sup>62</sup> Confirming this behavior would require *in situ* characterization of the pore structure, such as through small-angle X-ray scattering.<sup>61</sup> Nevertheless, PXRD patterns of our products are shown in Figure 4.3 and indicate crystalline material at all temperatures investigated. At 250 °C, the cations segregated into separate phases, namely  $Gd(OH)_3$  and  $\alpha\text{-ScOOH}$ , for reasons that will be

expanded upon below. At temperatures greater than 300 °C, the PXRD patterns matched predominately with GdScO<sub>3</sub>. Under these conditions, the precursor can decompose along at least two different reaction pathways depending on the temperature of the reaction:



Reducing the free energy of water by raising the temperature (which would increase the entropic contribution to the free energy of water) or reducing the amount of water will push both reactions 4.1 and 4.2 to the right, reaction 4.2 more so than reaction 4.1. To explore this in more detail, the effect of the activity of water in the system was investigated. First, 10 g of the GdSc(OH)<sub>6</sub> · xH<sub>2</sub>O hydrogel was sealed inside the autoclave and heated to 350 °C for 2 days. The resulting PXRD pattern in Figure 4.4 shows that this led to less GdScO<sub>3</sub> being formed, in favor of Gd(OH)<sub>3</sub> and ScOOH, owing to how when a greater amount of gel is sealed inside the autoclave, a greater amount of water is sealed in with it. To further this, an additional 10 mL of distilled water was added to again 10 g of the GdSc(OH)<sub>6</sub> · xH<sub>2</sub>O hydrogel to the autoclave and heated to 350 °C for 2 days. The resulting products, as seen by the PXRD pattern in Figure 4.4, imply that only reaction 4.1 occurred, as expected. Based on these results, the formation of Gd(OH)<sub>3</sub> and α-ScOOH in the products grown at 400 °C and 450 °C (Figure 4.3) was attributed to variability in the amount of hydrogel placed in the autoclave; an increase in the amount of hydrogel would increase the amount and activity of water, and hence promote reaction 4.1.

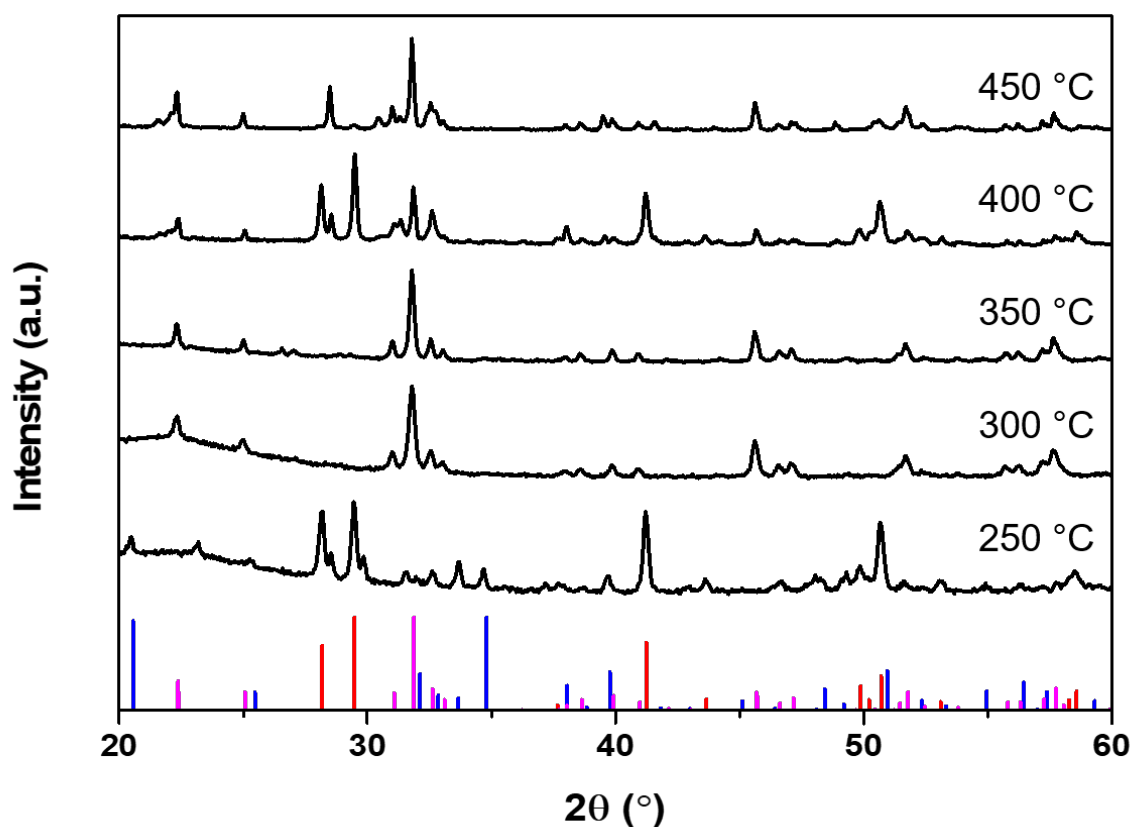


Figure 4.3. PXRD patterns of the products obtained after heating the gel in an autoclave at (from top to bottom) 450 °C, 400 °C, 350 °C, 300 °C, and 250 °C. The calculated peak locations and relative peak intensity for  $\text{GdScO}_3$  (pink, PDF 01-074-4353),  $\text{Gd(OH)}_3$  (red, PDF 01-083-2037), and  $\alpha\text{-ScOOH}$  (blue, PDF 01-073-1790) are plotted at the bottom.  $\text{GdScO}_3$  was formed at 300 °C, 350 °C, 400 °C, and 450 °C;  $\text{Gd(OH)}_3$  and  $\alpha\text{-ScOOH}$  were formed at 250 °C, 400 °C, and 450 °C.

We note that these results explain the failure of simple hydrothermal synthesis of  $\text{LnScO}_3$ ; the use of water as a solvent again pushes the reaction towards these hydrated phases. To cross-validate, hydrothermal conditions similar to those previously used for several other rare-earth perovskites such as  $\text{LnCrO}_3$ ,<sup>63</sup>  $\text{LnMnO}_3$ ,<sup>64</sup> and  $\text{LnFeO}_3$ ,<sup>65</sup> were attempted. To briefly summarize, stoichiometric amounts of  $\text{Gd(NO}_3)_3 \cdot 6\text{H}_2\text{O}$  and

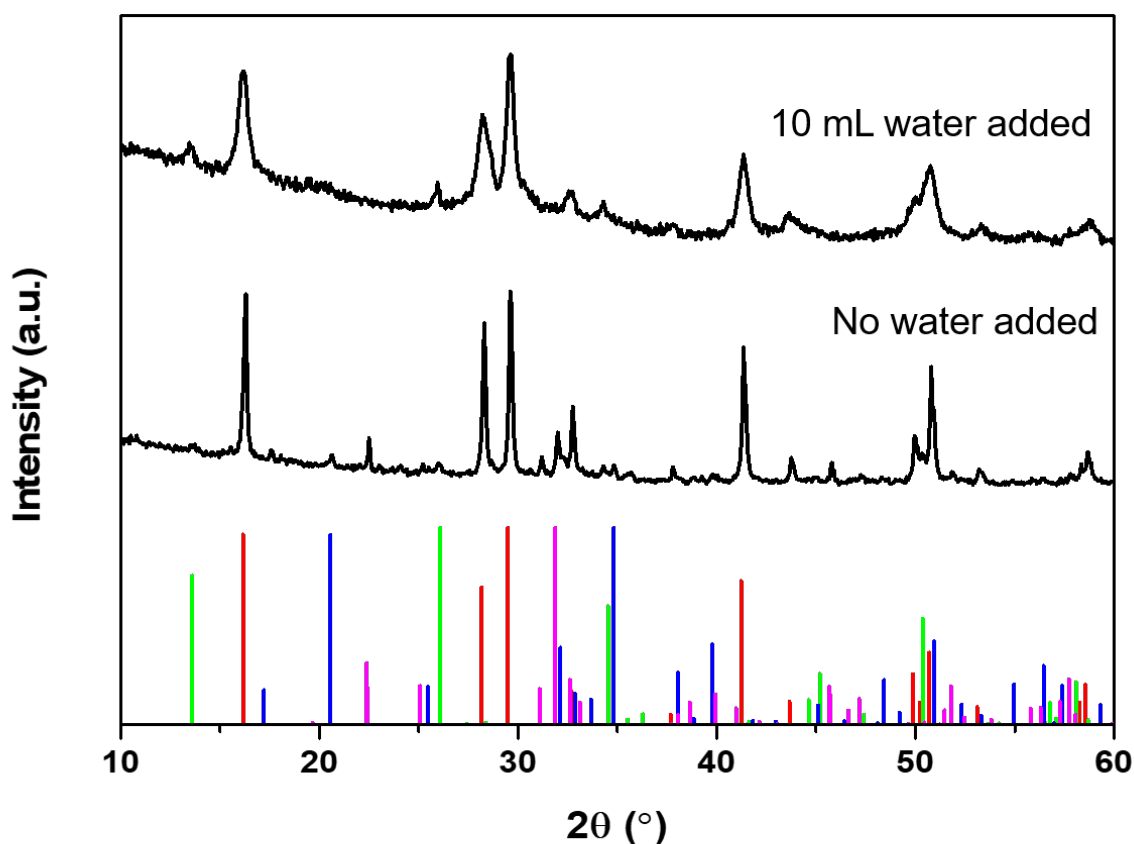


Figure 4.4. PXRD pattern of the product obtained after heating the gel in an autoclave at 350 °C with (top) 10 mL of distilled water added to the autoclave or (bottom) no additional water. The calculated peak locations and relative peak intensity for GdScO<sub>3</sub> (pink, PDF 01-074-4353), Gd(OH)<sub>3</sub> (red, PDF 01-083-2037), α-ScOOH (blue, PDF 01-073-1790), and γ-ScOOH (green, PDF 01-072-0360) are plotted at the bottom. The increased amount of gel increased the amount of water and formed more Gd(OH)<sub>3</sub> and ScOOH phases as a result, and the addition of water furthered this such that no GdScO<sub>3</sub> was formed.

ScCl<sub>3</sub> · 6H<sub>2</sub>O were heated to 250 °C in a high concentration KOH solution ranging from 10-20 M. Under these hydrothermal conditions, only Gd(OH)<sub>3</sub> and α-ScOOH could be produced, and only Gd(OH)<sub>3</sub> formed under sufficiently alkaline conditions (20 M KOH

solution) that dissolved the  $\alpha$ -ScOOH. Therefore, we conclude that a hydro-sauna treatment in which the water activity can be controlled is necessary to produce perovskite GdScO<sub>3</sub>.

GdScO<sub>3</sub> particles produced via this hydro-sauna synthesis at 300 °C were characterized for their crystalline quality through several techniques. Rietveld refinement of the sample, plotted in Figure 4.5, shows good agreement with literature values of GdScO<sub>3</sub> grown as a powder by high-temperature solid-state reaction and grown as a single crystal by the Czochralski method in Table 4.1. In addition, Raman spectroscopy in Figure 4.7 was consistent with that of GdScO<sub>3</sub> single crystals with the A<sub>g</sub> modes at 248, 321, 418, 452, and 501 cm<sup>-1</sup>, B<sub>1g</sub> modes at 223, 373, and 490 cm<sup>-1</sup>, B<sub>2g</sub> modes at 298, 351, 463, and 532 cm<sup>-1</sup>, and B<sub>3g</sub> modes at 300, 450, and 481 cm<sup>-1</sup>, observed.<sup>57</sup> Simultaneous TG-DTA in Figure 4.6 showed a constant change in heat and a slow but steady rate of mass loss over a temperature range of 100 to 550 °C and was attributed to the release of water adsorbed on the particle surface. These observations all suggest that GdScO<sub>3</sub> of high quality can be synthesized under hydro-sauna conditions at temperatures as low as 300 °C.

The morphology of GdScO<sub>3</sub> particles produced via this hydro-sauna synthesis was characterized using secondary electron imaging in a scanning transmission electron microscope (Figure 4.8). Reaction temperature had a clear effect on the resulting particle morphology. At 300 °C, particles have no preferential faceting and are small; Scherrer analysis of the PXRD pattern using MDI Jade software determined the average crystallite size to be 63.7 ± 8.7 nm. Since this crystallite size is consistent with the secondary electron images, peak broadening in the diffraction pattern are assumed to be caused

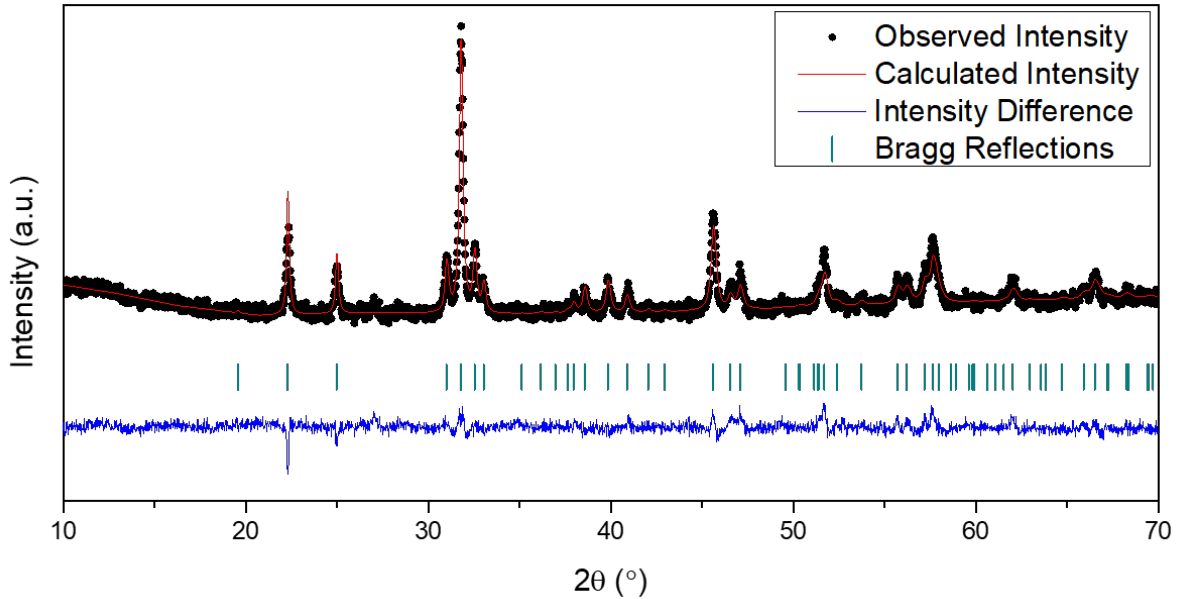


Figure 4.5. Rietveld refinement plot of the PXRD data for  $\text{GdScO}_3$  grown in hydro-sauna conditions at 300 °C. Black dots indicate observed data, the red line indicates the calculated pattern, the blue line is the difference between the observed and calculated intensities, and the dark green bars indicate the allowed Bragg reflections for  $\text{GdScO}_3$ .

by the crystallite size and not strain. As the temperature increased, the particle size increased pass the measurement limit of 100 nm for Scherrer analysis, with particles roughly 100 nm in dimension at 350 °C and up to several hundreds of nanometers by a reaction temperature of 450 °C. In addition, higher temperatures allowed for faster diffusion for the particles to adopt a Wulff shape.<sup>57</sup> Faceting is observed starting at 400 °C. The formation of cuboidal particles at 450 °C implies that the  $\{110\}$  and  $\{001\}$  facets of the orthorhombic perovskite phase, or equivalently the  $\{001\}$  facets of the pseudo-cubic unit cell, either have the lowest surface energies or have the slowest growth rate normal to them.

Table 4.1. Rietveld refined cell parameters for  $\text{GdScO}_3$  produced in hydro-sauna conditions at 300 °C compared to that of  $\text{GdScO}_3$  produced via high-temperature solid-state reactions<sup>53</sup> and the Czochralski technique.<sup>66</sup> Note that the single crystal data was originally presented for the  $Pnma$  space group so the data was transformed to the equivalent  $Pbnm$  space group here for comparison.

Synthesis Method	Hydro-sauna at 300 °C	High temperature solid-state reaction (PDF 01-074-4353) <sup>53</sup>	Czochralski technique (single crystal) <sup>66</sup>
$a$ (Å)	5.4864(8)	5.4862(1)	5.481(1)
$b$ (Å)	5.7505(9)	5.7499(1)	5.745(1)
$c$ (Å)	7.934(13)	7.9345(1)	7.929(2)
$V$ (Å <sup>3</sup> )	250.33(9)	250.299(5)	249.8(1)
$\text{Gd}^{3+} : x$	0.013(2)	0.0163(2)	0.01631(6)
$y$	0.9403(1)	0.9406(2)	0.9407(5)
$z$	0.25000	0.25000	0.25000
$\text{Sc}^{3+} : x$	0	0	0
$y$	0.50000	0.50000	0.50000
$z$	0	0	0
$\text{O}^{2-}(1) : x$	0.888(7)	0.8817(17)	0.8791(8)
$y$	0.535(7)	0.5535(18)	0.5501(7)
$z$	0.25000	0.25000	0.25000
$\text{O}^{2-}(2) : x$	0.699(7)	0.6931(13)	0.6912(5)
$y$	0.290(7)	0.3007(14)	0.3052(5)
$z$	0.953(5)	0.9444(10)	0.9372(4)
No. of free parameters	27	46-67	30
Goodness-of-fit	1.31	1.39	1.138
$R_p, R_{wp}, R_{exp}$	2.8, 3.64, 2.74	3.81, 12.11, 8.72	Not provided

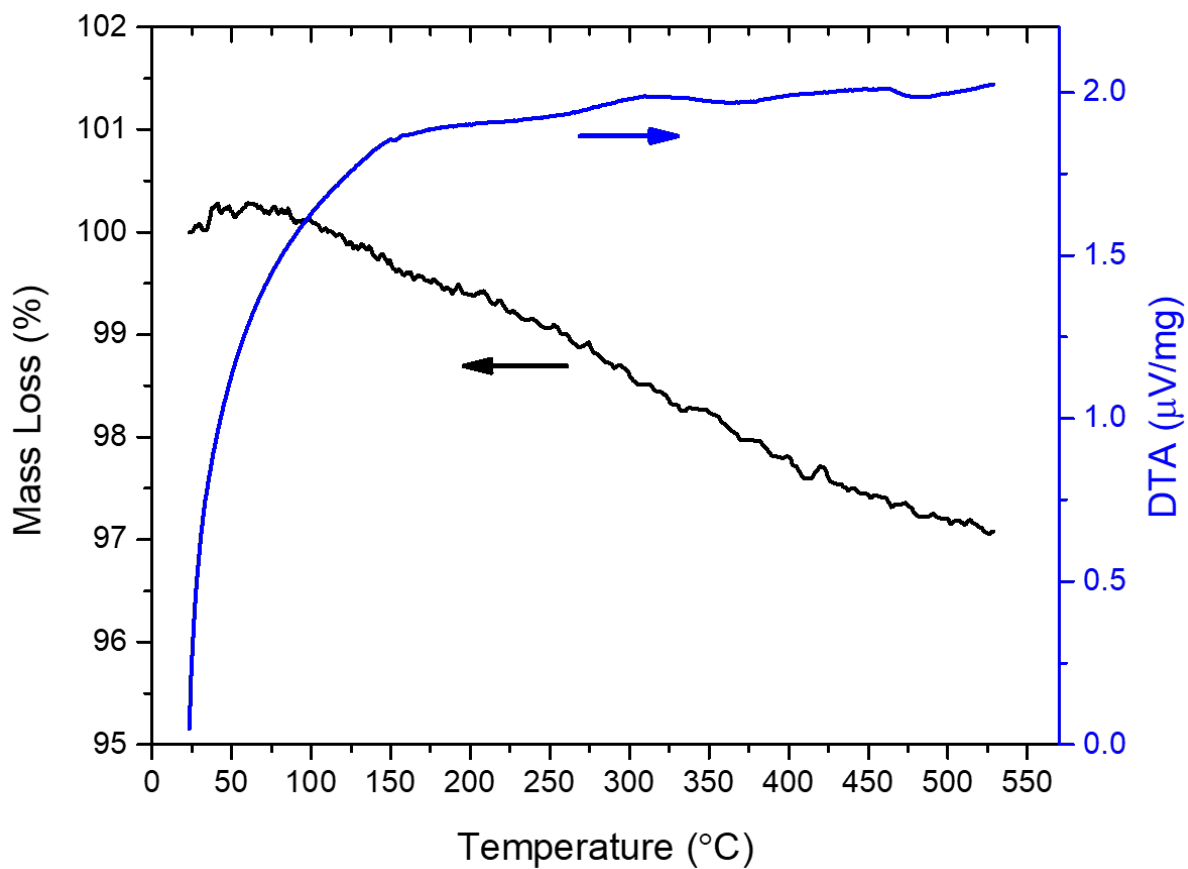


Figure 4.6. Simultaneous TGA (black) and DTA (blue) curves of GdScO<sub>3</sub> grown at 300 °C under hydro-sauna conditions. The constant change in heat and small mass loss suggest the release of water adsorbed on the surface and that hydroxide groups in the material are minimal.

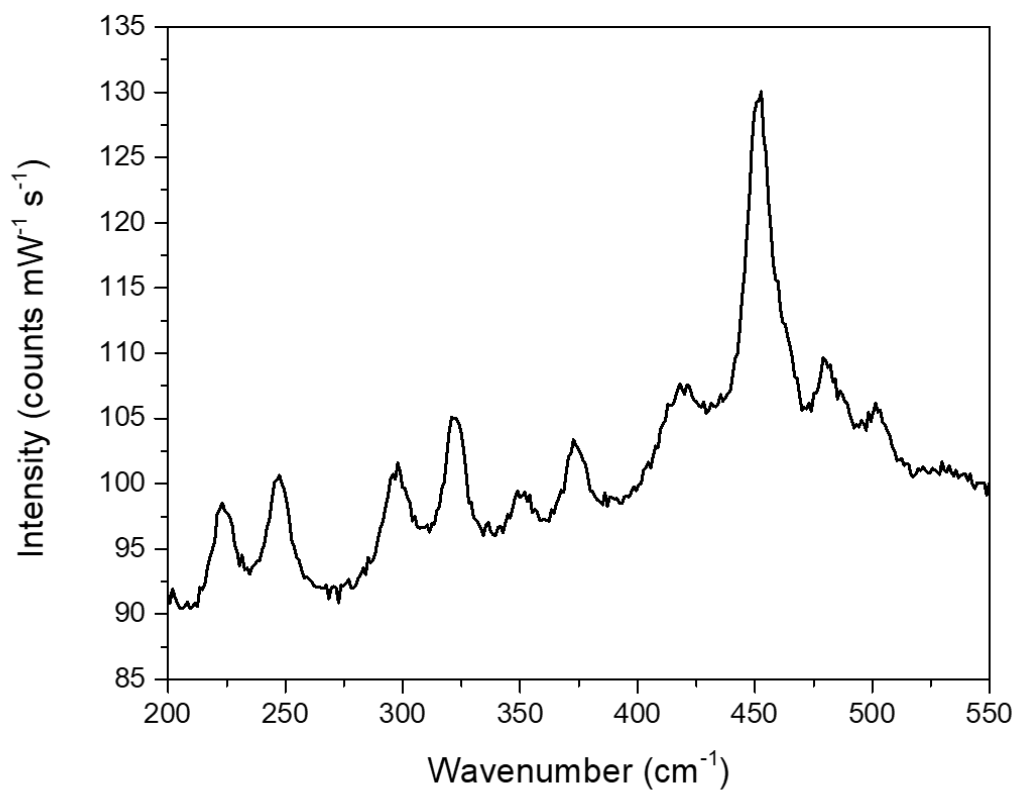


Figure 4.7. Raman spectrum of GdScO<sub>3</sub> grown at 300 °C under hydro-sauna conditions. The 11 peaks are produced due to A<sub>g</sub> modes at 248, 321, 418, 452, and 501 cm<sup>-1</sup>, B<sub>1g</sub> modes at 223, 373, and 490 cm<sup>-1</sup>, B<sub>2g</sub> modes at 298, 351, 463, and 532 cm<sup>-1</sup>, and B<sub>3g</sub> modes at 300, 450, and 481 cm<sup>-1</sup>.

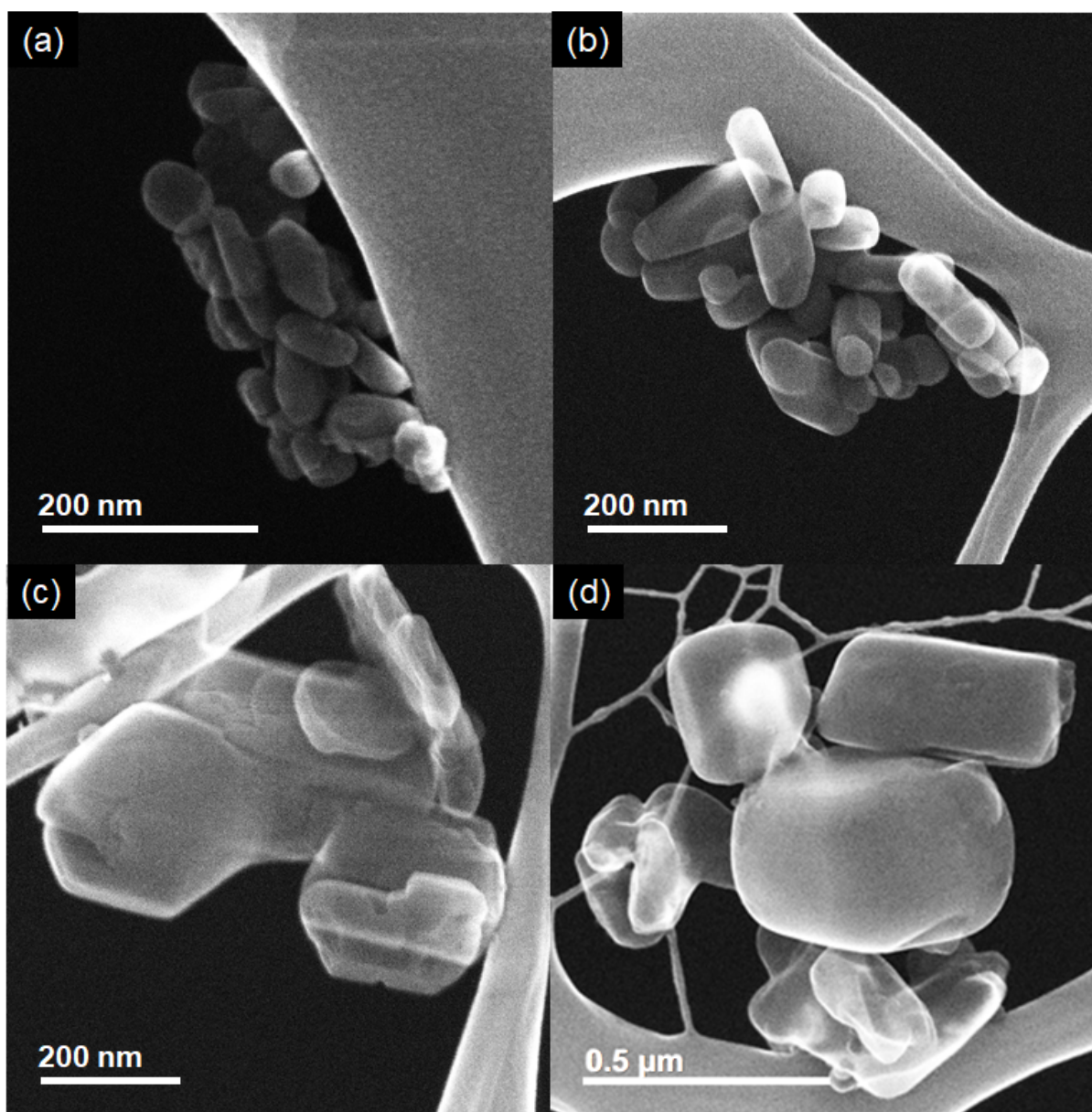


Figure 4.8. Secondary electron images for the products obtained after heating the gel in an autoclave at (a) 300 °C, (b) 350 °C, (c) 400 °C, and (d) 450 °C.

#### 4.5. Conclusion

A mixed cation hydroxide gel with water encapsulated within the gel matrix was produced. High surface area particles of  $\text{GdScO}_3$  were synthesized at low temperatures through the decomposition of this gel in a humid environment. Heating the hydrogel in a dry environment only formed an amorphous product owing to the collapse of the open matrix of the gel precursor. Increased water vapor pressure in the system promoted the formation of (oxy)hydroxide phases, namely  $\text{Gd}(\text{OH})_3$  and  $\alpha\text{-ScOOH}$ ; as the water vapor pressure increases with the amount of hydrogel in the autoclave, only a limited amount of material may be produced.  $\text{GdScO}_3$  was produced with intermediate water vapor pressures at temperatures as low as 300 °C. Higher temperatures increased the diffusion and reaction rates, which favored the formation of larger particles that better adopted a Wulff shape. This method is generalizable to the other lanthanide scandates, and should be to other complex oxide materials as well, as an alternative low temperature synthetic route to producing high surface area materials.

## CHAPTER 5

## Controlled Two-Step Formation of Faceted Perovskite Rare-Earth Scandate Nanoparticles

With the hydro-sauna method, it is possible to synthesize the various  $\text{LnScO}_3$  particles. In the previous chapter however, there were limitations in how much material could be produced at a time (roughly 100 mg) and the process did not produce faceted particles. This chapter goes into how creating a humid environment in a tube furnace rather than an autoclave allows for a greater yield of material, and how using a two-temperature heat treatment can create better faceted particles. This procedure will be used to prepare the  $\text{LnScO}_3$  supports throughout the remainder of this thesis.

The work in this chapter was done in collaboration with Tiffany Ly and Zachary Mansley. Much of this chapter formed the article "Controlled Two-Step Formation of Faceted Perovskite Rare-Earth Scandate Nanoparticles",<sup>67</sup> from which many of these figures are reproduced.

### 5.1. Introduction

Nanoparticles are used in an impressive number of applications, such as heterogeneous catalysis,<sup>68</sup> plasmonics,<sup>69</sup> cosmetics,<sup>70</sup> reinforcing agents in advanced metals,<sup>71</sup> and drug delivery,<sup>72</sup> to name only a few. Nanomaterials containing lanthanide elements have particular functionality in biomedical applications and luminescence because of their low toxicity, chemical stability, and unique f-electrons.<sup>73,74</sup> The size of a particle can affect its

electronic properties,<sup>75,76</sup> optical properties,<sup>77,78</sup> and coupled phenomena such as ferroelectricity.<sup>79,80</sup> In some cases, the size may also alter which phase is formed, which can change the properties altogether.<sup>81</sup> Nanoparticle surfaces play an important role in dictating the overall properties with decreasing size. Different surfaces exhibit different adsorption behavior, which in turn affects the ability of a material to catalyze reactions,<sup>82-84</sup> to act as a gas sensor,<sup>85-87</sup> or to be functionalized with various molecules.<sup>88,89</sup> The shape of a particle also plays a role in tuning material properties such as ferromagnetism<sup>90-92</sup> or cellular internalization.<sup>93</sup> Therefore, it is the combination of nanoparticle composition, size, surfaces, and shape that ultimately defines their properties.

A notorious issue with producing nanoparticles is reproducibly controlling their shape and size. There are two ways one can handle this issue scientifically. The first is to deal with producing the material as a nucleation and growth problem. In the thermodynamic limit, what should be produced is the thermodynamic Wulff shape.<sup>94-96</sup> With step-flow growth in the kinetic limit, the kinetic Wulff shape should be produced.<sup>97,98</sup> Other cases, such as when diffusion in the fluid during growth is rate-limited,<sup>99-101</sup> are also well established. With estimates or measurements of terms such as activation energy barriers, one can predict how to control the particle shape and size. However, in many cases, particularly for solution-based growth, the product is often more empirical, and a second approach is used; one iteratively varies parameters with some informed knowledge to produce the desired shape. In the contemporary literature, this has led to approaches that frequently work, but success is not guaranteed. There are advantages to approaching the problem as one of nucleation and growth instead. In a recent analysis of the growth of  $\text{KTaO}_3$  nanoparticles,<sup>102</sup> it was determined that the growth process could be subdivided

into two regimes, one with a high chemical potential difference where terrace nucleation and rough-stepped surfaces dominated, and one with a lower chemical potential difference where step-flow growth annihilated steps to smooth surfaces. This analysis leads to predictions regarding which parameters need to be varied to control the nucleation and growth processes, ultimately tuning the conditions to produce particles with specific shapes or sizes.

Our target materials here are the lanthanide scandates ( $\text{LnScO}_3$ ), which can adopt a wide range of lattice parameters by varying the lanthanide used.<sup>49</sup> Only the larger lanthanides ( $\text{Ln} = \text{La-Dy}$ ) form in the perovskite phase with scandium, whereas the bixbyite structure is formed with the smaller lanthanides ( $\text{Ln} = \text{Y, Ho-Lu}$ ).<sup>103-105</sup>  $\text{LuScO}_3$ , for example, has only formed the perovskite phase when epitaxially stabilized on a  $\text{NdGaO}_3$  or  $\text{DyScO}_3$  substrate.<sup>106</sup> As these materials have mostly been used as dielectrics,<sup>48</sup> substrates,<sup>49</sup> and recently, flexoelectrics,<sup>107</sup> they have often been prepared as thin films by atomic layer deposition<sup>50</sup> or pulsed laser deposition,<sup>51,52</sup> or as single crystals using the Czochralski technique.<sup>49</sup> Using these materials in applications that require high surface area powders, such as heterogeneous catalysis<sup>108</sup> or gas capture<sup>109</sup> and separation,<sup>110</sup> requires a different approach. Unfortunately, there are currently no reports of any solvothermal synthesis of  $\text{LnScO}_3$ , likely owing to the negligible solubilities of the basic large rare-earth oxides in the alkaline conditions typically used to produce oxide nanoparticles.<sup>55</sup>

I reported in my last chapter (Chapter 4) that high surface area  $\text{GdScO}_3$  particles could be produced at 300 °C through the decomposition of a mixed-cation hydroxide hydrogel in a humid environment within a sealed autoclave,<sup>47</sup> but it was not able to produce particles with a controlled size, surface structure, or morphology. The intention of this chapter is to

provide specific information on a two-step approach where we have successfully exploited nucleation and growth to produce well-faceted particles of lanthanide scandates by first using a higher temperature in a furnace with better control of the humidity to nucleate the relevant oxide, then a lower temperature to control step-flow growth to smooth the surface. We suggest that this is a route towards consistent and reproducible production of shape-controlled nanoparticles that we argue is quite general.

## 5.2. Experimental Section

Faceted  $\text{LnScO}_3$  nanoparticles were produced as follows. First, a rare-earth nitrate precursor was prepared by dissolving 4 mmol of  $\text{Ln}_2\text{O}_3$  ( $\text{Ln} = \text{La}, \text{Nd}, \text{Sm}, \text{Gd}$ ) and  $\text{Sc}_2\text{O}_3$  in 20 mL of 15.8 N nitric acid maintained at 80 °C until the liquid evaporated. The nitrate precursor was then dissolved in 20 mL of deionized water and added dropwise to 50 mL of 10 M NaOH to precipitate a gel. This gel was cleaned several times by rinsing with deionized water and centrifuged before being transferred to an alumina boat and then to a tube furnace. Argon gas was flowed through a bubbler filled with deionized water placed upstream to create a humid growth environment. The water vapor pressure after the bubbler was estimated to be 23.4 mbar, assuming complete saturation of the Ar flow at room temperature. For completeness, we note that compared to prior work in autoclaves, the chemical potential of the water vapor was better controlled because the amount of water in the closed autoclave was a function of how much hydrogel was used, whereas using the bubbler and tube furnace provided less humidity and was independent of the amount of material. The gel was either subjected to a one-step heat treatment at a temperature between 200 and 450 °C for 2 days to determine the optimum reaction conditions, or a two-step heat treatment with a high-temperature step at 450 °C for 2 days

followed by a low-temperature step at 300 °C for 1 day, to produce faceted nanoparticles. Based upon the results of the one-step heat treatments, these temperatures were identified as appropriate for nucleation (450 °C) and surface smoothing (300 °C), respectively. The final products were rinsed with deionized water and centrifuged several times, then put into an oven at 80 °C to dry overnight.

Powder X-ray diffraction (PXRD) was performed on a Rigaku Ultima diffractometer (Rigaku Corporation, Tokyo, Japan) using a Cu K $\alpha$  source operated at 40 kV and 44 mA. Secondary electron (SE) imaging was performed on a Hitachi HD-2300 (Hitachi, Ltd., Tokyo, Japan) scanning transmission electron microscope operated at 200 kV. For completeness, we note that the SE images did not show the surfaces of these materials as clearly as with other oxides, owing to the long mean-free path of the low-energy secondary electrons and the near co-incidence of the vacuum level and band gap as discussed elsewhere.<sup>107</sup> High-resolution electron microscopy (HREM) was performed on a JEOL ARM300F GrandARM S/TEM (JEOL, Ltd., Tokyo, Japan) operated at 300 kV.

### 5.3. Results

Figure 5.1 shows PXRD patterns of the GdScO<sub>3</sub> nanoparticles produced using a single temperature between 200 and 450 °C for 2 days in a humid environment. At 200 °C, only Gd(OH)<sub>3</sub> was formed. At 250 and 300 °C, GdScO<sub>3</sub> was the primary phase, but GdOOH was also present. At higher temperatures, the product was nearly entirely GdScO<sub>3</sub>, with a minimal amount of Gd<sub>2</sub>O<sub>3</sub> present as a secondary phase. The dehydration of the secondary phase with increasing temperature is consistent with observations described in Chapter 3. The morphology of GdScO<sub>3</sub> particles produced at different temperatures was studied using SE imaging (Figure 5.2). The lower temperature conditions yielded

large particles with evident faceting. In contrast, at higher temperatures, the perovskite particles were smaller in size and had less-defined faceting. Scherrer analysis of the X-ray diffraction patterns indicated that the average particle size decreased with increasing reaction temperature; average particle sizes of 93.4(7) nm, 58.5(4) nm, and 51.0(4) nm were calculated for particles produced at 350, 400, and 450 °C, respectively.

A two-step heat treatment (450 °C for 2 days, followed by 300 °C for 1 day) was performed for several LnScO<sub>3</sub> (Ln = La, Nd, Sm, Gd). Only the larger Ln elements were investigated, because only they react to form the perovskite phase. In fact, an attempt to make LuScO<sub>3</sub> only produced a solid solution in the bixbyite structure, as expected.<sup>103-105</sup> PXRD patterns of the LnScO<sub>3</sub> (Ln = La, Nd, Sm, Gd) (Figure 5.3) confirmed that perovskite LnScO<sub>3</sub> was the primary phase, with minimal amounts of Ln(OH)<sub>3</sub> and/or Ln<sub>2</sub>O<sub>3</sub> as secondary phases. The perovskite particles were faceted as shown in the SE images of Figure 5.4; an example HREM image and corresponding power spectrum of a NdScO<sub>3</sub> particle in Figure 5.5 show that the particles were primarily pseudo-cubic {100}- and {110}-terminated.

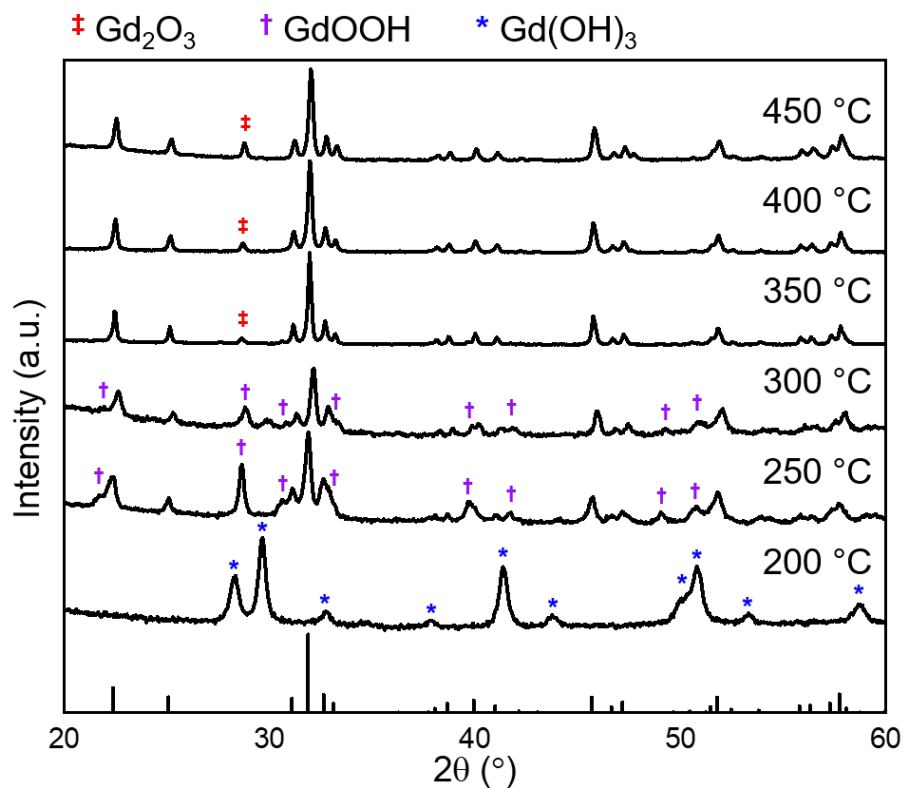


Figure 5.1. PXRD patterns of the products obtained from the hydro-sauna synthesis attempts of  $\text{GdScO}_3$  at temperatures between 200 °C and 450 °C for 2 days. The calculated pattern for  $\text{GdScO}_3$  is plotted on the bottom.  $\text{Gd(OH)}_3$  (blue \*) was the only crystalline product formed at 200 °C, implying that  $\Delta G_{\text{rxn}}$ , as defined in the text, is positive. Between 250 °C and 300 °C, both  $\text{GdScO}_3$  and  $\text{GdOOH}$  (purple †) are formed, suggesting  $\Delta G_{\text{rxn}}$  is negative but small. Above 300 °C,  $\text{GdScO}_3$  is the primary phase, with only a small amount of  $\text{Gd}_2\text{O}_3$  (red ‡) as a secondary phase, so  $\Delta G_{\text{rxn}}$  is negative and large.

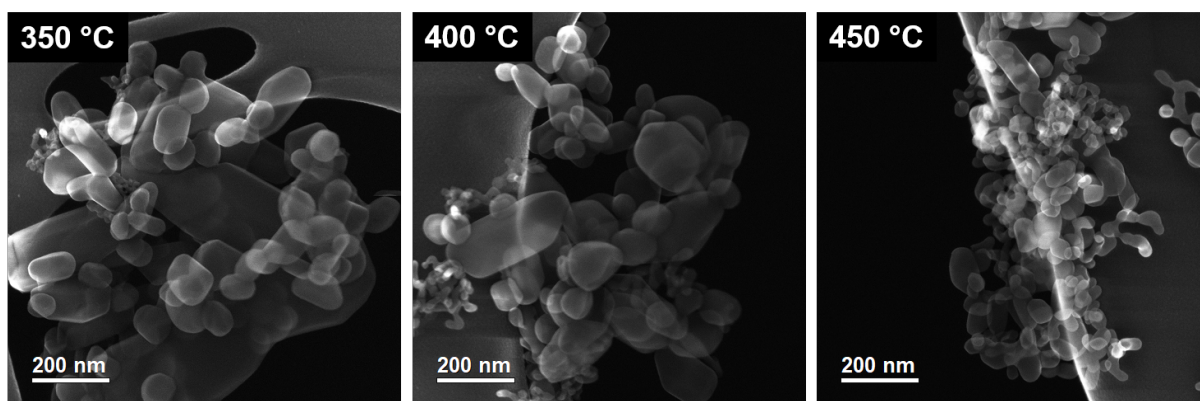


Figure 5.2. SE images of GdScO<sub>3</sub> synthesized at 350 °C, 400 °C, and 450 °C. GdScO<sub>3</sub> grown at lower temperatures had a less negative  $\Delta G_{\text{rxn}}$  and consequently had more faceting and were larger than particles grown at higher temperatures. Note that SE images do not show the surfaces of GdScO<sub>3</sub> as clearly as with other oxides, as discussed in the text.

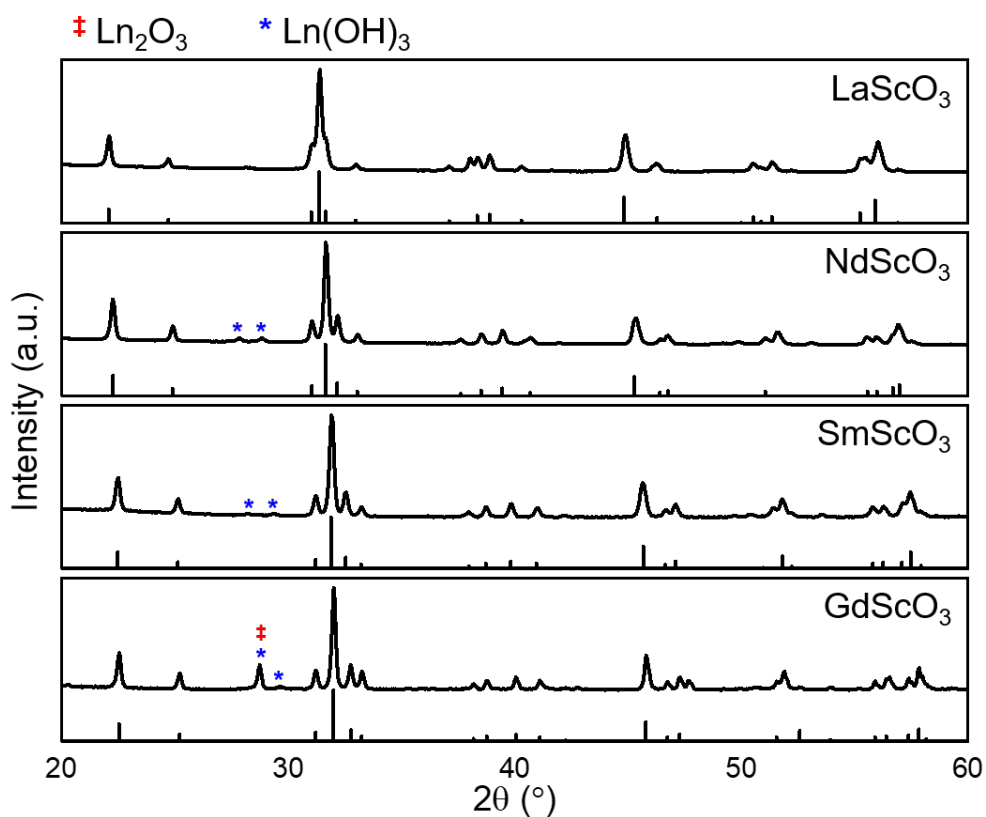


Figure 5.3. PXRD patterns of the products obtained from the hydro-sauna syntheses of LnScO<sub>3</sub> (Ln = La, Nd, Sm, Gd) using the two-temperature treatment at 450 °C for 2 days and then 300 °C for 1 day. The calculated patterns for the corresponding LnScO<sub>3</sub> are plotted below. The perovskite phase was the primary product, with trace Ln(OH)<sub>3</sub> (blue \*) or Ln<sub>2</sub>O<sub>3</sub> (red ‡) as secondary products.

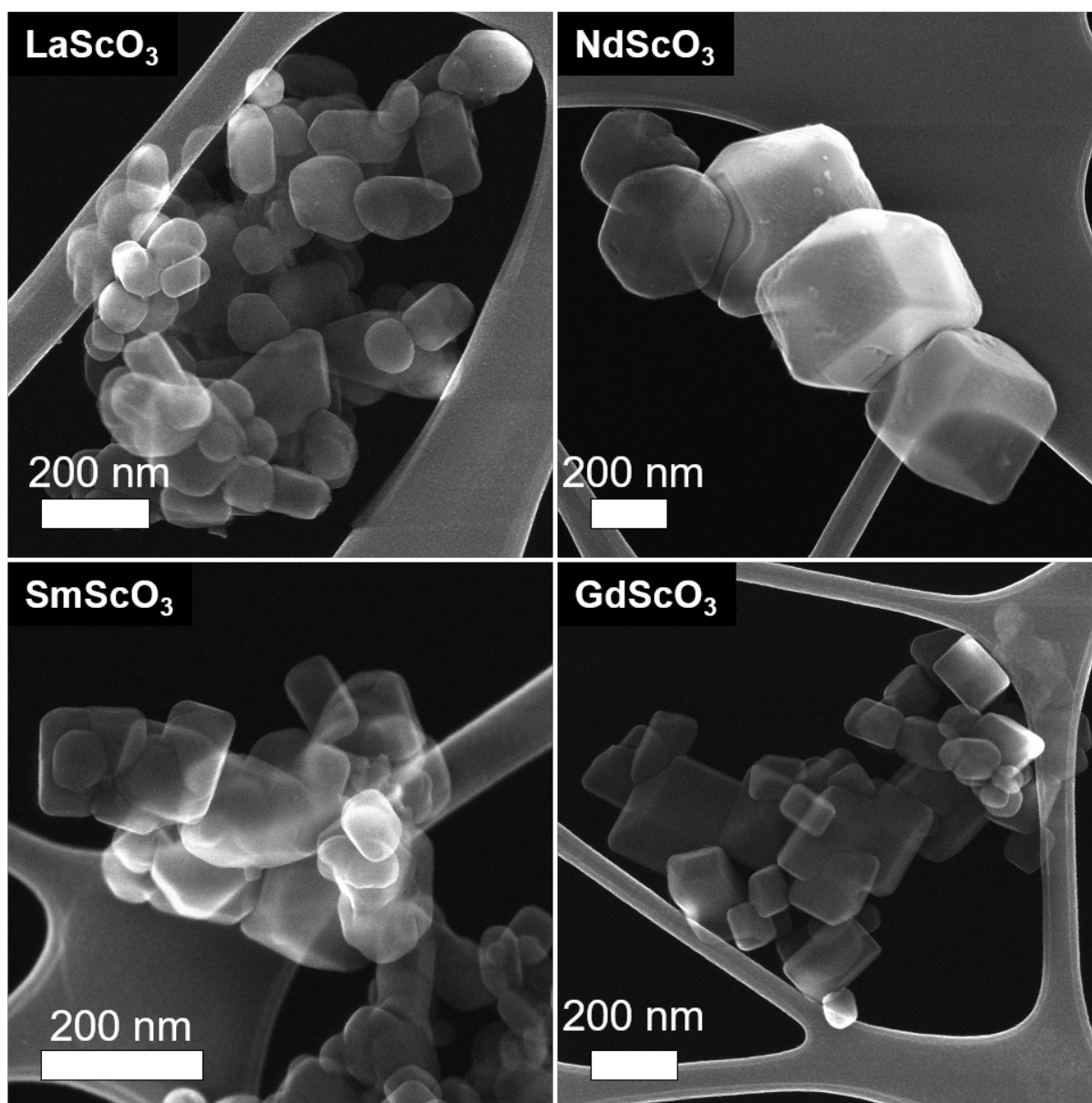


Figure 5.4. SE images of LnScO<sub>3</sub> (Ln = La, Nd, Sm, Gd) synthesized using the two-temperature treatment at 450 °C for 2 days and then 300 °C for 1 day. Smaller particles were produced because the high temperature step had a more negative  $\Delta G_{\text{rxn}}$  which led to a higher nucleation rate. The particles are better faceted because the low temperature step had a less negative  $\Delta G_{\text{rxn}}$  so terrace growth dominated. Note that SE images do not show the surfaces of LnScO<sub>3</sub> as clearly as with other oxides, as discussed in the text.

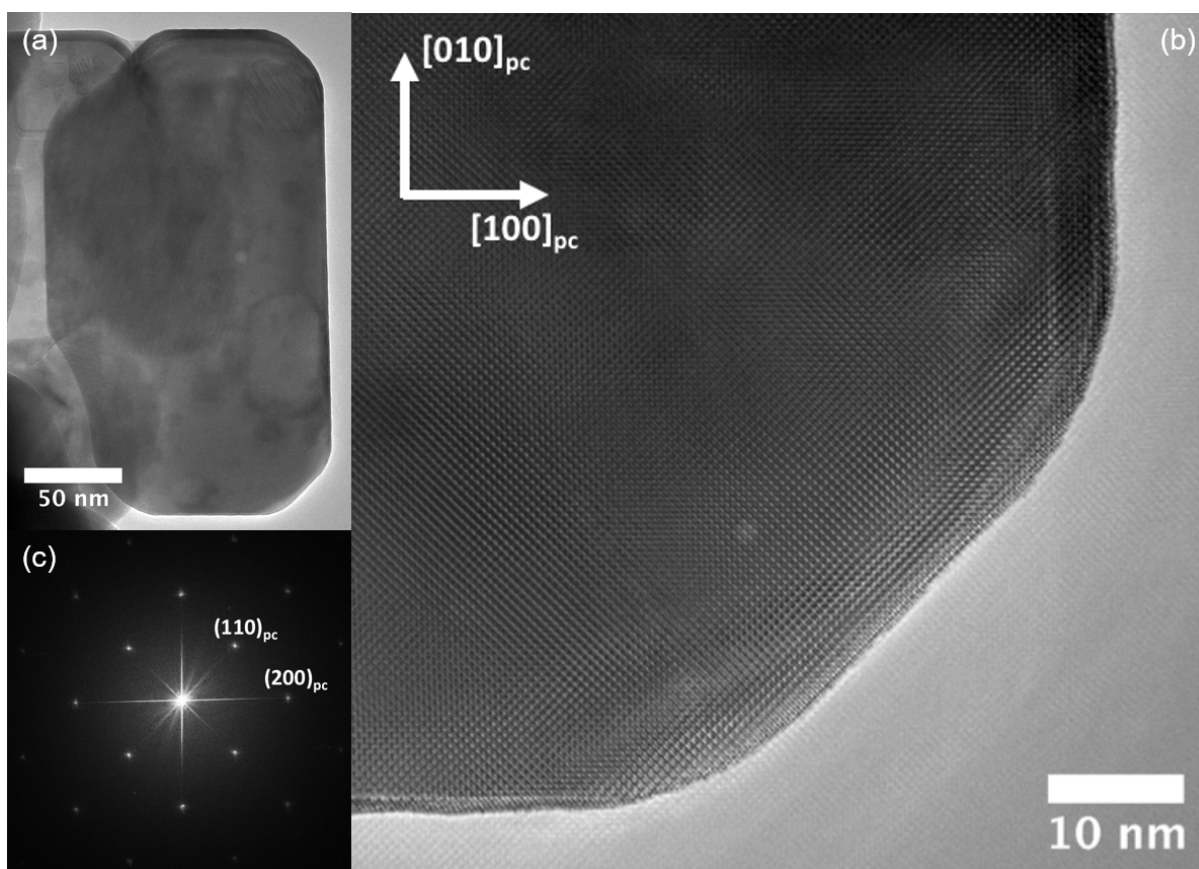
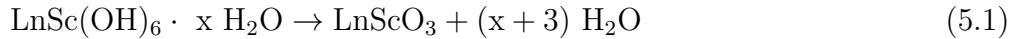


Figure 5.5. (a) HREM image of a faceted  $\text{NdScO}_3$  particle synthesized using the two-temperature treatment at 450 °C for 2 days and then 300 °C for 1 day. (b) HREM image of the lower-right corner of the nanoparticle. (c) Corresponding FFT of the entire particle indexed to show that it is terminated with the pseudo-cubic  $\{100\}$  and  $\{110\}$  surfaces.

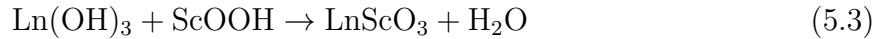
## 5.4. Discussion

The results illustrate an approach where higher temperatures are exploited for nucleation, and lower temperatures for growing well-faceted nanoparticles. We will begin by discussing the reaction from the rare-earth hydroxide hydrogel to the perovskite  $\text{LnScO}_3$ , then the approach to size and shape control.

Our previous report<sup>47</sup> on the formation of crystalline  $\text{GdScO}_3$  from a mixed-cation hydroxide hydrogel in a water vapor-assisted reaction<sup>111</sup> noted the role that the humid conditions played in both preserving an open gel matrix and providing the necessary diffusion for the reactions that produced the perovskite, as insufficient diffusion instead produced an amorphous xerogel. Based on the observed products, there were two competing reactions at play:



Reaction 5.1 accounts for the formation of our desired products (the perovskite phase and water), whereas reaction 5.2 produces undesired phases which may be in the form of rare-earth oxides, hydroxides, or oxide hydroxides. Equivalently, this competition can be represented by the following reaction:



In reaction 5.3, the non-standard state Gibbs free energy change of reaction ( $\Delta G_{\text{rxn}}$ ) is the difference between the non-standard state Gibbs free energy change of reaction of the

desired products (the perovskite phase and water) versus that of the possible undesired products (rare-earth oxides, hydroxides, or oxide hydroxides). When  $\Delta G_{\text{rxn}}$  is negative, the perovskite phase and water will form; when positive, the rare-earth oxides, hydroxides, or oxide hydroxides. Increasing the amount of water will increase  $\Delta G_{\text{rxn}}$  and lead to the formation of the rare-earth hydroxides. In the previous chapter, the gel was heated in a sealed autoclave, where increases in temperature also increased the pressure. However, temperature and pressure affect the chemical potential of the water vapor in opposite ways—higher temperatures decrease the chemical potential, whereas higher pressures increase the chemical potential, with the former having a greater effect—which confounds good experimental control. Under such conditions, the increasing temperature increases the vapor pressure of the water, and while the increase in temperature decreases the chemical potential of the water because of the greater entropic contribution of the water vapor, the increase in pressure increases the chemical potential because of the greater work done by the water vapor. In this chapter, the pressure does not change, so the consequences of increasing the temperature are much more predictable.

PXRD studies (Figure 5.1) of the products at various temperatures provided insight into the  $\Delta G_{\text{rxn}}$  of forming  $\text{GdScO}_3$  from the mixed cation hydroxide gel. Below 250 °C,  $\Delta G_{\text{rxn}}$  was positive so  $\text{GdScO}_3$  was not formed. Between 250 and 300 °C,  $\text{GdScO}_3$  began to form, suggesting that  $\Delta G_{\text{rxn}}$  was negative but close to zero in this temperature range. With increasing temperature,  $\Delta G_{\text{rxn}}$  became increasingly more negative, which increased the driving force to forming  $\text{GdScO}_3$ . We note that the identity of the non-perovskite phase changed as a function of temperature. At 200 °C, when no perovskite was produced, the phase that was formed was  $\text{Gd}(\text{OH})_3$ . Between 250 and 300 °C, where the perovskite

phase began forming, the other phase was GdOOH rather than Gd(OH)<sub>3</sub>. At higher temperatures still, the secondary phase was Gd<sub>2</sub>O<sub>3</sub>. This increased dehydration from Gd(OH)<sub>3</sub> to GdOOH to Gd<sub>2</sub>O<sub>3</sub> was expected with increasing temperature because of the substantial entropy of gaseous H<sub>2</sub>O. The fact that the onset of forming the perovskite phase correlated with the onset of GdOOH may imply that the dehydration from Gd(OH)<sub>3</sub> to GdOOH was a necessary step for subsequent reaction into GdScO<sub>3</sub>.<sup>112,113</sup> We note that the ancillary evidence supports the hypothesis that the formation of LnOOH is a necessary step for the hydrothermal synthesis of LnMnO<sub>3</sub>.<sup>41</sup> However, the formation of LnOOH was not observed with LaScO<sub>3</sub>, NdScO<sub>3</sub>, and SmScO<sub>3</sub>, where Ln(OH)<sub>3</sub> was the only other identified secondary phase. The possibility of LnOOH rehydrating into Ln(OH)<sub>3</sub> upon cooling could not be discounted, and requires in situ experiments to investigate further.

Turning to the particle shape, in addition to the phase, the dominant nucleation and growth mechanisms also evolved with changes in  $\Delta G_{\text{rxn}}$ . The three key components are (1) particle nucleation, where a small particle is nucleated from the gel, (2) terrace nucleation, where new terraces are nucleated atop existing terraces, and (3) terrace growth, where existing terraces on the particle surface grow laterally until they reach the edge of the particle and are annihilated, leading to smooth facets. While all three mechanisms occur, it is the mechanism with the highest rate that will dominate and determine the final shape and size. When  $\Delta G_{\text{rxn}}$  is positive, the desired reaction to produce the perovskite does not occur. When  $\Delta G_{\text{rxn}}$  is negative but small, the reaction occurs with a relatively small driving force and growth processes owing to heterogeneous nucleation, such as terrace nucleation and terrace growth, are favored so large particles with smooth

surfaces are formed. With an increasingly negative  $\Delta G_{\text{rxn}}$ , the driving force of the reaction increases such that processes due to homogeneous nucleation can occur more readily, which leads to a high particle nucleation rate and consequently small particles. Between the two growth mechanisms, terrace nucleation has a higher rate than terrace growth, so the particle surfaces are rougher. These understandings agree well with the particle size and morphology observed through the SE imaging (Figure 5.2) of  $\text{GdScO}_3$  produced at various temperatures. At lower temperatures, where  $\Delta G_{\text{rxn}}$  was small and negative, terrace nucleation and growth dominated, which led to the formation of larger particles with smoother facets. With increasing temperature,  $\Delta G_{\text{rxn}}$  became increasingly more negative, such that particle nucleation dominated and produced more particles that were smaller and had less well-defined surfaces and morphology. Scherrer analysis of the X-ray diffraction patterns indicated that the average particle size decreased with increasing reaction temperature, as predicted. At the lower temperatures, nucleation of the lanthanide scandates can proceed over an extended time, which will lead to a distribution of sizes; the small  $\text{GdScO}_3$  particulates also observed in Figure 5.2 reflect this.

Two different sequential reaction conditions are necessary for better-faceted and smaller nanoparticles: a step with a large negative  $\Delta G_{\text{rxn}}$  to promote the reaction to the desired product and nucleate many small but rough particles with high surface area, followed by a step with a small negative  $\Delta G_{\text{rxn}}$  to promote terrace growth that smooths the surfaces leading to well-defined facets. For this particular reaction, meeting these conditions involved a high-temperature nucleation step followed by a low-temperature smoothing step. Temperatures of 450 and 300 °C were chosen for nucleation and smoothing, based on the one-step heat treatment results. SE imaging of  $\text{LnScO}_3$  ( $\text{Ln} = \text{La}, \text{Nd}, \text{Sm}, \text{Gd}$ ) particles

(Figure 5.4) confirmed that these conditions lead to smaller and better faceted particles, as the  $\text{GdScO}_3$  particles produced with the two-step heat treatment (Figure 5.4) were more faceted than those produced with only a single nucleation step (Figure 5.2). Increasing the nucleation temperature further would likely increase the nucleation rate and reduce particle size.<sup>102</sup> In addition, the small particulates found in the one-step samples were no longer present in the two-step heat treatment. This follows expectations; at the lower temperature of the second step, homogeneous nucleation of new particles will be suppressed, while growth via (slow) nucleation of new terraces on existing particles and (faster) step-flow growth will dominate.  $\text{NdScO}_3$ ,  $\text{SmScO}_3$ , and  $\text{GdScO}_3$  formed particles that were cuboidal in shape, terminated by pseudo-cubic  $\{001\}$  surfaces, with edges truncated by the pseudo-cubic  $\{110\}$  surfaces. Evidence for this can be found in the HREM image and corresponding power spectrum of an  $\text{NdScO}_3$  particle in Figure 5.5. Further analysis of the  $\text{LnScO}_3$  surface structures is ongoing.  $\text{LaScO}_3$  appeared to be less faceted, a difference that may suggest the temperature for terrace growth is lower for  $\text{LaScO}_3$  than for the other  $\text{LnScO}_3$ . We hypothesize that a higher yield of particles with strong faceting can be achieved by optimizing the temperature and duration of the nucleation and smoothing steps for each material.

## 5.5. Conclusion

A method for producing faceted  $\text{LnScO}_3$  nanoparticles based upon a two-step process is described. Higher temperatures are used in the first step to nucleate particles and lower temperatures in the second step to promote surface smoothing. This approach—exploiting the nucleation and growth mechanisms—is not unique to this system, and

can be utilized to inform reaction conditions and thereby tailor morphology and surface structure in general.

## CHAPTER 6

**Lanthanide Scandate Formation Energies**

Last chapter, it was stressed that, in order to develop faceted nanoparticles, it is necessary for the Gibbs free energy difference of the reaction to be small and negative at those conditions. In lieu of time-consuming syntheses and characterization to figure out what reaction conditions are necessary, computational methods may be used to better gauge what reaction conditions are appropriate. When synthesizing the RE<sub>2</sub>ScO<sub>7</sub> nanoparticle supports, a temperature of 300 °C was chosen because PXRD of GdScO<sub>3</sub> suggested that  $\Delta G_{\text{rxn}}$  was small and negative at that temperature. As a result, the two-temperature heat treatment successfully produced well-faceted nanocuboids of GdScO<sub>3</sub>. Likewise, NdScO<sub>3</sub> and SmScO<sub>3</sub> were also well-faceted. However, LaScO<sub>3</sub> was less faceted. One possibility that we feel is unlikely is that the surface energies of the pseudo-cubic LaScO<sub>3</sub> {100} facets were not as low compared to the other possible surfaces so no one family of surfaces dominated. More likely was that the synthesis of LaScO<sub>3</sub> was done under conditions in which  $\Delta G_{\text{rxn}}$  was not small so surface smoothing never occurred. In order to better prove this, density functional theory was performed to investigate how the enthalpy of formations of the various RE<sub>2</sub>ScO<sub>7</sub> changed as a function of RE. If the enthalpy of formation of LaScO<sub>3</sub> is sufficiently more negative than that of the other RE<sub>2</sub>ScO<sub>7</sub> then the necessary temperature for the smoothing of LaScO<sub>3</sub> would need to be lower.

In this work, we found that in these compounds, the RE<sup>3+</sup> cations can be subject to relatively significant crystal field splitting, on the order of several hundreds of meV.<sup>114</sup>

$\text{RE}^{3+}$  ions have six nearest neighbors and sit in a (pseudo) trigonal prismatic environment. Since there are seven  $f$ -orbitals that an electron can choose from, there are seven different eigenstates that that electron may adopt which may have different energies. We found that the lowest energy eigenstates were through the axis of the trigonal prism or within the plane. Calculations with every possible combination of eigenstates were performed to confirm that the lowest energy configuration had been reached.

A special thanks to Chris Mizzi, Tiffany Ly, and Laurence Marks for all of their help in learning and running DFT calculations, and countless questions about WIEN2k and troubleshooting thereof.

## 6.1. Introduction

While crystal field splitting is observed in the actinides, it is often considered to be negligible for the lanthanides owing to their more shielded orbitals.<sup>115</sup> However, in the case of many distorted lanthanide perovskites, the significant rotations of the rigid octahedra disrupt the more spherical symmetry found in cubic perovskites such that six of the twelve oxygen anions are close enough to the lanthanide to produce crystal field splitting. As a means to investigate how each orbital responds, density functional theory was performed on the lanthanide scandates. Different eigenstates were selectively occupied to see the effect on the resulting energy of the structure, which informed to which eigenstates are greater in energy as a result of the crystal field splitting.

## 6.2. Density Functional Theory

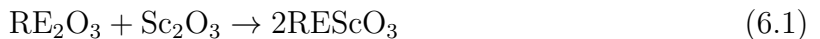
Density functional theory (DFT) is a computational method based in quantum mechanics. In quantum mechanics, one can know everything about the system if the wavefunction is solved through the Schrödinger equation. However, solving the wavefunction exactly is only possible for very specific systems, such as the popular “particle in a box” or for a single hydrogen atom. However, even cases as “simple” as a helium atom or an H<sub>2</sub> molecule do not have analytic solutions. Part of the problem is the difficulty in solving for the potential associated with electron-electron interactions.

Instead, Kohn-Sham DFT considers a system of non-interacting electrons in an effective potential that produces an equivalent electron density.<sup>116</sup> This breaks up the N-electron Schrödinger equation into N one-electron self-consistent Kohn-Sham equations. However, things become trickier to deal with when the often poorly understood *f*-electrons are taken into account. Often, calculations treat the 4*f* states as atomic-like by adding a Hubbard *U* term that places the 4*f*-electrons deep in the valence band. Instead, an on-site hybrid approach was used, as done by Mizzi et al., as the results thereof showed excellent agreement for these materials with X-ray photoelectron spectroscopy.<sup>117</sup> DFT calculations were performed using WIEN2k, an all-electron augmented plane wave + local orbitals code. Onsite-exact-exchange was used, with hybrid fractions of 0.50, 0.38, and 0.80 used for the RE5d, RE4f, and Sc3d orbitals, respectively. A PBEsol functional was used. Muffin tin radii of 2.02, 1.82, and 1.68 were used for the lanthanides, scandium, and oxygen, respectively, to minimize the inclusion of O2p tails within the metal muffin tins which perturbs the calculation of the exact-exchange corrections inside the muffin tins for Sc and the different RE. The plane-wave expansion parameter  $RK_{\max}$  was 6.5. The

strictest allowed convergences were used: 0.0001 e charge convergence, 0.0001 Ry energy convergence, and 1 mRy/a.u. force convergence. Prior to the calculation, all of the electrons were removed from the RE6s, RE5d, Sc4s, and Sc3d orbitals and placed into the O2p orbital to start with the appropriate RE<sup>3+</sup>, Sc<sup>3+</sup>, and O<sup>2-</sup> ions. A Watson sphere radius of 2.4 bohr was used for the O<sup>2-</sup> ion to stabilize the ion. Volume optimization calculations were performed for all of the perovskites and binary oxides. Volumes were varied with the ratio of the three lattice parameters kept fixed. A cubic polynomial was fit to calculated energies as a function of volume and the local minimum found was used as the energy for the phase. Energy as a function of volume and the cubic polynomial fits for all the calculations and the minimum of that cubic fit were then rescaled by the number of formula units in order to solve for the enthalpy of formation; there is a single formula unit in the unit cell for the A-RE<sub>2</sub>O<sub>3</sub> phase, three for the B-RE<sub>2</sub>O<sub>3</sub> phase, eight for the C-RE<sub>2</sub>O<sub>3</sub> phase, and four for the orthorhombic perovskite phase. For all of the REScO<sub>3</sub> investigated, every possible filling of the 4f electron eigenstates was tested to determine which eigenstates led to the lowest energy structure.

### 6.3. Results

As the enthalpy of formation of a compound is relative, DFT investigating the energies of RE<sub>2</sub>O<sub>3</sub> and Sc<sub>2</sub>O<sub>3</sub> was also necessary. The enthalpy of formation was calculated by considering the following reaction:



There are three different thermodynamically stable rare-earth sesquioxide phases. The largest rare-earths (La-Nd) form the hexagonal (space group  $P32/m$ ) A-RE<sub>2</sub>O<sub>3</sub> phase. Rare-earths of intermediate size (Pm-Eu) form the monoclinic (space group  $C2/m$ ) B-RE<sub>2</sub>O<sub>3</sub> phase. The smaller rare-earths (Gd-Lu, Y, Sc) all form in the bixbyite phase (cubic, Ia3), also called the C-RE<sub>2</sub>O<sub>3</sub> phase. The appropriate binary oxide phase was chosen for all of the calculations. The perovskite phase is orthorhombic and has space group 62 ( $Pnma$  or  $Pbnm$ ). As LuScO<sub>3</sub> does not exist in the perovskite structure,<sup>105</sup> the initial structure was the same as DyScO<sub>3</sub> but with lattice parameters extrapolated from the observed lattice parameters of REScO<sub>3</sub> with the RE<sup>3+</sup> ionic radius.

First, I will consider only the oxides and scandates of lanthanum, gadolinium, lutetium, and yttrium, as those RE<sup>3+</sup> exclusively contain empty (La, Y), half-filled (Gd), or completely filled (Lu) orbitals. The enthalpy of formation of these compounds correlates well with inverse of the RE<sup>3+</sup> ionic radius (Figure 6.1), consistent with calorimetric measurements of REAlO<sub>3</sub> and REGaO<sub>3</sub>.<sup>118</sup> This suggests that, since yttrium is not in the lanthanide series, the enthalpy of formation depends on the structure rather than the atomic number of the A site.

However, the enthalpy of formation deviated from this linear behavior when ions with partially filled *f*-orbitals were considered. To address this, crystal field splitting of the lanthanide needed to be considered such that the DFT calculation would result in the global minimum, rather than a local minimum. While the cubic perovskite structure has a 12-coordinate A-site, the rotation of the BO<sub>6</sub> octahedra reduces the A-site coordination. With the significant rotation of the ScO<sub>6</sub> octahedra in REScO<sub>3</sub> perovskites, the

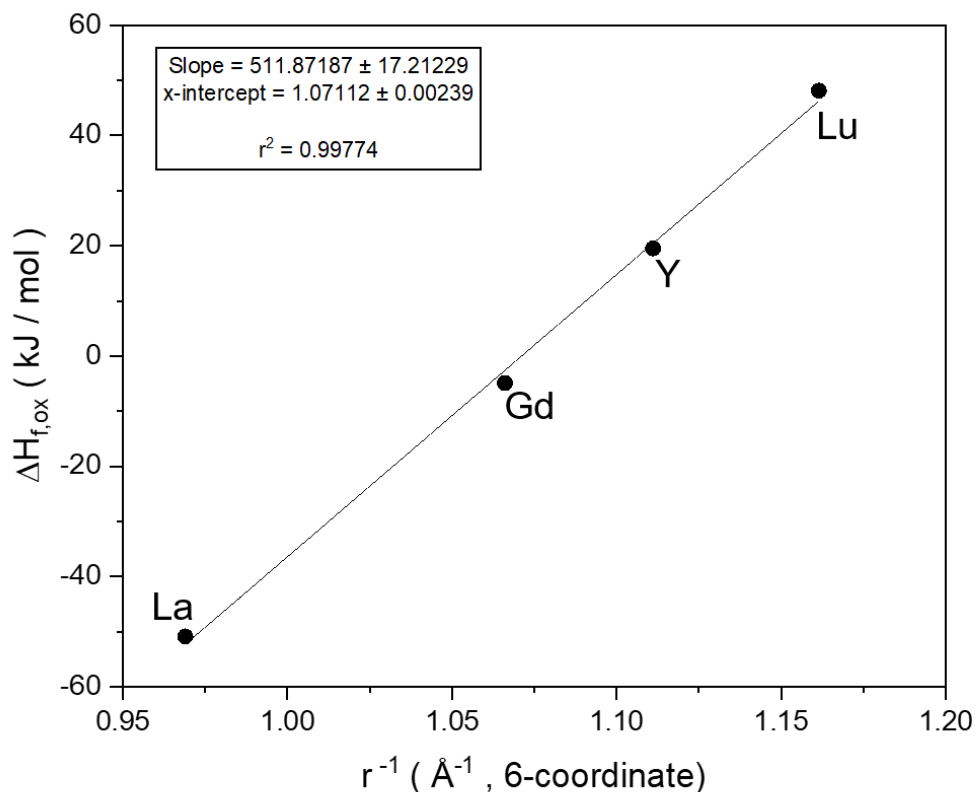


Figure 6.1. Calculated enthalpy of formation of  $REScO_3$  relative to the appropriate binary oxides as a function of the inverse of the six-coordinate Shannon ionic radius for  $RE^{3+}$ .

coordination environment becomes similar to that of a trigonal prism, as shown in Figure 6.2. When considering that coordination with transition metals, the  $d$ -orbitals are rotated such that  $z$  points along the axis of the prism and that  $x$  and  $y$  point in-plane. The same convention will be used herein, noting that trigonal prism points along  $a$  when using the  $Pnma$  space group and along  $b$  when using  $Pbnm$ . In the transition metals, the lowest energy state points along the axis of the prism, the next lowest energy states lie completely in the plane, and the highest energy states have both in- and out-of-plane

behavior. This should be similar in the case of the  $f$ -orbitals, though they tend to be harder to interpret.

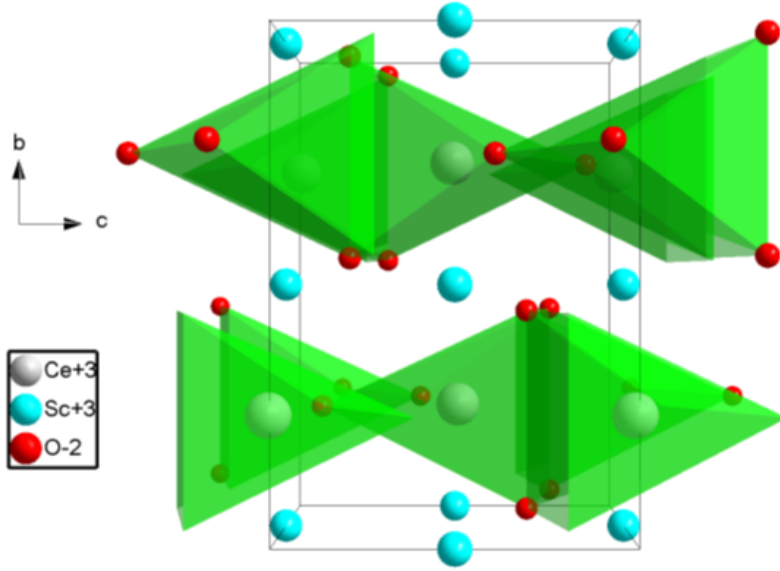


Figure 6.2. Crystal structure of CeScO<sub>3</sub>, with CeO<sub>6</sub> trigonal prisms shown.

The eigenstates and the occupancies thereof for the  $f$ -electrons can be calculated through diagonalizing their density matrix, where the eigenvalues are the probability of the electron being in that particular eigenstate. On first inspection, the 7 eigenstates appeared to take two different forms: four contained contributions from the odd basis states only, and the other three contained contributions from the even basis states only. Basis states 1 and 7 correspond to the orbitals with quantum number  $m = \pm 3$ , which account for the orbitals proportional to  $z^0 (x(x^2 - 3y^2) \text{ and } y(3x^2 - y^2))$ . Basis states 2 and 6 correspond to the orbitals with  $m = \pm 2$ , which account for the orbitals proportional to  $z^1 (xyz \text{ and } z(x^2 - y^2))$ . Basis states 3 and 5 correspond to the orbitals with  $m = \pm 1$ , which account for the orbitals proportional to  $z^2 (xz^2 \text{ and } yz^2)$ . Lastly, basis state 4

corresponds to  $m = 0$ , which directly leads to the  $z^3$  orbital. As such, eigenstates with odd basis states only contain orbitals even in  $z$  and eigenstates with even basis states only contain orbitals odd in  $z$ . Various new starting density matrices were constructed by changing the occupancy with these eigenstates to determine which eigenstate produced the lowest energy. In addition, the density of states (DOS) of each state were calculated to see what  $f$ -orbitals were contributing and 3D electron density maps were produced to see the resulting orbital shape within the structure.

To ease analysis, we will look first at  $\text{CeScO}_3$ , as it only has a single  $f$ -electron to consider. The lowest energy state corresponded to when the  $z^3$  orbital was filled. Correspondingly, the resulting DOS showed that the only occupied  $f$ -orbital was the  $z^3$  and the 3D electron density map shows an shape consistent with the  $z^3$  pointing along the  $z$ -axis. The next four lowest energies were all similar in value, roughly 132 meV per formula unit greater than the energy for the  $z^3$  orbital, and the 3D electron density map showed that their commonality stems from the resulting orbital shape which resembles the  $xyz$  or  $z(x^2 - y^2)$  orbital. While two of those four states are formed from those two orbitals, the other two result from a linear combination of the  $x(x^2 - 3y^2)$ ,  $y(3x^2 - y^2)$ ,  $xz^2$ , and  $yz^2$  states. Lastly the two highest energy states, 219 meV greater than the  $z^3$  state, also have similar orbital shapes according to the 3D electron density map, with orbitals shaped like the  $z^3$  orbital but pointing in the  $xy$ -plane. I note that this result shows that the  $\text{RE}^{3+}$  ion ultimately adopts the cubic set of  $f$ -orbitals rather than the general set. Equivalently, the two highest energy states are  $x^3$  and  $y^3$  in behavior, and the four intermediate states are  $xyz$ ,  $z(x^2 - y^2)$ ,  $x(z^2 - y^2)$ , and  $y(z^2 - x^2)$ .

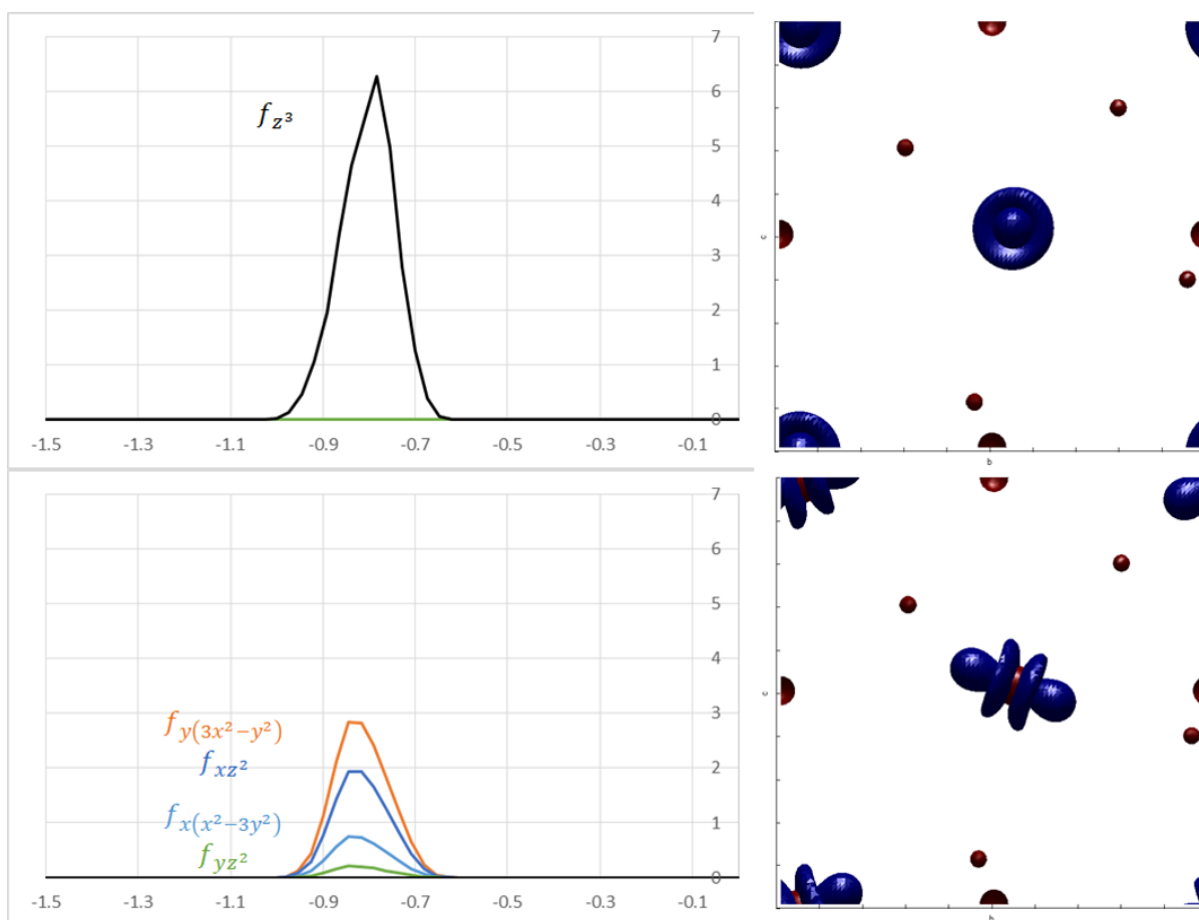


Figure 6.3. (a,c) The DOS in eV of the occupied eigenstate and (b,d) the corresponding eigenstate orbital shape according to the 3D electron density map. (a,b) The lowest in energy structure corresponded to the state with an out-of-plane orbital shape, whereas (c,d) the highest energy occurred because its lobes pointed closer to an oxygen anion.

In this next case example, we will look at  $\text{YbScO}_3$ , which has seven up  $f$ -electrons, but only six down  $f$  electrons. 3D electron density maps were produced showing the difference between the up and down electron densities, so the resulting image is indicative of which is the lone  $f$ -orbital without a down electron. The highest energy state is then indicative of what the lowest energy orbital should be. Here, we see that different orbitals were constructed. The energy of the state with an unoccupied  $z^3$  orbital is actually the second

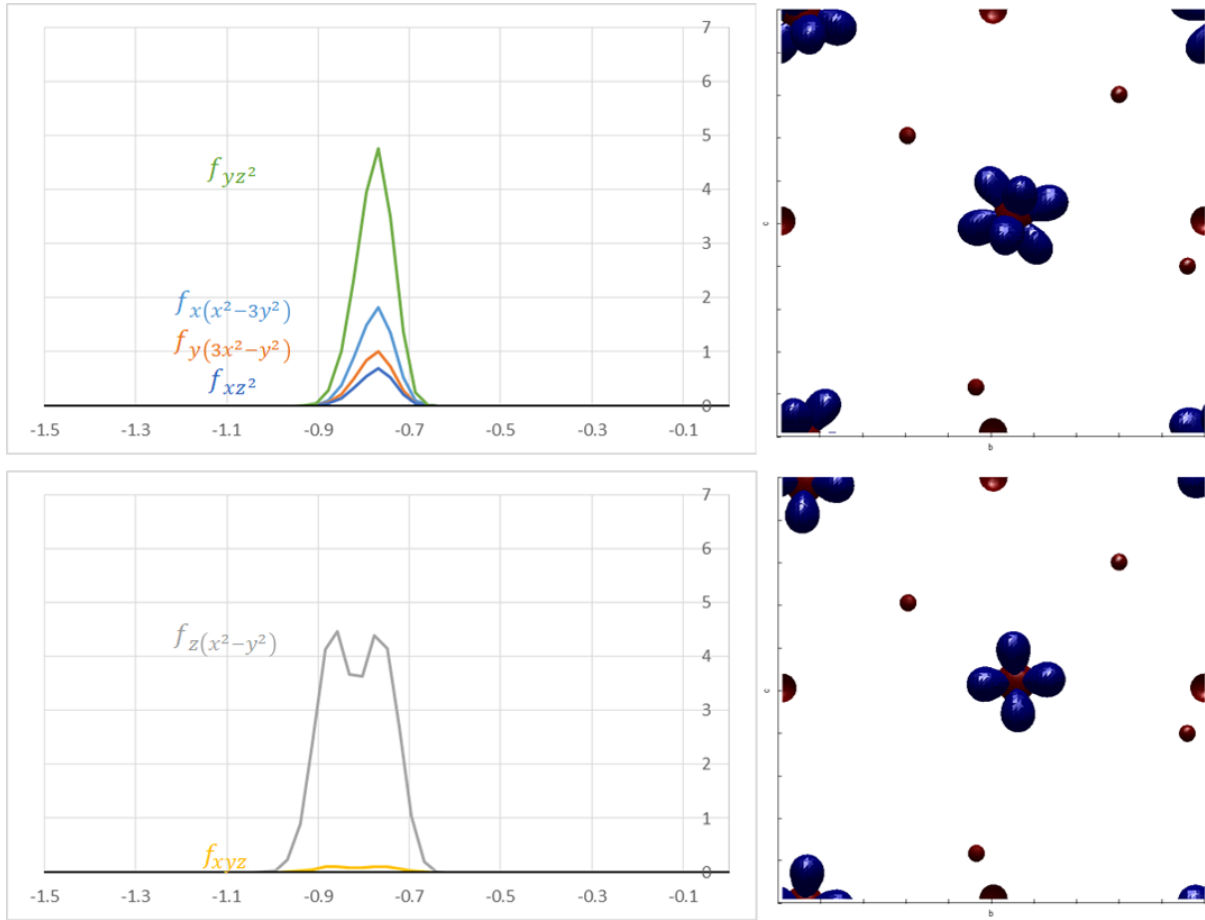


Figure 6.4. (a,c) The DOS in eV of the occupied eigenstate and (b,d) the corresponding eigenstate orbital shape according to the 3D electron density map. They are both intermediate in energy.

highest in energy, around 60 meV per formula unit lower than the highest energy state. Looking at the 3D electron density map of that state, the state it lacks shows three-fold symmetry and lies completely in plane, which explains why it must be a low energy state. Deconvoluting the eigenvector into the orbitals it is comprised of show that that state is equivalent to the  $x(x^2 - 3y^2)$  orbital. However, the in-plane states are higher than the out-of-plane states when  $d$ -orbitals are concerned. This deviation likely arises from how the  $z^2$  orbital which has the lowest energy contains a ring that is in the plane, whereas

$z^3$  has a two rings and neither of them are themselves in the plane. The five remaining eigenstates again share a similar looking orbital to that of  $xyz$ , but with various different rotations.

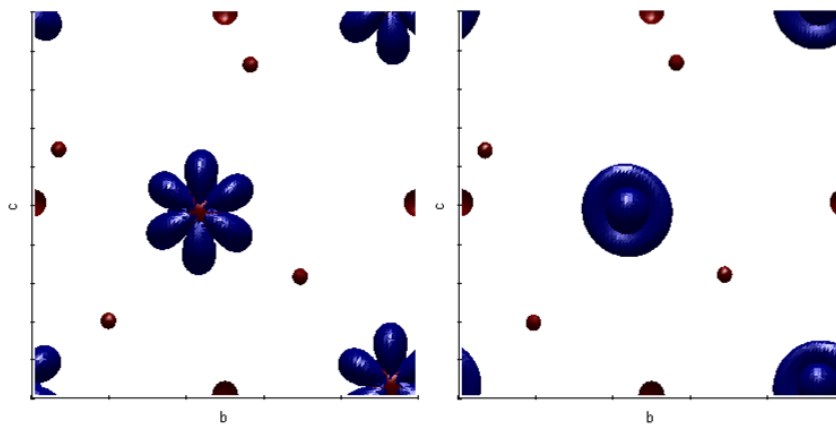


Figure 6.5. 3D electron density maps showing the remaining unoccupied orbital shape. These structures had the highest energy because of the low energy of the in-plane (left) and out-of-plane (right) orbitals.

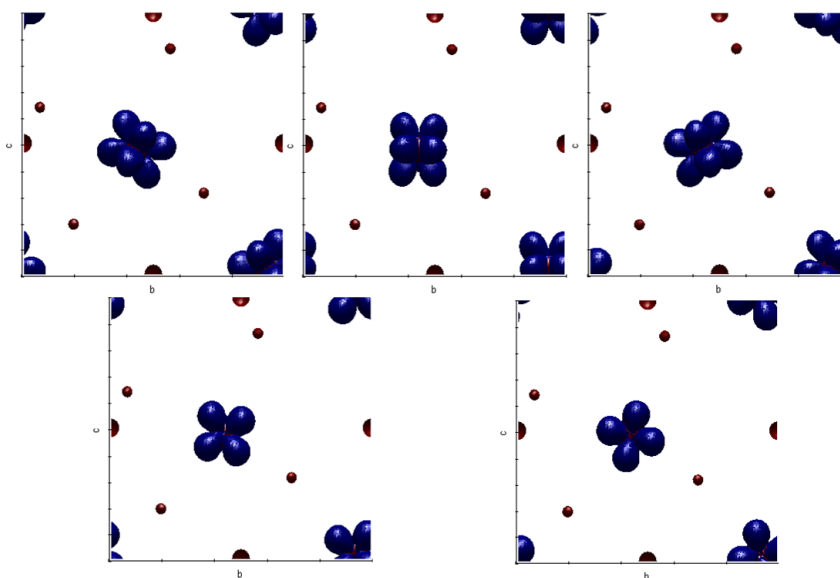


Figure 6.6. 3D electron density maps showing the remaining unoccupied orbital shape for the other five eigenstates. All orbitals look similar and differ only by rotation.

While more work needs to be done to determine exactly the which orbitals are preferred and whether or not the filling of certain orbitals further affects the filling of other, by iterating through every possible eigenstate combination, the true lowest minimum state for all the RE<sub>2</sub>ScO<sub>3</sub> could be reached. By then plotting the newly calculated enthalpy of formation relative to the binary oxides, it appears that the linear relationships is mostly preserved (Figure 6.7), although there are multiple deviations from this behavior, especially for those involving down electrons. This trend is consistent with experiments that show that the larger rare-earths form perovskite whereas the smaller rare-earths instead form the bixbyite (C-RE<sub>2</sub>O<sub>3</sub>) phase.<sup>105</sup>

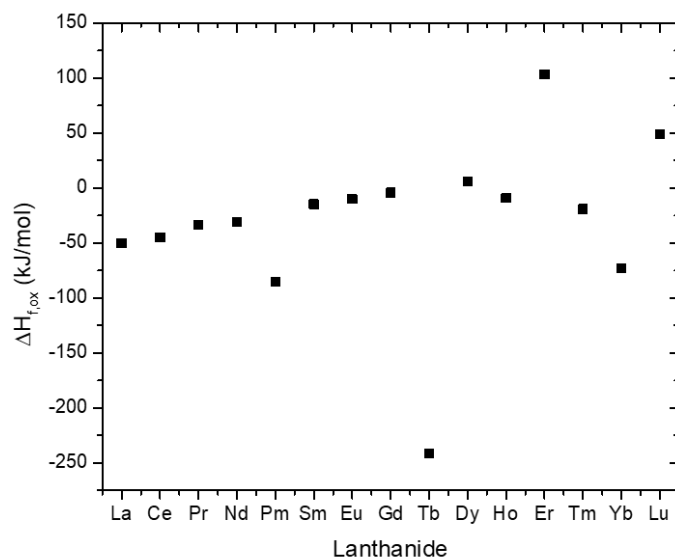


Figure 6.7. Calculated enthalpy of formation of RE<sub>2</sub>ScO<sub>3</sub> relative to the appropriate binary oxides as a function of lanthanide.

These deviations could result from the several approximations we took. For completeness, the binary oxides should undergo the same treatment of having all eigenstate

combinations investigated, which may alleviate some of these deviations, or potentially exacerbate the  $\text{ErScO}_3$  deviation. We also neglected spin-orbit coupling, possible spin-waves, and assumed the system was ferromagnetic although some of the structures are antiferromagnetic at 0 K ( $\text{DyScO}_3$ , for one, has a Néel temperature of 3.1 K)<sup>119</sup>. We also assumed that the muffin tin radii and the exact-exchange hybrid fractions were the same for each lanthanide (and yttrium), regardless of structure. In the above analysis, we also failed to account for statistical occupancy. There may also be intrinsic errors in the  $\text{RE}_2\text{O}_3$  reference materials.

Owing to the fairly similar energies of each individual state, the partition function for the  $f$  occupancy was constructed to determine the energy of mixed states. As an example, looking again at  $\text{YbScO}_3$ , there are five states that could be occupied statistically. At room temperature, the lowest energy state only has a 28.1% chance of being occupied, with four other states accounting for 22.1%, 21.6%, 18.3%, and 9.9%, and the calculated Helmholtz energy of mixing is 3.66 kJ/mol (32.8 meV). By 900 K, the probability of each of these five states becomes nearly equal (15-21%). Therefore, there will be a distribution of occupied states in ytterbium scandates; these five occupied states have different rotations about Yb, which on average in a real crystal may effectively produce a spherically symmetric electron distribution.

#### 6.4. Conclusion

Significant crystal field splitting of the  $4f$  orbitals occurs in  $\text{REScO}_3$ , where the  $\text{RE}^{3+}$  ions sit in a distorted trigonal prism, often differing by several hundreds of meV per formula unit. As such, the lowest energy states are composed of  $f$ -orbitals that lie in-plane, followed by the  $z^3$  orbital which points along the axis of the trigonal prism. These states

were often many hundreds of meV lower in energy than the other orbitals, which contained in- and out-of-plane behavior. Finding these lower energy states, either selectively or through iteration, can guarantee that the global minimum energy structure be reached and is necessary for finding the formation energies of distorted rare-earth perovskites and better understanding their properties.

## CHAPTER 7

**Syntheses of Lanthanide Gallates**

In this chapter, I will discuss several different approaches that I took trying to produce various  $\text{LnGaO}_3$ . I was only able to successfully grow  $\text{LaGaO}_3$  and  $\text{NdGaO}_3$  as perovskites, and the methods used to do so did not allow for a controlled surface termination. Smaller lanthanides led to the formation of other phases that were more thermodynamically preferred, such as garnet ( $\text{Ln}_3\text{Ga}_5\text{O}_{12}$ ) or noncentrosymmetric  $\text{Ln}_3\text{GaO}_6$ , or failed to react with the gallium at all. This chapter will discuss what worked to produce the perovskite phase and will rationalize the failures in producing the others so that others may better know what is necessary to produce these materials. Doing so also helped reveal some of the mechanisms and considerations at play in hydro-sauna syntheses.

**7.1. Introduction**

Lanthanide gallates single crystals are extensively used as substrates for epitaxial  $\text{YBa}_2\text{Cu}_3\text{O}_7$ ,<sup>120</sup> owing to their similar lattice matching and thermal expansion properties, as well as having reasonable dielectric properties<sup>121</sup> and high thermal stability necessary for processing.  $\text{LnGaO}_3$  are also studied as fuel cell electrolytes<sup>122</sup> or more recently as phosphor hosts with various lanthanide substitutions.<sup>123</sup> In this work,  $\text{LnGaO}_3$  with different lanthanides were wanted as an alternative to the series of lanthanide scandates as supports. Perovskite  $\text{LnGaO}_3$  is isostructural with  $\text{LnScO}_3$ , adopting an orthorhombic crystal structure. Owing to the smaller ionic radius of six-coordinate  $\text{Ga}^{3+}$  relative to

$\text{Sc}^{3+}$  (0.620 Å and 0.745 Å, respectively), the  $\text{GaO}_6$  octahedra in  $\text{LnGaO}_3$  are less rotated than that of the  $\text{ScO}_6$  octahedra in  $\text{LnScO}_3$ . Like  $\text{LnScO}_3$ ,  $\text{LnGaO}_3$  are irreducible oxides and therefore are stable under many redox reaction conditions. Using  $\text{LnGaO}_3$  gives a smaller set of lattice parameters than  $\text{LnScO}_3$  does,<sup>124</sup> which would allow for Pt and Pd catalysts to be investigated under compressive strain or for smaller metals (e.g. Rh, Ir) to be epitaxially matched. In addition, Ga is amphoteric, whereas Sc is basic; this change in acid-base behavior may be important in many reactions. In order to investigate how these changes would affect various catalytic reactions, the lanthanide gallates need to be produced with high surface area and controlled surface termination, much like what was done with the lanthanide scandates.

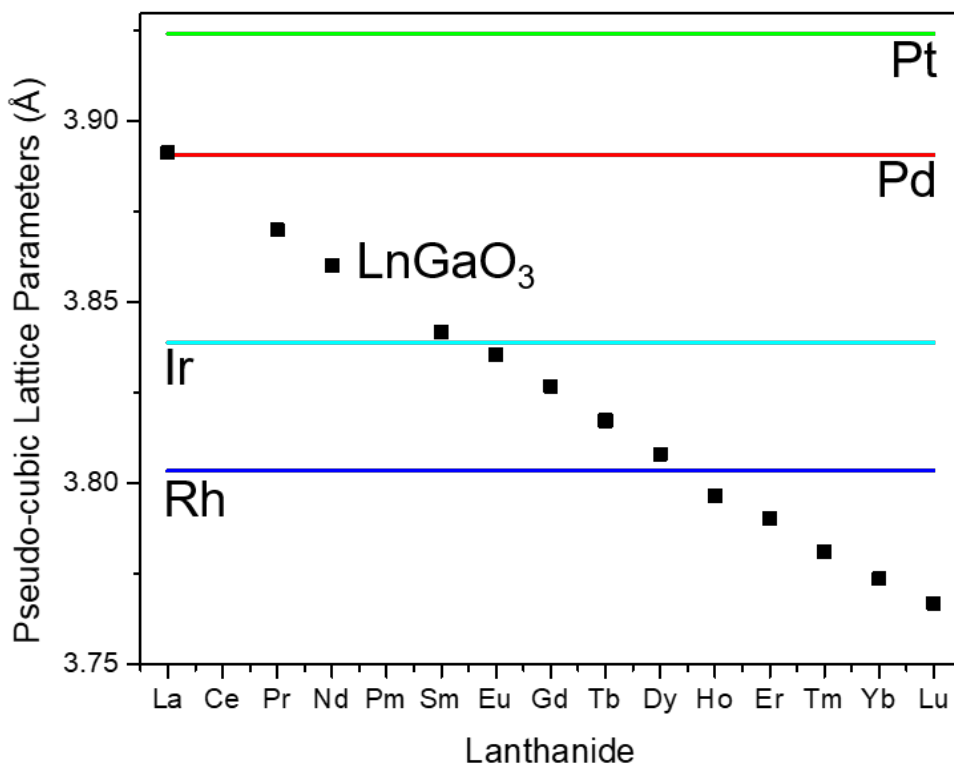


Figure 7.1. The pseudo-cubic lattice parameters of the different  $\text{LnGaO}_3$  compared to several noble metals.

## 7.2. Pechini Method

One technique used to make these materials is the Pechini method.<sup>125,126</sup> The Pechini method is an effective approach for producing ceramics with mixed cations. A wide variety of cations can be used, including those that do not form stable hydroxo species and those that have different acid-base properties. The appropriate mixture of cations is dissolved from salts into water and then chelated with a hydroxycarboxylic acid. The chelates are then cross-linked together with a polyalcohol to form a gel through esterification. The

cations are trapped in this gel, which largely prevents cation segregation. The gel is then calcined to burn off the organics and to form the mixed cation oxide.

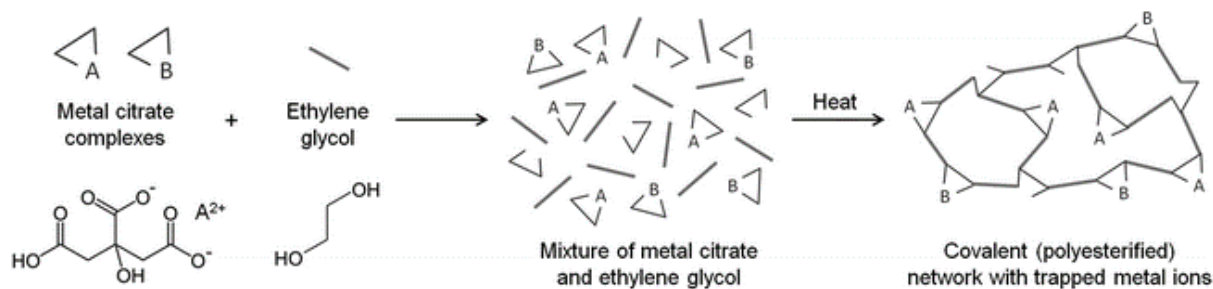


Figure 7.2. Schematic of the Pechini method in making a mixed cation gel.<sup>127</sup>

The approach used herein is adapted from work synthesizing Sr-doped lanthanum gallate.<sup>128</sup> First, 2 mmol of  $\text{Ln}(\text{NO}_3)_3 \cdot 6\text{H}_2\text{O}$  and 2 mmol of  $\text{Ga}(\text{NO}_3)_3 \cdot x\text{H}_2\text{O}$  were dissolved into 30 mL of deionized water. Note that the gallium nitrate is assumed to be an octahydrate ( $x = 8$ ), consistent with what is reported in literature.<sup>129</sup> 12 mmol of citric acid was added as a chelating agent. The resulting solution had an equimolar ratio of citric acid to nitrates. The pH was raised to 7 through the addition of a solution of 28%  $\text{NH}_3$  in  $\text{H}_2\text{O}$ . The solution was then heated to 90 °C and 12 mmol of ethylene glycol was added. After stirring for 4 hours, the chelates are cross-linked and a gel is formed through esterification. Afterwards, the solution was dried at 80 °C for several days. This created a resin or gel that contained an equimolar amount of lanthanide and gallium. This resin was calcined at 1100 °C for 36 hours to produce the final product.

This process produced  $\text{LaGaO}_3$  and  $\text{NdGaO}_3$  powders with minimal secondary phases, as shown in Figure 7.3. However, no  $\text{SmGaO}_3$  nor  $\text{GdGaO}_3$  could be produced. Rather, a number of different lanthanide gallium oxides were produced instead, such as the garnet phase ( $\text{Ln}_3\text{Ga}_5\text{O}_{12}$ ) and non-centrosymmetric  $\text{Ln}_3\text{GaO}_6$  (Figure 7.3). It should be noted

that these phases all include tetrahedrally-coordinated Ga, whereas Ga in the perovskite phase would only be octahedrally-coordinated. This preference for the tetrahedral coordination prevents the perovskite from being formed. This can also be seen by considering  $\text{Ga}_2\text{O}_3$  by itself;<sup>130</sup> the most stable form is  $\beta\text{-Ga}_2\text{O}_3$ , which contains Ga in both octahedral and tetrahedral coordinations. Only under high pressure does  $\alpha\text{-Ga}_2\text{O}_3$  form, which is the only phase of  $\text{Ga}_2\text{O}_3$  in which the Ga is all octahedrally-coordinated. Likewise, the remaining  $\text{LnGaO}_3$  have only been synthesized under high pressure (greater than 45 kbar).<sup>131,132</sup>

In addition, it is difficult to control particle shape or size using the Pechini method. As can be seen in Figure 7.4, the products have sharp facets, but include many different surface terminations. Since the Pechini method is effective for mixed metal oxides because the cations are “trapped” in the polymer network of the gel, material growth is inherently diffusion limited, which prevents controlled growth on particular facets. As a result, while this method yields the appropriate phase for  $\text{LaGaO}_3$  and  $\text{NdGaO}_3$ , there are no means in which to produce a material with a controlled or consistent surface structure, making this method inappropriate for producing supports with the desired properties for this project.

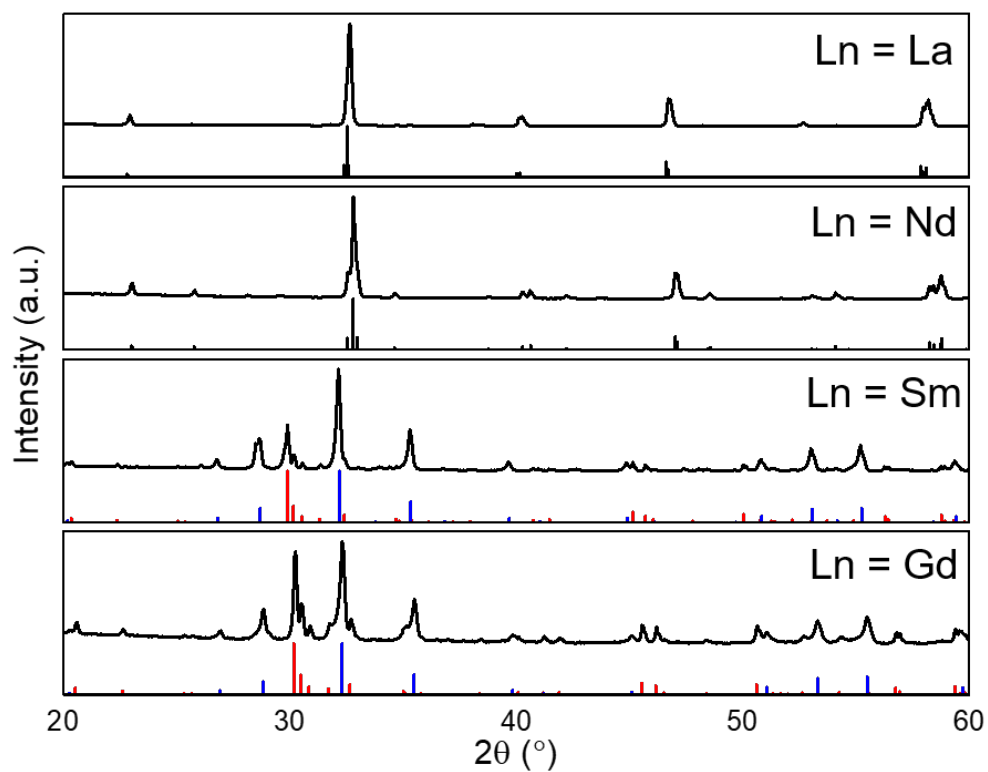


Figure 7.3. The PXRD patterns of the product from Pechini syntheses for  $\text{LnGaO}_3$ . Black bars are  $\text{LnGaO}_3$ , whereas red and blue bars are for  $\text{Ln}_3\text{GaO}_6$  and  $\text{Ln}_3\text{Ga}_5\text{O}_{12}$ , respectively.

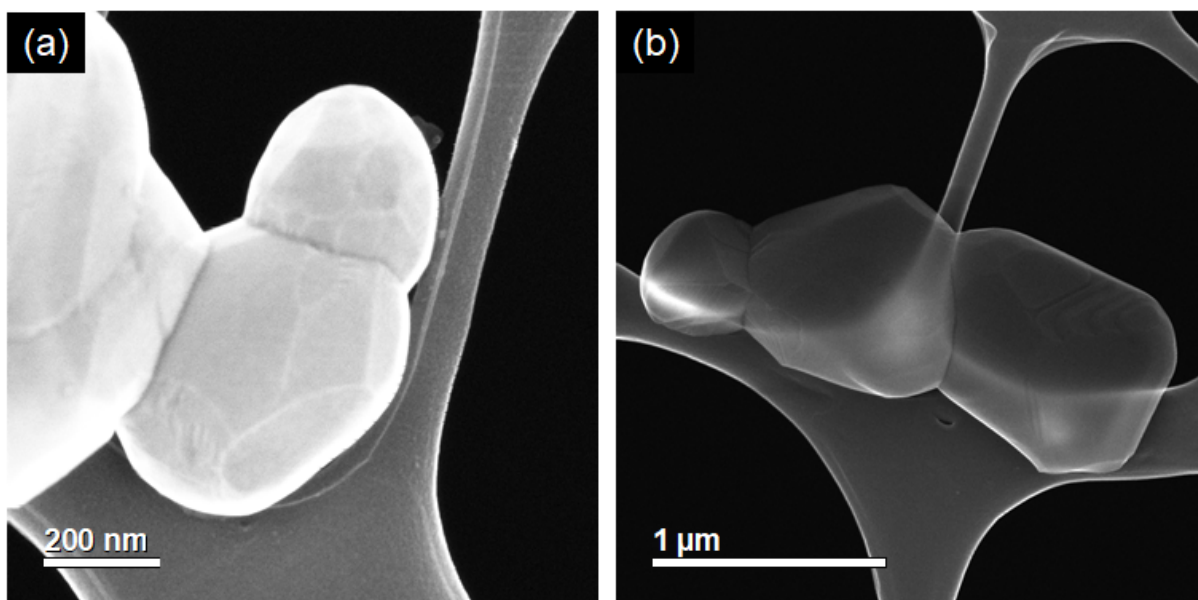


Figure 7.4. SE image of (a) LaGaO<sub>3</sub> and (b) NdGaO<sub>3</sub> particles.

### 7.3. Hydro-Sauna Method

The Pechini method could not be used to control particle shape and size and could not be used to successfully produce a sufficient number of the  $\text{LnGaO}_3$  series because the reaction conditions allowed for Ga to adopt its preferred tetrahedral coordination. If a precursor gel contained Ga in the appropriate octahedral coordination, the mild reaction conditions of hydro-sauna synthesis may be sufficient to preserving the octahedral Ga units. Conveniently, the gallium in its trihydroxide is octahedrally-coordinated, so a lanthanide gallium hydroxide hydrogel analogous to the  $\text{LnSc}(\text{OH})_6 \cdot x\text{H}_2\text{O}$  used before may be effective.

The general outline for hydro-sauna synthesis is the creation of a mixed cation solution, precipitation of an equimolar gel, and the humid heat treatment of the gel to allow for crystallization. Therefore, producing  $\text{LnGaO}_3$  would warrant several changes than the approach for  $\text{LnScO}_3$ . First is the use of  $\text{Ln}(\text{NO}_3)_3 \cdot 6\text{H}_2\text{O}$  and  $\text{Ga}(\text{NO}_3)_3 \cdot x\text{H}_2\text{O}$  as precursors because the dissolution of  $\text{Ga}_2\text{O}_3$  in water or  $\text{HNO}_3$  was found to be slow or unfavorable. Again, it is assumed that the precursor is gallium nitrate octahydrate.<sup>129</sup> Second, 10 M NaOH could not be used as a precipitation agent because of the amphoteric nature of Ga for, if 10 M NaOH was used, Ga would dissolve as  $\text{Ga}(\text{OH})_4^-$  instead of precipitating as  $\text{Ga}(\text{OH})_3$ . Ga has its minimum solubility at a pH of 7-8, so an excess of base may not be used. Instead, 28%  $\text{NH}_3$  in  $\text{H}_2\text{O}$  (referred to as ammonium hydroxide going forward) was added to raise the pH to 7 and precipitate an equimolar lanthanide gallium hydroxide hydrogel. The gel was then cleaned with water several times before the humid heat treatment. The hydro-sauna synthesis at 350 °C, however, resulted in an amorphous product as shown in Figure 7.5a, much like what occurred when the lanthanide

scandium hydroxide hydrogel was heated in a dry environment. EDX (Figure 7.5b), however, did confirm that the product was equimolar in Ln and Ga.

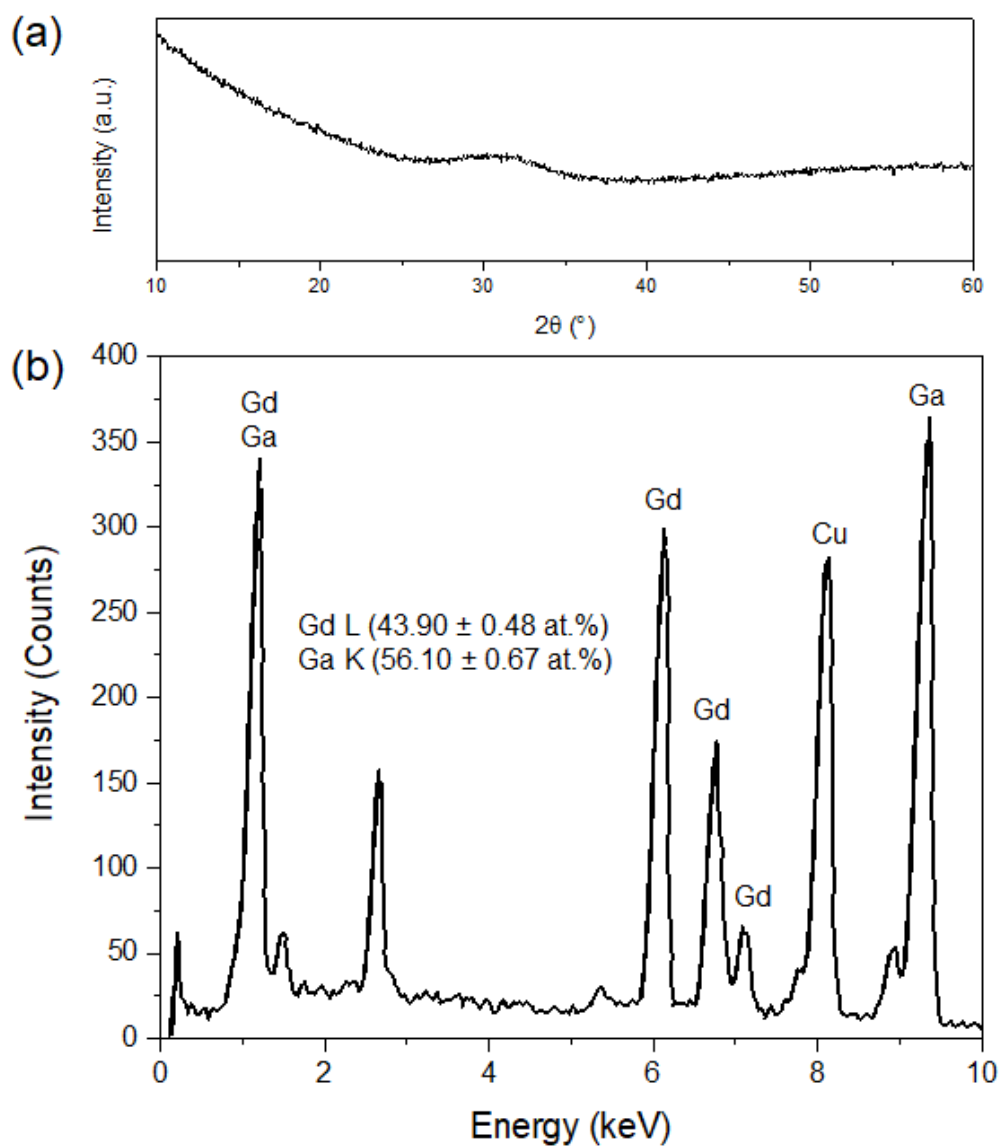


Figure 7.5. (a) PXRD pattern and (b) EDX of the product from hydro-sauna synthesis on a  $\text{LnGa}(\text{OH})_6 \cdot x\text{H}_2\text{O}$  gel precipitated with ammonium hydroxide.

It is worth now thinking about what a gel is and what it undergoes in the hydro-sauna reaction in order to figure out why  $\text{LnGaO}_3$  failed to crystallize as  $\text{LnScO}_3$  had. A gel, as defined by Brinker, is an amorphous solid network that encapsulates a liquid phase.<sup>58</sup> In the case of the  $\text{LnScO}_3$  synthesis, the gel consists of a  $\text{LnSc}(\text{OH})_6$  solid network that encapsulates some sodium hydroxide solution. I note now that, while a 10 M NaOH solution is used to precipitate the gel, the encapsulated solvent may have a lower concentration because the gel is washed several times in water. In this case for  $\text{LnGaO}_3$ , the encapsulated liquid phase is now that of ammonium hydroxide. This difference in encapsulated solvent may account for the difference in crystallization behavior. As discussed in Chapter 4, when a liquid-gas interface forms within the pores of the gel, capillary forces exist to collapse the solid network into an amorphous xerogel. The capillary forces scale linearly with the surface tension of the liquid-gas interface, which in turn scales logarithmically with the vapor pressure of the solvent;<sup>58</sup> a solvent with a high vapor pressure would increase the capillary forces and cause the solid network to collapse more strongly. This rationale also helps explain the success of the humid environment in hydro-sauna syntheses: the surface tension of the water-gas interface decreases with increasing humidity as the added steam reduces the net evaporation of the encapsulated solution.<sup>59</sup> Summed up, a low vapor pressure solvent, such as sodium hydroxide, in a humid environment is necessary to preserve the open gel matrix.

Since the ammonium hydroxide solution is needed to precipitate the equimolar precursor, the goal then becomes to change the encapsulated solvent after precipitation. Doing so is called a solvent exchange. Washing and centrifuging the gel twice in ethanol removes the ammonium hydroxide solution and replaces it with the ethanol. Washing and

centrifuging twice with the desired solvent would then remove the ethanol in favor of the desired solvent. In principle, we want 10 M NaOH as the solvent since its vapor pressure was sufficient for the hydro-sauna synthesis of  $\text{LnScO}_3$ . If 10 M NaOH is exchanged in, the resulting product is indeed crystalline, but the use of the strong base not surprisingly caused the dissolution of the gallium hydroxide within the gel, so the resulting product was only the appropriate  $\text{Ln}(\text{OH})_3$  or  $\text{LnOOH}$ . If water is instead exchanged in, the Ga will not be dissolved away, but the resulting product was amorphous, suggesting that water itself still has too high of a vapor pressure. These results imply changing the encapsulated liquid may allow for crystallization, but the solvent must have a lower vapor pressure than water alone and not be excessively alkaline. Therefore, going forward, water with different salts should be tried, as many solid salts would lower the vapor pressure of the water solution. In addition, increasing the humidity to decrease the surface tension of the liquid-gas interface may also aid in the synthesis but doing so risks the formation of the hydroxides.<sup>47</sup>

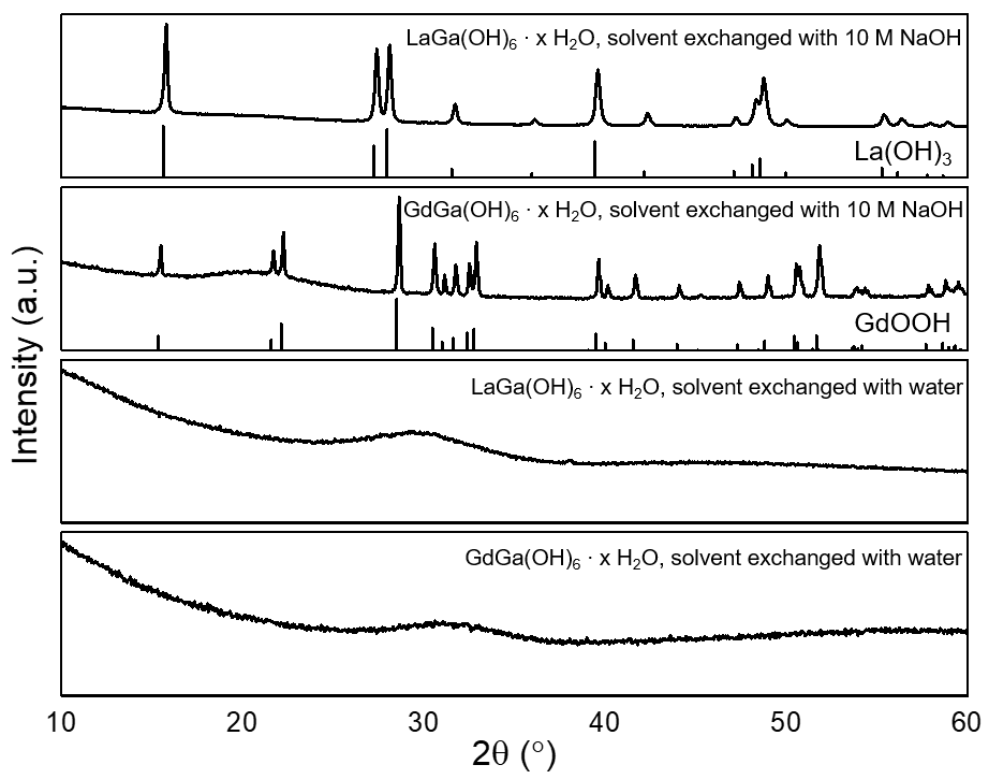


Figure 7.6. The PXRD patterns of the product from hydro-sauna synthesis on  $\text{LnGa}(\text{OH})_6 \cdot x\text{H}_2\text{O}$  ( $\text{Ln} = \text{La}$  or  $\text{Gd}$ ) gels that underwent a solvent exchange to 10 M NaOH or to water.

#### 7.4. Hydrothermal Synthesis

Solvothermal synthesis was described in Chapter 3. A distinct advantage of this technique is the ability to produce crystalline particles with controlled morphology, either through the preservation of the thermodynamic Wulff shape at the mild reaction conditions or through a kinetic Wulff shape achieved by varying different processing parameters (e.g. temperature, pH, different reagents or concentrations thereof) or adding surfactants.

The mild conditions and possibility of forming faceted crystallites makes studying this approach for producing shaped-controlled  $\text{LnGaO}_3$  supports worthwhile.

Synthesis of  $\text{LnMnO}_3$  has been demonstrated to occur under conditions that formed both  $\text{LnOOH}$  and  $\text{Mn}(\text{OH})_4^-$ .<sup>41</sup> Gallium oxide is amphoteric, so it readily dissolves in both acids and bases and forms the hydroxyl complex  $\text{Ga}(\text{OH})_4^-$  in basic media. The formation of the more soluble and reactive  $\text{LnOOH}$  required the dehydration of  $\text{Ln}(\text{OH})_3$ , which either required higher temperatures or lower pressures as discussed in Chapter 3. However, the presence of  $\text{LnOOH}$  and  $\text{Ga}(\text{OH})_4^-$  alone does not guarantee the subsequent reaction into  $\text{LnGaO}_3$  as it seemed to do for the growth of  $\text{LnMnO}_3$ .<sup>41</sup> As an example, when the exact conditions used to form  $\text{YbMnO}_3$  were used (225 °C in a 2.5 M NaOH solution), only  $\text{YbOOH}$  crystals precipitated out and appeared in the PXRD pattern in Figure 7.7, meaning the Ga remained in solution. While the exact reaction is not known, it is possible that  $\text{LnOOH}$  dissolves into  $\text{LnO}(\text{OH})_2^-$  in alkaline media, and the subsequent reaction between  $\text{LnO}(\text{OH})_2^-$  and  $\text{Ga}(\text{OH})_4^-$  would be a base-base reaction and have a large energy barrier.

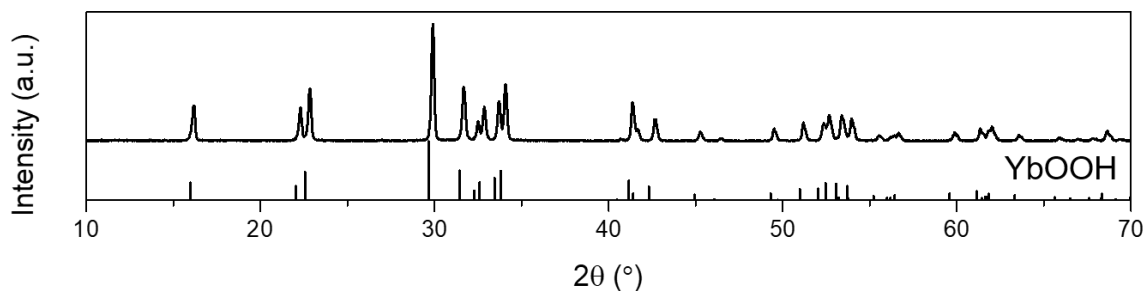


Figure 7.7. A PXRD pattern of the product from a hydrothermal synthesis on equimolar amount of  $\text{Yb}_2\text{O}_3$  and  $\text{Ga}_2\text{O}_3$  in 2.5 M NaOH at 225 °C. Identical conditions using  $\text{Mn}_2\text{O}_3$  instead of  $\text{Ga}_2\text{O}_3$  produced  $\text{YbMnO}_3$ . However, in this case  $\text{YbOOH}$  was produced rather than  $\text{YbGaO}_3$ .

Another option is to create the same  $\text{LnGa}(\text{OH})_6 \cdot x\text{H}_2\text{O}$  used in the hydro-sauna method, dry it, and then use that as a precursor in a hydrothermal reactor. Again, the relatively mild reaction conditions may be sufficient to preserve the octahedral coordination of the gallium. However, hydrothermal treatment at 340 °C resulted in gadolinium gallium garnet,  $\text{Gd}_3\text{Ga}_5\text{O}_{12}$ , as evidenced by the PXRD pattern in Figure 7.8. Like before,  $\text{GdGaO}_3$  is not thermodynamically stable at those conditions. While the hydrothermal reactor is at an increased pressure, it is “only” at 150 bar, several orders of magnitude less than the potentially necessary 45 kbar. In addition, water or alkaline conditions at high temperatures can be corrosive to the T316 stainless steel reaction vessel so  $\text{GdCrO}_4$  was also found in the final product (Figure 7.8).

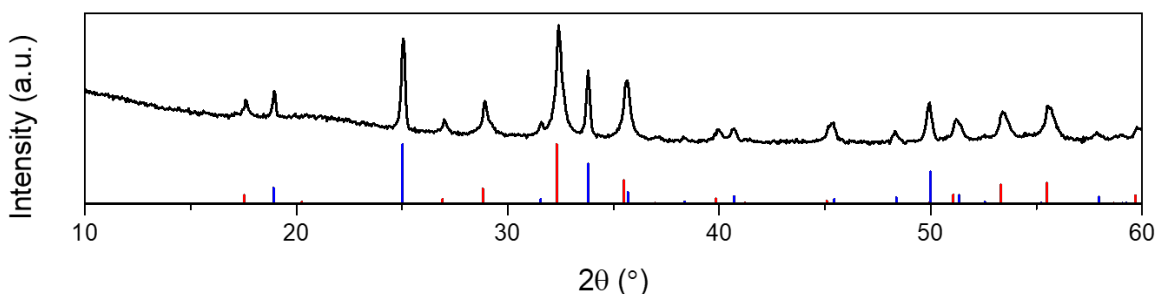


Figure 7.8. A PXRD pattern of the product from a hydrothermal treatment on a dried  $\text{GdGa}(\text{OH})_6$  gel.  $\text{Gd}_3\text{Ga}_5\text{O}_{12}$  was thermodynamically preferred (red), but  $\text{GdCrO}_4$  (blue) was also produced because of corrosion of the hydrothermal reactor.

## 7.5. Conclusion

$\text{LnGaO}_3$  would make an interesting comparison point to the  $\text{LnScO}_3$  studied throughout this thesis. While  $\text{LaGaO}_3$  and  $\text{NdGaO}_3$  are thermodynamically stable, the gallium preferred to be tetrahedrally coordinated and therefore failed to adopt the perovskite

structure. Understanding the different gallium (hydr)oxides may inform in how to produce the remaining LnGaO<sub>3</sub> series; both Ga(OH)<sub>3</sub> and the high-pressure phase of Ga<sub>2</sub>O<sub>3</sub> contain octahedrally coordinated gallium. The mild reaction conditions of hydro-sauna syntheses may then be sufficient to preserve the coordination, so this approach is worth investigating further. It was discovered that humid conditions are not sufficient to preserve the open gel matrix, but a lower vapor pressure encapsulated solvent may be needed to not cause collapse the gel matrix.

## CHAPTER 8

**Effect of Support Interface on the Stability of Au Catalysts**

One of the goals of this project was to investigate how the interfacial energy between the support and catalyst affected the catalyst orientation and stabilized the catalyst during reaction. Looking at  $\text{LnScO}_3$ -supported gold nanoparticles, we found that the resulting catalyst shape and orientation was dependent on the interfacial energy, which was a function of the support and of the size of the gold. The stability of the gold particles in CO oxidation was then investigated. We found that when the gold was well lattice matched to the support, it adopted different orientations, sintered more significantly, and had the greatest deactivation constant as a result.

This work was done in collaboration with Zachary Mansley, Louisa Saveride, Abha Gosavi, and Justin Notestein. Zachary performed the electron microscopy, Louisa performed the catalytic reactions, and Abha performed the deposition-precipitation of the supported gold nanoparticles. The results of this chapter are preliminary and more recent results may suggest a different rationale for the difference in sintering.

**8.1. Introduction**

While gold is typically the most noble (and therefore unreactive!) metal, it has been found in the last few decades that Au nanoparticles less than 10 nm in size make excellent catalysts for several different reactions.<sup>133</sup> One such example is CO oxidation, including at temperatures below room temperature<sup>134</sup> (or even below 200 K)<sup>135</sup> or for preferential

oxidation of CO over  $\text{H}_2$ .<sup>136</sup> Some proposed that charge transfer across the gold-support interface was critical in obtaining active Au catalysts.<sup>137</sup> Still others proposed that the formation of hydroxyls on the oxide support near the gold was necessary.<sup>138</sup>

In fact, the role that the support may have on a catalyst or the catalytic performance is not always well understood, and is often simply referred to as a “metal-support interaction”. In cases that lack these metal-support interactions, a support is simply considered to be a mechanical framework that keeps nanoparticle catalysts dispersed from one another. However, it is important to consider that different supports will create different catalyst-support interfaces and therefore affect the stability of a catalyst during reaction. One key parameter in this must be the interfacial energy, which will govern the catalyst shape and orientation, which can be quantitatively described by the Winterbottom construction. To study this, we use different lanthanide scandates as supports for gold catalysts because changing the lanthanide changes the lattice parameter, which can be used to affect the catalyst-support lattice (mis)match and further affect the interfacial energy. We also investigate how the change in interfacial energy affects the stability of Au catalysts during CO oxidation. We find that different catalyst orientations are possible with well lattice-matched supports and that, in the case of Au for CO oxidation, the supported particles are less active and more prone to sintering.

## 8.2. Methods

$\text{LnScO}_3$  supports were prepared as discussed in Chapter 5. Au nanoparticles were then deposited through deposition-precipitation, as follows.<sup>139</sup> An aqueous solution containing  $\text{HAuCl}_4 \cdot 3 \text{H}_2\text{O}$  and a 10:1 molar ratio of urea: Au was prepared. Then, the  $\text{LnScO}_3$  powder was added to the solution to achieve a certain weight loading of Au. The solution

was then kept at 80 °C for 16 hours. The urea decomposes in water to form  $\text{NH}_3$  to raise the pH such that  $\text{Au}(\text{OH})_3$  nanoparticles precipitate out and deposit onto the support surface and subsequently reduce to metallic gold. The samples were then washed by centrifugation in water several times. The target weight loading was well correlated with the actual weight loading determined by ICP-OES.

High resolution images of the Au nanoparticles were acquired using a JEOL ARM300F at Northwestern University operated at 300 kV, a FEI Talos at Argonne National Lab operated at 200 kV, and the Argonne Chromatic Aberration-corrected TEM (ACAT, a Cs/Cc corrected FEI Titan 80/300) operated at 200 kV. These images were taken with a parallel beam geometry and care was taken to minimize the dose rate of the electron beam to preserve the Au structures. Size distributions were obtained using the aforementioned FEI Talos in STEM mode.

The activity and stability of the  $\text{LnScO}_3$ -supported Au catalysts during CO oxidation was studied to see what effect different  $\text{LnScO}_3$  supports would have. Samples were subjected to temperatures between 50 °C and 350 °C at 25 °C or 50 °C intervals in a gas feed of 4:1  $\text{O}_2$ :CO. The conversion of CO to  $\text{CO}_2$  was measured to determine the activity. The stability was investigated by tracking the change in rate as a function of time at 250 °C for 12 hours in a 4:1  $\text{O}_2$ :CO mixture feed.

### 8.3. Size and Orientation of Supported Au Nanoparticles

Different weight loadings of Au were deposited onto the various supports in an effort to affect the size of the gold nanoparticles; as said before, the activity of gold has been found to be a strong function of the particle size.<sup>140</sup> While the average particle size did increase with weight loading, the size was also dependent on the support used, potentially

a result of the different number of nucleation sites on each support (proportional to the support surface area) and the different interfacial energies.

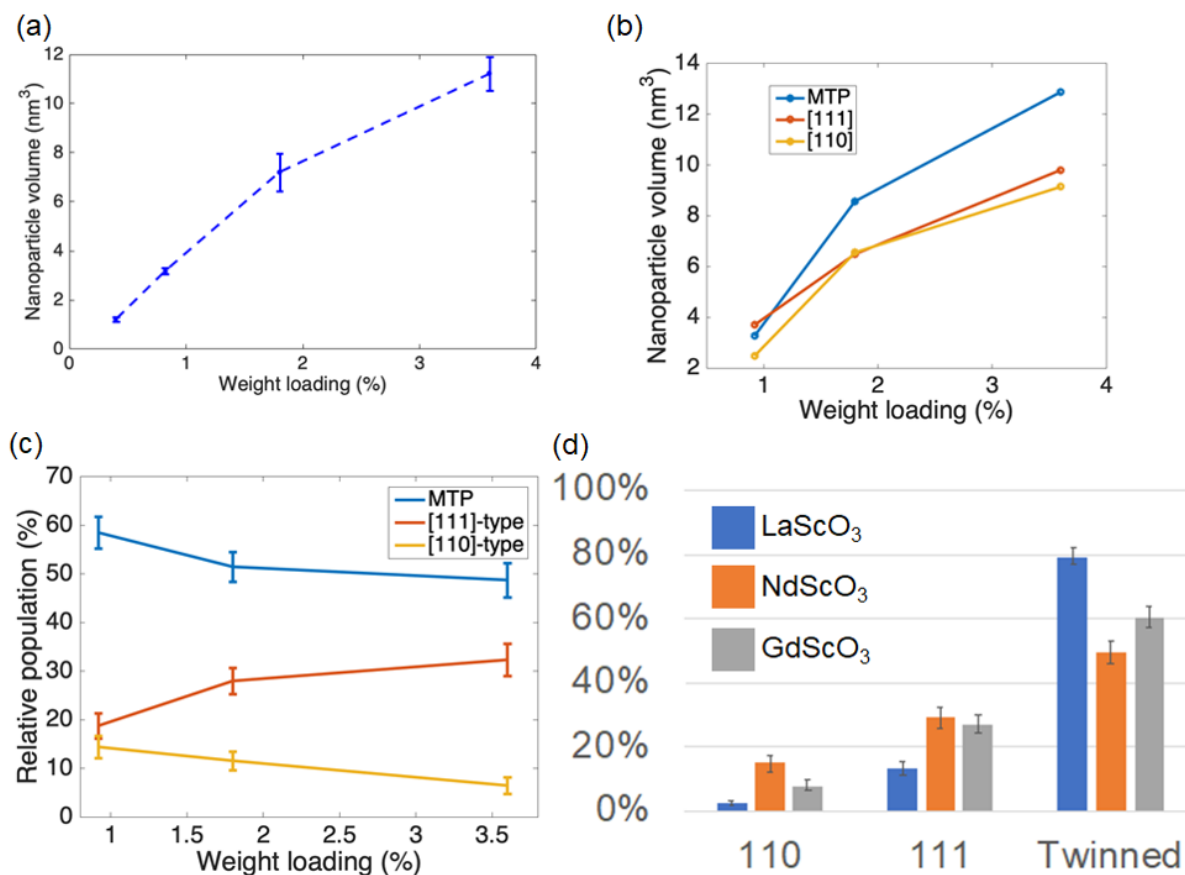


Figure 8.1. The nanoparticle volume of Au on NdScO<sub>3</sub> as a function of weight loading (a) for the particles as a whole and (b) for the different populations types. The relative populations of {110}, {111}, and multiply-twinned particles (c) as a function of weight loading on NdScO<sub>3</sub> and (d) as a function of support at a fixed weight loading of 0.4% Au.

There were three main populations of gold nanoparticles found. A plurality of the particles had multiple twins, which primarily led to particles terminated in {111} surfaces; several different examples are shown in Figure 8.2. The other populations were single-crystalline particles but with different orientations atop the support. The shape of the

single crystals followed the expected Wulff construction of a truncated octahedra (a type of tetradecahedron, or a 14-faced polyhedron), where there were 6 square faces terminated with the  $\{100\}$  surface and 8 hexagonal faces terminated with the  $\{111\}$  surface. When this was the case, it was usually the  $\{111\}$  plane of the gold that interfaced with the support; as the  $\{111\}$  surface is the most close-packed, it has the lowest surface energy. The last population had the rectangular  $\{110\}$  surface of the gold atop the square lattice of the pseudocubic- $\{100\}$  support. For completeness, a few particles were found that showed cube-on-cube epitaxy, where the  $\{100\}$  face of the metal lined up with the pseudocubic- $\{100\}$  facet of the support.

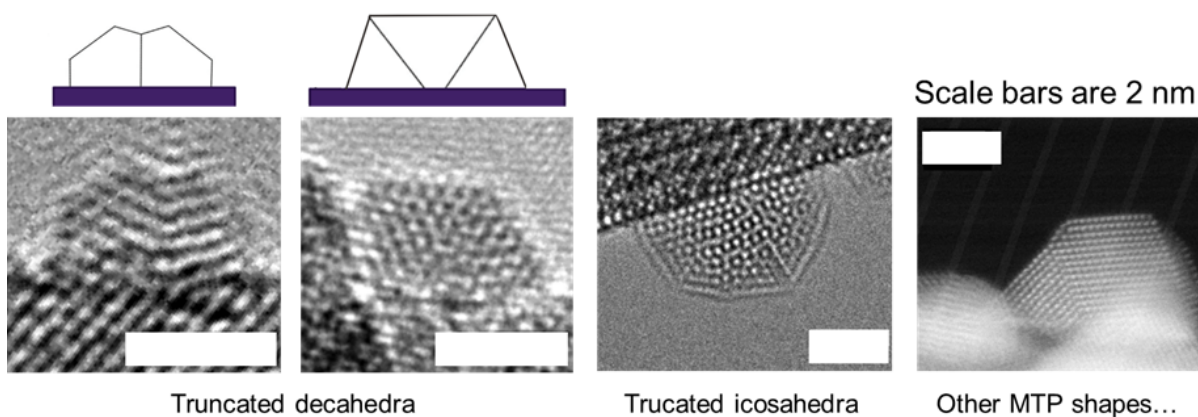


Figure 8.2. Examples of gold as truncated decahedra, icosahedra, and other MTP shapes on  $\text{LnScO}_3$ .

The orientation of the catalyst on the support is determined by the Winterbottom construction, which is a function of the surface energy of the support face, the catalyst face, and the interfacial energy between the two. The orientation that minimizes the sum of these energies is chosen. Since the support surfaces investigated were the pseudocubic- $\{100\}$  faces, that is a constant for any given  $\text{LnScO}_3$  support (and likely does not

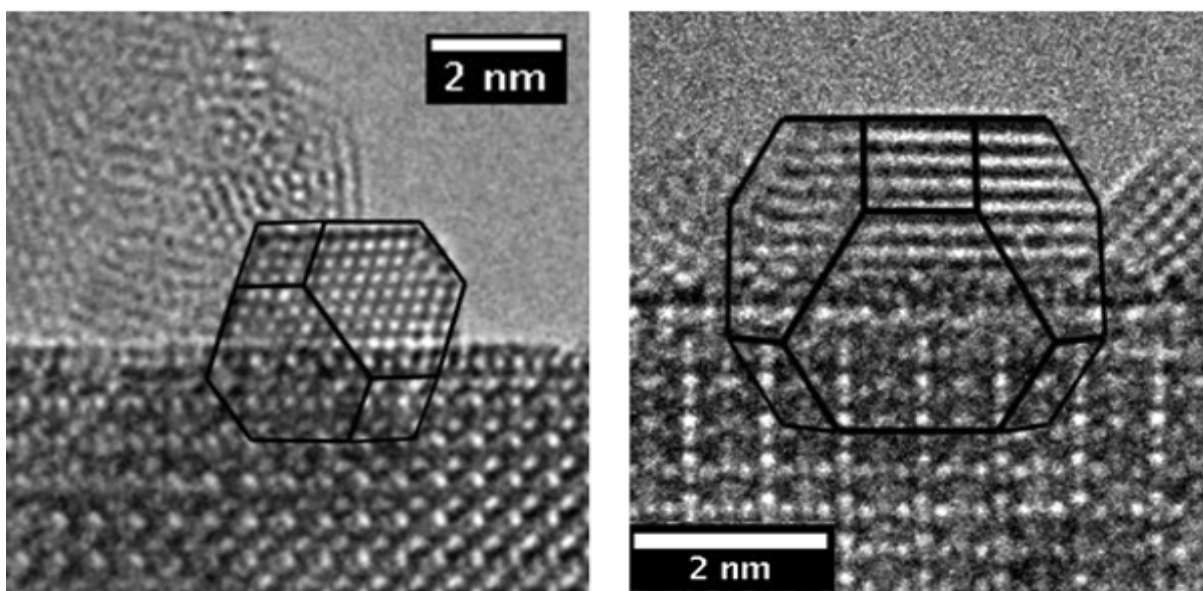


Figure 8.3. Representative image of  $\text{LnScO}_3$ -supported Au with the gold oriented with the  $\{111\}$  facet on the surface.

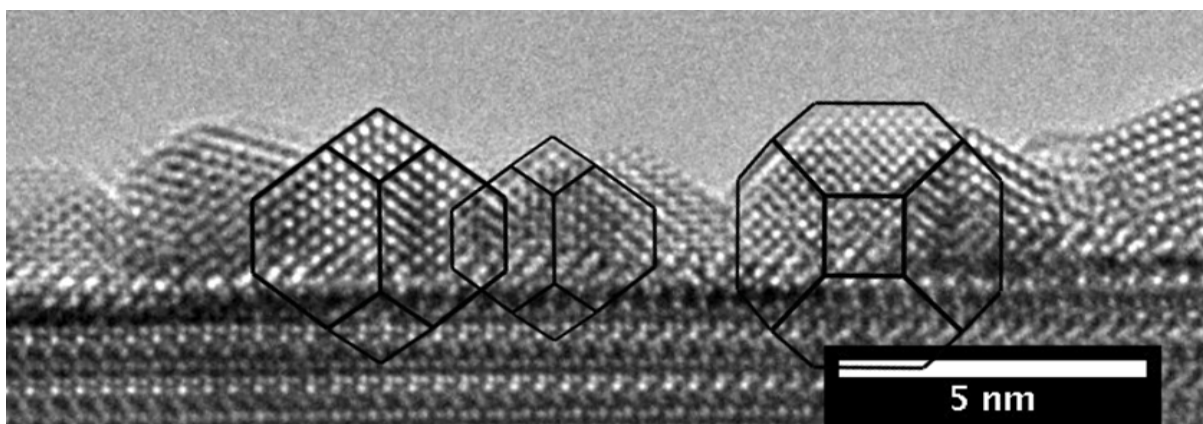


Figure 8.4. Representative image of  $\text{LnScO}_3$ -supported Au with the gold oriented with the  $\{110\}$  facet on the surface.

vary much across the  $\text{LnScO}_3$  series). Therefore, any change in orientation is dependent only on the surface energy of the facet orientation chosen and its interfacial energy with the pseudo-cubic- $\{100\}$   $\text{LnScO}_3$  (which will vary across the series owing to the different degrees of lattice matching). Since multiple populations of orientations are observed, the

energies associated with the different orientations must be similar. Starting with the surface energies of the different gold surfaces, the three lowest in energy are the ones with low Miller indices, namely the {111}, {100}, and {110}, in that order. As a result, if there was no effect from the interfacial energy, the gold would prefer to sit with the {111} orientation. The other observed population had the {110} orientation, which not only has a higher surface energy than the {111} surface but also a higher surface energy than the {100} surface! The fact that this orientation forms at all indicates that it must be stabilized by some favorable interfacial energy with the support.

Rather than follow a monotonic trend across the lanthanide series, the highest proportion of the {110} population is observed on NdScO<sub>3</sub> (Figure 8.1). Looking deeper, the proportion of this population decreases with decreasing particle size. To reconcile this behavior, the relationship between the lattice parameter of the support and the lattice parameter of the gold is considered. At first glance in Figure 8.5, one might think that the least amount of strain would be on LaScO<sub>3</sub>, with an increase in the amount of compressive strain as one moves along the series. However, this is true only considering the bulk lattice parameter of gold. As the gold particle size decreases, the ratio of the surface area to the volume increases. Owing to the dangling bonds present by exposing a surface, the lattice parameter of the surface contracts to minimize the underbonding. Therefore, as the particle size decreases, the lattice parameter does as well; the lattice parameter of gold can decrease as much as 1-3% for particles smaller than 5 nm in diameter.<sup>141,142</sup> With this, the smallest lattice strain is not found on LaScO<sub>3</sub>, but rather is size dependent. For particles roughly 2 nm in size, a lattice contraction of roughly 1.5% is expected, which would decrease the lattice parameter to 4.008 Å, which is in excellent agreement with the

pseudo-cubic lattice parameter of  $\text{NdScO}_3$  (4.009 Å). The largest proportion of {110}-oriented particles was found for smaller Au particles on  $\text{NdScO}_3$ . Therefore, the most favorable interfacial energy between the {110}-surface and support occurs when the lattice parameters are similar. When the lattice parameters begin to deviate, the interfacial energy would increase, resulting in a higher proportion of {111}-oriented particles.

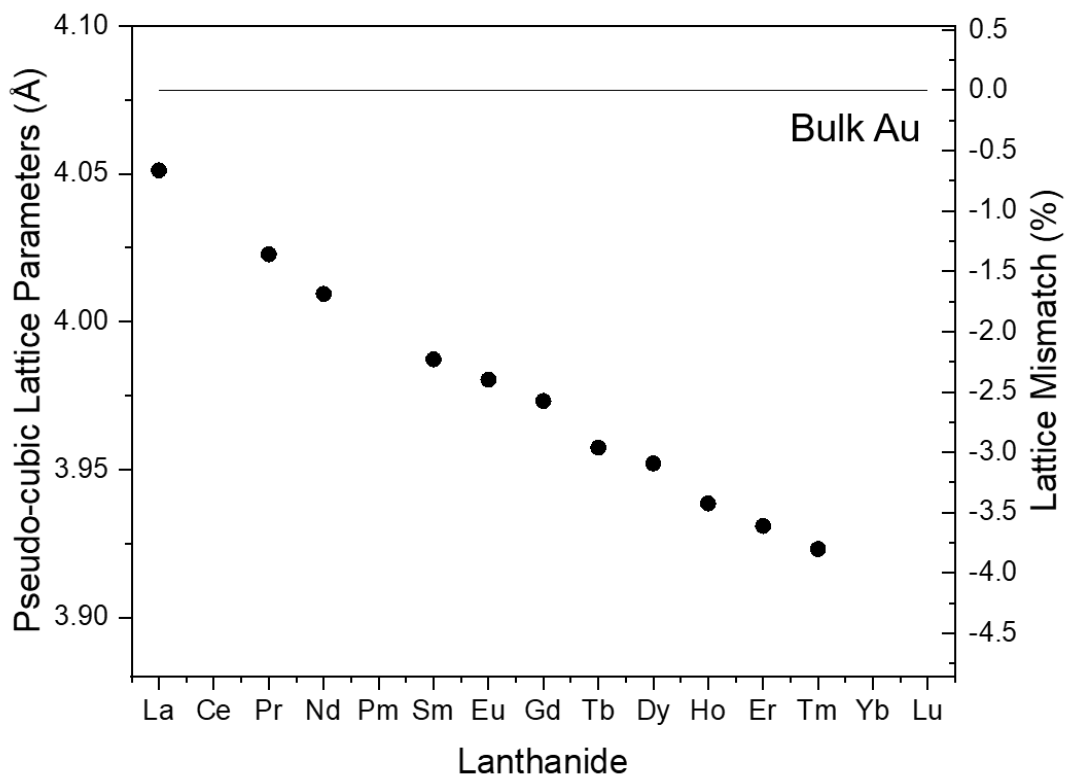


Figure 8.5. The lattice parameters of the different  $\text{LnScO}_3$  and the lattice mismatch with the lattice parameter of bulk gold.

#### 8.4. CO Oxidation and Sintering

The activity and stability of the LnScO<sub>3</sub>-supported Au catalysts during CO oxidation was studied to see what effect different LnScO<sub>3</sub> supports would have. In all cases discussed here, an attempted weight loading of 0.4% was used; the actual weight loadings were 0.58%, 0.57%, and 0.72% on LaScO<sub>3</sub>, NdScO<sub>3</sub>, and GdScO<sub>3</sub>, respectively. Experiments investigating the activity and stability on other weight loadings are in progress. TEM was used to determine the average particle size, as its activity is supposed to be strongly dependent on the size. The as-grown samples are fairly similar in size, with gold diameters of  $2.23 \pm 0.56$ ,  $1.29 \pm 0.49$ , and  $1.55 \pm 0.34$  nm on LaScO<sub>3</sub>, NdScO<sub>3</sub>, and GdScO<sub>3</sub>, respectively. Normalized to the weight of Au, the activity is greatest when Au is deposited on GdScO<sub>3</sub> and lowest on NdScO<sub>3</sub>, despite the gold particle size being smallest on NdScO<sub>3</sub>. Nonetheless, apparent activation energies calculated through an Arrhenius relationship showed little change across the support series, all being roughly 17 kJ/mol (Figure 8.6), suggesting a similar mechanism for each sample. Since Au/NdScO<sub>3</sub> had the highest population of {110}-orientated samples and were the least active, it could suggest that {110}-orientated particles are particularly inactive.

The stability was investigated by tracking the change in rate as a function of time (Figure 8.7). Typically, there are three ways a catalyst may deactivate: sintering, coking, or poisoning. Coking is more common with reactions involving hydrocarbons where a carbonaceous solid (called coke) covers the surface of the catalyst and blocks the active sites. Poisoning occurs when reactants, products, or impurities in the feed chemisorb irreversibly (under the reaction conditions) onto the catalyst surface, effectively occupying

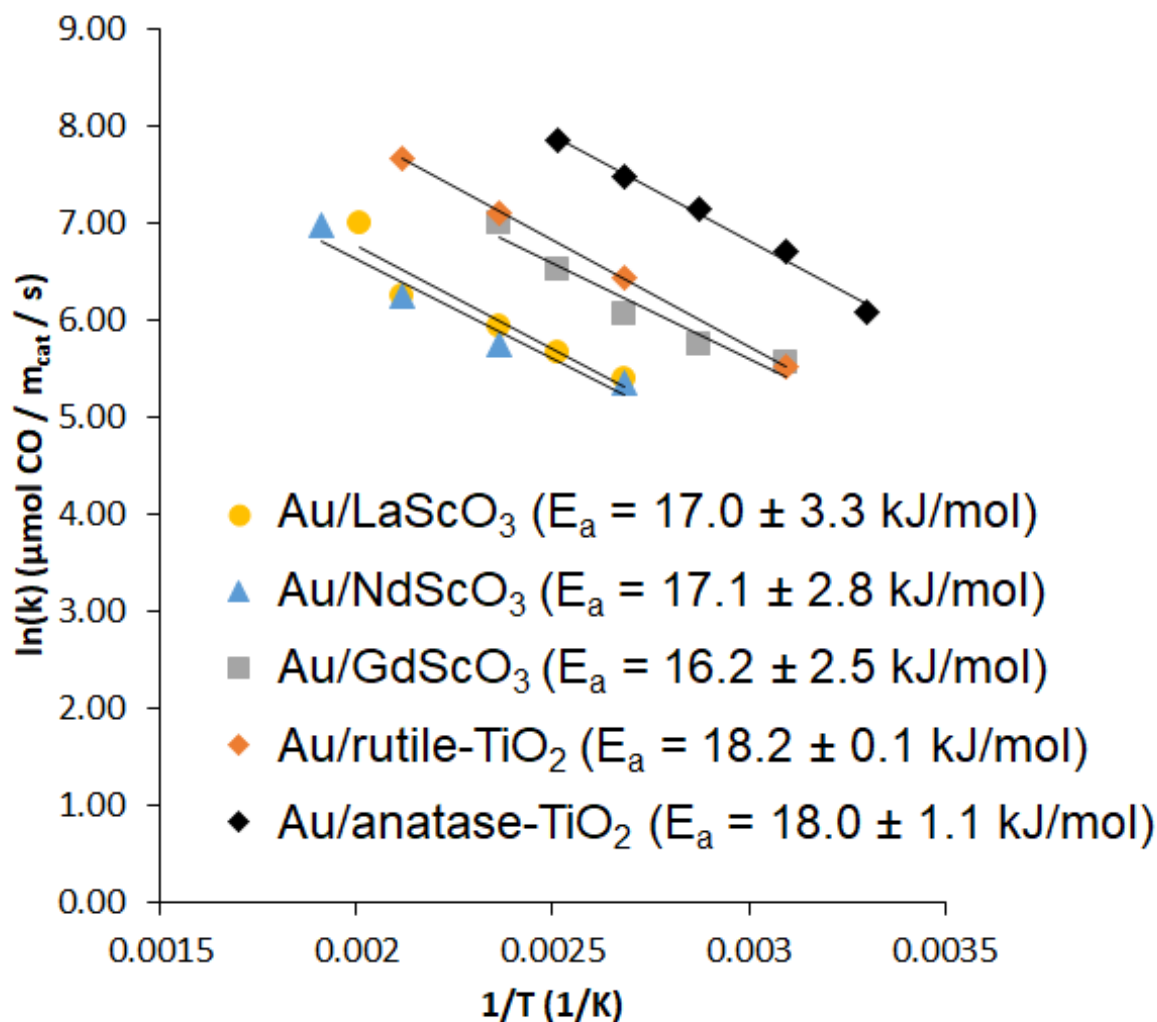


Figure 8.6. The Arrhenius relationship between the CO oxidation rate and the temperature for the various Au/LnScO<sub>3</sub> and Au/TiO<sub>2</sub>.

the active site permanently and preventing further reaction. Sintering reduces the activity because the loss of surface area from particle growth results in a loss of active sites.

After the 12 hrs of CO oxidation, the particle sizes were found to have increased, reaching  $3.22 \pm 1.1$ ,  $3.32 \pm 1.2$ , and  $2.39 \pm 0.88$  nm on LaScO<sub>3</sub>, NdScO<sub>3</sub>, and GdScO<sub>3</sub>,

which are increases of 44%, 158%, and 54%, respectively. Sintering is typically modeled as a second-order decay of activity with time; solving this further finds that the inverse of the activity increases linearly with time. Following this model, a deactivation constant could be calculated. Gold on LaScO<sub>3</sub> and GdScO<sub>3</sub> deactivated at about the same rate, whereas Au/NdScO<sub>3</sub> deactivated roughly twice as quickly. These two results are consistent, suggesting that Au sinters more significantly and therefore deactivates more quickly on NdScO<sub>3</sub> than LaScO<sub>3</sub> or GdScO<sub>3</sub>.

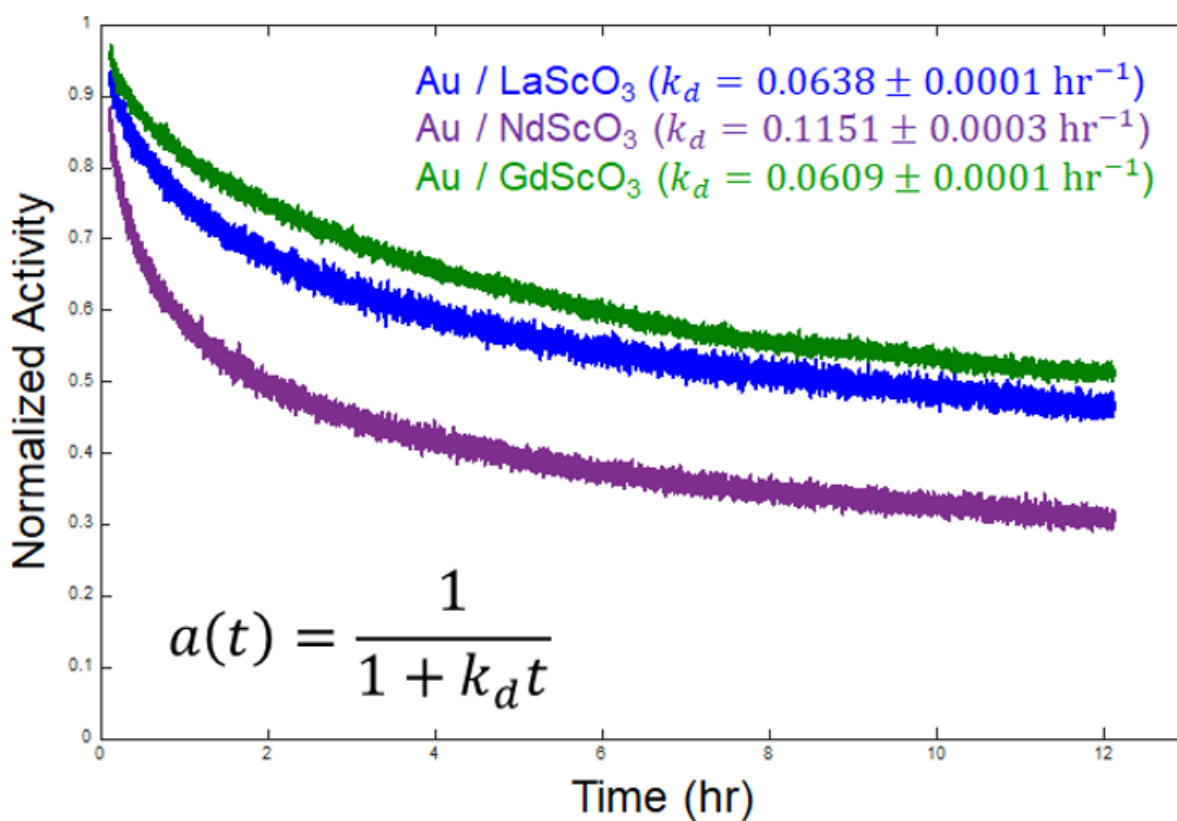


Figure 8.7. The change in activity (normalized to the initial activity) as a function of time.

## 8.5. Conclusion

LnScO<sub>3</sub>-supported Au catalysts were synthesized and investigated to see how the interfacial energy between the catalyst and support further affected the stability of the catalysts during CO oxidation. When the lattice parameters of the LnScO<sub>3</sub> (dependent on the Ln used) and gold (size-dependent) were most similar, the interfacial energy favored the formation of {110}-oriented particles; as the lattice parameters were further apart, {111}-oriented particles were favored because of the low surface energy of the {111}-surface. The CO oxidation rate was slowest and deactivated the quickest on NdScO<sub>3</sub>, when these {110}-oriented particles were most prevalent. Further investigations using different Au nanoparticle sizes and adding SmScO<sub>3</sub> as a support are in progress so the results herein are preliminary and more data may suggest a different explanation.

## CHAPTER 9

## Strain Engineering for CO Chemisorption on Platinum Nanoparticles

While strain engineering is a common practice in thin films, it has not been well explored experimentally in heterogeneous catalysis. In this chapter, we use the faceted  $\text{LnScO}_3$  nanoparticles developed here as a means to introduce strain in Pt nanoparticles, where larger  $\text{Ln}^{3+}$  ions lead to larger  $\text{LnScO}_3$  pseudo-cubic lattice parameters and increased tensile strain in the Pt. Temperature-programmed desorption and infrared spectroscopy was used to understand how the binding of CO changed as a function of strain. We find that, with increasing tensile strain, the proportion of CO bound in a bridged configuration and the amount of more weakly bound CO both increased.

Particular thanks to Emily Greenstein for helping run many of the experiments in this chapter. Zachary Mansley performed the electron microscopy and Dr. Ryan Hackler (initially from Prof. Peter Stair's group and now with Dr. Massimiliano Delferro at Argonne National Laboratory) performed the atomic layer deposition of the platinum nanoparticles.

### 9.1. Introduction

Heterogeneous catalysts rely on the adsorption of reactants onto the catalyst surface. The binding of the adsorbates to the catalyst can depend on many electronic and structural features of the catalyst. Historically, in order to achieve different binding strengths,

using different metals or applying electrochemical potentials have been necessary. Platinum metal, for example, typically binds CO strongly, which leads to deactivation through CO poisoning. One variable that has not been well explored experimentally is strain. While the effect of strain on the electronic structure has been computationally explored, the effect of this in real catalysts has not yet been well investigated, with only electrocatalytic cases or unsupported metals being investigated. A difficulty in studying this effect in typical heterogeneous catalysts is the apparent lack of thermally stable crystalline supports with appropriate lattice parameters. Strained metal catalysts are usually made by depositing the metal on another metal which creates a ligand effect, where the base metal may now accept electrons from or donate electrons to the metal catalyst of interest, which would further affect the binding properties. In this chapter, we use crystalline  $\text{LnScO}_3$  particles as supports, as the lattice parameter of the support can be varied by selecting different lanthanides, so a variable amount of tensile strain can be epitaxially applied. The effect of this strain on the binding of CO will be explored.

## 9.2. Methods

Faceted  $\text{LnScO}_3$  nanoparticles were prepared as outlined in Chapter 5. Platinum nanoparticles were then deposited onto the supports through atomic layer deposition. Trimethyl(methylcyclopentadienyl)platinum(IV) ( $\text{MeCpPtMe}_3$ ) and ozone were used as the platinum source and counter-reagent, respectively.  $\text{MeCpPtMe}_3$  was kept in a bubbler at 50 °C to achieve a partial pressure of 0.05 torr and the ozone had a partial pressure of 0.2 torr. First, the samples were cleaned in 400 sccm 10%  $\text{O}_3$  in  $\text{O}_2$  at 200 °C. A 90 sccm flow of  $\text{N}_2$  was used as a carrier gas and created a base pressure of 0.9 torr. Then a 200 s pulse of  $\text{MeCpPtMe}_3$  was introduced into the sample chamber with the vacuum closed,

creating a “static” pulse. Afterwards the vacuum was reopened and the sample chamber was purged with  $N_2$  for 50 s. The hydrocarbon ligands on the Pt precursor were then oxidized and removed using a 200 s ozone pulse which was purged afterwards with 50 s of the  $N_2$  purge. A single one of these “MeCpPtMe<sub>3</sub> static pulse -  $N_2$  purge - ozone pulse -  $N_2$  purge” ALD cycles was used, but an increased number of cycles would increase the total Pt deposition. Pulse chemisorption experiments were run using an AMI-200 with CO as a probe molecule to determine the surface area of the metal. 100 mg of sample was mixed with sand as a diluent. The samples were first heated to 300 °C in He. The sample was kept at that temperature for 1.5 hrs, where the first 30 min were in  $H_2$  to reduce any platinum oxide surface species. As this produces CO that could adsorb onto the Pt surface (see Chapter 10), the last hour was spent in He to give sufficient time for the CO to desorb. The sample was then cooled to 40 °C for the pulse chemisorption experiment, where 20 pulses of 595  $\mu$ L of 5% CO in He were injected. Unadsorbed gas passed through a TCD to measure its amount. Imaging of the Pt nanoparticles was done using a JEOL JEM-2100 FasTEM operated at 200 kV in TEM mode.

A typical pretreatment for investigating CO binding would involve heating the samples in  $H_2$  to remove any surface oxide on the metal and then cooling back to room temperature. After, a background spectrum would be collected under an Ar gas flow and CO would then be flowed over the sample under saturation. Doing just that, Figure 9.1 shows that resulting spectra. Of particular note and concern is that a negative peak appears on the Pt/GdScO<sub>3</sub> sample; such a feature suggests that a species that was absorbing at some wavenumber prior to the introduction of CO no longer is. One such cause could be

increasing CO saturation, which would shift the peaks towards higher wavenumbers and result in a negative peak where the initial CO was absorbing.

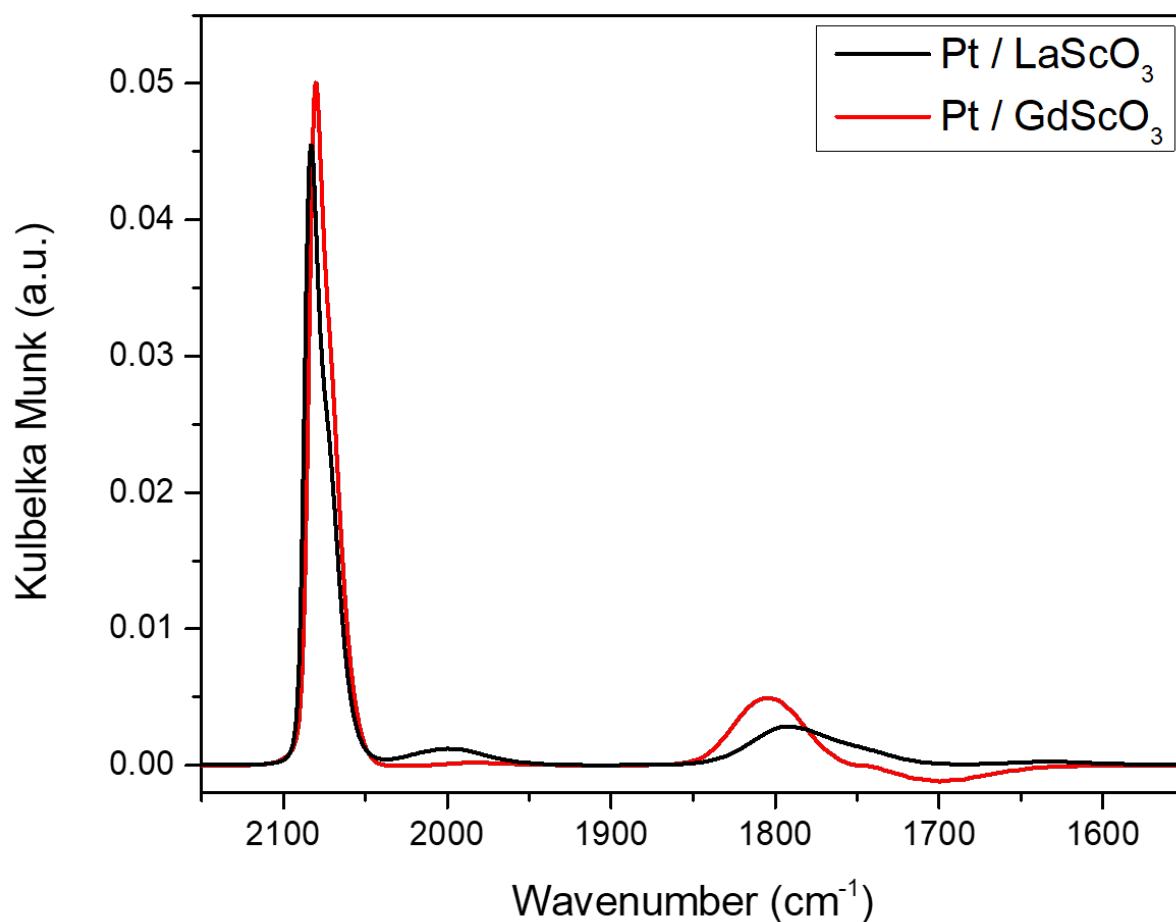


Figure 9.1. DRIFTS spectra of CO adsorbed on Pt after reduction in H<sub>2</sub>.

As discussed in Chapter 10, this CO was produced via the reverse water-gas shift (RWGS) reaction between hydrogen and CO<sub>2</sub>-containing groups on the basic oxide surface. Simultaneous TGA-DTA-GC-MS was performed on an as-grown LaScO<sub>3</sub> support (Figure 9.2), which showed that CO<sub>2</sub> loss was observed over the entire temperature range, confirming that the samples contained CO<sub>2</sub> prior to the DRIFTS experiment. To confirm

that CO was then produced after the H<sub>2</sub> pretreatment over the catalyst, DRIFTS was performed before and after the pretreatment. As shown in Figure 9.3, there is a clear peak from CO absorption after the H<sub>2</sub> flow. However, if the sample is maintained at high temperature in Ar, CO desorbs and its peak weakens completely after roughly an hour. Therefore, all investigations of CO binding on metals supported on basic oxides should include a prolonged period at temperature post-reduction in order to fully desorb any CO that formed from the RWGS reaction. Doing so will prevent any premature CO binding and prevent any negative peaks. With this pretreatment in mind, DRIFTS could be performed to investigate how CO bound differently on Pt as a function of different LnScO<sub>3</sub>,<sup>143</sup> which varied the tensile strain on the Pt nanoparticle.

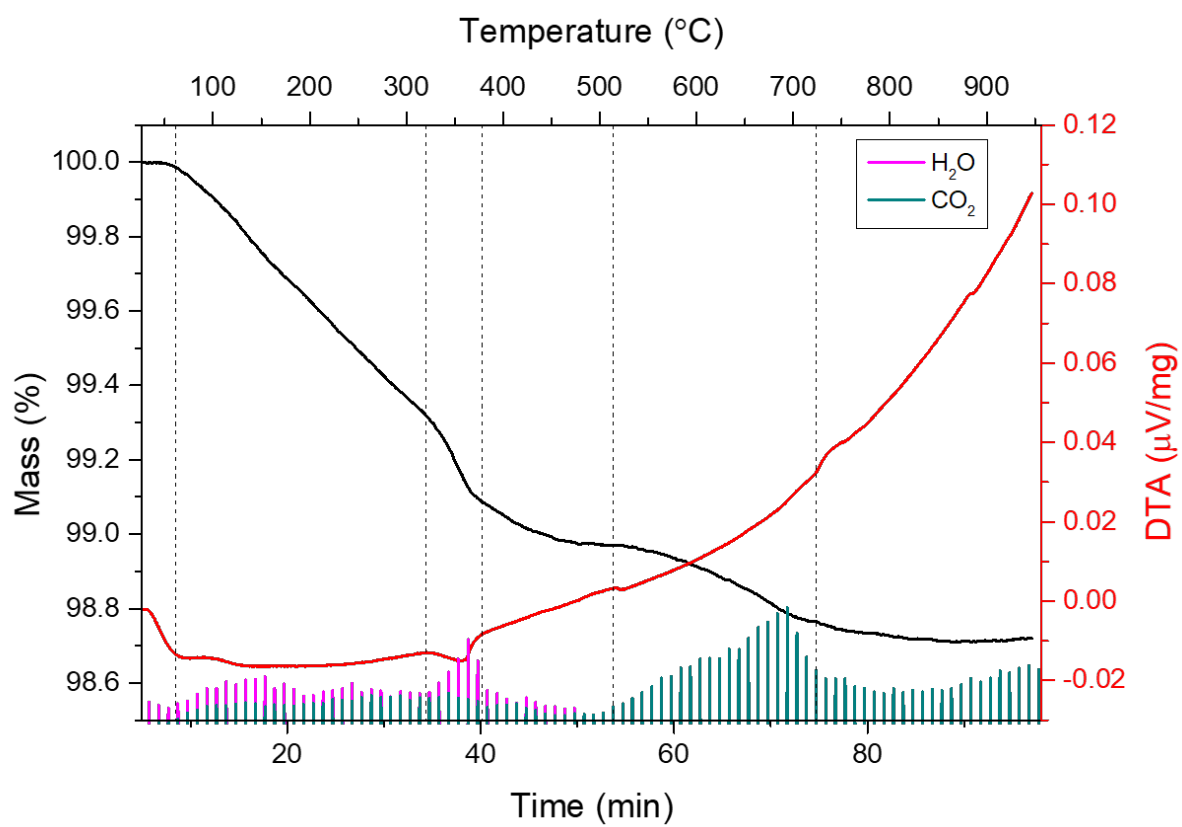


Figure 9.2. Simultaneous TGA-DTA-GC-MS on a bare  $\text{LaScO}_3$  support.

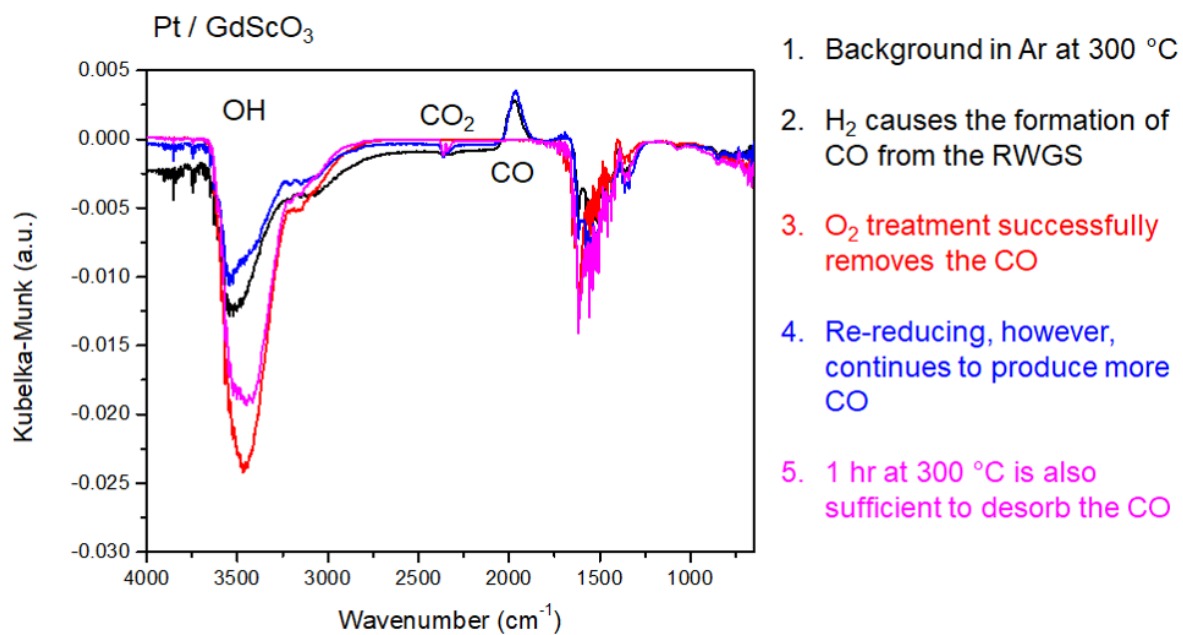


Figure 9.3. DRIFTS spectra collected at 300 °C during typical catalyst pretreatment.

### 9.3. Results

Using high-resolution electron microscopy, the size of the Pt nanoparticles were found to be monodisperse and similar on the different supports used, with Pt particle diameters of  $1.63 \pm 0.34$  nm,  $1.46 \pm 0.28$  nm, and  $1.65 \pm 0.31$  nm on  $\text{LaScO}_3$ ,  $\text{NdScO}_3$ , and  $\text{SmScO}_3$ , respectively. DRIFTS with CO as a probe molecule was used to characterize the different CO binding sites (Figure 9.5). Each sample was first treated at 300 °C with hydrogen for 30 min to remove any surface oxide and then argon for another hour to remove any CO produced via the reverse water-gas shift (see Chapter 10). Afterwards, the sample was brought back down 30 °C for CO to be chemisorbed onto the Pt surface. Most metallic platinum binds CO linearly, which absorbs from roughly 2000 to 1900  $\text{cm}^{-1}$ . CO binding may also be shared between several Pt atoms; CO bridged between two Pt atoms absorbs near 1900 to 1700  $\text{cm}^{-1}$  or between 3-4 Pt atoms near 1700 to 1500  $\text{cm}^{-1}$ . Afterwards, the sample was heated at 5 °C/min to see how the different bindings desorbed. Pt on  $\text{LaScO}_3$  shows a higher percentage of these bridged sites, whereas Pt on  $\text{NdScO}_3$  and  $\text{SmScO}_3$  shows primarily linear CO.

Temperature-programmed desorption was performed after CO chemisorption to characterize the binding strength of the CO (Figure 9.6). Since the  $\text{LnScO}_3$  dehydrates in this temperature range as well, gas chromatography was performed simultaneously to determine the temperature of maximum CO desorption specifically. All samples showed two local maxima for CO desorption, implying two different CO binding strengths. The higher temperature peak was 590 °C, 600 °C, and 587 °C, and the lower temperature peak was at 487 °C, 501 °C, and 405 °C, on Pt supported on  $\text{LaScO}_3$ ,  $\text{NdScO}_3$ , and  $\text{SmScO}_3$ , respectively.

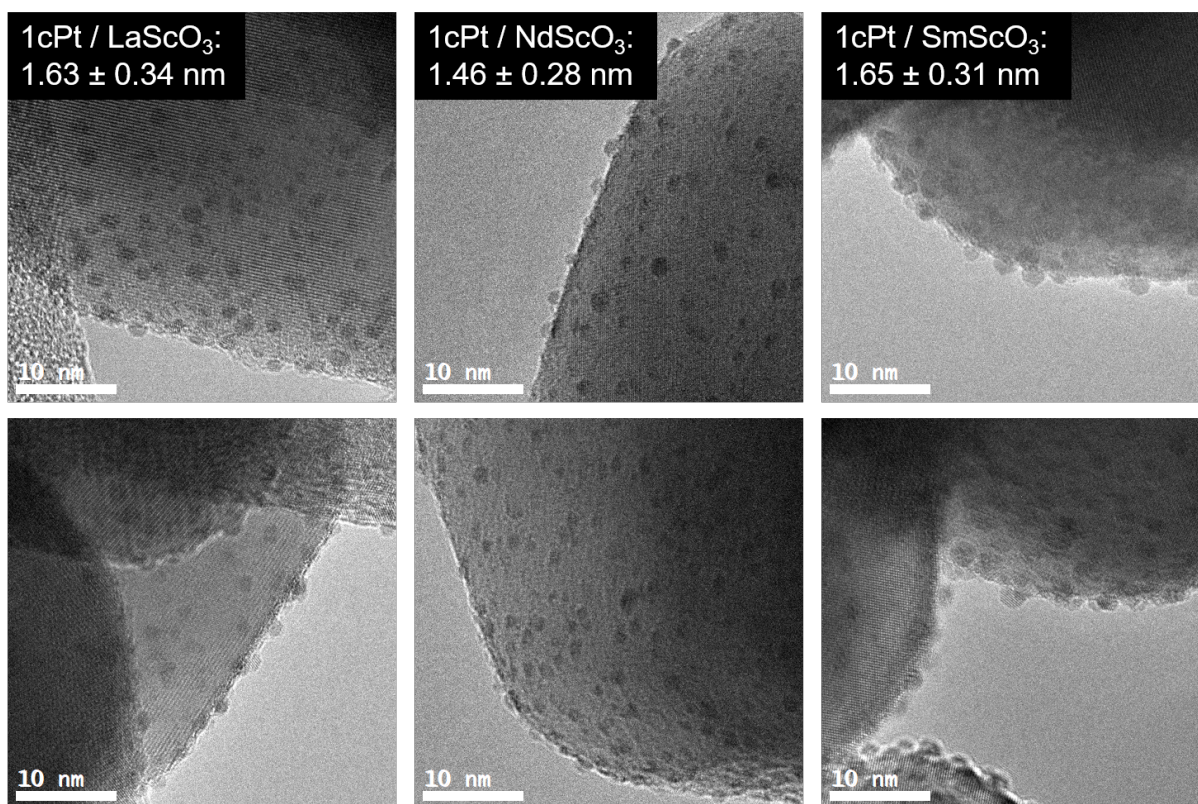


Figure 9.4. Representative HRTEM images of Pt dispersed on (left) LaScO<sub>3</sub>, (center) NdScO<sub>3</sub>, and (right) SmScO<sub>3</sub>.

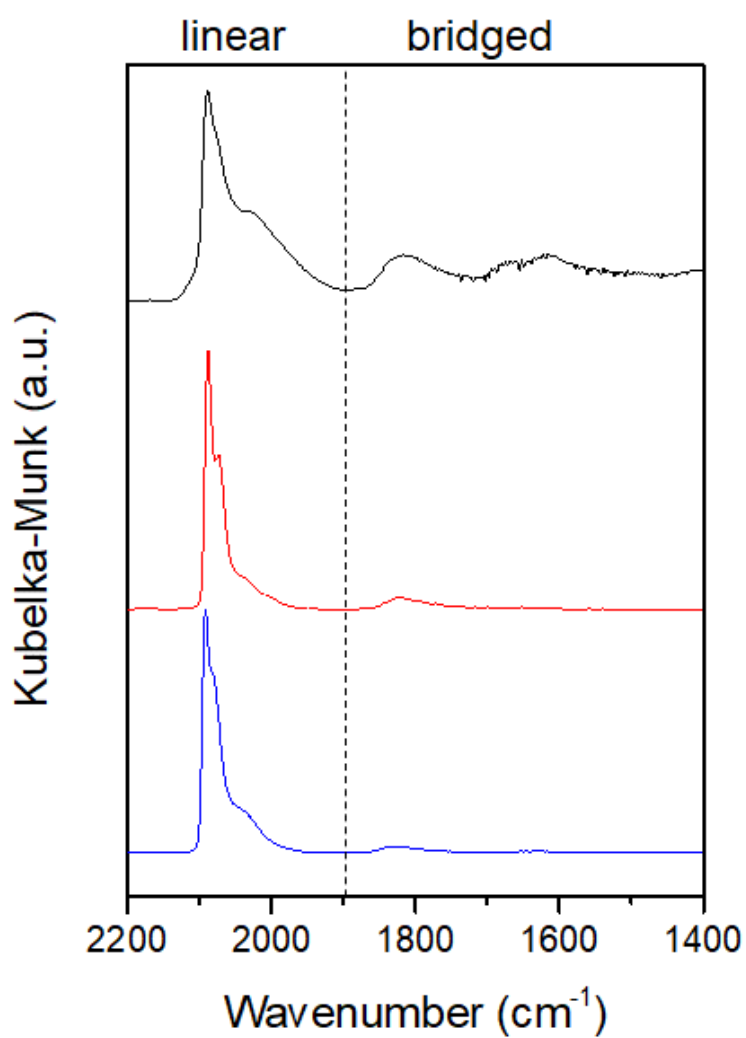


Figure 9.5. DRIFTS spectra of CO chemisorbed on Pt/LnScO<sub>3</sub>.

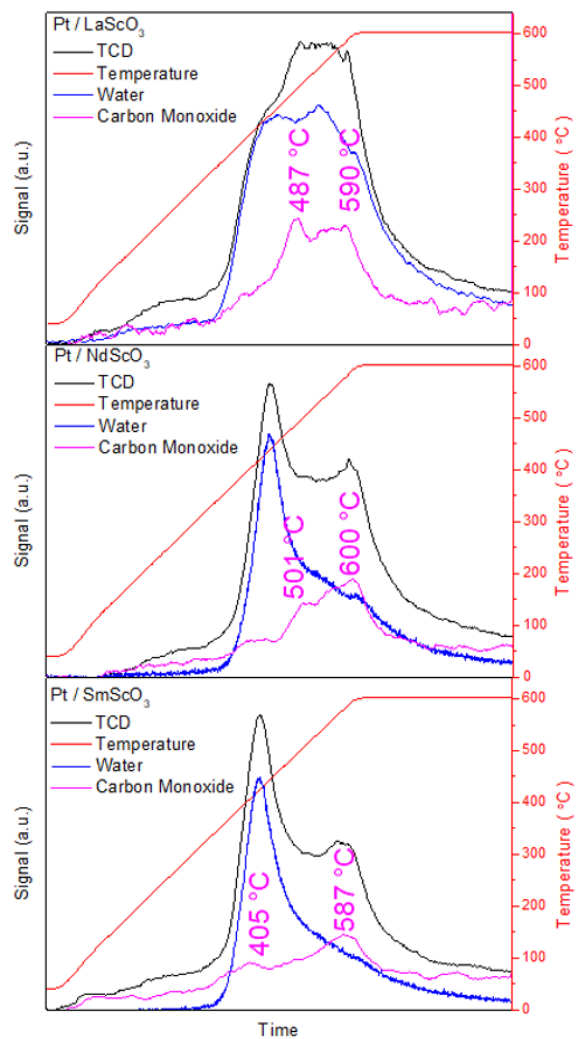


Figure 9.6. Temperature-programmed desorption of CO that had been chemisorbed on Pt/LnScO<sub>3</sub>. Black shows the TCD signal, which is representative of all gasses (other than hydrogen or helium), red shows the temperature, blue shows the MS signal from the water, and magenta shows the MS signal from the CO.

## 9.4. Discussion

Similar particle diameters were observed for all the Pt samples, on average 1.63, 1.46, and 1.65 nm. The particle sizes are also fairly monodisperse, all with standard deviations of about 0.3 nm. Owing to the small particle sizes, it is unlikely for the Pt metal lattice to fully relax to its bulk value. Defining the strain to be relative lattice mismatch between the bulk lattice parameters of Pt and the given LnScO<sub>3</sub>, tensile strains of 3.23%, 2.17%, and 1.61% on LaScO<sub>3</sub>, NdScO<sub>3</sub>, and SmScO<sub>3</sub>, respectively, can be obtained. We note now here that the actual lattice parameter for Pt nanoparticles is size dependent, with a contraction of the lattice parameter with decreasing Pt diameters. Since the particle sizes across the different supports are relatively unchanged, we assume that a similar lattice contraction would occur in each case and therefore increase the amount of tensile strain by the same amount.

DRIFTS of CO chemisorbed on Pt inform to the binding configuration of the CO on the Pt. Typically, Pt nanoparticles shows that CO is bound linearly atop Pt atoms. The bands from 2150 to 1900 cm<sup>-1</sup> were attributed to CO bound linearly atop the Pt, whereas the bands from 1900 to 1500 cm<sup>-1</sup> were attributed to CO bound on bridged sites (shared between 2 to 4 Pt atoms). Integrating the area between these bands acts a proxy for how much CO is bound in each configuration. Pt/LaScO<sub>3</sub> had the highest percentage of CO bound on bridged sites (55.8%), and the percentage decreased monotonically with decreasing Ln size (10.4% and 5.9% for Pt on NdScO<sub>3</sub> and SmScO<sub>3</sub>, respectively). Bridged CO sites on Pt have been correlated to be more active in several different reactions, such as CO oxidation or the water-gas shift reaction.<sup>25,145,146</sup>

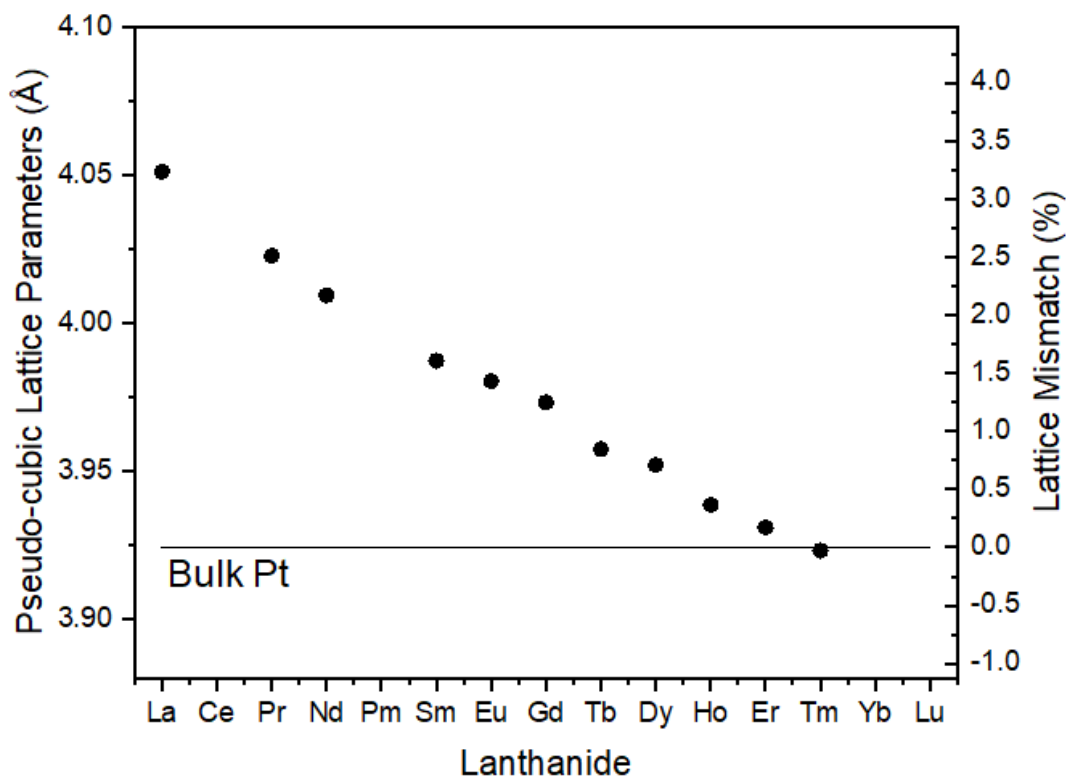


Figure 9.7. The pseudo-cubic lattice parameters of the various  $\text{LnScO}_3$ , as found in the Inorganic Crystal Structure Database (ICSD),<sup>144</sup> relative to the lattice parameter of bulk platinum.

Temperature-programmed desorption was performed after CO chemisorption to characterize the binding strength of the CO. All samples showed two local maxima for CO desorption, implying two different CO binding strengths. The binding strength of the higher temperature peak did not differ much between each sample, but was greatest for Pt/NdScO<sub>3</sub> at 600 °C, followed by 590 °C and 587 °C for Pt/LaScO<sub>3</sub> and Pt/SmScO<sub>3</sub>, respectively. However, while this peak showed the greatest desorption for Pt/NdScO<sub>3</sub> and Pt/SmScO<sub>3</sub>, it was the lower temperature peak that showed a greater desorption for

Pt/LaScO<sub>3</sub>, which implies that there are a greater percentage of weaker bound CO sites for Pt/LaScO<sub>3</sub>. The binding strength for this weaker bound CO was similar on Pt/LaScO<sub>3</sub> and Pt/NdScO<sub>3</sub> (487 °C and 501 °C, respectively), but was much more weakly bound on Pt/SmScO<sub>3</sub> (405 °C).

DRIFTS and CO TPD both show two different CO binding populations. From DRIFTS, the proportion of bridged CO sites increases with the amount of tensile strain. The most tensile strained sample, Pt/LaScO<sub>3</sub>, showed the highest percentage of weakly bound CO from CO TPD. This implies that the bridged CO is more weakly bound, so increasing the tensile strain on the Pt increases the amount of weakly bound CO sites. Temperature-programmed DRIFTS (Figure 9.8) on LaScO<sub>3</sub>-supported Pt also showed that, as the temperature increased, the peaks owing to bridged CO decreased at a faster rate than peaks owing to linear CO, further supporting that bridged CO is the weaker bound species.

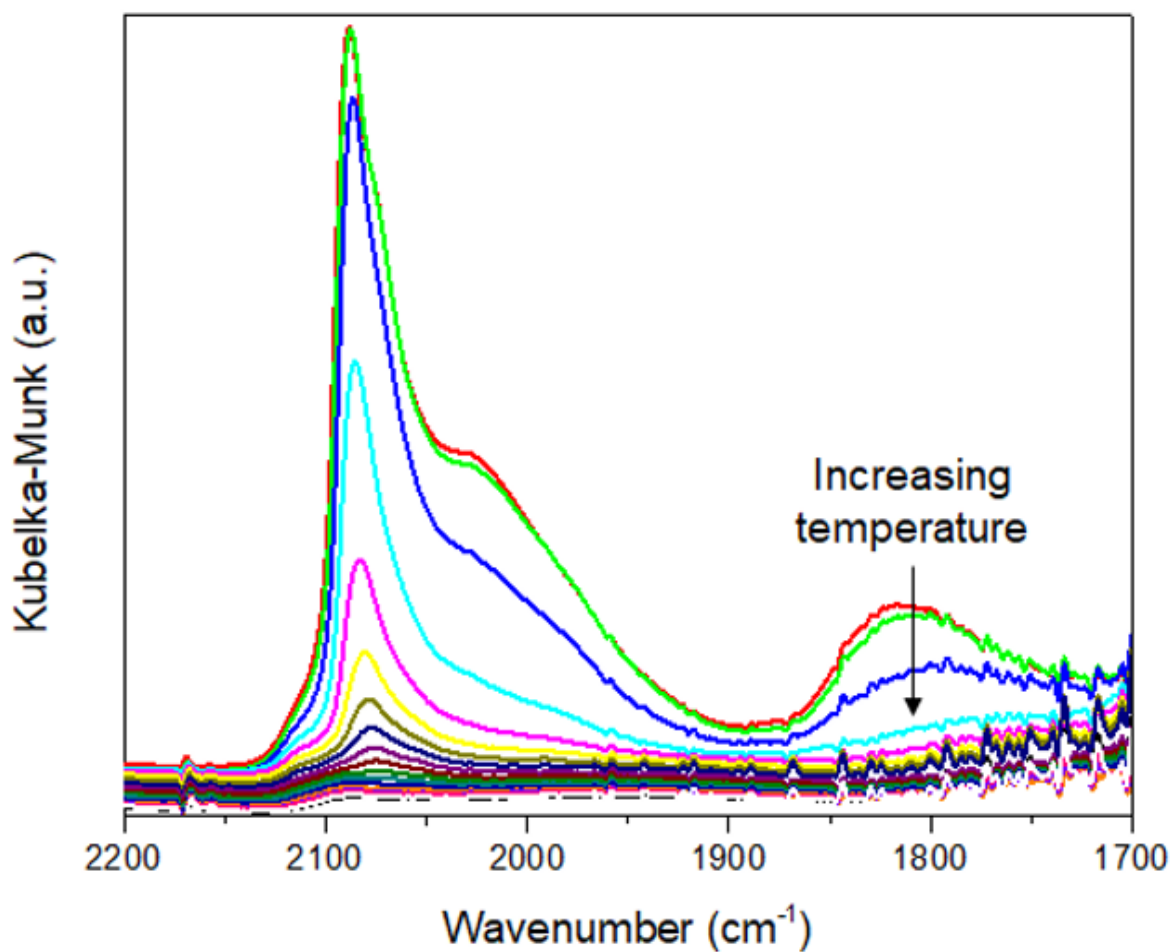


Figure 9.8. DRIFTS spectra with increasing temperature of CO bound on Pt/LaScO<sub>3</sub>.

## 9.5. Conclusion

LnScO<sub>3</sub>-supported Pt particles, where the platinum metal could experience different amounts of epitaxial tensile strain when different lanthanides were used, were explored to see the effect of strain on Pt in the binding behavior of CO. It was found that there was greater percentage of CO on bridged sites with increasing tensile strain. Further,

temperature-programmed desorption also found a distribution of sites and that the percentage of more weakly bound CO increased with tensile strain. Correlating these results suggest that bridged CO is more weakly bound and favored under increasing tensile strain. Further, the effect of strain on Pt particles may be easily probed using IR spectroscopy, with binding between a greater number of metal centers with increasing strain.

## CHAPTER 10

**CO<sub>2</sub>-Driven Reverse Water-Gas Shift and CO Oxidation over  
LnScO<sub>3</sub>-Supported Pt Catalysts**

In this chapter, we will explore how LnScO<sub>3</sub>-supported Pt nanoparticles catalyze both the reverse water-gas shift and CO oxidation reactions. CO<sub>2</sub> hydrogenation reactions like the reverse water-gas shift are good model reactions for studying catalysis at the support-catalyst interface, as the hydrogen will only readily dissociate on the metallic platinum and the CO<sub>2</sub> will only readily adsorb on basic oxide sites. Our metric for basicity (desorption temperature of acidic CO<sub>2</sub>) of the support surprisingly did not change monotonically across the lanthanide series, but was instead maximum with NdScO<sub>3</sub>. In addition, this chapter will briefly discuss methanol adsorption as a means to investigate the oxide surface basicity. The basicity of the support was then correlated to the degree of reverse water-gas shift reaction that took place according to DRIFTS and to the CO oxidation rate. Both reactions were found to be dependent on the affinity of the support for CO<sub>2</sub>, where strong CO<sub>2</sub> binding on the support led to greater CO oxidation rates and less reverse water-gas shift.

Particular thanks to Prof. Peter Stair (and his post-doc Dr. Xin Tang) for discussions regarding DRIFTS and for his talk at NAM26 in Chicago, where his group looked at the reverse water-gas shift of Pt on more traditional oxide supports, which proved to be very fruitful in the experimental design shown here. I would also like to thank Dr. Selim

Alayoglu for performing the MeOH DRIFTS and assistance in its analysis, and Dr. Ryan Hackler for doing the Pt ALD.

## 10.1. Introduction

Heterogeneous catalysts control the rate of reactions by introducing a different reaction pathway that utilizes lower activation barriers of various intermediate states through adsorption on, reaction at, and desorption off the catalyst surface. When a certain adsorbate is only bound weakly, the intermediate state does not have a strong driving force to be reached so the total reaction is not well catalyzed. On the other hand, if the adsorbate is bound strongly, the driving force to leave the intermediate state is weak so again the reaction is not well catalyzed. This is Sabatier's principle and suggests that, for every reaction, there is a descriptor that needs to be balanced to achieve maximum activity. Here, we find that the binding strength of  $\text{CO}_2$  on the support was critical in both the reverse water-gas shift and CO oxidation on  $\text{LnScO}_3$ -supported Pt catalysts.

Both CO oxidation and  $\text{CO}_2$  hydrogenation are commercially relevant catalytic reactions. Oxidation of CO into  $\text{CO}_2$  is used as a means to reduce harmful emissions of CO from automobiles. There has also been an increasing focus on reducing  $\text{CO}_2$  emissions into the atmosphere, so this  $\text{CO}_2$  may instead be captured and chemically transformed into more valuable products. One such reaction is known as the reverse water-gas shift (RWGS), in which  $\text{CO}_2$  and  $\text{H}_2$  react to form CO and water.<sup>147</sup> This reaction (and the reverse, the water-gas shift) is practiced in industry as it affects the composition of syngas (CO,  $\text{CO}_2$ , and  $\text{H}_2$ ), which is used to produce various hydrocarbons through the Fischer-Tropsch reaction, methanol, and ammonia.

$\text{CO}_2$ , as an acidic oxide, adsorbs strongly onto basic oxide sites, but very weakly onto metallic Pt.  $\text{H}_2$  dissociates strongly onto Pt but not onto some oxides. Therefore, reaction between the two likely occurs at the perimeter of the Pt-oxide interface. To highlight this and the role that the basic oxide support plays, we use  $\text{LnScO}_3$ -supported Pt catalysts as a means to study the reverse water-gas shift reaction. This system was considered for CO oxidation, where CO would now bind on the metal but there is often a question of whether the reaction occurs on the Pt metal or at the metal-oxide interface. We find that the CO oxidation rate was dependent on the  $\text{CO}_2$  binding strength of the support, implying that this reaction occurs for this system at the metal-support interface.

## 10.2. Methods

Faceted  $\text{LnScO}_3$  nanoparticles were prepared as outlined in Chapter 5. Temperature-programmed desorption of the supports as synthesized was performed on an Altamira AMI-200 in REACT, where 100 mg was heated at 10 °C/min to 800 °C to fully desorb any water and  $\text{CO}_2$ . Simultaneous TGA-DTA-GC-MS was also performed on  $\text{LaScO}_3$  to show that desorption at lower temperatures was of water and only desorption at higher temperatures was of carbon dioxide (see Chapter 3 for more information about dehydration of the rare-earth hydroxides). The temperature of maximum carbon dioxide desorption was used as a proxy for the basicity of the supports. DRIFTS of MeOH chemisorbed onto  $\text{LaScO}_3$ ,  $\text{La}_2\text{O}_3$ , and  $\text{Sc}_2\text{O}_3$  on a Nicolet 6700 FT-IR in REACT was also used to characterize their chemical basicity. There, the samples were pretreated by flowing 10%  $\text{O}_2$  in Ar at 260 °C. MeOH chemisorption was accomplished at 65 °C with a 10%  $\text{O}_2$  in Ar carrier gas flowing at 40 sccm over 50  $\mu\text{L}$  of methanol.

Platinum nanoparticles were then deposited onto the supports through atomic layer deposition as discussed in Chapter 9. DRIFTS was performed to investigate the reverse water-gas shift reaction as a function of time and temperature. First, oxygen gas was flowed over the sample to remove any and all CO that may have already been adsorbed to the Pt surface. Next, carbon dioxide was flowed to saturate the LnScO<sub>3</sub> surface with CO<sub>2</sub>-containing groups. The reactor was then purged with Ar and hydrogen was introduced into the system. This produced CO that could subsequently be adsorbed onto Pt surface and detected with DRIFTS. Lastly, CO was flowed over the sample to saturate the Pt surface with CO. This O<sub>2</sub>-CO<sub>2</sub>-H<sub>2</sub>-CO procedure was performed several times at various different temperatures.

CO oxidation reactions were studied using an Altamira BenchCAT 4000 batch reactor in REACT. Roughly 20 mg of sample was diluted with quartz was used as the catalyst. A premixed cylinder of 0.5% CO and 20% O<sub>2</sub> was used with varying flow rates from 60 and 100 sccm between temperatures from 60 °C to 120 °C. The gas output was injected into a gas chromatograph to separate the CO and CO<sub>2</sub> from one another. The carbon oxides were then methanized and subsequently detected using a flame ionization detector to precisely measure the relative amount of CO and CO<sub>2</sub>. The reaction rates were extracted by the slope of the conversion as a function of the contact time at low conversions. The apparent activation barrier was calculated through an Arrhenius relationship.

### 10.3. Results

Characteristic vibrations of both methyl and methoxy groups can be probed using DRIFTS after MeOH is chemisorbed onto the oxide surface. At higher wavenumbers (3000–2750 cm<sup>-1</sup>), the asymmetric and symmetric vibrations of methyl groups can be

seen.  $\text{LaScO}_3$ ,  $\text{Sc}_2\text{O}_3$ , and  $\text{La}_2\text{O}_3$  all show a single peak for the asymmetric vibration. For the symmetric methyl vibration, both  $\text{LaScO}_3$  and  $\text{Sc}_2\text{O}_3$  have a single peak and  $\text{La}_2\text{O}_3$  shows a doublet. At lower wavenumbers ( $1100\text{--}1000\text{ cm}^{-1}$ ), contributions from vibrations of the methoxy group can be observed.  $\text{La}_2\text{O}_3$  showed the greatest contribution from a methoxy group shared between three metal centers (tridentate), and very little to no contribution from a methoxy group shared between two metal centers (bidentate).  $\text{LaScO}_3$  and  $\text{Sc}_2\text{O}_3$  shows its strongest contribution from the bidentate methoxy and a smaller but noticeable contribution from tridentate.

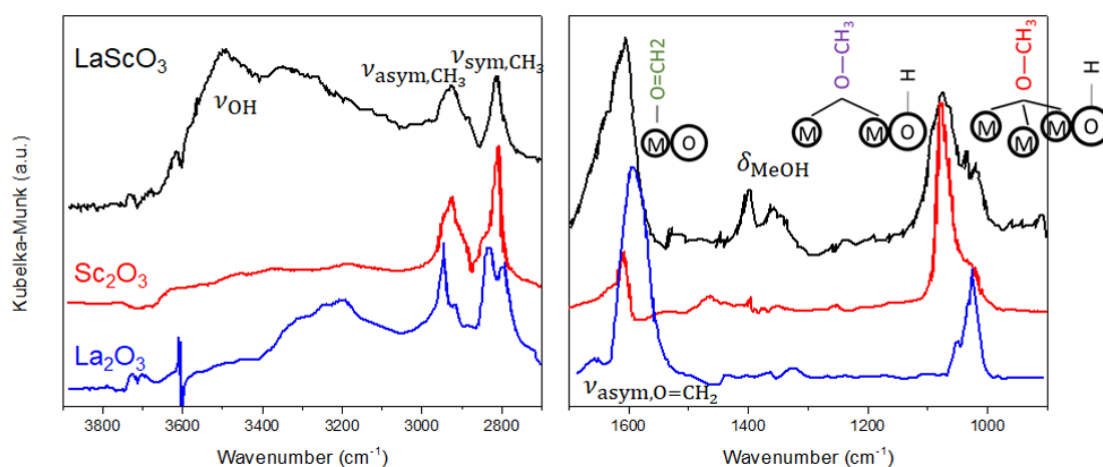


Figure 10.1. DRIFTS spectra collected at  $65\text{ }^\circ\text{C}$  of methanol chemisorbed on  $\text{LaScO}_3$  (black),  $\text{Sc}_2\text{O}_3$  (red), and  $\text{La}_2\text{O}_3$  (blue).

The different lanthanide scandates have different surface basicities owing to differences in the scandium oxide surface termination. As a means to probe the total basicity of the support, temperature-programmed desorption (TPD) was performed, where the temperature of maximum desorption of  $\text{CO}_2$  was used as a proxy for basicity (Figure 10.2).

The highest desorption temperature occurred on NdScO<sub>3</sub> at 781 °C, followed by LaScO<sub>3</sub> (664 °C) and SmScO<sub>3</sub> (530 °C).

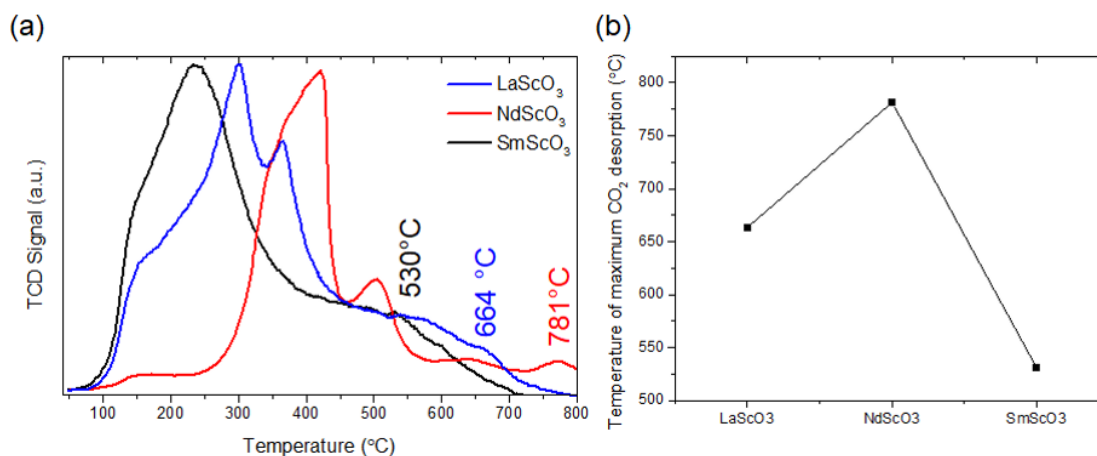


Figure 10.2. (a) TPD showing water and carbon dioxide loss on the various LnScO<sub>3</sub> and (b) the temperature of maximum CO<sub>2</sub> desorption as a function of support. The water is known to desorb in the range of 300-500 °C (see Chapter 3) so the highest temperature desorption peak was attributed to CO<sub>2</sub>, consistent with the GC-MS data in Figure 10.3.

ICP-OES was used to quantify the weight loading of Pt to the various different supports. For consistency, the amount of Pt was normalized to the amount of Sc and the support was assumed to be 100% LnScO<sub>3</sub>. The weight loading of Pt was 4.7%, 2.2%, and 5.4%, on LaScO<sub>3</sub>, NdScO<sub>3</sub>, and SmScO<sub>3</sub>, respectively. Pulse chemisorption of CO to get the uptake of CO on each sample found 6.49 μmol/g, 0.50 μmol/g, and 12.6 μmol/g, which correlate with the weight loadings. The samples were looked at through high-resolution electron microscopy to characterize the size of the Pt catalysts (Figure 10.4). Images were under-focused to make it easier to see the supported Pt particles. Particles appear to be isotropic in shape, consistent with the expected Wulff shape of platinum. Particle sizes

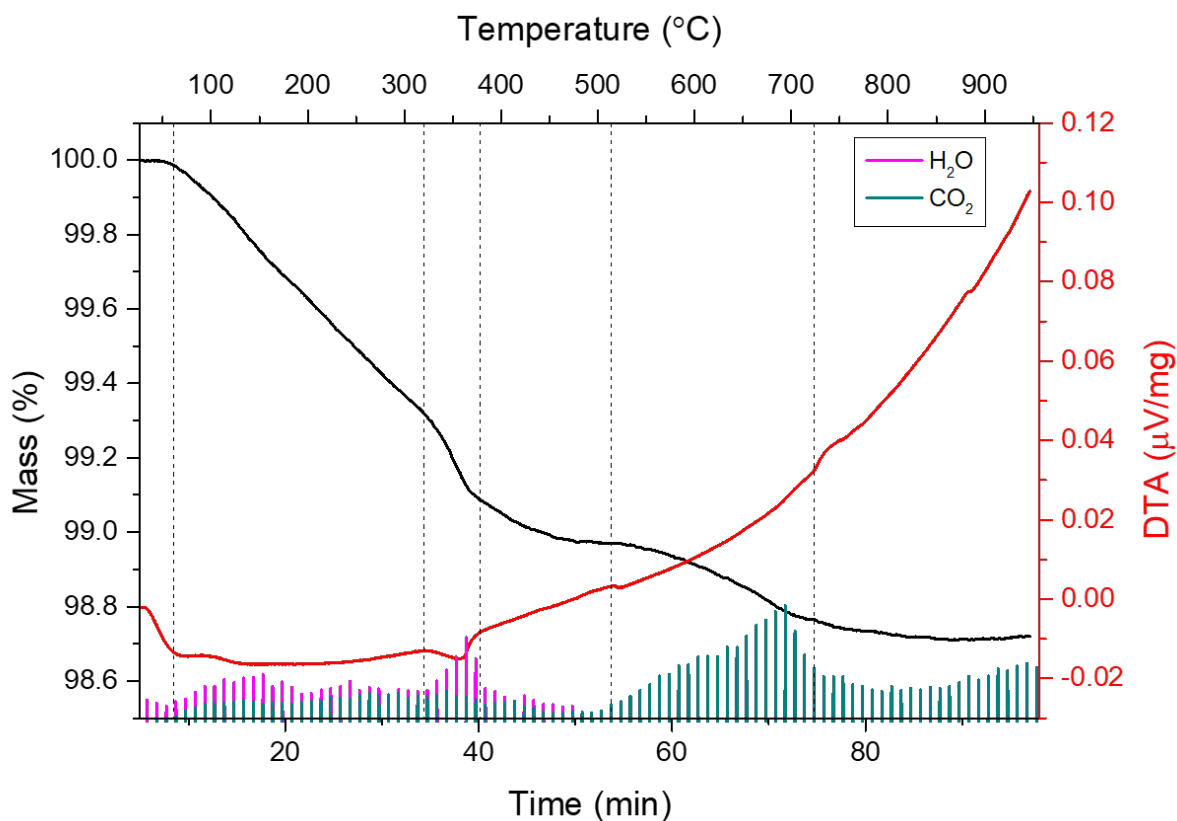


Figure 10.3. Simultaneous TGA-DTA-GC-MS on a bare LaScO<sub>3</sub> support.

were similar across each sample, with particle diameters of  $1.63 \pm 0.34$  nm,  $1.46 \pm 0.28$  nm, and  $1.65 \pm 0.31$  nm.

CO oxidation reactions were carried out to determine if and how Pt catalyzes CO oxidation differently on the different supports. Normalized to the surface area of platinum, the CO oxidation rate was greatest with Pt on NdScO<sub>3</sub>, and lower for Pt on LaScO<sub>3</sub> and SmScO<sub>3</sub>. Extracting the apparent activation barrier using an Arrhenius relationship were found to be within error of one another, with energies of  $69.9 \pm 1.8$  kJ/mol (Pt/LaScO<sub>3</sub>),  $66.7 \pm 1.2$  kJ/mol (Pt/NdScO<sub>3</sub>), and  $70.0 \pm 2.8$  kJ/mol (Pt/SmScO<sub>3</sub>).

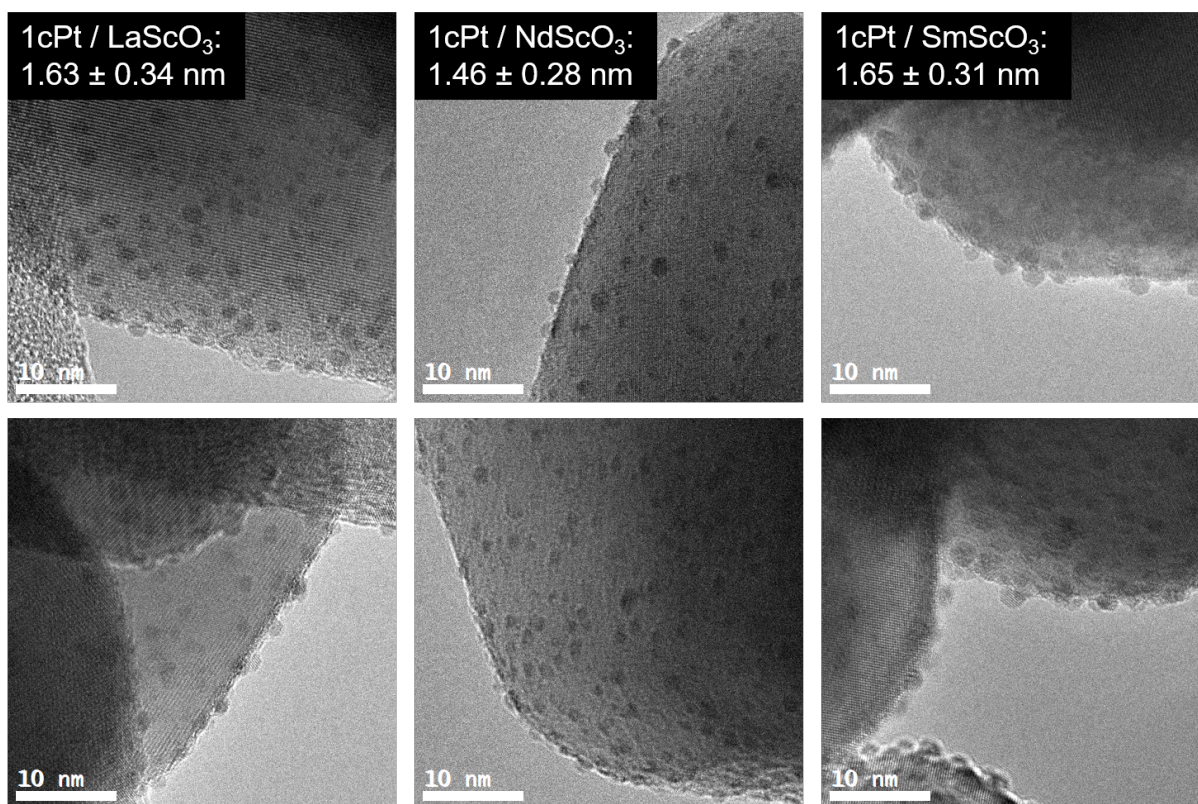


Figure 10.4. Representative HRTEM images of Pt dispersed on (left) LaScO<sub>3</sub>, (center) NdScO<sub>3</sub>, and (right) SmScO<sub>3</sub>.

The reverse water-gas shift reaction was probed using DRIFTS. First, carbon dioxide was flowed over the sample to saturate the support surface with CO<sub>2</sub>-containing groups. Then, hydrogen gas was flowed over the sample, which dissociated on the Pt surface and reacted with the CO<sub>2</sub>-containing groups, consuming them and producing CO on the Pt metal. Lastly, CO was flowed in to fully saturate the Pt surface with CO. The integrated intensity of peaks owing to CO from the RWGS alone relative to the integrated intensity after full CO saturation was used as a proxy for the degree of RWGS that occurred. The relative amount of CO produced from the reverse water-gas shift alone increased with increasing temperature (Figure 10.6). The relative amount of CO produced was

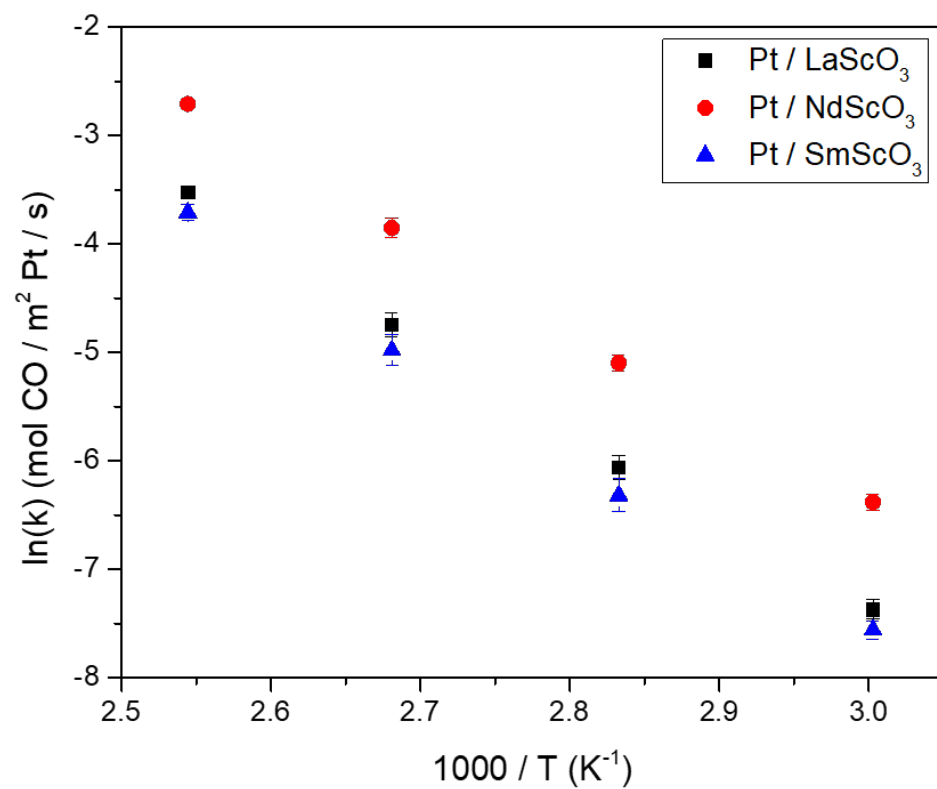


Figure 10.5. CO oxidation reaction rates as a function of temperature for Pt/LnScO<sub>3</sub>. dependent on the support, with the NdScO<sub>3</sub>-supported Pt always producing the least amount.

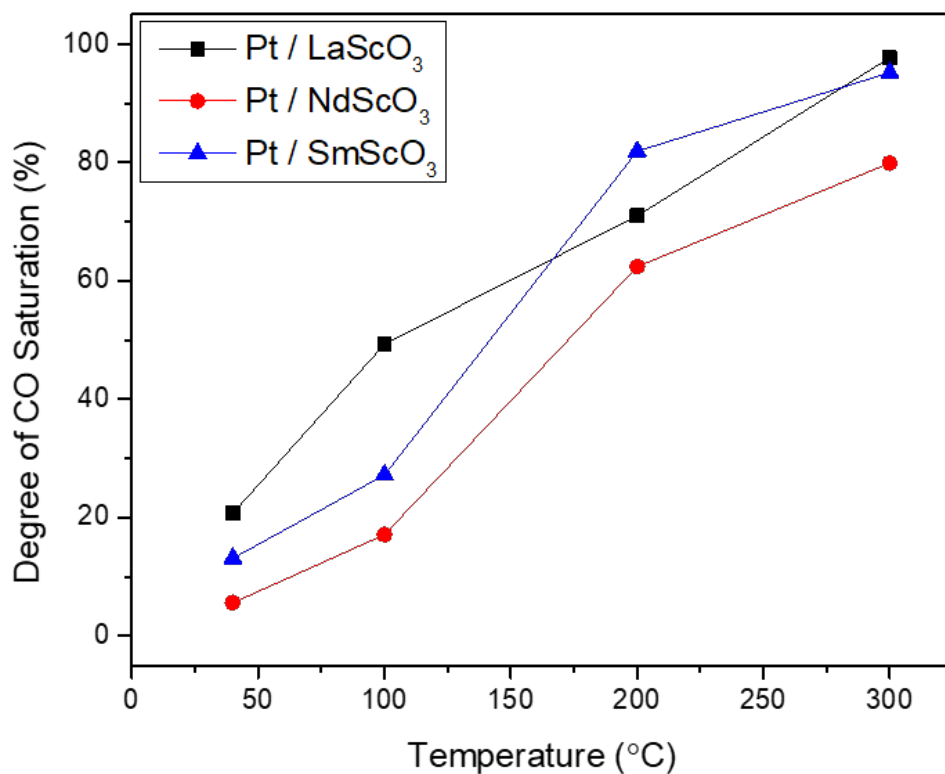


Figure 10.6. The percentage of CO saturation on each sample of Pt/LnScO<sub>3</sub> as a function of temperature.

#### 10.4. Discussion

The properties of both the metal and the support are important to understanding how the catalytic system undergoes CO oxidation and reverse water-gas shift reactions. The critical property of the support in this case is its ability to adsorb carbon dioxide. Equivalently, since CO<sub>2</sub> is an acidic oxide, the support basicity should be a characteristic proxy for defining the reaction activity.<sup>148</sup> Both the RWGS and CO oxidation were found to correlate with the relative CO<sub>2</sub>-support binding strength.

### 10.4.1. LnScO<sub>3</sub> Basicity

First, the chemical properties of the LnScO<sub>3</sub> supports was investigated. In particular, since CO<sub>2</sub> is present in both of the studied reactions, the binding strength of CO<sub>2</sub> should be an important proxy in defining how this system catalyzes each reaction. Equivalently, since CO<sub>2</sub> is an acidic oxide, the basicity of the support should correlate with the systems ability to catalyze each reaction. Specifically it is the basicity of the support surface that is relevant. Angle-resolved X-ray photoelectron spectroscopy and high resolution electron microscopy of lanthanide scandate single crystals indicate that the surface termination is a double layer of scandium oxide.<sup>149</sup> To confirm that the chemistry of the surface is also representative of the scandium oxide, DRIFTS of LaScO<sub>3</sub>, La<sub>2</sub>O<sub>3</sub>, and Sc<sub>2</sub>O<sub>3</sub> with methanol chemisorbed on the surface was performed. Methanol (MeOH) is able to readily adsorb to many different metal oxides at low temperature (150 °C) and probe the different kinds of available sites, including acidic or basic sites. Infrared spectroscopy on MeOH chemisorption shows intact Lewis-bound methanol adsorption on acidic sites and dissociation into a methoxy (MeO-) group on basic sites.<sup>150</sup> In addition, the products obtained in MeOH oxidation reactions also reflect different sites, where redox sites produce H<sub>2</sub>CO, acidic sites produce CH<sub>3</sub>OCH<sub>3</sub>, and basic sites produce CO<sub>2</sub>.<sup>29</sup>

Characteristic vibrations of both methyl and methoxy groups can be probed using DRIFTS after MeOH is chemisorbed onto the oxide surface. At higher wavenumbers, the asymmetric (3000–2900 cm<sup>-1</sup>) and symmetric (2900–2750 cm<sup>-1</sup>) vibrations of methyl groups can be seen. LaScO<sub>3</sub> shows a single peak for the symmetric vibration, consistent with what is observed for Sc<sub>2</sub>O<sub>3</sub>, whereas La<sub>2</sub>O<sub>3</sub> shows a doublet, suggesting that methyl

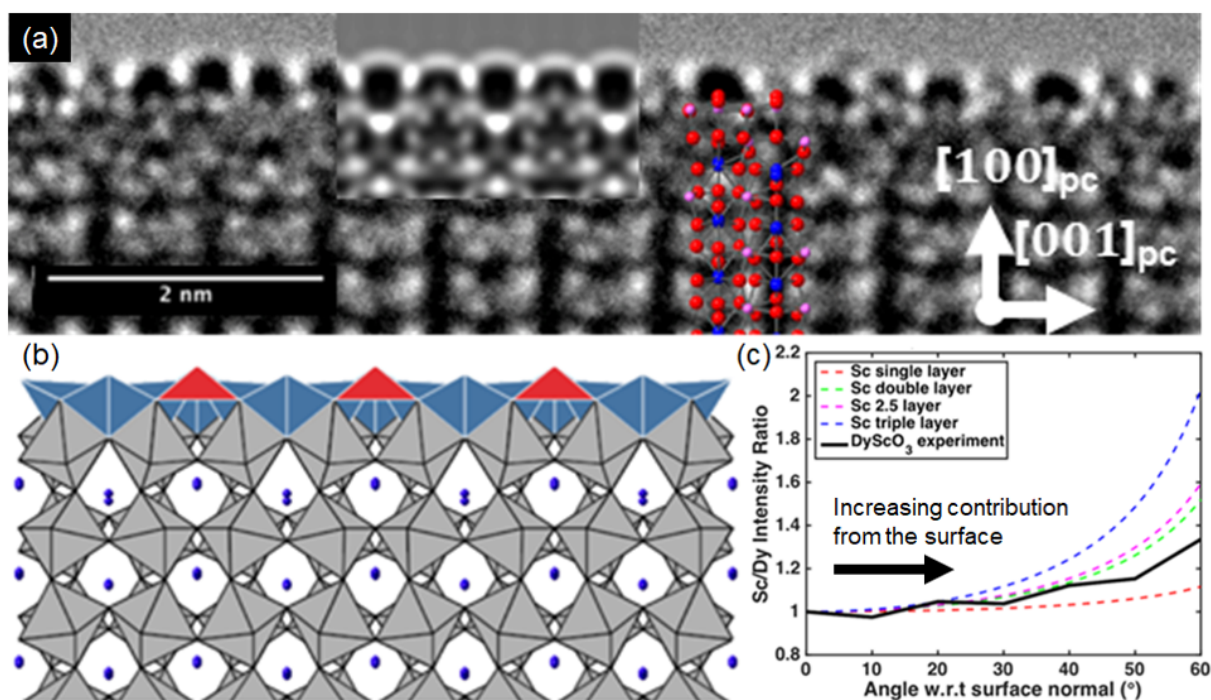


Figure 10.7. (a) A HRTEM image of a (110) GdScO<sub>3</sub> surface, with the crystal structure and slice imaging profile overlaid.<sup>149</sup> (b) Crystal structure showing the ScO<sub>6</sub> octahedra of the bulk with the double scandium oxide surface termination in blue and red.<sup>149</sup> (c) Angle-resolved X-ray photoelectron spectroscopy of a DyScO<sub>3</sub> single crystal, which shows an increase in the relative intensity of Sc relative to Dy with decreasing signal from the bulk relative to the surface.<sup>149</sup>

vibrations on LaScO<sub>3</sub> are more similar to that of Sc<sub>2</sub>O<sub>3</sub>. At lower wavenumbers, contributions from vibrations of the methoxy group can be observed. LaScO<sub>3</sub> shows both bidentate (1075–1000 cm<sup>-1</sup>) and tridentate (1100–1075 cm<sup>-1</sup>) methoxy binding, with a stronger contribution owing to the former. Similarly, the same methoxy binding is observed on Sc<sub>2</sub>O<sub>3</sub>, whereas La<sub>2</sub>O<sub>3</sub> showed primarily tridentate methoxy binding and little to no bidentate. These results suggest that the chemical basicity is derived from the scandium oxide, consistent with the observed surface termination.

As the different lanthanide scandates have different lattice parameters, the amount of epitaxial strain on the scandium oxide surface termination will differ and lend itself to different surface basicities. TPD of the supports as synthesized showed signal owing to the desorption of both water and CO<sub>2</sub>, with the former occurring at temperatures around 300-500 °C and the latter at higher temperatures. The desorption temperature of CO<sub>2</sub> was used as a proxy for the basicity, where higher temperatures imply stronger CO<sub>2</sub> binding. Surprisingly, the highest basicity occurred on NdScO<sub>3</sub>, then by LaScO<sub>3</sub> and SmScO<sub>3</sub>, although the basicity is usually assumed to change monotonically (La > Nd > Sm) across the lanthanide series.<sup>151</sup> To better understand this apparent discrepancy, the bond valence sums of scandium in the bulk perovskite was used as a proxy for the basicity, where a higher bond valence sum would imply less electronegativity from the scandium and hence act as a stronger Lewis base. We find that the CO<sub>2</sub> desorption temperature and the bond valence sum of the scandium correlate well with one another (Figure 10.8), suggesting that NdScO<sub>3</sub> is indeed the most basic of the supports investigated here.

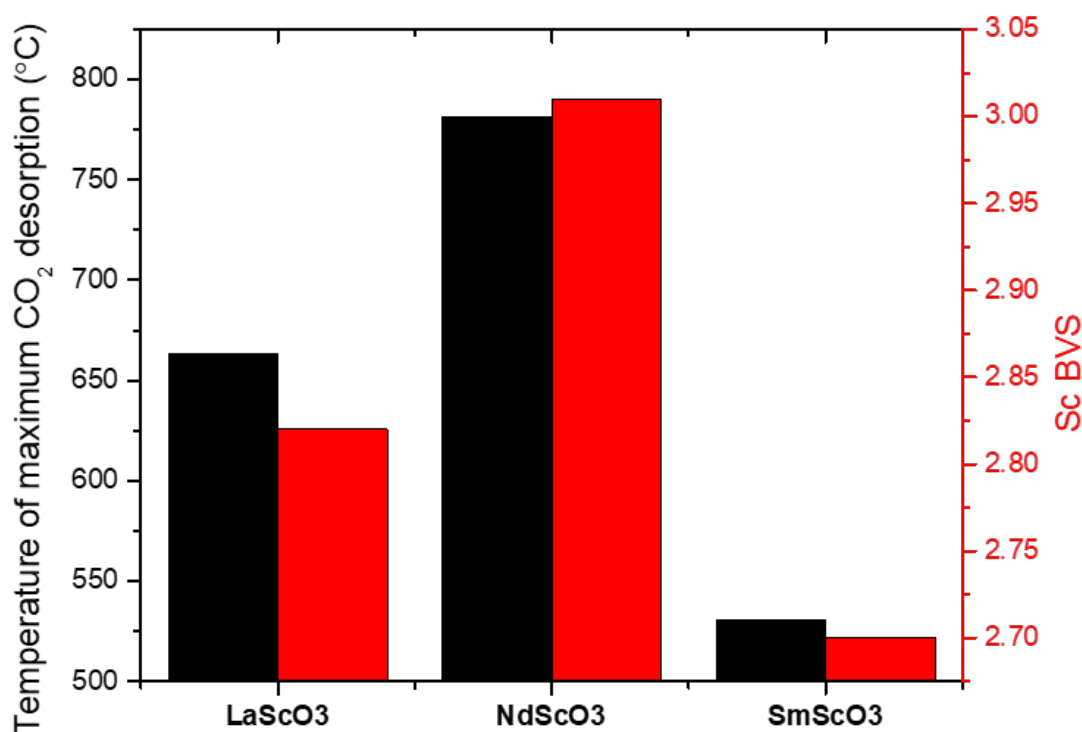


Figure 10.8. The temperature of maximum CO<sub>2</sub> desorption against the bond valence sum (BVS) of the scandium in the bulk LnScO<sub>3</sub> perovskite.

#### 10.4.2. Effect of CO<sub>2</sub> Affinity on CO Oxidation and the Reverse Water-Gas Shift

To probe the reverse water-gas shift reaction, *in situ* DRIFTS was performed. Prior to measurement, oxygen gas was flowed over the sample to clear off any CO that may have happened to already be on the platinum surface. Then, carbon dioxide was flowed into the system to adsorb onto the basic surface of the LnScO<sub>3</sub>. In this wavenumber range (1750–1200 cm<sup>-1</sup>), these CO<sub>2</sub>-containing groups may be in the form of carbonates, bicarbonates,

or formates.<sup>152,153</sup> There are no obvious feature changes on any different support, which could suggest that they are the same species forming owing to their similar scandium oxide terminations or that the vibrational frequency of the various CO<sub>2</sub>-containing groups does not change significantly on the three lanthanides investigated.

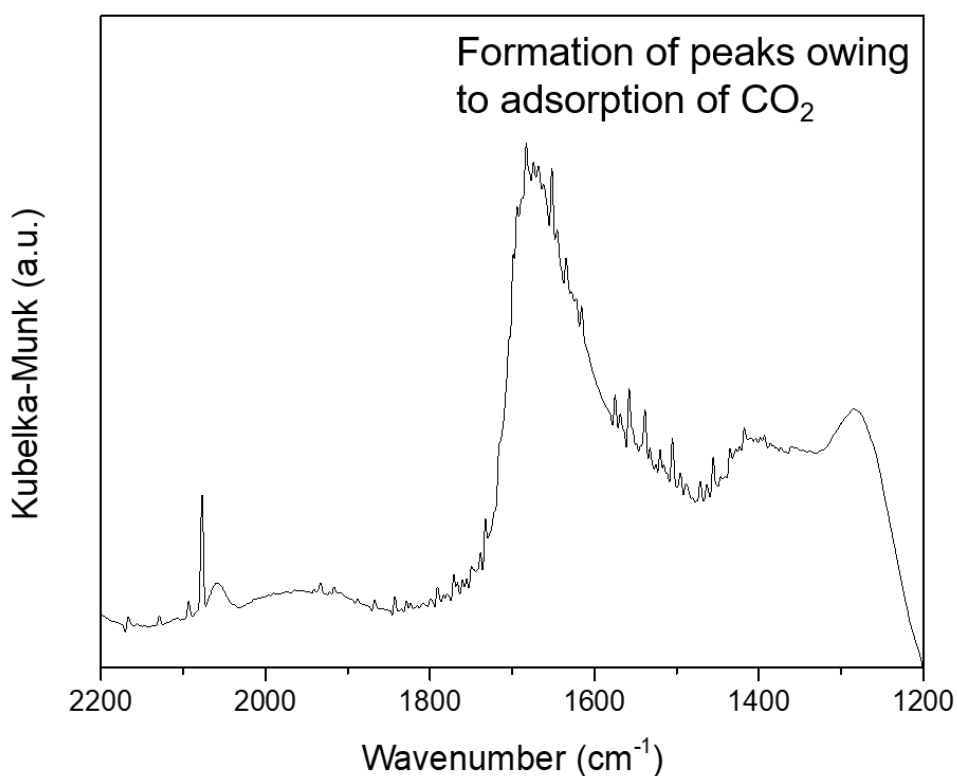


Figure 10.9. Example spectrum of Pt/LaScO<sub>3</sub> in CO<sub>2</sub> at 100 °C, showing the presence of peaks arising from adsorption of carbon dioxide in some form.

Hydrogen gas was then introduced into the system, which reduced any platinum oxide, dissociated on the Pt metal, and reacted with carbon dioxide. Correspondingly, peaks

owing to the  $\text{CO}_2$ -containing groups decreased in intensity and peaks owing to CO adsorbed on Pt appeared, both in the form of linear and bridged CO. The degree of CO saturation, defined here to be the amount of CO produced through the RWGS relative to how much CO fully saturated the Pt surface, that occurred depended on the support and on the temperature. To analyze this, the relative integrated intensity of the linear and bridged CO peaks was calculated at the end of the hydrogen treatment and again after CO treatment. The latter corresponds to a full saturation of CO so the former is a measure of what percentage of the sites were consumed from the RWGS alone.

As expected, in all cases the amount of CO produced increased as a function of temperature (Figure 10.11). The relative amount of CO produced though was also dependent on the support, with the  $\text{NdScO}_3$ -supported Pt always producing the least amount and  $\text{LaScO}_3$  consistently producing the most. Correlating this result to the basicity proxy, it is found that the support that has intermediate  $\text{CO}_2$  binding strength ( $\text{LaScO}_3$ ) had the highest rate of RWGS occurring, whereas supports that bound  $\text{CO}_2$  too strongly ( $\text{NdScO}_3$ ) or too weakly ( $\text{SmScO}_3$ ) had lower rates. This is consistent with expectation from Sabatier's principle and suggests that, for  $\text{CO}_2$  hydrogenation reactions to occur at the oxide-metal boundary that an oxide with a basicity similar to that of  $\text{LaScO}_3$  (and maybe  $\text{SmScO}_3$ ) is ideal.

In addition, CO oxidation reactions were also investigated to see what role the different supports played. In all three cases, the apparent activation barriers were similar (all within error of one another), suggesting that the same mechanism likely occurred on all of the samples. The rate of CO oxidation was greatest on Pt supported by  $\text{NdScO}_3$ . If the CO oxidation rate is compared to the desorption temperature of  $\text{CO}_2$ , it is found that supports

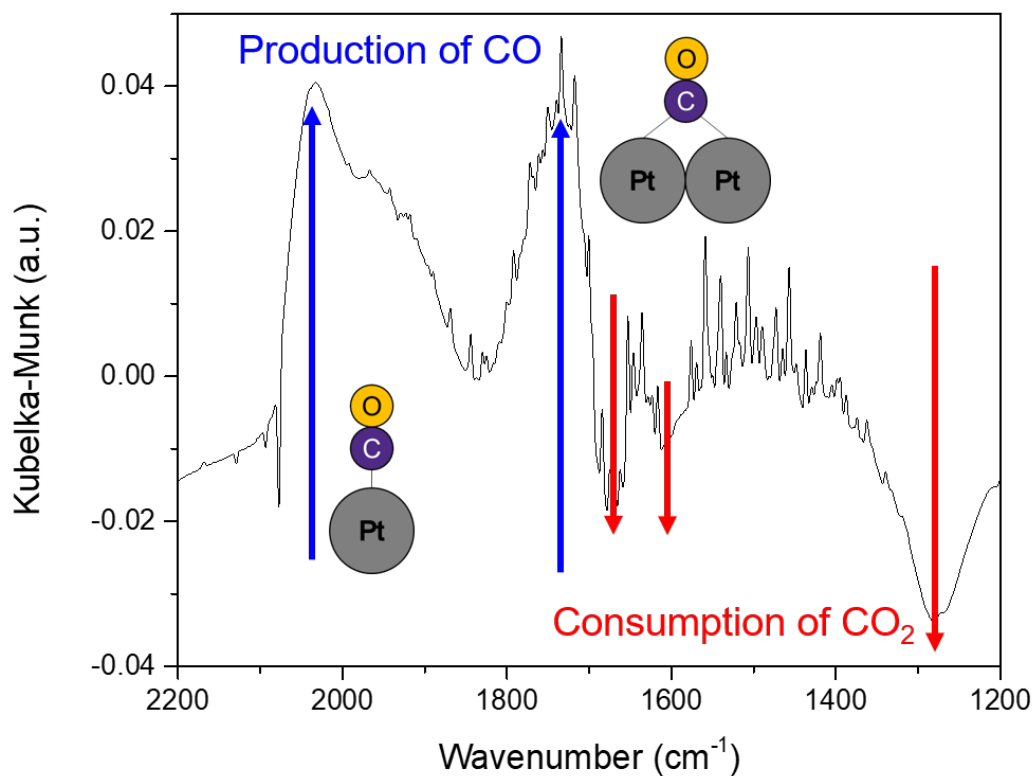


Figure 10.10. Example spectrum of Pt/LaScO<sub>3</sub> in H<sub>2</sub> at 100 °C, showing the consumption of CO<sub>2</sub>-containing groups in favor of CO bound to the Pt metal.

that more strongly bind CO<sub>2</sub> have greater CO oxidation rates. This suggests that the support's affinity for CO<sub>2</sub> has a role in the reaction, where supports that have a strong affinity for CO<sub>2</sub> have a greater preference for forming CO<sub>2</sub>. Since it is the binding of CO<sub>2</sub> on the support that affects the reaction rate, the oxidation of CO must be occurring at the Pt-LnScO<sub>3</sub> perimeter.

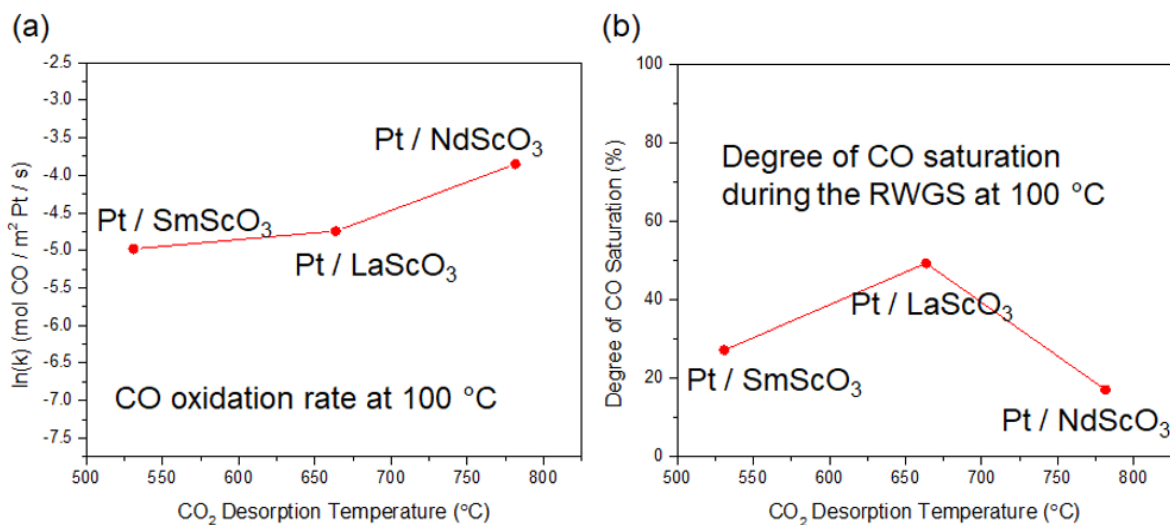


Figure 10.11. (a) The CO oxidation rate and (b) percentage of CO saturation on each sample of Pt/LnScO<sub>3</sub> as a function of the temperature of maximum CO<sub>2</sub> desorption.

## 10.5. Conclusion

Basic oxides like the lanthanide scandates readily adsorb acids like carbon dioxide. Even though the lanthanide scandates are all terminated with scandium oxide, the different lattice strain on the scandium oxide termination has a clear and pronounced effect on the total CO<sub>2</sub> binding strength. The different affinities for CO<sub>2</sub> binding on the LnScO<sub>3</sub> was found to act as a descriptor for both the reverse water-gas shift and CO oxidation, which implies that both reactions occur at Pt-LnScO<sub>3</sub> perimeter. A stronger driving force for binding CO<sub>2</sub> led to greater CO oxidation rates in order to produce CO<sub>2</sub> and less reverse water-gas shift in order to keep the adsorbed CO<sub>2</sub>.

## CHAPTER 11

**Conclusions and Future Work**

In this dissertation, lanthanide scandate-supported noble metal nanoparticles were used as a model catalytic system. While a number of different metals and reactions were investigated, we believe this to be the tip of the iceberg and that this library of materials can be used to explore how properties of the support affect the catalytic properties.

**11.1. Conclusion**

The series of lanthanide scandates make for a reliable model system to investigate supported noble metal catalysts because of their well-matched lattice parameters and tunability in the lattice parameter and support acidity. The lanthanide scandates can be made consistently with primarily pseudocubic- $\{100\}$  termination by using a two-temperature water vapor-assisted sol-gel synthesis. The interfacial energy between the support and the catalyst is complex, as the lattice parameter of the catalyst is size-dependent. Nonetheless, the variable strain that can be imparted by the support on the catalyst tunes the CO adsorption behavior of Pt catalysts. Additionally, the Pt-LnScO<sub>3</sub> interface is active for CO oxidation and the reverse water-gas shift, owing to the affinity of CO<sub>2</sub> on basic oxide supports. These examples illustrate how the chemical and physical properties of an oxide support can have significant effects on properties and performance of the catalytic system.

## 11.2. Future Work

The work outlined in this thesis laid the groundwork for much more work to be done. By introducing  $\text{LnScO}_3$  into the library of available supports, there is a wider range of lattice parameters and chemical properties that may be investigated. In addition to depositing other noble metals or looking at other reactions, we believe that this system is uniquely qualified to help understanding different sol-gel growth mechanisms and to control the shape and chemical composition of metal nanoparticles at the atomic scale.

### 11.2.1. Further Understandings of Hydro-Sauna Syntheses

In Chapter 4, a mechanism for which crystalline ceramics could be formed from a mixed cation hydroxide hydrogel was proposed. While the method (and its extension in Chapter 5) is effective at consistently producing a strong yield of perovskite particles, there still remains inconsistencies from one batch to another and even within the same batch (to borrow from the movie *Anchorman*: “60% of the time, it works every time”).

Visual inspection of a product shows material with a fine texture and material with a more coarse texture (Figure 11.1a), clearly indicating that the growth processes are not homogeneous throughout the entire product. PXRD, shown in Figure 11.1b, of the separate textures reveal that the finer powder is comprised nearly entirely of the perovskite phase, whereas the coarser powder (while also mostly perovskite) contains a greater percentage of secondary phases like the rare-earth oxides or hydroxides. Electron microscopy further reveals that the finer powder produced smaller and better faceted particles, while the coarser powder consisted of many larger and irregularly shaped particles.

While varying synthetic parameters can lead to better understanding what is going on during the growth, it is difficult to fully understand what mechanisms are at play.

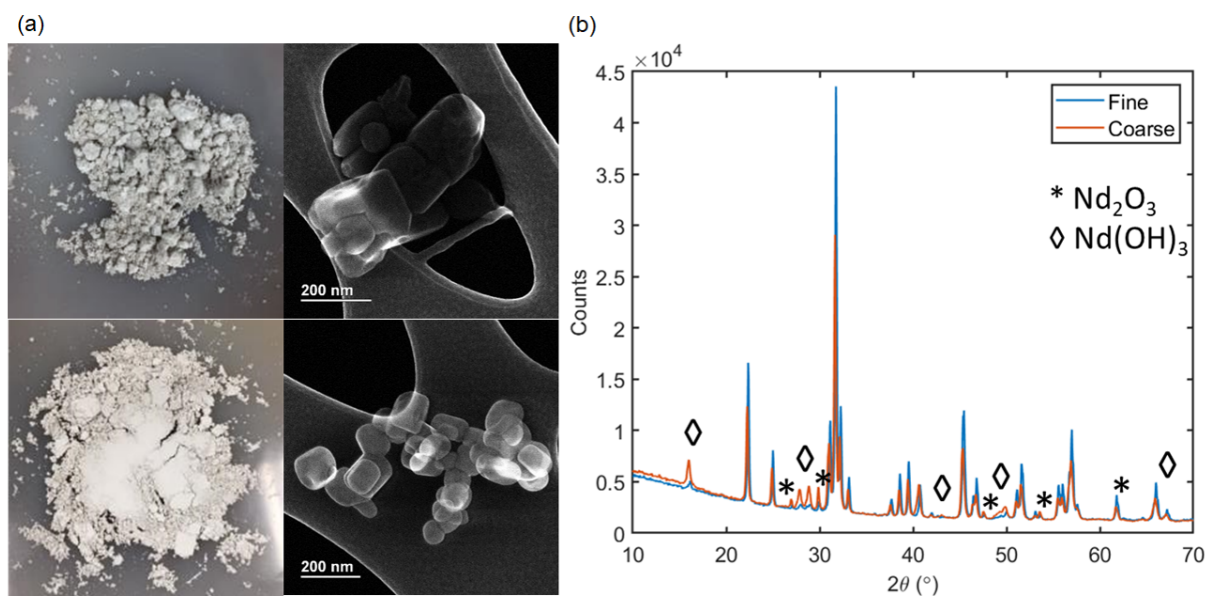


Figure 11.1. (a) Optical pictures (left) and SE images (right) of coarse (top) and fine (bottom)  $\text{NdScO}_3$  powders. (b) PXRD of the coarse and the fine powders. The PXRD pattern for coarse powder contains a greater percentage of undesired secondary phases than that of the fine powder.

Therefore, *in situ* studies would be necessary to address these details. For one, *in situ* PXRD could be used to investigate as a function of temperature and time how and when certain crystalline phases form and address whether the gel produces a crystalline intermediate before yielding the final perovskite phase. Also, in order to understand how the gel as a whole is structured, *in situ* small angle X-ray scattering would inform to the larger size features of the gel, which may better explain how the pore size of the hydrogel changes with temperature and humidity.

### 11.2.2. Hydro-Sauna Synthesis of Redox-Active Rare-Earth Perovskites

There is no reason to assume that this procedure would only work for  $\text{LnScO}_3$ , especially after it is better understood. This technique could be applying to other perovskite oxides, such as lanthanide ferrites, chromites, or manganites, where the perovskite B-site

is now a transition metal and redox-active. While many perovskites have been investigated as catalysts for decades,<sup>154</sup> the controlled faceting produced in the hydro-sauna method would provide a high-surface area of a particular surface, helping close the material gap. Further, the effects of the lattice strain on different transition metal oxide surface terminations through the use of the various lanthanides could be investigated. By better understanding this relationship, catalyst supports with appropriately tuned properties to maximize catalytic performance can be designed and selected.

These new systems would allow for exploration of a wider variety of catalytic reactions and properties. Much like studying CO oxidation and the reverse water-gas shift on LnScO<sub>3</sub>-supported platinum in Chapter 10, other reactions that occur at the metal-oxide perimeter could be probed with these model systems. Using different transition metals in the place of scandium would lead to a reducible surface oxide of the perovskite and would allow for strong metal-support interactions to be probed, and an effect of oxide reducibility as a function of strain can be explored. Using reducible rare-earths in tandem with a transition metal B-site would create overcoats of mixed composition, which would further lead to a variety of active sites (from the metal, rare-earth oxide, and transition metal oxide) all in intimate proximity with one another.

### **11.2.3. Exsolution of Supported Noble Metal Nanoparticles**

The way that many heterogeneous catalysts are made involves multiple steps: one making the support material, one where the support is exposed to some metal precursor, and then often another step treating the sample to produce the desired catalyst phase. Much like how we could make faceted oxides with a single technique, I propose making the complete supported heterogeneous catalyst in a single bound. The hydro-sauna synthesis,

being a sol-gel technique, has the advantage that all of the metal atoms are incorporated in the initial precursor. I envision adding a metal precursor during the solution step that would then precipitate out into the gel. One such example could be adding  $\text{Ag}(\text{NO}_3)$  to the  $\text{Ln}^{3+}$  and  $\text{M}^{3+}$  nitrate solution. Adding this solution to the 10 M NaOH solution would then precipitate out an  $\text{LnMAg}_x(\text{OH})_{6+x}$  hydrogel, where  $x$  can be chosen to achieve a given weight loading of catalyst. The new precursor can now be treated using the hydro-sauna method and, when reducing conditions such as hydrogen gas are used, the silver (or whichever low reduction potential metal is used) will exsolve to the surface. Using exsolved catalysts can have their own advantages; Ni catalysts exsolved from  $\text{LaNiO}_3$  were found to be more resistant to coking and sintering owing to their perimeter being protected by so-called “nano-sockets”.<sup>155,156</sup> Such systems may also be used for “smart catalysts”, where the active metal may return into the host oxide under oxidizing conditions and be exsolved and dispersed again when exposed to reducing conditions.<sup>157</sup> This proposal would therefore create catalysts stable under a variety of different reaction conditions using a single synthetic method.

#### 11.2.4. Interface-Mediated Bimetallic Catalysts

In addition to having a larger suite of noble metals that can be epitaxially matched, the tunability of the  $\text{LnScO}_3$  lattice parameters offers a new opportunity to use this variable interfacial energy in controlling mixed metal catalysts. Bimetallic particles can adopt different crystal structures, including different solid solutions, where one metal sits on random sites of the other metal so there is no long range order, and intermetallic phases, where each metal adopts specific sites. For a system with a given composition, there will be phase segregation into the intermetallic and an alloy, as illustrated in Figure 11.2.

For many heterogeneous catalysts, it is the chemical properties of the surface specifically that dominate the catalytic performance, so designing catalysts with controlled surface composition is important. In order to minimize interfacial energies in the system, the bimetallic catalyst will elect to segregate the phase with the better lattice matching with the interface to the interface (towards the core of the particle) and consequently the other phase will segregate towards the surface. Such a system would utilize the catalyst-support interface as a means to control the composition of the catalyst surface. In addition, since the core of the bimetallic particle will elect to be well-matched to the support, the catalyst should be more resistant to sintering.<sup>11</sup>

Examples of how this would work are demonstrated schematically in Figure 11.3. A gold-rich alloy matches well with  $\text{LaScO}_3$  and will be stabilized at the interface so the intermetallic phase will segregate to the surface. Alternatively, on  $\text{GdScO}_3$  the intermetallic phase will be favored at the interface so the surface will instead consist of the alloy. For completeness, the electronegativity of the support will also affect which phase is preferred at its interface and there is a possibility that at a compositional gradient could be kinetically trapped. Understanding precisely how strain and electronegativity in the oxide support affect the chemical potential of different metal atoms could lead us closer to designing catalysts on the atomic level.

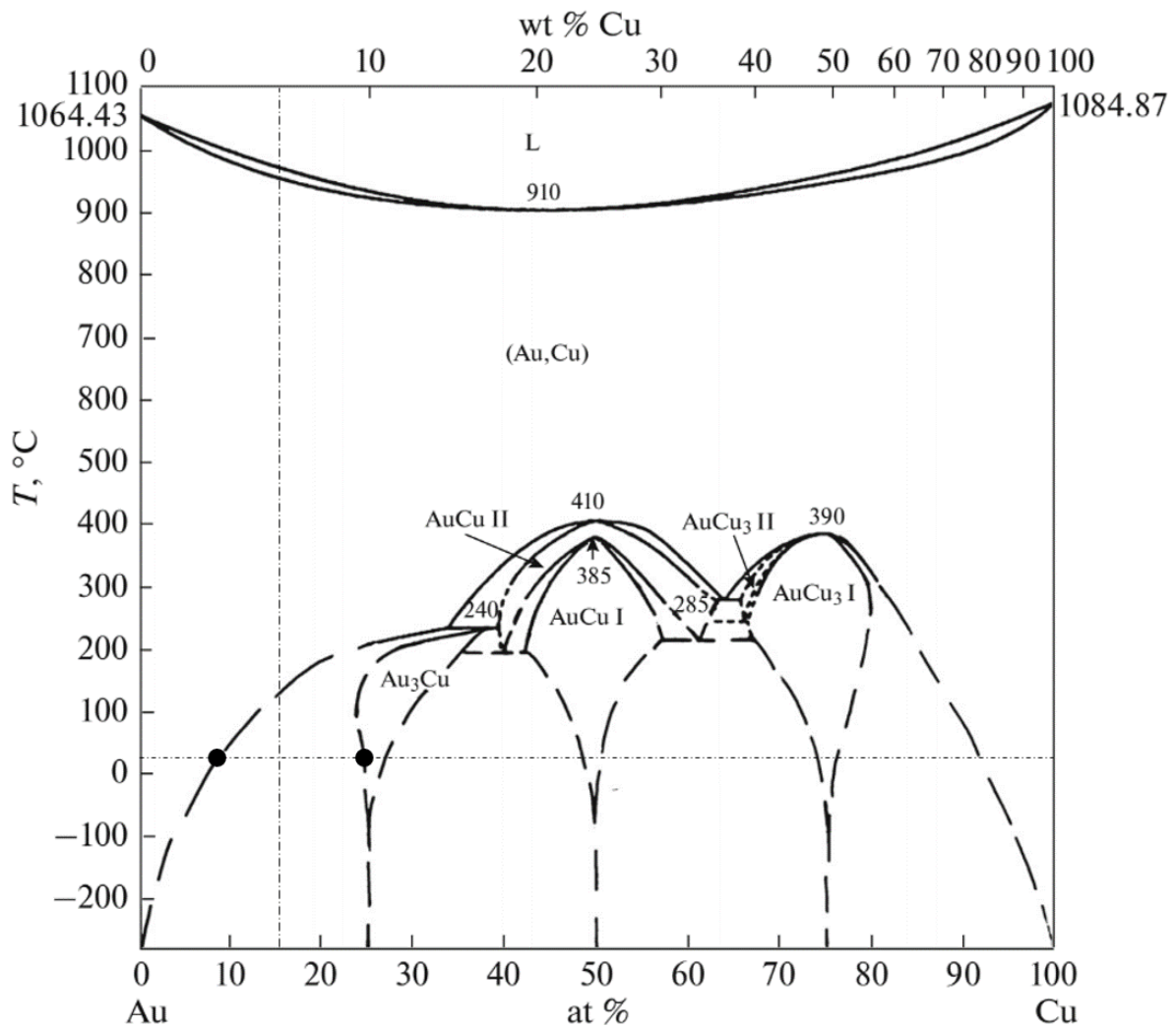


Figure 11.2. The gold-copper phase diagram showing phase segregation at room temperature of a mixture consisting of 85% gold and 15% copper.<sup>158</sup>

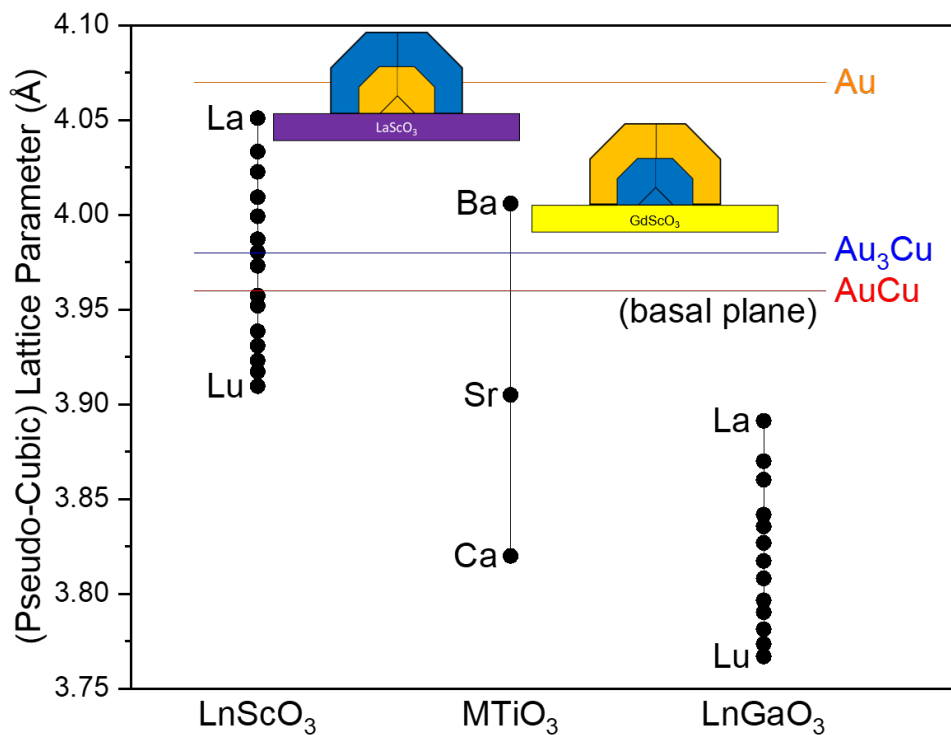


Figure 11.3. The lattice parameters of the various perovskite supports compared to that of gold and gold-copper intermetallic phases. Insets show how phase segregation of the alloy and intermetallic should manifest themselves on some model supports. The intermetallic phase (blue) is well lattice-matched to GdScO<sub>3</sub> and will segregate to the support-metal interface and the gold-rich solid solution will remain on the particle surface. Similarly, the gold-rich solid solution (gold) is well lattice-matched to LaScO<sub>3</sub> and will segregate to the support-metal interface so the intermetallic phase will remain on the particle surface.

## References

- <sup>1</sup>M. Rayner-Canham, M. Rayner-Canham, and G. Rayner-Canham, *Women in Chemistry: Their Changing Roles from Alchemical Times to the Mid-twentieth Century* (Chemical Heritage Foundation, 2001).
- <sup>2</sup>A. M. Thayer, “Nobel Prizes Recognized Notable Developments in Catalysis”, *Chemical and Engineering News* **91**, 68 (2013).
- <sup>3</sup>J. H. Sinfelt, “Influence of technology on catalytic science”, *Industrial & Engineering Chemistry Fundamentals* **25**, 2–9 (1986).
- <sup>4</sup>J. R. H. Ross, *Heterogeneous Catalysis: Fundamentals and Applications*, Heterogeneous Catalysis (Elsevier, Amsterdam, 2012), p. 222.
- <sup>5</sup>J. Armor, *What is Catalysis or Catalysts, So what?*, Web Page, 2008.
- <sup>6</sup>A. M. Thayer, “Catalyst Suppliers Face Changing Industry”, *Chemical & Engineering News Archive* **70**, 27–49 (1992).
- <sup>7</sup>A. M. Thayer, “The Catalysis Chronicles”, *Chemical and Engineering News* **91**, 64–68 (2013).
- <sup>8</sup>B.-R. Chen, C. George, Y. Lin, L. Hu, L. Crosby, X. Hu, P. C. Stair, L. D. Marks, K. R. Poeppelmeier, R. P. Van Duyne, and M. J. Bedzyk, “Morphology and oxidation state of ALD-grown Pd nanoparticles on TiO<sub>2</sub>- and SrO-terminated SrTiO<sub>3</sub> nanocuboids”, *Surface Science* **648**, 291–298 (2016).

- <sup>9</sup>W. L. Winterbottom, “Equilibrium shape of a small particle in contact with a foreign substrate”, *Acta Metallurgica* **15**, 303–310 (1967).
- <sup>10</sup>J. A. Enterkin, R. M. Kennedy, J. Lu, J. W. Elam, R. E. Cook, L. D. Marks, P. C. Stair, C. L. Marshall, and K. R. Poeppelmeier, “Epitaxial Stabilization of Face Selective Catalysts”, *Topics in Catalysis* **56**, 1829–1834 (2013).
- <sup>11</sup>J. A. Enterkin, W. Setthapun, J. W. Elam, S. T. Christensen, F. A. Rabuffetti, L. D. Marks, P. C. Stair, K. R. Poeppelmeier, and C. L. Marshall, “Propane Oxidation over Pt/SrTiO<sub>3</sub> Nanocuboids”, *ACS Catalysis* **1**, 629–635 (2011).
- <sup>12</sup>T. V. W. Janssens, B. S. Clausen, B. Hvolbk, H. Falsig, C. H. Christensen, T. Bli-gaard, and J. K. Nørskov, “Insights into the reactivity of supported Au nanoparticles: combining theory and experiments”, *Topics in Catalysis* **44**, 15 (2007).
- <sup>13</sup>G. K. Williamson and W. H. Hall, “X-ray line broadening from filed aluminium and wolfram”, *Acta Metallurgica* **1**, 22–31 (1953).
- <sup>14</sup>P. Scherrer, “Bestimmung der Größe und der inneren Struktur von Kolloidteilchen mittels Röntgenstrahlen”, *Nachrichten von der Gesellschaft der Wissenschaften zu Göttingen, Mathematisch-Physikalische Klasse* (1918).
- <sup>15</sup>A. L. Patterson, “The Scherrer Formula for X-Ray Particle Size Determination”, *Physical Review* **56**, 978–982 (1939).
- <sup>16</sup>H. Rietveld, “A profile refinement method for nuclear and magnetic structures”, *Journal of Applied Crystallography* **2**, 65–71 (1969).
- <sup>17</sup>P. B. Hirsch, A. Howie, R. B. Nicholson, D. W. Pashley, and M. J. Whelan, *Electron Microscopy of Thin Crystals* (Butterworths, 1965).

- <sup>18</sup>D. B. Williams and C. B. Carter, *Transmission Electron Microscopy*, 2nd ed. (Springer US, 2009), p. 775.
- <sup>19</sup>J. L. Falconer and R. J. Madix, “Flash desorption activation energies: DCOOH decomposition and CO desorption from Ni (110)”, *Surface Science* **48**, 393–405 (1975).
- <sup>20</sup>S. Brunauer, P. H. Emmett, and E. Teller, “Adsorption of Gases in Multimolecular Layers”, *Journal of the American Chemical Society* **60**, 309–319 (1938).
- <sup>21</sup>P. B. Wells, “Characterization of the standard platinum/silica catalyst euopt-1. 5.chemisorption of carbon monoxide and of oxygen”, *Applied Catalysis* **18**, 259–272 (1985).
- <sup>22</sup>C. Lentz, S. P. Jand, J. Melke, C. Roth, and P. Kaghazchi, “DRIFTS study of CO adsorption on Pt nanoparticles supported by DFT calculations”, *Journal of Molecular Catalysis A: Chemical* **426**, 1–9 (2017).
- <sup>23</sup>M. J. Kappers and J. H. van der Maas, “Correlation between CO frequency and Pt coordination number. A DRIFT study on supported Pt catalysts”, *Catalysis Letters* **10**, 365–373 (1991).
- <sup>24</sup>H. A. Aleksandrov, K. M. Neyman, K. I. Hadjiivanov, and G. N. Vayssilov, “Can the state of platinum species be unambiguously determined by the stretching frequency of an adsorbed CO probe molecule?”, *Physical Chemistry Chemical Physics* **18**, 22108–22121 (2016).
- <sup>25</sup>K. Ding, A. Gulec, A. M. Johnson, N. M. Schweitzer, G. D. Stucky, L. D. Marks, and P. C. Stair, “Identification of active sites in CO oxidation and water-gas shift over supported Pt catalysts”, *Science* (2015).
- <sup>26</sup>H. V. Thang, G. Pacchioni, L. DeRita, and P. Christopher, “Nature of stable single atom Pt catalysts dispersed on anatase TiO<sub>2</sub>”, *Journal of Catalysis* **367**, 104–114 (2018).

- <sup>27</sup>C. De La Cruz and N. Sheppard, “An exploration of the surfaces of some Pt/SiO<sub>2</sub> catalysts using CO as an infrared spectroscopic probe”, *Spectrochimica Acta Part A: Molecular Spectroscopy* **50**, 271–285 (1994).
- <sup>28</sup>J. N. Kuhn and U. S. Ozkan, “Surface properties of Sr- and Co-doped LaFeO<sub>3</sub>”, *Journal of Catalysis* **253**, 200–211 (2008).
- <sup>29</sup>M. Badlani and I. E. Wachs, “Methanol: A Smart Chemical Probe Molecule”, *Catalysis Letters* **75**, 137–149 (2001).
- <sup>30</sup>G Wulff, “On the question of speed of growth and dissolution of crystal surfaces”, *Z. Kristallogr* **34**, 449–530 (1901).
- <sup>31</sup>L. D. Marks and L. Peng, “Nanoparticle shape, thermodynamics and kinetics”, *Journal of Physics: Condensed Matter* **28**, 053001 (2016).
- <sup>32</sup>L. Dong, H. Shi, K. Cheng, Q. Wang, W. Weng, and W. Han, “Shape-controlled growth of SrTiO<sub>3</sub> polyhedral submicro/nanocrystals”, *Nano Research* **7**, 1311–1318 (2014).
- <sup>33</sup>L. A. Crosby, R. M. Kennedy, B.-R. Chen, J. Wen, K. R. Poeppelmeier, M. J. Bedzyk, and L. D. Marks, “Complex surface structure of (110) terminated strontium titanate nanododecahedra”, *Nanoscale* **8**, 16606–16611 (2016).
- <sup>34</sup>X.-L. Wang and Z. Yang, “Hydrothermal Synthesis and Characterization of LaAlO<sub>3</sub>:0.05Eu<sup>3+</sup> Microcrystals”, *Chemical Journal of Chinese Universities* **34**, 36–39 (2013).
- <sup>35</sup>X.-L. Wang, Z. Yang, J. Li, W.-F. Fu, P. Tang, Y.-F. Chen, J. Guo, Z.-H. Gao, Y. Huang, and Y. Tao, “Hydrothermal synthesis, morphology and luminescent properties of GdAlO<sub>3</sub>:Eu<sup>3+</sup> microcrystals”, *Journal of Alloys and Compounds* **614**, 40–43 (2014).

- <sup>36</sup>W. C. Sheets, E. Mugnier, A. Barnabé, T. J. Marks, and K. R. Poeppelmeier, “Hydrothermal Synthesis of Delafossite-Type Oxides”, *Chemistry of Materials* **18**, 7–20 (2006).
- <sup>37</sup>M. Kurushkin and D. Kurushkin, “AcidBase Behavior of 100 Element Oxides: Visual and Mathematical Representations”, *Journal of Chemical Education* **95**, 678–681 (2018).
- <sup>38</sup>A. Rabenau, “The Role of Hydrothermal Synthesis in Preparative Chemistry”, *Angewandte Chemie International Edition in English* **24**, 1026–1040 (1985).
- <sup>39</sup>J. Krey, “Dampfdruck und Dichte des Systems  $\text{H}_2\text{ONaOH}$ ”, *Zeitschrift für Physikalische Chemie* **81**, 252 (1972).
- <sup>40</sup>B. Craig, D. Anderson, and A. International, *Handbook of Corrosion Data* (ASM International, 1994).
- <sup>41</sup>E. S. Stampler, W. C. Sheets, W. Prellier, T. J. Marks, and K. R. Poeppelmeier, “Hydrothermal Synthesis of  $\text{LnMnO}_3$  ( $\text{Ln} = \text{Ho-Lu}$  and  $\text{Y}$ ): Exploiting Amphoterism in Late Rare-Earth Oxides”, *Journal of Materials Chemistry* **19**, 4375–4381 (2009).
- <sup>42</sup>J. Tareen and T. R. N. Kutty, “Hydrothermal phase equilibria in  $\text{Ln}_2\text{O}_3\text{-H}_2\text{O}$  systems”, *Proceedings of the Indian Academy of Sciences - Chemical Sciences* **89**, 277–282 (1980).
- <sup>43</sup>M. W. Shafer and R. Roy, “Rare-Earth Polymorphism and Phase Equilibria in Rare-Earth Oxide-Water Systems”, *Journal of the American Ceramic Society* **42**, 563–570 (1959).
- <sup>44</sup>S. Mroczkowski and J. Eckert, “Hydrothermal growth of single crystals of heavy rare earth hydroxides”, *Journal of Crystal Growth* **13-14**, 549–551 (1972).

- <sup>45</sup>S. Wang, X. Wu, T. Wang, J. Zhang, C. Zhang, L. Yuan, X. Cui, and D. Lu, “Mild Hydrothermal Crystallization of Heavy Rare-Earth Chromite  $\text{RECrO}_3$  (RE = Er, Tm, Yb, Lu) Perovskites and Magnetic Properties”, *Inorganic Chemistry* **58**, 2315–2329 (2019).
- <sup>46</sup>H. Perthuis and P. Colomban, “Sol-gel routes leading to nasicon ceramics”, *Ceramics International* **12**, 39–52 (1986).
- <sup>47</sup>R. J. Paull, Z. R. Mansley, T. Ly, L. D. Marks, and K. R. Poeppelmeier, “Synthesis of Gadolinium Scandate from a Hydroxide Hydrogel”, *Inorganic Chemistry* **57**, 4104–4108 (2018).
- <sup>48</sup>C. Zhao, T. Witters, B. Brijs, H. Bender, O. Richard, M. Caymax, T. Heeg, J. Schubert, V. V. Afanasev, A. Stesmans, and D. G. Schlom, “Ternary Rare-Earth Metal Oxide High-k Layers on Silicon Oxide”, *Applied Physics Letters* **86**, 132903 (2005).
- <sup>49</sup>R. Uecker, B. Velickov, D. Klimm, R. Bertram, M. Bernhagen, M. Rabe, M. Albrecht, R. Fornari, and D. G. Schlom, “Properties of Rare-Earth Scandate Single Crystals (Re=NdDy)”, *Journal of Crystal Growth* **310**, 2649–2658 (2008).
- <sup>50</sup>P. Myllymaki, M. Roeckerath, J. M. Lopes, J. Schubert, K. Mizohata, M. Putkonen, and L. Niinisto, “Rare Earth Scandate Thin Films by Atomic Layer Deposition: Effect of the Rare Earth Cation Size”, *Journal of Materials Chemistry* **20**, 4207–4212 (2010).
- <sup>51</sup>H. M. Christen, G. E. Jellison, I. Ohkubo, S. Huang, M. E. Reeves, E. Cicerrella, J. L. Freeouf, Y. Jia, and D. G. Schlom, “Dielectric and Optical Properties of Epitaxial Rare-Earth Scandate Films and Their Crystallization Behavior”, *Applied Physics Letters* **88**, 262906 (2006).

- <sup>52</sup>S. Iacopetti, P. Shekhter, R. Winter, T. C. U. Tromm, J. Schubert, and M. Eizenberg, “The Asymmetric Band Structure and Electrical Behavior of the GdScO<sub>3</sub>/GaN System”, *Journal of Applied Physics* **121**, 205303 (2017).
- <sup>53</sup>R. P. Liferovich and R. H. Mitchell, “A structural study of ternary lanthanide orthoscandate perovskites”, *Journal of Solid State Chemistry* **177**, 2188–2197 (2004).
- <sup>54</sup>S. N. Amanyan, P. A. Arsen’ev, K. S. Bagdasarov, A. M. Kevorkov, D. I. Korolev, A. V. Potemkin, and V. V. Femin, “Synthesis and examination of GdScO<sub>3</sub> single crystals activated by Nd<sup>3+</sup>”, *Journal of Applied Spectroscopy* **38**, 343–348 (1983).
- <sup>55</sup>T. Moeller and H. E. Kremers, “The Basicity Characteristics of Scandium, Yttrium, and the Rare Earth Elements”, *Chemical Reviews* **37**, 97–159 (1945).
- <sup>56</sup>V. Grover, R. Shukla, D. Jain, S. K. Deshpande, A. Arya, C. G. S. Pillai, and A. K. Tyagi, “Complex GdSc<sub>1-x</sub>In<sub>x</sub>O<sub>3</sub> Oxides: Synthesis and Structure Driven Tunable Electrical Properties”, *Chemistry of Materials* **24**, 2186–2196 (2012).
- <sup>57</sup>O. Chaix-Pluchery and J. Kreisel, “Raman scattering of perovskite DyScO<sub>3</sub> and GdScO<sub>3</sub> single crystals”, *Journal of Physics: Condensed Matter* **21**, 175901 (2009).
- <sup>58</sup>C. J. Brinker and G. W. Scherer, *Sol-Gel Science: The Physics and Chemistry of Sol-Gel Processing* (Academic Press, San Diego, 1990), p. 912.
- <sup>59</sup>J. L. Pérez-Díaz, M. A. Álvarez-Valenzuela, and J. C. García-Prada, “The effect of the partial pressure of water vapor on the surface tension of the liquid waterair interface”, *Journal of Colloid and Interface Science* **381**, 180–182 (2012).
- <sup>60</sup>S. L. Nail, J. L. White, and S. L. Hem, “Structure of Aluminum Hydroxide Gel I: Initial Precipitate”, *Journal of Pharmaceutical Sciences* **65**, 1188–1191 (1976).

- <sup>61</sup>R. Deshpande, D.-W. Hua, D. M. Smith, and C. J. Brinker, “Pore structure evolution in silica gel during aging/drying. III. Effects of surface tension”, *Journal of Non-Crystalline Solids* **144**, 32–44 (1992).
- <sup>62</sup>T. Tatsuoka and N. Koga, “Effect of Atmospheric Water Vapor on the Thermally Induced Crystallization in Zirconia Gel”, *Journal of the American Ceramic Society* **95**, 557–564 (2012).
- <sup>63</sup>S. Wang, K. Huang, C. Hou, L. Yuan, X. Wu, and D. Lu, “Low temperature hydrothermal synthesis, structure and magnetic properties of  $\text{RECrO}_3$  (RE = La, Pr, Nd, Sm)”, *Dalton Transactions* **44**, 17201–17208 (2015).
- <sup>64</sup>Y. Wang, X. Lu, Y. Chen, F. Chi, S. Feng, and X. Liu, “Hydrothermal synthesis of two perovskite rare-earth manganites,  $\text{HoMnO}_3$  and  $\text{DyMnO}_3$ ”, *Journal of Solid State Chemistry* **178**, 1317–1320 (2005).
- <sup>65</sup>Z. Zhou, L. Guo, H. Yang, Q. Liu, and F. Ye, “Hydrothermal synthesis and magnetic properties of multiferroic rare-earth orthoferrites”, *Journal of Alloys and Compounds* **583**, 21–31 (2014).
- <sup>66</sup>B. Veličkov, V. Kahlenberg, R. Bertram, and M. Bernhagen, “Crystal chemistry of  $\text{GdScO}_3$ ,  $\text{DyScO}_3$ ,  $\text{SmScO}_3$  and  $\text{NdScO}_3$ ”, *Zeitschrift für Kristallographie* **222**, 466 (2007).
- <sup>67</sup>R. J. Paull, T. Ly, Z. R. Mansley, K. R. Poepfelmeier, and L. D. Marks, “Controlled Two-Step Formation of Faceted Perovskite Rare-Earth Scandate Nanoparticles”, *Crystals* **9** (2019) 10.3390/cryst9040218.
- <sup>68</sup>A. Z. Moshfegh, “Nanoparticle Catalysts”, *Journal of Physics D: Applied Physics* **42**, 233001 (2009).

- <sup>69</sup>E. Ringe, B. Sharma, A.-I. Henry, L. D. Marks, and R. P. Van Duyne, “Single Nanoparticle Plasmonics”, *Physical Chemistry Chemical Physics* **15**, 4110–4129 (2013).
- <sup>70</sup>S. Raj, S. Jose, U. S. Sumod, and M. Sabitha, “Nanotechnology in Cosmetics: Opportunities and Challenges”, *Journal of Pharmacy & Bioallied Sciences* **4**, 186–193 (2012).
- <sup>71</sup>A. K. Basak, A. Pramanik, M. N. Islam, and V. Anandakrishnan, “Challenges and Recent Developments on Nanoparticle-Reinforced Metal Matrix Composites”, in *Fillers and Reinforcements for Advanced Nanocomposites*, edited by Y. Dong, R. Umer, and A. K.-T. Lau (Woodhead Publishing, Sawston, Cambridge, United Kingdom, 2015) Chap. 14, pp. 349–367.
- <sup>72</sup>W. H. De Jong and P. J. A. Borm, “Drug Delivery and Nanoparticles: Applications and Hazards”, *International Journal of Nanomedicine* **3**, 133–149 (2008).
- <sup>73</sup>A. Escudero, I. Becerro Ana, C. Carrillo-Carrión, O. Núñez Nuria, V. Zyuzin Mikhail, M. Laguna, D. González-Mancebo, M. Ocaña, and J. Parak Wolfgang, “Rare earth based nanostructured materials: synthesis, functionalization, properties and bioimaging and biosensing applications”, *Nanophotonics* **6**, 881–921 (2017).
- <sup>74</sup>A. Escudero, C. Carrillo-Carrión, M. V. Zyuzin, and W. J. Parak, “Luminescent Rare-earth-based Nanoparticles: A Summarized Overview of their Synthesis, Functionalization, and Applications”, *Topics in Current Chemistry* **374**, 48 (2016).
- <sup>75</sup>E. Roduner, “Size Matters: Why Nanomaterials Are Different”, *Chemical Society Reviews* **35**, 583–592 (2006).
- <sup>76</sup>A. M. Smith and S. Nie, “Semiconductor Nanocrystals: Structure, Properties, and Band Gap Engineering”, *Accounts of Chemical Research* **43**, 190–200 (2010).

- <sup>77</sup>K. L. Kelly, E. Coronado, L. L. Zhao, and G. C. Schatz, “The Optical Properties of Metal Nanoparticles: The Influence of Size, Shape, and Dielectric Environment”, *Journal of Physical Chemistry B* **107**, 668–677 (2003).
- <sup>78</sup>U. Kreibig, “Electronic Properties of Small Silver Particles: The Optical Constants and Their Temperature Dependence”, *Journal of Physics F: Metal Physics* **4**, 999–1014 (1974).
- <sup>79</sup>J. Varghese, R. W. Whatmore, and J. D. Holmes, “Ferroelectric Nanoparticles, Wires and Tubes: Synthesis, Characterisation and Applications”, *Journal of Materials Chemistry C* **1**, 2618–2638 (2013).
- <sup>80</sup>H. Ge, Y. Huang, Y. Hou, H. Xiao, and M. Zhu, “Size Dependence of the Polarization and Dielectric Properties of KNbO<sub>3</sub> Nanoparticles”, *RSC Advances* **4**, 23344–23350 (2014).
- <sup>81</sup>H. Cheng, N. Yang, Q. Lu, Z. Zhang, and H. Zhang, “Syntheses and Properties of Metal Nanomaterials with Novel Crystal Phases”, *Advanced Materials* **30**, 1707189 (2018).
- <sup>82</sup>I. Lee, R. Morales, M. A. Albiter, and F. Zaera, “Synthesis of Heterogeneous Catalysts with Well Shaped Platinum Particles to Control Reaction Selectivity”, *Proceedings of the National Academy of Sciences* **105**, 15241–15426 (2008).
- <sup>83</sup>G. Collins, M. Schmidt, C. O’Dwyer, D. Holmes Justin, and P. McGlacken Gerard, “The Origin of Shape Sensitivity in Palladium-Catalyzed SuzukiMiyaura Cross Coupling Reactions”, *Angewandte Chemie International Edition* **53**, 4142–4145 (2014).
- <sup>84</sup>G. Geng, P. Chen, B. Guan, L. Jiang, Z. Xu, D. Di, Z. Tu, W. Hao, Y. Yi, C. Chen, M. Liu, and W. Hu, “Shape-Controlled Metal-Free Catalysts: Facet-Sensitive Catalytic

- Activity Induced by the Arrangement Pattern of Noncovalent Supramolecular Chains”, *ACS Nano* **11**, 4866–4876 (2017).
- <sup>85</sup>Y.-F. Sun, S.-B. Liu, F.-L. Meng, J.-Y. Liu, Z. Jin, L.-T. Kong, and J.-H. Liu, “Metal Oxide Nanostructures and Their Gas Sensing Properties: A Review”, *Sensors* **12**, 2610–2631 (2012).
- <sup>86</sup>X. Rao, X. Su, C. Yang, J. Wang, X. Zhen, and D. Ling, “From Spindle-Like  $\beta$ -FeOOH Nanoparticles to  $\alpha$ -Fe<sub>2</sub>O<sub>3</sub> Polyhedral Crystals: Shape Evolution, Growth Mechanism and Gas Sensing Property”, *CrystEngComm* **15**, 7250–7256 (2013).
- <sup>87</sup>J. Jońca, A. Ryzhikov, M. L. Kahn, K. Fajerweg, B. Chaudret, A. Chapelle, P. Menini, and P. Fau, “Shape-Controlled ZnO Nanostructures for Gas Sensing Applications”, *Procedia Engineering* **87**, 907–910 (2014).
- <sup>88</sup>R. Subbiah, M. Veerapandian, and K. S. Yun, “Nanoparticles: Functionalization and Multifunctional Applications in Biomedical Sciences”, *Current Medicinal Chemistry* **17**, 4559–4577 (2010).
- <sup>89</sup>R. Mout, D. F. Moyano, S. Rana, and V. M. Rotello, “Surface Functionalization of Nanoparticles for Nanomedicine”, *Chemical Society Reviews* **41**, 2539–2544 (2012).
- <sup>90</sup>A. G. Kolhatkar, A. C. Jamison, D. Litvinov, R. C. Willson, and T. R. Lee, “Tuning the Magnetic Properties of Nanoparticles”, *International Journal of Molecular Sciences* **14**, 15977–16009 (2013).
- <sup>91</sup>Y. Li, Y. Li, and T. Wang, “The Size and Shape Dependence of Ferromagnetism in Nanomagnets”, *Journal of Nanomaterials* **2012**, 897023 (2012).

- <sup>92</sup>L.-F. Cao, D. Xie, M.-X. Guo, H. S. Park, and T. Fujita, “Size and Shape Effects on Curie Temperature of Ferromagnetic Nanoparticles”, *Transactions of Nonferrous Metals Society of China* **17**, 1451–1455 (2007).
- <sup>93</sup>S. E. A. Gratton, P. A. Ropp, P. D. Pohlhaus, J. C. Luft, V. J. Madden, M. E. Napier, and J. M. DeSimone, “The effect of particle design on cellular internalization pathways”, *Proceedings of the National Academy of Sciences* **105**, 11613–11618 (2008).
- <sup>94</sup>D. W. Hoffman and J. W. Cahn, “A Vector Thermodynamics for Anisotropic Surfaces: I. Fundamentals and Application to Plane Surface Junctions”, *Surface Science* **31**, 368–388 (1972).
- <sup>95</sup>J. I. Cahn and D. I. Hoffman, “A Vector Thermodynamics for Anisotropic Surfaces II. Curved and Faceted Surfaces”, *Acta Metallurgica* **22**, 1205–1214 (1974).
- <sup>96</sup>A. Dinghas, “Über einen geometrischen Satz von Wulff für die Gleichgewichtsform von Kristallen”, *Zeitschrift für Kristallographie - Crystalline Materials* **105**, 304–314 (1943).
- <sup>97</sup>S. Angenent and M. E. Gurtin, “Multiphase Thermomechanics with Interfacial Structure 2. Evolution of an Isothermal Interface”, *Archive for Rational Mechanics and Analysis* **108**, 323–391 (1989).
- <sup>98</sup>E. Yokoyama and R. F. Sekerka, “A Numerical Study of the Combined Effect of Anisotropic Surface Tension and Interface Kinetics on Pattern Formation During the Growth of Two-Dimensional Crystals”, *Journal of Crystal Growth* **125**, 389–403 (1992).
- <sup>99</sup>W. F. Berg, “Crystal Growth from Solutions”, *Proceedings of the Royal Society of London, Series A: Mathematical, Physical and Engineering Sciences* **164**, 79–95 (1938).
- <sup>100</sup>F. S. Ham, “Theory of Diffusion-Limited Precipitation”, *Journal of Physics and Chemistry of Solids* **6**, 335–351 (1958).

- <sup>101</sup>W. K. Burton, N. Cabrera, and F. C. Frank, “The Growth of Crystals and the Equilibrium Structure of Their Surfaces”, Proceedings of the Royal Society of London, Series A: Mathematical, Physical and Engineering Sciences **243**, 299–358 (1951).
- <sup>102</sup>T. Ly, J. Wen, and L. D. Marks, “Kinetic Growth Regimes of Hydrothermally Synthesized Potassium Tantalate Nanoparticles”, Nano Letters **18**, 5186–5191 (2018).
- <sup>103</sup>S. J. Schneider, R. S. Roth, and J. L. Waring, “Solid state reactions involving oxides of trivalent cations”, Journal of Research of the National Bureau of Standards - A. Physics and Chemistry **65A**, 345–374 (1961).
- <sup>104</sup>J. M. Badie and M. Foex, “Determination experimentale, calcul et prevision de certains diagrammes  $\text{Sc}_2\text{O}_3\text{-Ln}_2\text{O}_3$ ”, Journal of Solid State Chemistry **26**, 311–319 (1978).
- <sup>105</sup>D. M. Giaquinta and H.-C. zur Loye, “Structural Predictions in the  $\text{ABO}_3$  Phase Diagram”, Chemistry of Materials **6**, 365–372 (1994).
- <sup>106</sup>T. Heeg, M. Roeckerath, J. Schubert, W. Zander, C. Buchal, H. Y. Chen, C. L. Jia, Y. Jia, C. Adamo, and D. G. Schlom, “Epitaxially stabilized growth of orthorhombic  $\text{LuScO}_3$  thin films”, Applied Physics Letters **90**, 192901 (2007).
- <sup>107</sup>P. Koirala, C. A. Mizzi, and L. D. Marks, “Direct Observation of Large Flexoelectric Bending at the Nanoscale in Lanthanide Scandates”, Nano Letters **18**, 3850–3856 (2018).
- <sup>108</sup>G. A. Somorjai and Y. Li, *Introduction to surface chemistry and catalysis* (John Wiley & Sons, 2010).
- <sup>109</sup>E. S. Sanz-Pérez, C. R. Murdock, S. A. Didas, and C. W. Jones, “Direct Capture of  $\text{CO}_2$  from Ambient Air”, Chemical Reviews **116**, 11840–11876 (2016).

- <sup>110</sup>Z. D. Pozun, K. Tran, A. Shi, R. H. Smith, and G. Henkelman, “Why Silver Nanoparticles Are Effective for Olefin/Paraffin Separations”, *The Journal of Physical Chemistry C* **115**, 1811–1818 (2011).
- <sup>111</sup>T. Kozawa, K. Yanagisawa, and Y. Suzuki, “Water Vapor-Assisted Solid-State Reaction for the Synthesis of Nanocrystalline BaZrO<sub>3</sub> powder”, *Journal of the Ceramic Society of Japan* **121**, 308–312 (2013).
- <sup>112</sup>P. V. Klevtsov and L. P. Sheina, “Hydrothermal synthesis and crystal structure of rare-earth hydroxides”, *Izv. Akad. Nauk SSSR, Neorg. Mater* **1**, 912–917 (1965).
- <sup>113</sup>P. V. Klevtsov and L. P. Sheina, “Thermographic and x-ray studies of crystalline hydroxides of the rare earth elements and yttrium”, *Izv. Akad. Nauk SSSR, Neorg. Mater* **1**, 2219–2226 (1965).
- <sup>114</sup>V. S. Sastri, J.-C. Bunzli, V. R. Rao, G. V. S. Rayudu, and J. R. Perumareddi, “Chapter 8 - spectroscopy of lanthanide complexes”, in *Modern aspects of rare earths and their complexes*, edited by V. S. Sastri, J.-C. Bunzli, V. R. Rao, G. V. S. Rayudu, and J. R. Perumareddi (Elsevier, Amsterdam, 2003), pp. 569–731.
- <sup>115</sup>J. Jung, M. Atanasov, and F. Neese, “Ab Initio Ligand-Field Theory Analysis and Covalency Trends in Actinide and Lanthanide Free Ions and Octahedral Complexes”, *Inorganic Chemistry* **56**, 8802–8816 (2017).
- <sup>116</sup>W. Kohn and L. J. Sham, “Self-Consistent Equations Including Exchange and Correlation Effects”, *Physical Review* **140**, A1133–A1138 (1965).
- <sup>117</sup>C. A. Mizzi, P. Koirala, and L. D. Marks, “Electronic structure of lanthanide scandates”, *Physical Review Materials* **2**, 025001 (2018).

- <sup>118</sup>Y. Kanke and A. Navrotsky, “A Calorimetric Study of the Lanthanide Aluminum Oxides and the Lanthanide Gallium Oxides: Stability of the Perovskites and the Garnets”, *Journal of Solid State Chemistry* **141**, 424–436 (1998).
- <sup>119</sup>X. Ke, C. Adamo, D. G. Schlom, M. Bernhagen, R. Uecker, and P. Schiffer, “Low temperature magnetism in the perovskite substrate  $\text{DyScO}_3$ ”, *Applied Physics Letters* **94**, 152503 (2009).
- <sup>120</sup>R. L. Sandstrom, E. A. Giess, W. J. Gallagher, A. Segmüller, E. I. Cooper, M. F. Chisholm, A. Gupta, S. Shinde, and R. B. Laibowitz, “Lanthanum gallate substrates for epitaxial hightemperature superconducting thin films”, *Applied Physics Letters* **53**, 1874–1876 (1988).
- <sup>121</sup>D. C. Dube, H. J. Scheel, I. Reaney, M. Daglish, and N. Setter, “Dielectric properties of lanthanum gallate ( $\text{LaGaO}_3$ ) crystal”, *Journal of Applied Physics* **75**, 4126–4130 (1994).
- <sup>122</sup>M. Feng, J. B. Goodenough, K. Huang, and C. Milliken, “Fuel cells with doped lanthanum gallate electrolyte”, *Journal of Power Sources* **63**, 47–51 (1996).
- <sup>123</sup>X. Liu and J. Lin, “ $\text{Dy}^{3+}$ - and  $\text{Eu}^{3+}$ -doped  $\text{LaGaO}_3$  nanocrystalline phosphors for field emission displays”, *Journal of Applied Physics* **100**, 124306 (2006).
- <sup>124</sup>A. Kumar and A. S. Verma, “Lattice constant of orthorhombic perovskite solids”, *Journal of Alloys and Compounds* **480**, 650–657 (2009).
- <sup>125</sup>M. P. Pechini, “Method of Producing High Purity Ceramic Dielectric Materials”, pat. CA759514A (1967).
- <sup>126</sup>M. P. Pechini, “Barium Titanium Citrate, Barium Titanate and Processes for Producing Same”, pat. US3231328A (1967).

- <sup>127</sup>A. E. Danks, S. R. Hall, and Z. Schnepp, “The evolution of ‘sol-gel’ chemistry as a technique for materials synthesis”, *Materials Horizons* **3**, 91–112 (2016).
- <sup>128</sup>F. Belkhiria, F. I. H. Rhouma, S. Hcini, M. Daoudi, H. Gammoudi, M. Amlouk, and R. Chtourou, “Polycrystalline  $\text{La}_{0.8}\text{Sr}_{0.2}\text{GaO}_3$  perovskite synthesized by solgel process along with temperature dependent photoluminescence”, *Journal of Luminescence* **181**, 1–7 (2017).
- <sup>129</sup>V. Berbenni, C. Milanese, G. Bruni, and A. Marini, “Thermal decomposition of gallium nitrate hydrate  $\text{Ga}(\text{NO}_3)_3 \times x\text{H}_2\text{O}$ ”, *Journal of Thermal Analysis and Calorimetry* **82**, 401–407 (2005).
- <sup>130</sup>H. Y. Playford, A. C. Hannon, E. R. Barney, and R. I. Walton, “Structures of Uncharacterised Polymorphs of Gallium Oxide from Total Neutron Diffraction”, *Chemistry A European Journal* **19**, 2803–2813 (2013).
- <sup>131</sup>M. Marezio, J. P. Remeika, and P. D. Dernier, “High pressure synthesis of  $\text{YGaO}_3$ ,  $\text{GdGaO}_3$  and  $\text{YbGaO}_3$ ”, *Materials Research Bulletin* **1**, 247–255 (1966).
- <sup>132</sup>M. Marezio, J. P. Remeika, and P. D. Dernier, “Rare earth orthogallates”, *Inorganic Chemistry* **7**, 1337–1340 (1968).
- <sup>133</sup>M. Haruta, “When Gold Is Not Noble: Catalysis by Nanoparticles”, *The Chemical Record* **3**, 75–87 (2003).
- <sup>134</sup>M. Haruta, T. Kobayashi, H. Sano, and N. Yamada, “Novel Gold Catalysts for the Oxidation of Carbon Monoxide at a Temperature far Below 0 °C”, *Chemistry Letters* **16**, 405–408 (1987).
- <sup>135</sup>T. Takei, I. Okuda, K. K. Bando, T. Akita, and M. Haruta, “Gold clusters supported on  $\text{La}(\text{OH})_3$  for CO oxidation at 193K”, *Chemical Physics Letters* **493**, 207–211 (2010).

- <sup>136</sup>J. Saavedra, T. Whittaker, Z. Chen, C. J. Pursell, R. M. Rioux, and B. D. Chandler, “Controlling activity and selectivity using water in the Au-catalysed preferential oxidation of CO in H<sub>2</sub>”, *Nature Chemistry* **8**, 584–589 (2016).
- <sup>137</sup>B. N. Reinecke, K. P. Kuhl, H. Ogasawara, L. Li, J. Voss, F. Abild-Pedersen, A. Nilsson, and T. F. Jaramillo, “Elucidating the electronic structure of supported gold nanoparticles and its relevance to catalysis by means of hard X-ray photoelectron spectroscopy”, *Surface Science* **650**, 24–33 (2016).
- <sup>138</sup>M. S. Ide and R. J. Davis, “The Important Role of Hydroxyl on Oxidation Catalysis by Gold Nanoparticles”, *Accounts of Chemical Research* **47**, 825–833 (2014).
- <sup>139</sup>R. Zanella, S. Giorgio, C.-H. Shin, C. R. Henry, and C. Louis, “Characterization and reactivity in CO oxidation of gold nanoparticles supported on TiO<sub>2</sub> prepared by deposition-precipitation with NaOH and urea”, *Journal of Catalysis* **222**, 357–367 (2004).
- <sup>140</sup>I. Laoufi, M. C. Saint-Lager, R. Lazzari, J. Jupille, O. Robach, S. Garaudée, G. Cabailh, P. Dolle, H. Cruguel, and A. Bailly, “Size and Catalytic Activity of Supported Gold Nanoparticles: An in Operando Study during CO Oxidation”, *The Journal of Physical Chemistry C* **115**, 4673–4679 (2011).
- <sup>141</sup>Q. Jiang, L. H. Liang, and D. S. Zhao, “Lattice Contraction and Surface Stress of fcc Nanocrystals”, *The Journal of Physical Chemistry B* **105**, 6275–6277 (2001).
- <sup>142</sup>I. N. Leontyev, A. B. Kuriganova, N. G. Leontyev, L. Hennet, A. Rakhmatullin, N. V. Smirnova, and V. Dmitriev, “Size dependence of the lattice parameters of carbon supported platinum nanoparticles: X-ray diffraction analysis and theoretical considerations”, *RSC Advances* **4**, 35959–35965 (2014).

- <sup>143</sup>M. B. Mitchell, “Fundamentals and applications of diffuse reflectance infrared fourier transform (drift) spectroscopy”, in *Structure-property relations in polymers*, Vol. 236, Advances in Chemistry (American Chemical Society, 1993) Chap. 13, pp. 351–375.
- <sup>144</sup>G. Bergerhoff, I. D. Brown, and F. Allen, “Crystallographic databases”, International Union of Crystallography, Chester **360**, 77–95 (1987).
- <sup>145</sup>V. J. Cybulskis, J. Wang, J. H. Pazmiño, F. H. Ribeiro, and W. N. Delgass, “Isotopic transient studies of sodium promotion of Pt/Al<sub>2</sub>O<sub>3</sub> for the watergas shift reaction”, *Journal of Catalysis* **339**, 163–172 (2016).
- <sup>146</sup>L. J. Santos, F. L. Bobadilla, A. M. Centeno, and A. J. Odriozola, “Operando DRIFTS-MS Study of WGS and rWGS Reaction on Biochar-Based Pt Catalysts: The Promotional Effect of Na”, *Journal of Carbon Research* **4** (2018) 10.3390/c4030047.
- <sup>147</sup>S. Saeidi, N. A. S. Amin, and M. R. Rahimpour, “Hydrogenation of co2 to value-added products a review and potential future developments”, *Journal of CO2 Utilization* **5**, 66–81 (2014).
- <sup>148</sup>F. A. Rabuffetti, P. C. Stair, and K. R. Poepelmeier, “Synthesis-dependent surface acidity and structure of sr<sub>2</sub>tio<sub>3</sub> nanoparticles”, *The Journal of Physical Chemistry C* **114**, 11056–11067 (2010).
- <sup>149</sup>R. Z. Mansley, C. A. Mizzi, P. Koirala, J. Wen, and L. D. Marks, “The structure of (110) LnScO<sub>3</sub> (Ln=Gd, Tb, Dy) surfaces”, *Phys. Rev. Mater.*, Under Review (2020).
- <sup>150</sup>L. J. Burcham, L. E. Briand, and I. E. Wachs, “Quantification of Active Sites for the Determination of Methanol Oxidation Turn-over Frequencies Using Methanol Chemisorption and in Situ Infrared Techniques. 1. Supported Metal Oxide Catalysts”, *Langmuir* **17**, 6164–6174 (2001).

- <sup>151</sup>N. Jeong, J. Lee, E. Tae, Y. Lee, and K. Yoon, “Acidity Scale for Metal Oxides and Sanderson’s Electronegativities of Lanthanide Elements”, *Angewandte Chemie International Edition* **47**, 10128–10132 (2008).
- <sup>152</sup>X. Wang, H. Shi, J. H. Kwak, and J. Szanyi, “Mechanism of CO<sub>2</sub> Hydrogenation on Pd/Al<sub>2</sub>O<sub>3</sub> Catalysts: Kinetics and Transient DRIFTS-MS Studies”, *ACS Catalysis* **5**, 6337–6349 (2015).
- <sup>153</sup>X. Li, Z.-J. Zhao, L. Zeng, J. Zhao, H. Tian, S. Chen, K. Li, S. Sang, and J. Gong, “On the role of Ce in CO<sub>2</sub> adsorption and activation over lanthanum species”, *Chemical Science* **9**, 3426–3437 (2018).
- <sup>154</sup>R. J. H. Voorhoeve, D. W. Johnson, J. P. Remeika, and P. K. Gallagher, “Perovskite Oxides: Materials Science in Catalysis”, *Science* **195**, 827 (1977).
- <sup>155</sup>D. Neagu, T.-S. Oh, D. N. Miller, H. Ménard, S. M. Bukhari, S. R. Gamble, R. J. Gorte, J. M. Vohs, and J. T. S. Irvine, “Nano-socketed nickel particles with enhanced coking resistance grown in situ by redox exsolution”, *Nature Communications* **6**, 8120 (2015).
- <sup>156</sup>S. Singh, D. Zubenko, and B. A. Rosen, “Influence of LaNiO<sub>3</sub> Shape on Its Solid-Phase Crystallization into Coke-Free Reforming Catalysts”, *ACS Catalysis* **6**, 4199–4205 (2016).
- <sup>157</sup>D. Burnat, R. Kontic, L. Holzer, P. Steiger, D. Ferri, and A. Heel, “Smart material concept: reversible microstructural self-regeneration for catalytic applications”, *Journal of Materials Chemistry A* **4**, 11939–11948 (2016).
- <sup>158</sup>P. P. Fedorov and S. N. Volkov, “AuCu Phase Diagram”, *Russian Journal of Inorganic Chemistry* **61**, 772–775 (2016).